

MICROCOPY RESOLUTION TEST CHART  
 NATIONAL BUREAU OF STANDARDS-1963-A

2

DTIC FILE COPY

AD-A188 387

# NAVAL POSTGRADUATE SCHOOL

Monterey, California



DTIC  
ELECTE  
JAN 28 1988  
S E D

FINAL TECHNICAL REPORT OF GRANT ATM-83-15175  
"TROPICAL AND MONSOONAL STUDIES"  
by  
Chih-Pei Chang and Roger T. Williams  
January 1988  
Final Report for Period June 1984-November 1987

Approved for public release; distribution unlimited.

Prepared for: National Science Foundation  
Washington, D.C. 20550

88 1 25 038

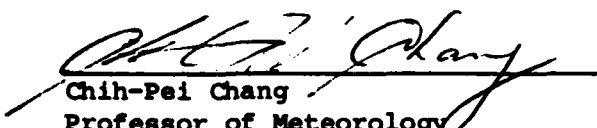
NAVAL POSTGRADUATE SCHOOL  
Monterey, California

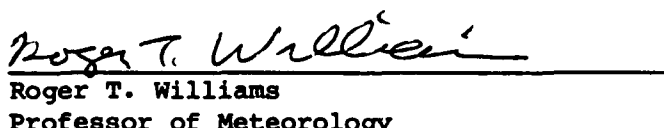
Rear Admiral R. Austin  
Superintendent

K. Marshall  
Provost (Acting)

The work reported herein was supported by the National Science Foundation, Division of Atmospheric Sciences, Global Atmospheric Research Program, under Grant ATM83-15175. Supplemental support for international travel to Taiwan was provided by the National Science Foundation, Division of International Programs, AIT-CCNA Cooperative Research Program, under Grant INT85-06450.

This report was prepared by:

  
Chih-Pei Chang  
Professor of Meteorology  
Department of Meteorology

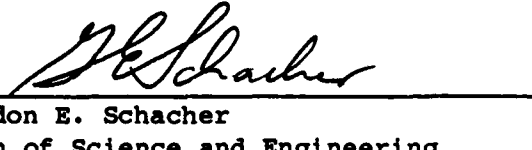
  
Roger T. Williams  
Professor of Meteorology  
Department of Meteorology

Publication of the report does not constitute approval of the sponsor for the findings or conclusions. It is published for information and for the exchange and stimulation of ideas.

Reviewed by:

Released by:

  
Robert J. Renard  
Chairman  
Department of Meteorology

  
Gordon E. Schacher  
Dean of Science and Engineering

REPORT DOCUMENTATION PAGE

ADP 188 387

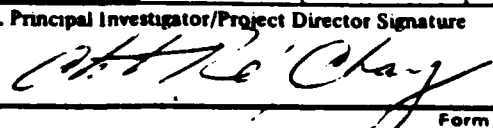
1a REPORT SECURITY CLASSIFICATION Unclassified		1b RESTRICTIVE MARKINGS	
2a SECURITY CLASSIFICATION AUTHORITY		3 DISTRIBUTION/AVAILABILITY OF REPORT Approved for public release; distribution unlimited.	
2b DECLASSIFICATION/DOWNGRADING SCHEDULE		5 MONITORING ORGANIZATION REPORT NUMBER(S)	
4 PERFORMING ORGANIZATION REPORT NUMBER(S) NPS-63-88-001		7a NAME OF MONITORING ORGANIZATION	
6a NAME OF PERFORMING ORGANIZATION Naval Postgraduate School	6b OFFICE SYMBOL (if applicable) 63	7b ADDRESS (City, State, and ZIP Code)	
6c ADDRESS (City, State, and ZIP Code) Monterey, California 93943		9 PROCUREMENT INSTRUMENT IDENTIFICATION NUMBER N6227184WE0094	
8a NAME OF FUNDING/SPONSORING ORGANIZATION National Science Foundation	8b OFFICE SYMBOL (if applicable) GARP	10 SOURCE OF FUNDING NUMBERS	
8c ADDRESS (City, State, and ZIP Code) Washington, D.C. 20550		PROGRAM ELEMENT NO	TASK NO
		PROJECT NO	WORK UNIT ACCESSION NO
11 TITLE (include Security Classification) Final Technical Report of Grant ATM-15175 "Tropical and Monsoon Studies"			
12 PERSONAL AUTHOR(S) Chih-Pei Chang and Roger T. Williams			
13a TYPE OF REPORT Technical	13b TIME COVERED FROM 6/1/84 TO 11/30/87	14 DATE OF REPORT (Year, Month, Day) January, 1988	15 PAGE COUNT 169
16 SUPPLEMENTARY NOTATION			
17a CUSAT CODES FIELD GROUP SUB-GROUP		17b SUBJECT TERMS (Continue on reverse if necessary and identify by block number) Tropical Meteorology Monsoon	
19 ABSTRACT (Continue on reverse if necessary and identify by block number) This project studies a variety of large-scale motions in the tropics and subtropics, particularly those associated with the Asian monsoon circulations. It consists of four parts: 1) <u>Theoretical studies of planetary scale motion forced by tropical heating.</u> The effects of vertical shear, vertical differential damping and planetary boundary layer were found to influence the forcing of midlatitude motions by tropical heat sources. In addition, the vertical interaction of simple modes may be responsible for the maintenance of the eastward propagating 30-50 day oscillations. 2) <u>Observational studies of planetary scale motions.</u> The day-to-day variation of the East Asian Jet was found to correlate positively with that of the tropical divergent flow south of it, suggesting the importance of tropical forcing through the local Hadley cell. The transient forcing of time-mean planetary scale circulation was also studied using a nine-year data set.			
20 DISTRIBUTION/AVAILABILITY OF ABSTRACT <input type="checkbox"/> UNCLASSIFIED UNLIMITED <input type="checkbox"/> SAME AS RPT <input type="checkbox"/> DTIC USERS		21 ABSTRACT SECURITY CLASSIFICATION	
22a NAME OF RESPONSIBLE INDIVIDUAL		22b TELEPHONE (include Area Code)	22c OFFICE SYMBOL

(continued on back)

Block 9, continued.

- 3) Theoretical studies of zonal asymmetry. Several differences between parallel flow and non-parallel flow instabilities in terms of spatial and time growth rates were found using the two-scale technique.
- 4) Studies of the Mei-Yu system of the East Asian summer monsoon. A numerical experiment suggested that the Low-Level Jet associated with intense Mei-Yu fronts receives energy through an equatorward, convection-driven secondary circulation which is quite different from the cross-frontal circulation associated with dry fronts.

# APPENDIX VII

<b>NATIONAL SCIENCE FOUNDATION</b> Washington, D.C. 20550		<b>FINAL PROJECT REPORT</b> NSF FORM 98A			
PLEASE READ INSTRUCTIONS ON REVERSE BEFORE COMPLETING					
<b>PART I-PROJECT IDENTIFICATION INFORMATION</b>					
1. Institution and Address Naval Postgraduate School Monterey, CA 93943	2. NSF Program GARP	3. NSF Award Number ATM 8315175	4. Award Period From 6/1/84 To 11/30/87		
		5. Cumulative Award Amount 312,100			
6. Project Title Tropical and Monsoon Studies					
<b>PART II-SUMMARY OF COMPLETED PROJECT (FOR PUBLIC USE)</b>					
<p>This project studies a variety of large-scale motions in the tropics and subtropics particularly those associated with the Asian monsoon circulations. It consists of four parts; --</p> <p>(1) <u>Theoretical studies of planetary scale motion forced by tropical heating:</u> The effects of vertical shear, vertical differential damping and planetary boundary layer were found to influence the forcing of midlatitude motions by tropical heat sources. In addition, the vertical interaction of simple modes may be responsible for the maintenance of the eastward propagating 30-50 day oscillations:</p> <p>(2) <u>Observational studies of planetary scale motions:</u> The day-to-day variation of the East Asian Jet was found to correlate positively with that of the tropical divergent flow south of it, suggesting the importance of tropical forcing through the local Hadley cell. The transient forcing of time-mean planetary scale circulation was also studied using a nine-year data set:</p> <p>(3) <u>Theoretical studies of zonal asymmetry:</u> Several differences between parallel flow and non-parallel flow instabilities in terms of spatial and time growth rates were found using the two-scale technique:</p> <p>(4) <u>Studies of the Mei-Yu system of the East Asian summer monsoon:</u> A numerical experiment suggested that the Low-Level Jet associated with intense Mei-Yu fronts receives energy through an equatorward, convection-driven secondary circulation which is quite different from the cross-frontal circulation associated with dry fronts.</p>					
<b>PART III-TECHNICAL INFORMATION (FOR PROGRAM MANAGEMENT USES)</b>					
1. ITEM (Check appropriate blocks)	NONE	ATTACHED	PREVIOUSLY FURNISHED	TO BE FURNISHED SEPARATELY TO PROGRAM	
				Check (✓)	Approx. Date
a. Abstracts of Theses		X			
b. Publication Citations		X			
c. Data on Scientific Collaborators	X				
d. Information on Inventions	X				
e. Technical Description of Project and Results		X			
f. Other (specify) Final Technical Report including the checked items above		X			
2. Principal Investigator/Project Director Name (Typed) Chih-Pei Chang	3. Principal Investigator/Project Director Signature 			4. Date 12/3/87	

## TABLE OF CONTENTS

1.	Description of Research and Results . . . . .	5
2.	Scientific Collaborators . . . . .	9
3.	List of Publications . . . . .	10
4.	Remarks . . . . .	10
5.	Thesis (Chou) . . . . .	105
6.	Thesis (Shield) . . . . .	152
7.	Reprints . . . . .	12
	Initial Distribution List . . . . .	169

<b>Accession For</b>	
NTIS GRA&I	<input checked="" type="checkbox"/>
DTIC TAB	<input checked="" type="checkbox"/>
Unannounced	<input type="checkbox"/>
Justification	
By _____	
Distribution/	
<b>Availability Codes</b>	
<b>Dist</b>	<b>Avail and/or Special</b>
<b>A-1</b>	



## 1. DESCRIPTION OF PROJECT RESULTS

### (i) Theoretical studies of planetary scale motion forced by tropical heating

In the current project we have continued the study of the midlatitude tropical interactions related to tropical heating. Several numerical studies (e.g., Hoskins and Karoly, 1981) have modeled the observed tropical-midlatitude teleconnection patterns. In these models, purely internal (zero at top and bottom boundary) heating in the tropics was used to force prominent external mode Rossby wave responses whose influence covers a large latitudinal and longitudinal span. These responses resemble the observed teleconnection patterns. However, we have pointed out that in the absence of other factors, it is very difficult for internal heating to excite directly such external mode responses (Lim and Chang, 1983). A similar conclusion was also implied by Kasahara (1984). To study this problem, a simple two-level model was used to investigate the effects of vertical shear, differential damping and the planetary boundary layer on the responses to internal heating.

We found that all three effects can allow a transfer of energy from the internal-mode motions, which are directly forced by the internal heating, to external-mode motions. To generate external-mode divergent motions, it is necessary to have a planetary boundary layer or other equivalent effects that force vertical motion at the bottom of the atmosphere. The efficiency of generation increases with the horizontal scale. On the other hand, vertical shear is normally the main mechanism for generating external-mode rotational motions, and the efficiency of generation decreases with horizontal scale. In addition, this efficiency depends strongly on the relative vertical shear (vertical shear divided by vertical mean wind). When the relative vertical shear is  $>1$ , the external mode finally attains an amplitude larger than that of the internal mode. We also solved an initial value problem and found that in tropical regions, the process of energy transfer from internal to external mode motions takes about two weeks to complete. This rather slow rate of energy transfer to external mode motions implies that in a given vertical shear, the responses to a transient heating which lasts for only a few days will have a stronger internal mode (more baroclinic) structure than the response to a steady-state heating. These results were reported in Lim and Chang (1986).

We have also extended the study of heating-forced planetary scale motions to the 30-50 day oscillations which were first observed by Madden and Julian (1971, 1972). Recently there have been many more reports of these oscillations, mainly in the monsoon flows (e.g., Yasunari, 1979; Krishnamurti and Subrahmayan, 1983; Krishnamurti et al., 1985; Murakami et al., 1984; Murakami and Nakazawa, 1985; Lau and Chan, 1985, 1986; Madden, 1986). Two categories of theories have been proposed to explain the observed oscillations: 1) those based on eastward propagating Kelvin waves maintained by cumulus heating (Chang, 1977); and 2) those based on interactions with stationary oscillations of the basic state (Webster, 1983; Goswami and Shukla, 1984; Yamaguta and Hayashi, 1984; Salby and Garcia, 1985; and Anderson and Stevens, 1986).

Since the traditional equatorial wave theory predicts very short vertical wavelengths for slow propagation speeds, a theory in the first

category must resolve the apparent discrepancy with the deep vertical structure of the observed oscillations. An earlier attempt was made by Chang (1977), who showed that when cumulus heating and dissipation effects are taken into account, a deep Kelvin wave mode with slow propagation speed arises because of a balance between heating and dissipation. Recent numerical modeling studies using CISK parameterization by Lau and Peng (1987) and Hayashi and Sumi (1987) have simulated certain important aspects of the oscillations, particularly the slower propagation speed as compared to the normal Kelvin waves. Motivated by these results which lends support to the first category, we carried out a linear theoretical analysis of the equatorial beta-plane wave-CISK with a focus on the Kelvin modes.

Our results (reported in Chang and Lim, 1986 and 1987) show that two types of CISK modes may arise from an interaction of vertical modes. For heating with a maximum in the lower troposphere, the instability is due to the lowest internal mode which gives a stationary, east-west symmetrical structure. When heating is maximum in the mid-troposphere, eastward propagating CISK modes occur resembling the observed and numerically-simulated oscillations. These modes result from the interaction between two internal modes which are locked in-phase vertically. A time-lagged CISK analysis suggests that the shallower mode, with its stronger influence on the low-level moisture convergence, slows down the deeper mode resulting in a combined mode which has a deep vertical structure and a relatively slow propagating speed. This slower phase speed may also be understood from the consideration of two effects: a CISK growth mechanism which is analogous to the viscous effect discussed by Chang (1977), and the reduction in effective static stability. A single mode analysis also suggests that the Rossby modes are less likely to become unstable. The results further imply that, in the absence of wave-CISK, the observed eastward propagating oscillations cannot be excited by stationary oscillations.

(ii) Observational studies of planetary scale motions during winter

This component was pursued on two fronts. For the synoptic time scale the results of our previous cold surge studies suggested a short-term midlatitude-tropical interaction such that the variations of the midlatitude jet over East Asia corresponds to variations in tropical convection. However, since cold surges occur during periods of intensified baroclinicity, it is also possible that the strengthening of the jet may be due entirely to midlatitude baroclinic development rather than any tropical circulation. In the present project the 200 mb wind data for the 1983/84 winter were analyzed to determine the cause and effect in such interactions. Significant positive correlations between the midlatitude jet acceleration and the tropical divergence were found in several regions in the Asia-Pacific Indian Ocean region. Among six major intensifications of the East Asian jet (EAJ) maximum during December 1983, three were related to tropical cyclone cases which led to the conclusion that the midlatitude jet can be influenced effectively by tropical convective activity on a day-to-day basis. The study also confirmed the downstream propagation of the strengthened jet streaks, which is probably due to self-advection, and the existence of thermally indirect circulations at the exit region of the jet, both in the time-

mean and in the transient fields. These results were reported in Chang and Lum (1985).

The other front was on the time mean circulation which was studied using a 9-year (1974/5-1982/3) data set. In order to properly describe the effect of transients, the concept of an extended Eliassen-Palm flux (E-vector) introduced by Hoskins (1983) and the related calculations were used to elucidate the dynamics of the time-mean subtropical jet streaks over East Asia, North America (NA<sub>m</sub>J) and North Africa (NA<sub>f</sub>J). Similarities and differences between the three jets were discussed in terms of transient momentum and vorticity forcings at both the synoptic and low-frequency time scales. The forcings of both time scales are basically barotropic. The exit regions of the EAJ and the NA<sub>m</sub>J are quite similar in structure with respect to many of the transient features, and are very similar to the schematic model presented by Hoskins (1983), but the distribution near the NA<sub>f</sub>J is different. On the other hand, the entrance region of the NA<sub>f</sub>J resembles that of NA<sub>m</sub>J, but not the EAJ. In this regard the NA<sub>f</sub>J may be considered the entrance region of the combined NA<sub>f</sub>J-EAJ system.

For low frequency eddies, both the subtropical E-vector and the tropical transient kinetic energy indicate an equatorward energy propagation and a tropical response at 200 mb over the mid-Pacific where the zonal wind is westerly. This seems to agree with the "westerly duct" theories. However, the maxima of these two fields, which are longitudinally aligned, do not coincide with the maximum tropical westerlies. An analogous situation was not observed over the Atlantic. The low frequency calculations also revealed barotropic instability regions in the exit regions of the EAJ and NA<sub>m</sub>J and poleward of the NA<sub>f</sub>J maximum. This instability distribution agrees with Simmons et al. (1983)'s modeling result near the EAJ, but differs from their results considerably elsewhere.

A comparison of the transient kinetic energy fields at the surface indicates the expected transition of a synoptic time scale maximum on the western side of the ocean basins to a low frequency maximum on the eastern side and further north. This is consistent with the history of baroclinic waves as the waves move east-northeastward while deepening and slowing down. The low frequency fields also tend to have an equivalent barotropic structure apparently due to the vertical development accompanied by deepening (Hoskins, 1983). The transients have little effect on the acceleration of the jet maximum and appear in some regions to have a decelerating effect.

### (iii) Theoretical studies of zonal asymmetry

In this component we have continued the investigation of stability properties of zonally varying mean flow. This topic was motivated by the observation of barotropic energy conversion associated with the 200 mb easterly jet over South Asia during the summer monsoon (Krishnamurti, 1971). The previous results of a linear numerical model by Tupaz, Williams and Chang (1978) on the barotropic stability of a downstream varying easterly jet were extended in a nonlinear modeling study. It was found that the lag effect remains in the nonlinear model, where the disturbance structure lags that of the parallel flow solution for the local mean wind profile. This is especially prominent in regions where the mean flow

changes rapidly downstream. This effect causes a downstream shifting of the growth rate distribution. These results were reported in Williams, Lim and Chang (1984).

The linear barotropic instability problem was also examined analytically with a two-scale expansion technique. It was found that the waves possessed properties which are different from those calculated from local parallel flow theory. The difference, which was obtained at a higher order in the streamwise variation parameter, depends on the first derivative of the parallel flow properties with respect to the streamwise direction. This higher order correction shifts the spatial growth rate profile for the nonparallel flow downstream relative to that for the parallel flow. The correction was found to be due to two effects: the lag effect as revealed by the numerical modeling studies, and an additional effect due to the phase speed difference between the parallel and non-parallel flows. If the disturbance propagates faster than predicted by parallel flow theory, the local spatial growth rate will be smaller than that calculated by the parallel flow and vice versa. The results were reported in Peng and Williams (1986). The accuracy of various formulae which relate the spatial and temporal growth rates for barotropic instability was also studied (Peng and Williams, 1987a).

Using the two-scale expansion, we have also investigated the baroclinic instability problem with a quasi-geostrophic two-layer model. The spatial growth approach was used and cases which could support absolute instability were not considered. It was found that regions of large vertical shear often do not have large spatial growth rates. The correction to the local solution were found to depend on the same effects as were discussed for the barotropic instability by Peng and Williams (1986). In particular, the streamwise correction turns out to be small unless the beta effect is large in comparison with the velocity dependence of the vertical structure of an unstable baroclinic wave on the vertical shear. Consequently, streamwise variations in the vertical shear have little effect on the disturbance structure. These results were reported in Peng and Williams (1987b).

In addition to the instability studies, the non-divergent barotropic vorticity equation was also used to study the beta effect on tropical cyclone motion. An analytical model and a linear numerical model both showed a westward stretching of the vortex due to the beta effect, without significant movement of the vortex center. The inclusion of non-linear terms in the numerical model produced a northwestward movement of the vortex. This movement increases with the maximum wind speed and the radius of maximum wind. A wind maximum was found to the northeast of the vortex, consistent with observations. The development of this asymmetry plays an important role in the motion of the vortex. These results are reported in Chan and Williams (1987).

#### (iv) Studies of the Mei-Yu system of the East Asian summer monsoon

The Mei-Yu system is a quasi-stationary belt of heavy precipitation imbedded in the summer monsoon trough over East Asia. Its influence covers a wide span of area encompassing both subtropical and midlatitude regions (Chen and Chang, 1980; Chen, 1983). In the current project a two

dimensional frontogenesis model (Williams et al., 1981) was used to study the Mei-Yu front, with a focus on its associated low-level jet (LLJ) which often occurs during intense convection. Several numerical experiments were carried out to simulate the quasi-steady frontal structures in different environments. The results resemble many observed features, such as the stronger temperature and moisture gradients in the midlatitude fronts and the stronger horizontal shears and LLJ's in the subtropical fronts. In the model the LLJ is most conspicuous in the subtropical simulation when high humidity and surface fluxes are included. It is developed and maintained through the Coriolis torque exerted by the low-level poleward branch of a "reversed Hadley cell" equatorward of the front. This thermally direct cell is different from the normal cross-frontal secondary circulation and its development depends on the occurrence of intense convection. These results are reported in a Ph.D dissertation by Chou (1986). We have also started other work on the Mei-Yu system, including a composite study of the development of the Mei-Yu front in June and July over southeastern China for a three-year period. This work is based on the calculation of the deformation field and the quasi-geostrophic tendency of potential temperature gradient, or Q-vector (Hoskins et al., 1978), to study the frontogenesis and vertical velocity fields associated with the development of the front. Preliminary results showing the importance of low-level large scale and topographic influences were reported in Chang and Peng (1985) in the 2nd U.S.-P.R.C. Monsoon Workshop. We have also cooperated with Professor George Chen of the National Taiwan University to carry out an evaluation of the numerical weather predictions of the Mei-Yu circulations (Chen, Wang and Chang, 1987).

## **2. SCIENTIFIC COLLABORATORS**

Dr. James S. Boyle, Adjunct Professor, Naval Postgraduate School

Dr. George T.J. Chen, Professor of Atmospheric Sciences, National Taiwan University

Mr. Lang C. Chou, graduate student

Dr. William K. Lau, Research Meteorologist, Goddard Laboratory for Atmospheres,  
NASA

Dr. Hock Lim, Professor of Physics, National University of Singapore

Mr. K.G. Lum, Meteorologist, Malaysian Meteorological Service

Dr. Melinda S. Peng, Adjunct Research Professor, Naval Postgraduate School

Ms. Kathy A. Shield, graduate student, Naval Postgraduate School

## **3. REMARKS**

This research was supported in part by the National Science Foundation, Division of International Programs, under Grant INT85-06450 which provided international travel funds.

This research is being continued under NSF Grant ATM87-11015.

#### 4. LIST OF PUBLICATIONS (INCLUDING THESE)

- Boyle, J., 1986a: Comparison of the synoptic conditions in midlatitudes accompanying cold surges over Eastern Asia for the months of December 1974 and 1978. Part I: Monthly mean fields, individual events and composites. Mon. Wea. Rev., 114, 903-918.
- Boyle, J., 1986b: Comparison of the synoptic conditions in midlatitudes accompanying cold surges over Eastern Asia for the months of December 1974 and 1978. Part II: Time evolution and relations to the general circulation. Mon. Wea. Rev., 114, 918-930.
- Boyle, J. and G.T. Chen, 1988: Synoptic aspects of the Asian winter monsoon. Monsoon Meteorology, Oxford University Press (in press).
- Chan, J., C.-L. Liou and R.T. Williams, 1987: Analytical and numerical studies of the beta-effect in tropical cyclone motion. Part I: Zero mean flow. J. Atmos. Sci., 44, 1257-1265.
- Chang, C.-P., 1984: A review of midlatitude tropical interactions over East Asia during cold surges. Papers Meteorol. Res., 7, 63-71.
- Chang, C.-P. and H. Lim, 1986: "Midlatitude-Tropical Interaction Associated with the Winter Monsoon", Report of the FGGE Seminar on Progress in Tropical Meteorology, GARP Special Report No. 44, World Meteorological Organization, VI 37-52.
- Chang, C.-P. and H. Lim, 1986: Kelvin wave CISK: A possible mechanism for the 30-50 day oscillations. Preprints, Int. Conf. Monsoon and Mesoscale Meteorology, November 1986, Taipei, 236-245.
- Chang, C.-P. and K.G. Lum, 1985: Midlatitude-tropical interaction over the Asia-Pacific region during the 1983-84 winter. Mon. Wea. Rev., 113, 1345-1356.
- Chang, C.-P. and M.S. Peng, 1985: Large-scale features of the summer monsoon fronts over China. Postprints, Second U.S.-P.R.C. Workshop on Monsoon Research, June 1985, Monterey, CA.
- Chen, G.T.J., Y.J. Wang and C.-P. Chang, 1987: Evaluation of the surface prognoses of cyclones and anticyclones of the JMA and FNOC models over East Asia and the western Pacific during the 1983 Mei-Yu season. Mon. Wea. Rev., 115, 235-250.
- Chen, G.T.J., T.E. Gerish and C.-P. Chang, 1986: Structure variations of the synoptic-scale cyclonic disturbances near Borneo during the WMDNEX Period. Papers Met. Res., 9, 117-135.
- Chou, L.C., 1986: A numerical simulation of a Mei-Yu front and the associated low-level jet. Ph.D. Thesis, Naval Postgraduate School, 153 pp.
- Lau, K.M. and C.-P. Chang, 1987: Planetary scale of the winter monsoon and atmospheric teleconnections. Monsoon Meteorology, Oxford University Press, (in press).

- Lau, K.M., J.S. Boyle and C.-P. Chang, 1984: Anomalous diabatic heating and large-scale circulation in the tropics during the 1976-77 and 1982-83 ENSO's. Tropical Atmosphere Newsletter, 24, 12-13.
- Lim, H. and C.-P. Chang, 1986: Generation of internal-and external-mode motions from internal heating: Effects of vertical shear and damping. J. Atmos. Sci., 43, 948-957.
- Lim, H. and C.-P. Chang, 1987: On the dynamics of midlatitude-tropical interactions and the winter monsoon. Monsoon Meteorology, Oxford University Press, (in press).
- Peng, M.S., and R.T. Williams, 1986: Spatial instability of the barotropic jet with slow streamwise variation. J. Atmos. Sci., 43, 2430-2442.
- Peng, M.S. and R.T. Williams, 1987a: A note on the relation between temporal and spatial growth rates. J. Atmos. Sci., 43, 1681-1695.
- Peng, M.S. and R.T. Williams, 1987b: Spatial instability of a baroclinic current with slow streamwise variation. J. Atmos. Sci., 44, 2668-2773.
- Shield, Kathy A., 1985: Possible cross equatorial influence of the Northeast monsoon on the equatorial westerlies over Indonesia. M.S. Thesis, Naval Postgraduate School, 73 pp.
- Williams, R.T., H. Lim and C.-P. Chang, 1984: Nonlinear and linear effects in an easterly jet with downstream variation. J. Atmos. Sci., 41, 621-636.

## Comparison of the Synoptic Conditions in Midlatitudes Accompanying Cold Surges over Eastern Asia for the Months of December 1974 and 1978. Part I: Monthly Mean Fields and Individual Events

JAMES S. BOYLE

*Department of Meteorology, Naval Postgraduate School, Monterey, CA 93943*

(Manuscript received 29 September 1983, in final form 31 October 1985)

### ABSTRACT

East Asian cold surges during two periods of contrasting surge intensity, December 1974 (strong) and December 1978 (weak), are studied. It is shown that the midlatitude mechanisms initiating cold surges during both months are quite similar in nature. Synoptic scale short waves passing through the long-wave trough position near the East Asian coast act to release the cold air southward from the main reservoir over eastern Siberia. Dynamic descent is initiated by these synoptic scale waves entering the northwesterly flow on the western side of the long-wave trough anchored on the coast. This is the descent center in the local direct circulation in the entrance region of the East Asian jet maximum at 200 mb.

The frequency and intensity of the cold air surges for a given month depend on the large scale circulation pattern. The average flow over Asia for December, 1974 and 1978, presents a contrast with respect to ridging over the midcontinent. In December 1978 the flow was characterized by a low zonal index over Asia and the low-level development forced by the smaller scale waves is not well-focused with respect to position. Strong ridging in the middle of the Asian continent during December 1974 yielded a stable pattern for descent on the East Asian coast.

The results indicate that the surge event is not the result of the expansion of an intensifying Siberian anticyclone but of a separate dynamically forced subsidence to the east and southeast of the Siberian anticyclone mean position; nor is the surge directly the result of cyclonic development off the East Asian coast. Such cyclogenesis follows the surge initiation and is triggered by the same synoptic short wave which initiated the surge as the wave passes to the eastern side of the long-wave trough position.

### 1. Introduction

One of the chief motivations for conducting the Winter Monsoon Experiment (Winter MONEX) was to study the cold surges occurring in winter along the coast of eastern Asia. A major objective of the experiment was to assess the link between eastward propagating upper tropospheric troughs and ridges at mid-latitudes and the low-level monsoonal surges which extend to the tropics. The research reported here is an attempt to document the midlatitude synoptic scale dynamics associated with cold surges. It has been well established that eastward moving waves in the baroclinic westerlies are the initiators of winter monsoon cold surges over eastern Asia, (e.g., Murakami, 1979; Danielsen and Ho, 1969; Kung and Chan, 1981; Chin, 1969; Joung and Hitchman, 1982). Murakami (1979) reported that it is the amplification of these disturbances as they reach the East China Sea that provides the impetus to thrust the cold continental air southward.

The nature of the studies of these surge initiation events have thus far taken on two aspects of the problem. The first, as typified by Danielsen and Ho (1969)

and Chu and Park (1984), is the intensive study of an individual event. The second approach is to study time series of data, focusing on composite results rather than individual situations. These investigations are typified, for example, by Chu (1978), Murakami (1979), Chang and Lau (1980), Kung and Chan (1981), Lau et al. (1983) and Lau and Lau (1984), although in some of these works selected cases are considered in detail.

This work and a companion paper, Boyle (1986), consider synoptic scale case studies of individual cold surge events over the period of a month. The emphasis will be on describing the physical mechanism behind each cold surge event, and to delineate the role these events play in the larger scale.

As documented by Chang and Lau (1980) and Chang et al. (1979), the month of December 1974 was one of considerable surge activity. Using the criterion of a surface temperature drop in Hong Kong of at least 6 K within 24 or 48 hours, Chang et al. (1979) have identified at least four strong surges occurring during December 1974. Because of this documented activity, typical of strong surge conditions, December 1974 was chosen as a period to be studied.

The month of December 1978 coincided with the first phase of the Winter MONEX. Thus the data gath-

ering effort for this period was as intense as could be realized. The month of December 1978 also presents an interesting contrast to December 1974. In 1978 the frequency of the surges during December was observed to be near normal (five occurred, Lau and Lau, 1984), but the surges were all somewhat weak, Lau et al. (1983). Comparison of the synoptic conditions of December 1974 and 1978 should provide some insight into the midlatitude circulation conditions which lead to strong surges and those which initiate only weak ones.

Figure 1 consists of time series of departures from the monthly average 1000 mb temperature at Hong Kong for December 1978 and December 1974. The times of the cold surges for the respective months are also indicated on the figure. The temperature at Hong Kong is used as a reference because of the interest in the cold surge as an event thrusting cold air equatorward. The position of Hong Kong at 20°N makes the measurements there a reliable indicator of cold air penetrating into the subtropics. In general, the surges of December 1974 have a greater negative excursion in the temperature deviation and have a longer time scale than those of December 1978.

The structure of the paper is as follows. The next section will provide details of the data sources and data handling procedures, as well as details of the various computational techniques. Section 3 presents a comparison of some of the monthly mean fields for December 1974 and 1978, both of which, will be compared to longer term climatology. Section 4 presents the documentation for one surge in each of the two Decembers. Those characteristics which have been ob-

served to be present in all surges will be pointed out. The final section will provide a summary of the results.

## 2. Data handling and computation procedures

### a. Data

The data for December 1974 was restricted to that available from the Navy Fleet Numerical Oceanography Center's (FNOC) gridded analyses. FNOC, at that time, produced two types of analysis on two different map projections. The first were, essentially, hemispheric analyses of heights and temperatures at mandatory levels up to 100 mb on a polar stereographic grid with a grid length of 381 km at 60°N. Wind analyses were available on a mercator grid with a grid length of 257 km at 20°N. The mercator grid extended from 60°N to 40°S and provided wind data at the surface and at 700, 400, 250 and 200 mb. The analysis technique was a successive corrections approximation adjusted using a variational calculus scheme, (Lewis and Grayson, 1972).

The data for December 1978 were the level III-B First Garp Global Experiment (FGGE) analyses generated by the European Center for Medium Range Weather Forecasts (ECMWF) and obtained from World Data Center (WDC-A) at Asheville, NC. These analyses were performed on a global latitude, longitude grid with a mesh size of 1.875 degrees using a multivariate optimum interpolation analysis scheme, Lorenc (1981). The fields provided were of heights, temperature, relative humidity, and wind at mandatory levels. Also included in these data were fields of pressure velocity ( $Dp/Dt$ ) which were obtained from the nonlinear normal modes initialization procedure. It should also be noted that the temperatures were not directly analyzed, but are the fields consistent with the mass and wind fields after the initialization has been performed. In order to facilitate comparison with the FNOC data, the ECMWF data were interpolated using a 16-point Bessel interpolation scheme to the FNOC polar stereographic and mercator grid. However the grid length of the polar stereographic grid was reduced by a half (190.5 km) to take advantage of the denser data in the ECMWF fields.

The ECMWF dataset, since it represents the culmination of the FGGE effort, is no doubt superior to the operational data of FNOC. The ECMWF fields evince a smoothness and consistency not found in the FNOC data. Nonetheless the FNOC data is adequate for comparison of the basic synoptic scale features of the December 1974 flow. The density of the wind data in the vertical is inferior in the FNOC fields; the ECMWF data having twice the number of analyzed levels in the vertical. The FNOC wind data is best in the lowest and highest parts of the troposphere, which allows it to be useful in this work. We will be considering space scales large enough that the relatively coarse

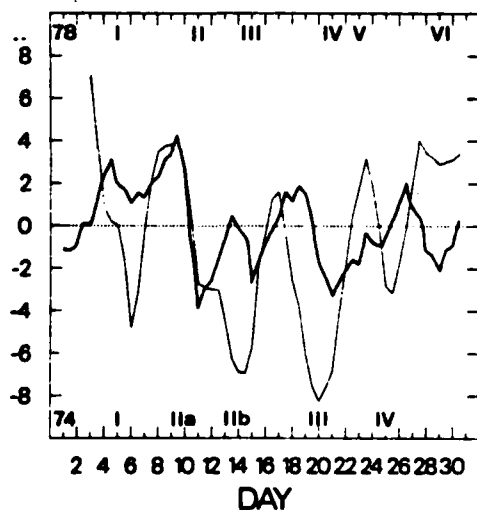


FIG. 1. Time series of deviations from the monthly mean 1000 mb temperature for a 5 × 5 degree latitude-longitude grid centered on 115°E, 24°N (Hong Kong) for December 1974 (thin line) and December 1978 (thick line). The ticks on the bottom are 12 hours apart. The roman numerals (I, II, etc.) designate cold surge events for the indicated year.

resolution of the FNOC data should not interfere with the interpretation.

### b. Computations

For both datasets the rotational and divergent parts of the wind were computed from the analyzed wind fields using the technique of Endlich (1967). This is an iterative procedure which does not require any assumptions about the nature of the wind field at the grid boundaries. It has been successfully used in other synoptic studies, (Chen et al., 1978).

The ECMWF global prediction model which provided the first-guess field for the objective analysis was initialized using an adiabatic, normal modes procedure. The consequence of the initialization is that the analysis seriously underestimates the divergent wind in the tropics (Kung and Tanaka, 1983; and Lau, 1984). The work presented here is restricted to latitudes poleward of 20°N and in these regions the ECMWF divergent wind is acceptable. Cross sections of the monthly mean of the meridional component of the divergent wind along 120°E from 60° to 20°N were prepared for both the ECMWF and FNOC data. These sections compare favorably with the wintertime average pattern of the ageostrophic meridional wind presented by Lau (1978, his Fig. 15b). The agreement is good in that with respect to the jet axis there is northerly ageostrophic flow in the lower troposphere and southerly ageostrophic flow at jet level in all the datasets. This result gives some confidence that the divergent wind north of 20°N is meaningful in both the ECMWF and FNOC data. In addition, Chang and Lum (1985) have found the FNOC wind data to be useful in describing daily variations in the divergent wind.

On the polar stereographic grid, quasi-geostrophic pressure velocity was calculated using the quasi-geostrophic omega equation given by Holton (1979, p. 180). A useful complementary approach to the omega equation for diagnosing the quasi-geostrophic forcing is to compute Q vectors. The Q vector is defined by Hoskins et al. (1978) and can be written in pressure coordinates as follows

$$Q = -\left(\frac{\partial V_x}{\partial x} \cdot \nabla \theta, \frac{\partial V_x}{\partial y} \cdot \nabla \theta\right),$$

where:  $V_x$  is the geostrophic wind and  $\theta$  is the potential temperature.  $V_x$  is computed from the analyzed height fields,  $\theta$  from the temperature fields. As described by McGinley (1982) and Hoskins and Pedder (1980), the sense of the secondary circulation is with the Q vector pointing in the direction of the lower-level ageostrophic motion and toward rising motion. Convergence (divergence) of the Q vectors implies ascent (descent). In frontogenetic regions the Q vectors will have a component across the isotherms from cold to warm air and vice-versa for frontolytic regions.

## 3. Monthly mean fields

### a. Introduction

The mean fields described in this section are simple averages taken over the 62 twelve-hour time periods that make up the synoptic times of the month. In order to compare the present monthly means with longer-term climatological data we will use the circulation statistics compiled by Crutcher and Meserve (1970), hereafter referred to by CM. The monthly mean data of CM is based on a maximum of 15 years of rawinsonde observations which were then averaged and contoured to produce the mean fields.

### b. Mean fields discussion

Figure 2 presents the monthly mean 1000 mb height, the 1000–500 mb thickness, the 300 mb height, and the 300–100 mb thickness for December 1974 and December 1978. In discussing the mean 700 mb height field for December 1974, Taubensee (1975) noted that there was a strong thermal gradient along the east coast of Asia, and a ridge dominated the circulation over Asia yielding northwesterly flow over central and northern Asia. These features are evident in Figs. 2a and 2c. The 1000–500 mb thickness contours indicate an intense baroclinic zone off the East Asian coast. The 300–100 mb thickness and 300 mb height pattern yield geostrophic cold advection over the position of the 1000 mb Siberian anticyclone. Such a configuration is noted by Fleagle (1947) to be important in anticyclogenesis. The Siberian anticyclone for December 1974 was stronger than the CM value by about 15 mb but was in virtually the same geographical location.

Taubensee (1979) describes the December 1978 700 mb flow as being characterized by above normal, temperature latitude (35°–55°N), westerly flow, with prominent blocking action over Greenland. A 700 mb trough over eastern Siberia was well-established and there were thermal fields favorable for baroclinic development to the north near Kamchatka. Figures 2b and 2d display similar characteristics. The 300 mb flow in Fig. 2d is fairly zonal over much of Asia, and the geostrophic cold advection aloft is not as well focused over the position of the Siberian anticyclone as it was in December 1974. The mean December 1978 Siberian anticyclone at 1000 mb was 105 m (about 14 mb) lower than the corresponding feature in December 1974 and located ten degrees farther to the south. The 1000–500 mb thickness trough over eastern Siberia is restricted to the north central and northeastern sections. This leads to a less intense baroclinic zone off the mid-East Asian coast than in December 1974. It should be noted that smaller values of thickness penetrate farther southward in December 1978. Thus, the lower troposphere is colder in the mean over southern China in December 1978, but the surface temperature devia-

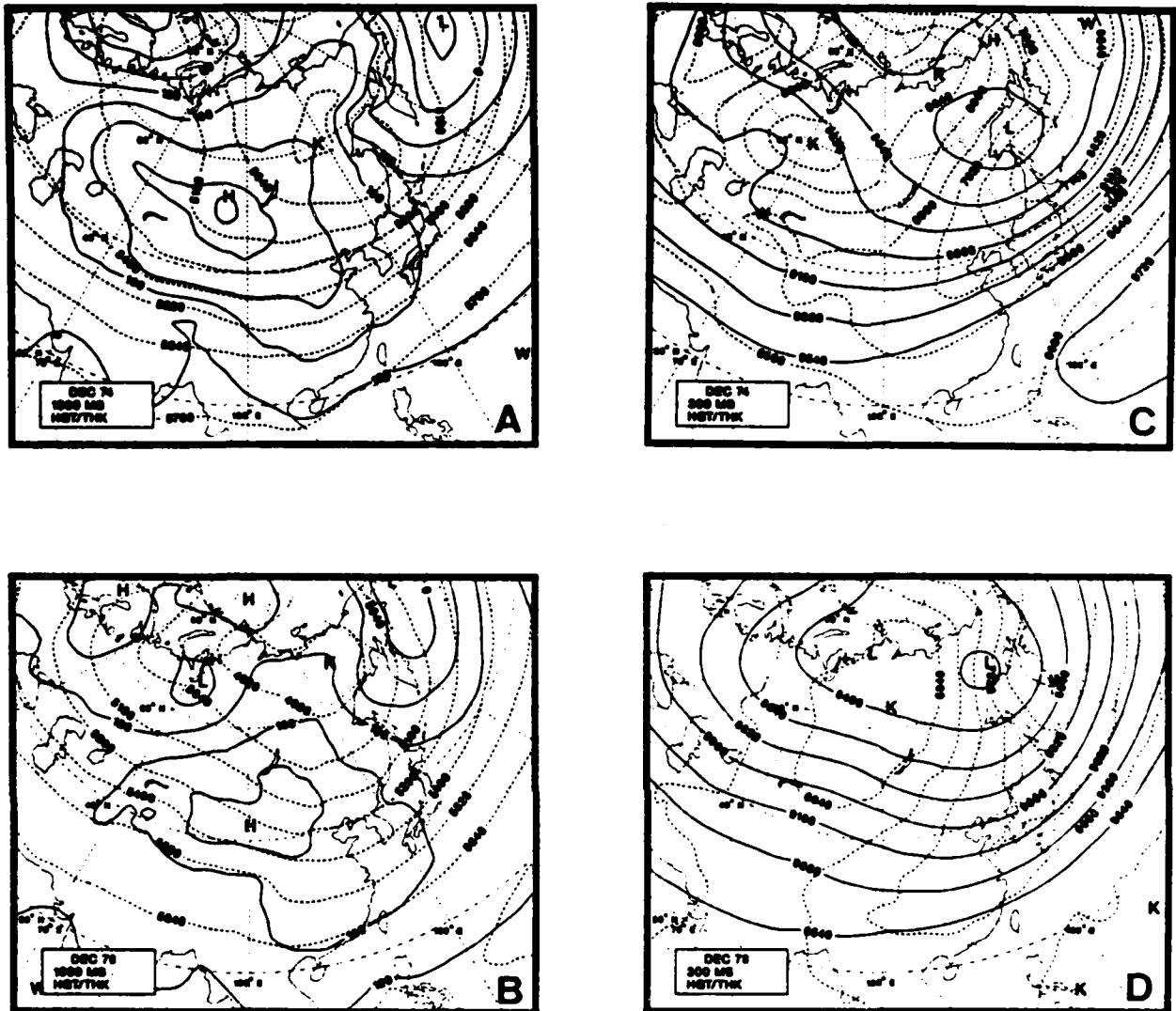


FIG. 2. (a) Average 1000 mb heights and 1000 to 500 mb thickness for December 1974. Contour interval is 30 m for the heights (solid) and 60 m for the thickness (dashed). Thickness maxima (minima) are labeled with  $W(K)$ . Height maxima (minima) are labeled with  $H(L)$ . (b) As in (a) except for December 1978. (c) Average 300 mb heights and 100 to 300 mb thickness for December 1974. Contour interval is 90 m for the heights (solid) and 45 m for the thickness (dashed). (d) As in (c) except for December 1978.

tions on synoptic time scales are greater in December 1974.

December 1974 over Asia appears to be an amplified version of the normals (CM). The positions of the major features are about normal but of greater intensity. In December 1978, the main features shift southward. December 1974 could be characterized as a low index type flow over Asia while December 1978 is a high index situation. The 700 mb anomaly fields for December 1974 and December 1978, presented in Taubensee (1975, 1979), demonstrate a difference between the two fields of almost 300 m at  $65^{\circ}\text{E}$ ,  $50^{\circ}\text{N}$  where a ridge in 1974 has been replaced by a weak trough in 1978. If the cold surge events are initiated by baroclinic events in midlatitudes one would expect the low index

flow of December 1974 to produce intense, well-spaced events while the high index flow of 1978 should yield less intense, shorter lived but more frequent surges. This is what is observed in comparing the surge events of the two months (see Fig. 1). In 1974 the strength of the surges seems to be due to the additive effect of short surges focussed by an enduring long wave.

The lower and upper level height fields for December 1974 and December 1978 bear a strong resemblance to the opposite polarities of the Siberian and Chinese patterns identified by Hsu and Wallace (1985). These strongly baroclinic patterns of low-pass time filtered data were associated with the cold surge phenomena by Hsu and Wallace (1985).

The mean 200 mb wind fields for December 1974

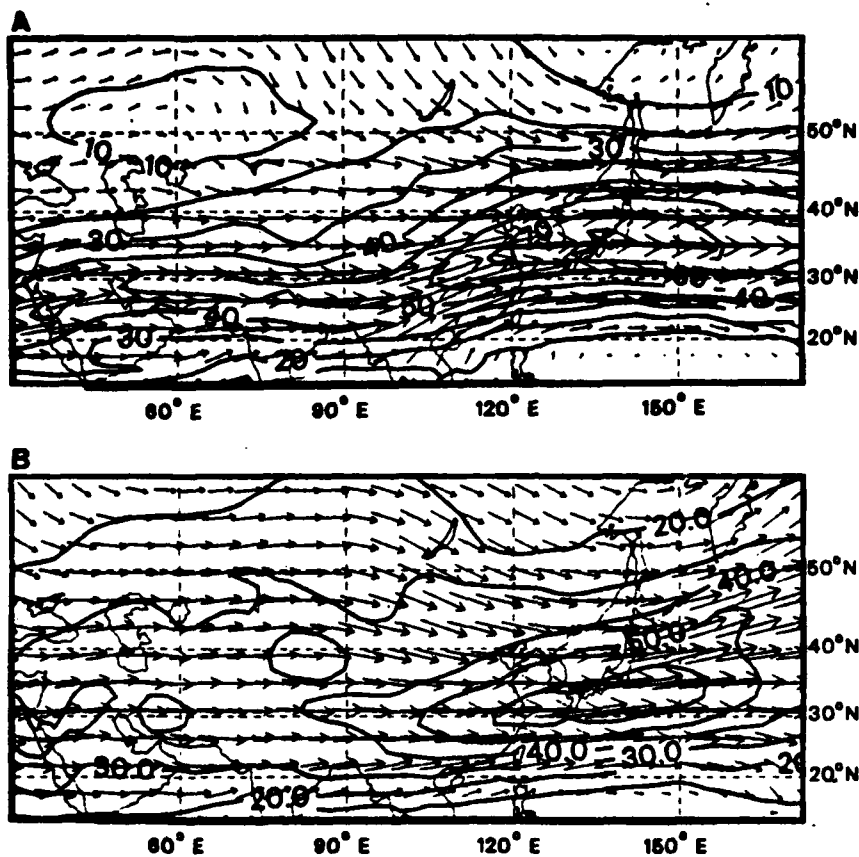


FIG. 3. Average 200 mb wind vectors and isotachs for (a) December 1974 and (b) December 1978. Contour interval for the isotachs is  $20 \text{ m s}^{-1}$ .

and December 1978 are shown in Fig. 3. The jet maximum in 1974 is about  $80 \text{ m s}^{-1}$  at  $37^\circ\text{N}$ ,  $135^\circ\text{E}$  which is farther north and stronger than the  $72 \text{ m s}^{-1}$  jet at  $34^\circ\text{N}$ ,  $136^\circ\text{E}$ , of CM. The ridge near  $60^\circ\text{E}$  is also evident in the wind field. The strong average jet maximum is a result of the frequent merging of the polar front jet and the subtropical jet during the month. The jet maximum is much reduced in December 1978, being only about  $62 \text{ m s}^{-1}$  and farther south ( $\sim 31^\circ\text{N}$ ) than in 1974. The weaker baroclinicity in December 1978, as seen in the 1000–500 mb thickness, is consistent with the weaker polar front jet.

#### 4. Individual surge discussion

##### a. December 1974 surges

There are four distinct cooling events evident in the December 1974 curve of Fig. 1. The first starts at about 1200 GMT 2 December, the second at 0000 GMT 10 December, the third at 0000 GMT 17 December and the fourth at 0000 GMT 24 December. There are designated events I, II, III and IV on the figure. The first two have a clear double structure with more intense cooling following the initial surge. The third has just a slight hint of this type of structure. The effects of

these first two events on the atmosphere in lower latitudes (equatorward of  $20^\circ\text{N}$ ) were discussed by Chang et al. (1979). In the next section details of the circulation accompanying the third surge event will be described.

It should be realized that the events accompanying each of the cooling periods at Hong Kong in December 1974 were very similar to the sequence described as follows. Composites of the flow fields constructed from periods centered on the cooling events also demonstrated a similar pattern. Each of the cooling events associated with the double structure of cold surges I and II had a similar forcing. The forcing for each part of the double structure was potent enough to produce a surge in its own right. However, the close spacing of the forcing in time precluded the second event from being classified as a separate surge. Surge III of December 1974 is selected for discussion because the dual structure is not as dominant in this case and this facilitates the comparison with the events in December 1978.

##### 1) SURGE III DECEMBER 1974

The synoptic events of surge III for December 1974 will be described in this section. The description will

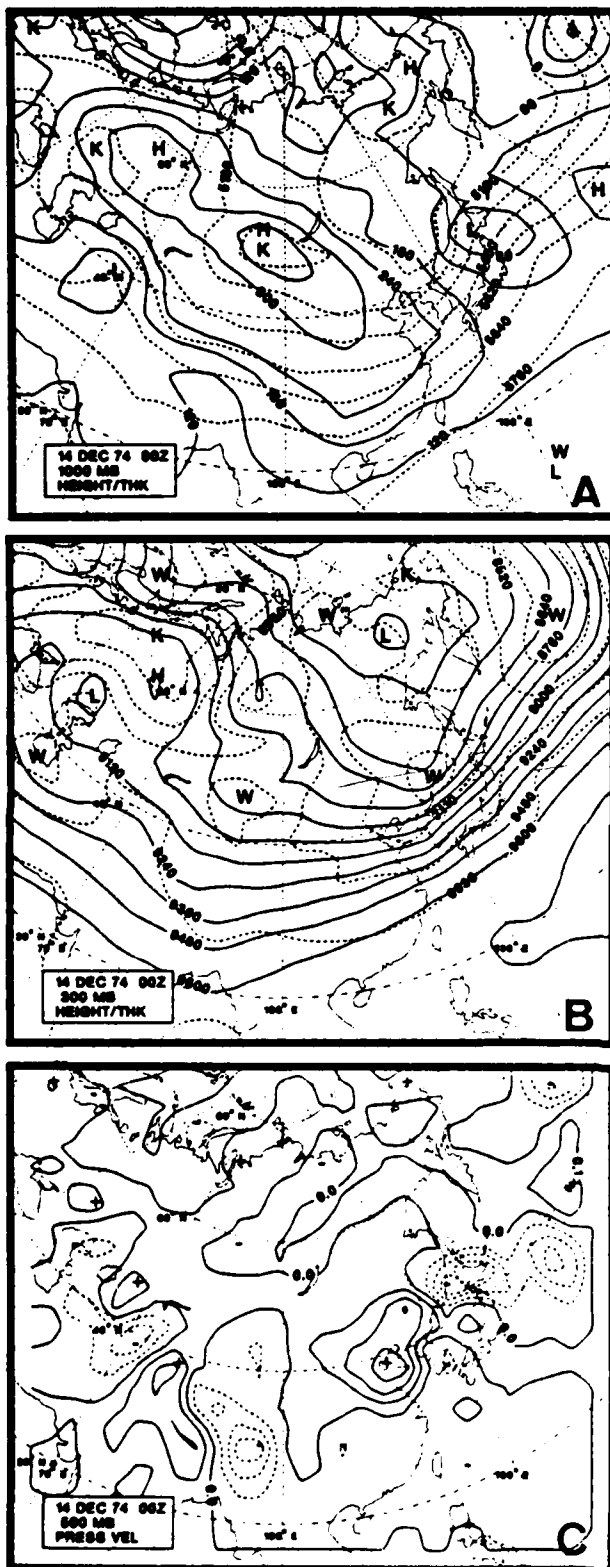


FIG. 4. (a) 1000 mb heights (solid) and 1000 to 500 mb thickness (dashed) for 0000 GMT 14 December 1974. Contour interval is 30 m for the heights and 60 m for thickness. Maxima and minima are labeled as in Fig. 2. (b) 300 mb heights (solid) and 100 to 300 mb

encompass the time period from 0000 GMT 14 December 1974 to 0000 GMT 20 December 1974. This time period begins at the time of greatest negative deviation of temperature of the previous cold surge at Hong Kong (Fig. 1) and ends at the peak of surge III. The intent here is to describe the synoptic-scale circulation features that initiate and sustain the surge event.

Figures 4–7 present the 300 mb heights, 100–300 mb thickness, 1000 mb heights and 1000–500 mb thickness, and 500 mb pressure velocity fields from 0000 GMT 14 December 1974 to 0000 GMT 20 December 1974, at intervals of 48 hours.

The fields at 0000 GMT 14 December 1974 (Fig. 4) represent the circulation at the time of the coldest temperature at Hong Kong during surge II of December 1974. To the southeast of Lake Baikal there is upper tropospheric cold advection. The vertical motion field at 500 mb has a prominent region of descent centered over the Yellow Sea region. The descent region is evidently the result of cold advection in lower and upper levels and an increase with height of anticyclonic vorticity advection to the west both of the upper-level long-wave trough and an upper-level short wave passing through the long-wave trough position. There is an ascent/descent couplet associated with a developing cyclone near Japan.

Forty-eight hours later, at 0000 GMT 16 December 1974 (Fig. 5), the 1000 mb heights have fallen over China and the thickness contours east of  $100^{\circ}\text{E}$  over China have moved northward as the effects of surge II subside. The cyclone off the coast has deepened and moved northeastward. The Siberian anticyclone is now about in its monthly mean position. There is strong upper-level cold advection east of Lake Baikal with a short-wave trough oriented northeast to southwest through the position of the lake. The vertical motion field shows a marked decrease in the descent around the Yellow Sea.

At 0000 GMT 18 December 1974 (Fig. 6) the cooling at Hong Kong associated with surge III is well underway. There is strong cold advection in the lower troposphere along the coast centered on the Yellow Sea. The 1000 mb heights have risen over China, with ridging to the east of  $100^{\circ}\text{E}$ . There is no cyclonic circulation off the coast. The thickness contours evince a southward movement although they are not as distorted as the 1000 mb heights. At 300 mb the trough along  $130^{\circ}\text{E}$  is deeper due to the short wave seen in Fig. 6b entering the long-wave trough position. The ridge over central

thickness (dashed) for 0000 GMT 14 December 1974. Contour interval for height is 90 m and 45 m for thickness. Maxima and minima are labeled as in Fig. 2. (c) Pressure vertical velocity at 500 mb at 0000 GMT 14 December 1974. Contour interval is  $1.0 \text{ Pa s}^{-1}$ . Negative values are dashed (ascent). Maxima (minima) are labeled with (+) (-).

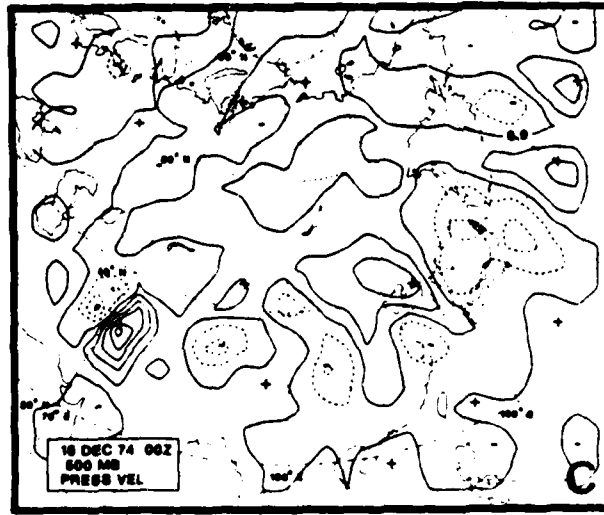
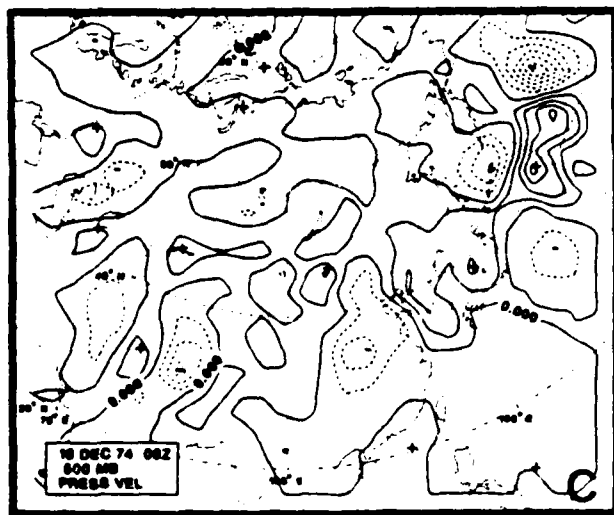
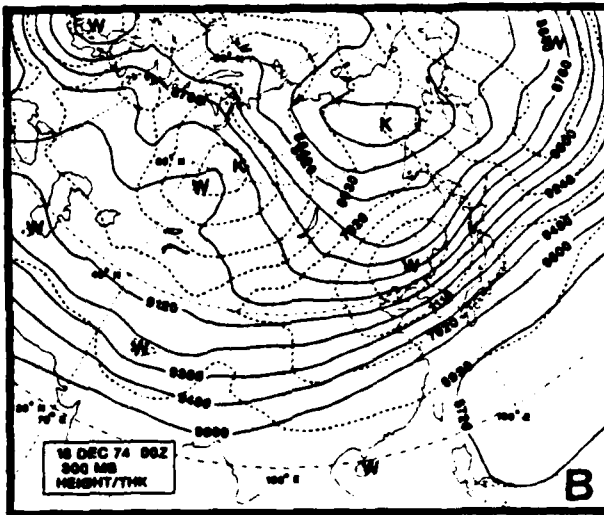
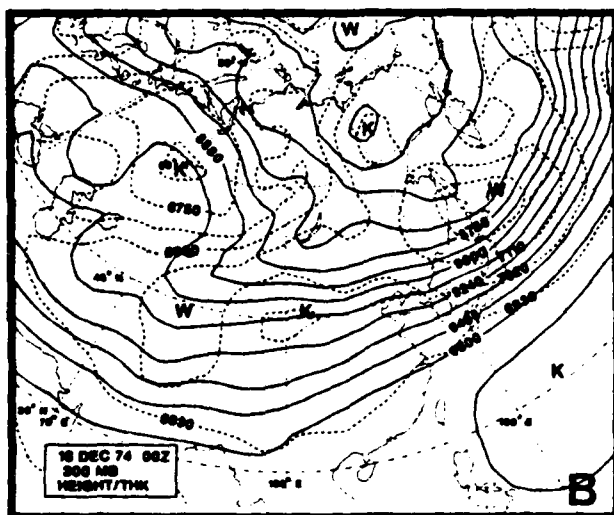
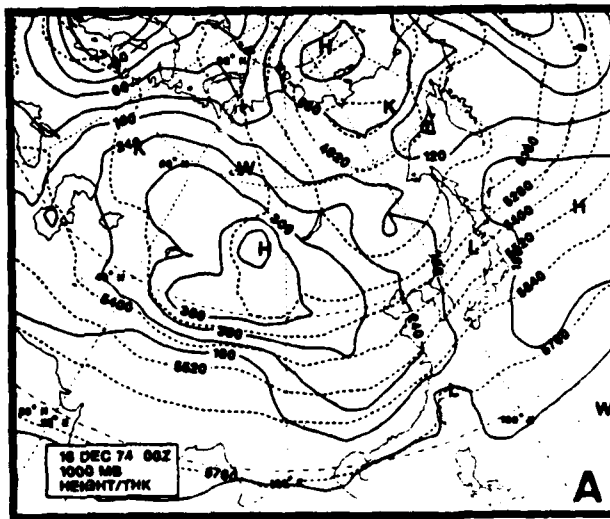
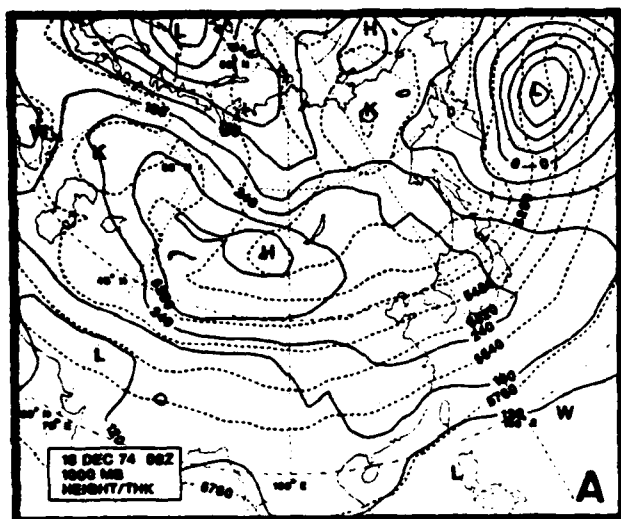


FIG. 5. As in Fig. 4 except for 0000 GMT 16 December 1974.

FIG. 6. As in Fig. 4 except for 0000 GMT 18 December 1974.

Asia at  $\sim 70^\circ\text{E}$  has moved eastward and this in combination with the troughing along the coast results in northwesterly geostrophic flow over Lake Baikal with another short wave in evidence southeast of the lake. There is cold advection from the northwest to the southeast of Lake Baikal in the upper troposphere and warm advection east of  $130^\circ\text{E}$ . The 500 mb descent center northwest of Korea is under the region of upper-level cold advection and to the west of the upper-level trough. The ascent to the east of the descent is under a region of upper-level warm advection and is to the east of the upper level trough.

By the 0000 GMT 20 December 1974 (Fig. 7) the coldest temperature has been reached at Hong Kong. At 1000 mb there is now a strong cyclone at  $50^\circ\text{N}$ ,  $160^\circ\text{E}$ . This storm has been developing over the previous 48 hours. There is strong cold advection to the rear of the cyclone, and also a separate region of cold advection centered on Korea. There is movement of the 180 m 1000 mb contour southward, but farther north the 240 m, and 300 m contours are nearly in the same location as 48 hours before. At 300 mb Lake Baikal is still in northwesterly flow, and the trough along the coast has developed further as the short wave of Fig. 6b has entered the region and there has been continued cold advection into the trough. There is upper-level cold advection southeastward from Lake Baikal to Korea. The ridge at  $60^\circ\text{N}$ ,  $100^\circ\text{E}$  has weakened, with evidence of another short wave just passing to the eastern side of the ridge. The increase of anticyclonic vorticity advection aloft and cold advection in the upper troposphere yields strong descent at 500 mb southeast of Lake Baikal to the Yellow Sea.

Two important elements of the sequence of events of this cold air outbreak are as follows. The first element is the strong ridging to the west and northwest of Lake Baikal at upper levels which leads to northwesterly flow aloft over the lake's position. The eastward movement of the ridge shortens the distance between it and the strengthening downstream trough. This could possibly result in unbalanced accelerating flow at the ridge crest (Bjerknes, 1951) and amplification of short wave features to the east of the ridge. The second factor is the presence of the very cold air anchored on the East Asian coast at  $50^\circ\text{N}$ , which creates a stationary cutoff long-wave trough. This mass of cold air protruding southward establishes a strong baroclinic zone on which the waves amplify and steers them farther south toward the latitude of the subtropical jet. The long wave remains in position as two short waves move through the northwesterly flow. There is a slight sign of the renewed cooling associated with the second wave in the December 1974 curve of Fig. 1 at 0000 GMT on the eighteenth.

There are several aspects of the cold surge circulation at 1000 mb which should be noted. First, during the initiation period of the surge, there is little cyclonic

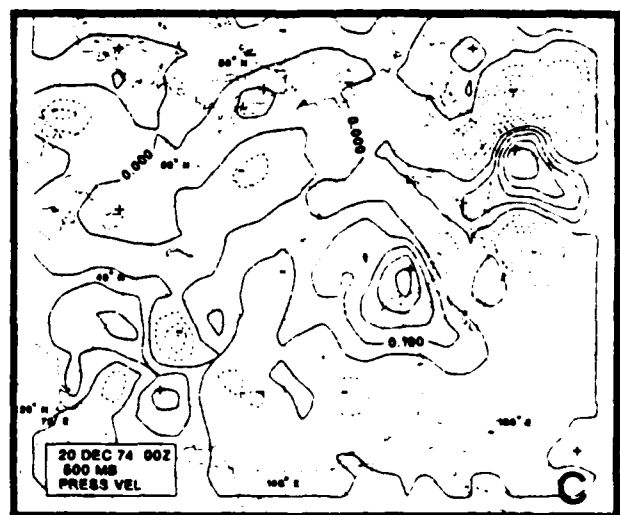
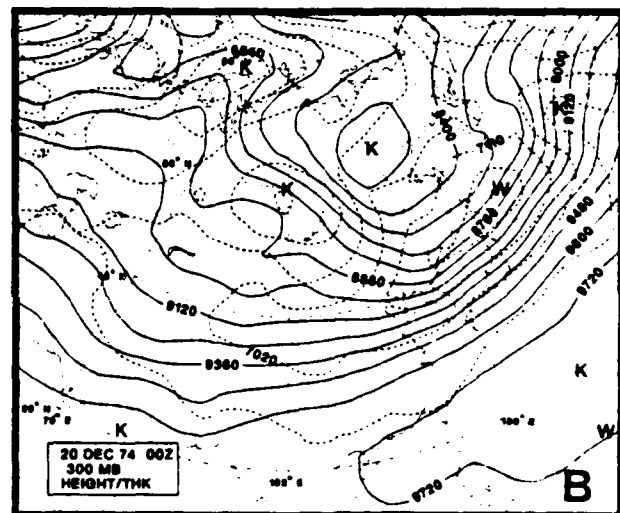
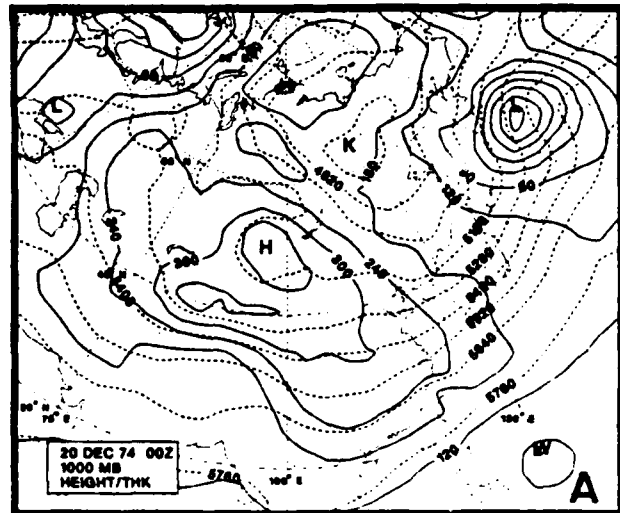


FIG. 7. As in Fig. 4 except for 0000 GMT 20 December 1974.

development off the coast. The thrust of cold air southward is due to the circulation about, and divergent outflow out of, the strongly intensifying descent center. The cyclone northeast of Japan in Fig. 7a developed after the cold surge had already been initiated. At the height of the surge on 0000 GMT 20 December 1974 the descent center at 500 mb (Fig. 7c) is quite distinct from that associated with the developing cyclone off the coast. The second point is that the anticyclonogenesis over China is not due to a rapid development of the Siberian anticyclone per se but rather, the Siberian anticyclone has decreased in intensity in the course of the surge development. The descent in northern China near the Yellow Sea is due to the dynamic effects of the short wave passage. The Siberian anticyclone decreases in intensity as the wave passes to the east. The cold advection aloft at 300 mb over the lower-level descent center is important to its development as found by Fleagle (1947), Bodurtha (1952), Danielsen and Ho (1969) and Boyle and Bosart (1983).

Figure 8 depicts the Q vectors and temperature contours at 800 mb for 1200 GMT 17 December 1974 over eastern Asia. The 800 mb level was chosen as the lowest level not intercepting the terrain yet still indicative of the forcing of the shallow surge circulation. The pattern of Q vectors indicates that  $\nabla \cdot \mathbf{Q} > 0$  near  $35^\circ\text{N}$ ,  $120^\circ\text{E}$ , which implies lower level descent in this region. The orientation of the vectors implies that there is low-level northerly ageostrophic flow along  $120^\circ\text{E}$  south to  $35^\circ\text{N}$ . The large cross isotherm component of the vectors towards the warmer air indicates front-

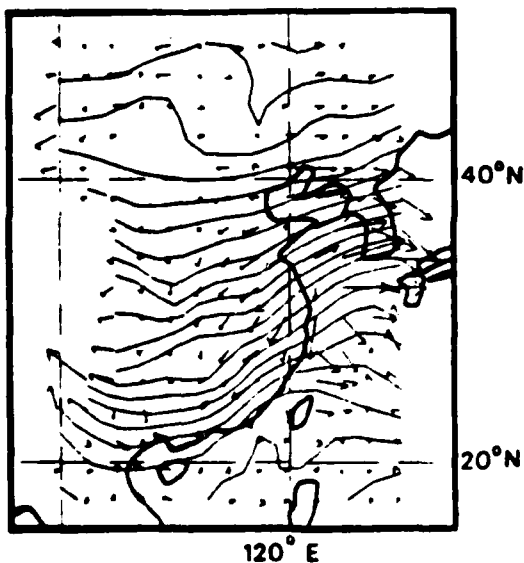


FIG. 8. Q vectors and temperature at 800 mb for 1200 GMT 17 December 1974. The length scale of the vectors is such that the longest vector corresponds to a magnitude of  $5 \times 10^{-1} \text{ Km}^{-1} \text{ m}^{-1}$ . The contour interval of the temperature is 2 K.

ogenesis along the East Asian coast. The pattern demonstrates the quasi-geostrophic forcing of the surge flow originating in middle latitudes. Also seen is a region of  $\nabla \cdot \mathbf{Q} < 0$  near Kyushu which is indicative of cyclone development.

## 2) DECEMBER 1974 CROSS SECTIONS

Figure 9 presents vertical cross sections of potential temperature, pressure velocity ( $Dp/Dt$ ), meridional component of the whole and divergent wind, for 1200 GMT 17 December 1974 from  $56^\circ$  to  $20^\circ\text{N}$  along  $115^\circ\text{E}$ . This is the time when the cooling of surge III is underway but 2.5 days prior to the lowest temperature at Hong Kong.

The potential temperature and pressure velocity sections evince a thermally direct circulation centered about  $35^\circ\text{N}$ . In conjunction with the Q vector analysis of Fig. 8 this figure shows that the secondary circulation is pushing the cold air southward and driving the surface frontogenesis south of  $35^\circ\text{N}$ . The sections of the meridional wind (Figs. 9c and 9d) illustrate the north-south circulation accompanying the cold surge. It is important to keep in mind the limited vertical resolution of the FNOC wind data when considering these figures. The wind was available at the surface and 700, 400, 250 and 200 mb. For the purposes of display and comparison the surface wind was set to a uniform level of 1000 mb. The northerly winds at the surface near the latitude of Hong Kong are strong ( $\sim 10 \text{ m s}^{-1}$ ) and are maintained as the surge progresses over the next three days. The divergent wind represents a substantial ( $5$  vs  $10 \text{ m s}^{-1}$ ) part of the northerly flow southwest of the descent center. The divergent meridional circulation is consistent with the pressure velocity values, in that it indicates low-level divergence and upper-level convergence (in the meridional plane) in the region of descent. The divergent flow pattern is also in agreement with the ageostrophic flow inferred from the Q vector field of Fig. 8.

### b. December 1978 surges

Lau et al. (1983) define five surges as occurring during the month of December 1978 and these are marked on Fig. 1. These surges begin about 0000 GMT 4 December 1978 (I), 0000 GMT 9 December 1978 (II), 1200 GMT 13 December 1978 (III), 1200 GMT 18 December 1978 (IV), 1200 GMT 22 December 1978 (V), and 1200 GMT 26 December 1978 (VI). Figure 1 shows that the strongest surge (in terms of cooling rate and minimum temperature) was the second (II) of the month and the event can be roughly timed as going from 1200 GMT 09 December 1978 to 1200 GMT 13 December 1978. The coldest air for this surge reaches Hong Kong on 0000 GMT 11 December 1978.

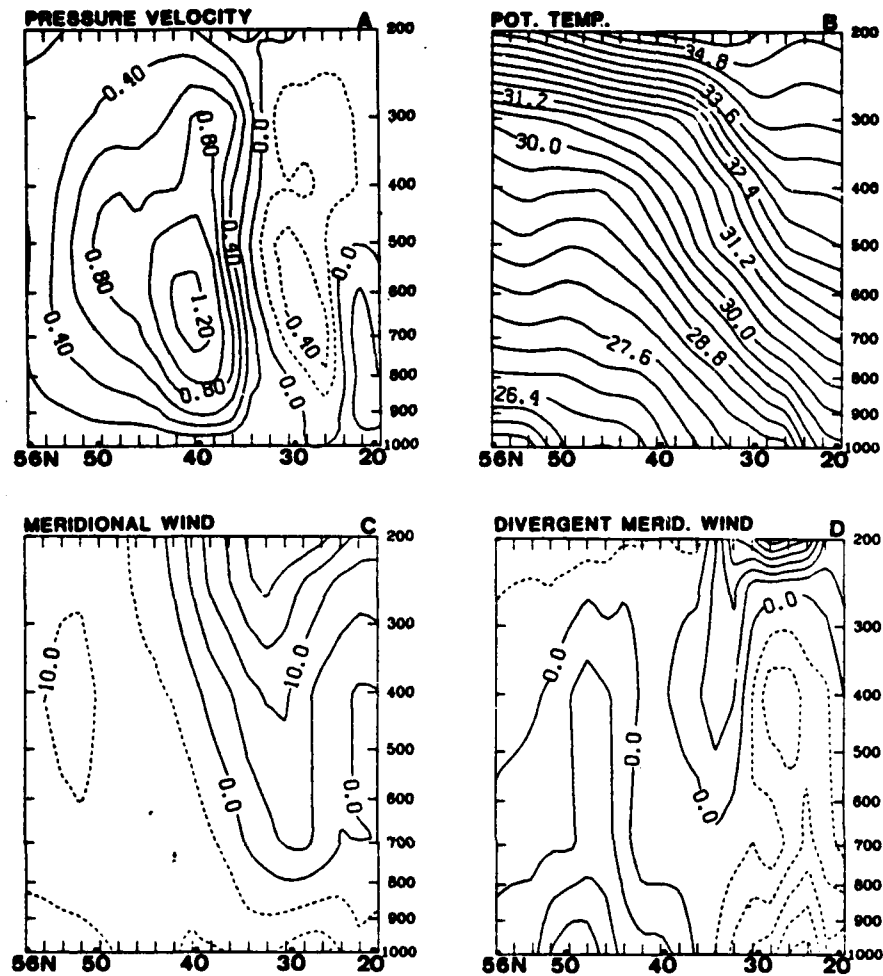


FIG. 9. (a) North-south cross section of pressure velocity from 56°N to 20°N along 115°E on 1200 GMT 17 December 1974. Contour interval is 0.25 Pa s<sup>-1</sup>. Negative values are dashed. Tick marks on the bottom are grid points of the mercator projection. Numbers on the bottom indicate the latitude. (b) As in (a) except for potential temperature. Contour interval is 4.0 K. (c) As in (a) except for the meridional component of the wind. Contour interval is 2.5 m s<sup>-1</sup>. (d) As in (a) except for the divergent component of the meridional wind. Contour interval is 1 m s<sup>-1</sup>.

### 1) SURGE II DECEMBER 1978

This section contains a synoptic description of the circulation during the period of surge II of December 1978. This period encompasses the period of time from 1200 GMT 08 December 1978 to 1200 GMT 11 December 1978. A detailed case study of the circulation patterns associated with this event is provided in Chu and Park (1984). Their emphasis was on the circulation in the subtropics in response to the surge.

Figures 10 to 13 present the 300 mb heights, 100–300 mb thickness, 1000 mb heights and 1000–500 mb thickness, and 500 mb pressure velocity fields from 1200 GMT 8 December 1978 to 1200 GMT 11 December 1978, at intervals of 24 hours.

At 1200 GMT 8 December 1978 (Fig. 10) the Siberian anticyclone maximum is nestled up against the

northeast corner of the Tibetan Plateau with the center at about 42°N, 95°E. There is strong warm advection to the northwest of the Siberian anticyclone. At 300 mb a ridge is building over this lower-level warm advection. The developing ridge initiates northwesterly flow over Lake Baikal. Strong descent at 500 mb is found near the Yellow Sea, with ascent farther inland and weak descent about Lake Baikal.

By 1200 GMT 9 December height rises have accumulated over eastern China and cold advection is occurring east of Korea. The cyclone to the northwest of the Siberian anticyclone (70°N, 80°E) is now filling but there is still warm advection over and to the northwest of Lake Baikal. The long-wave trough along the coast has deepened slightly. There is a short wave oriented southwest to northeast at 40°N, between 100 and 130°E. Upper tropospheric cold advection is oc-

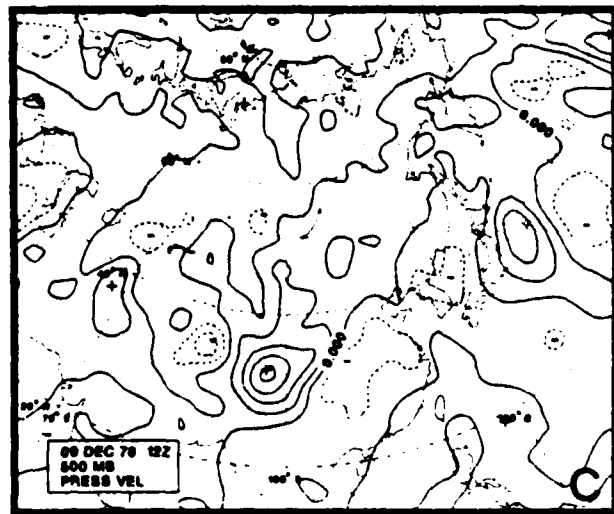
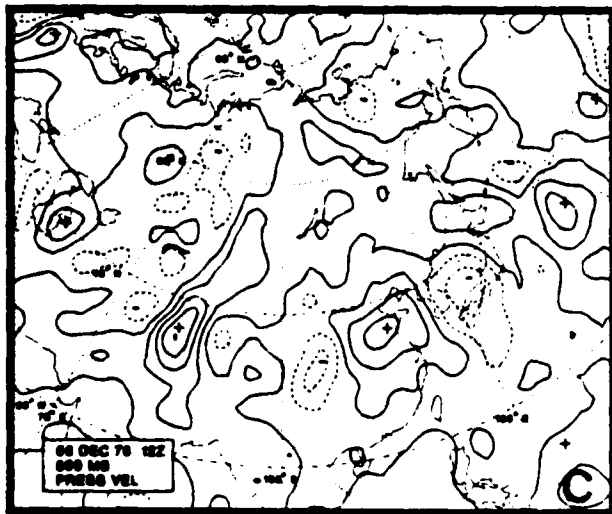
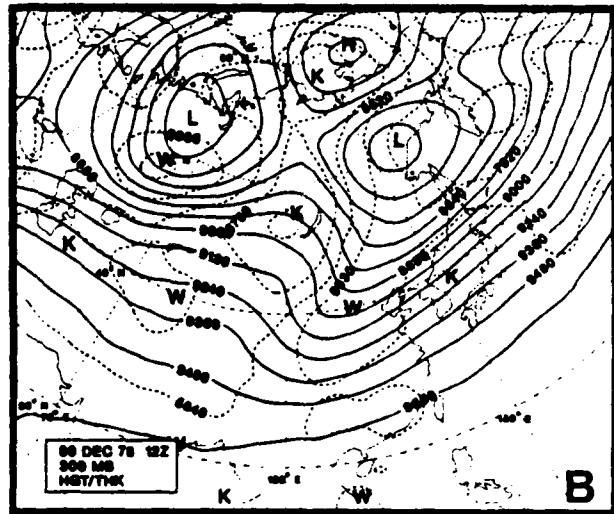
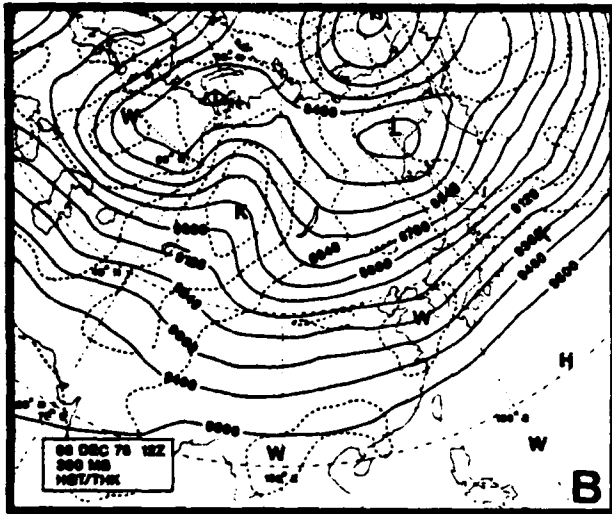
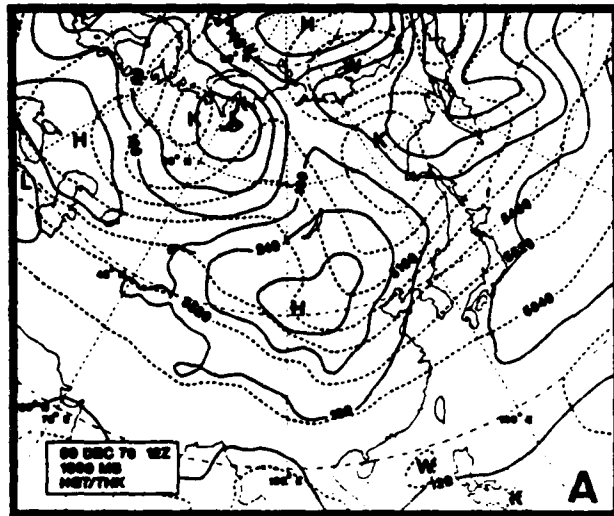
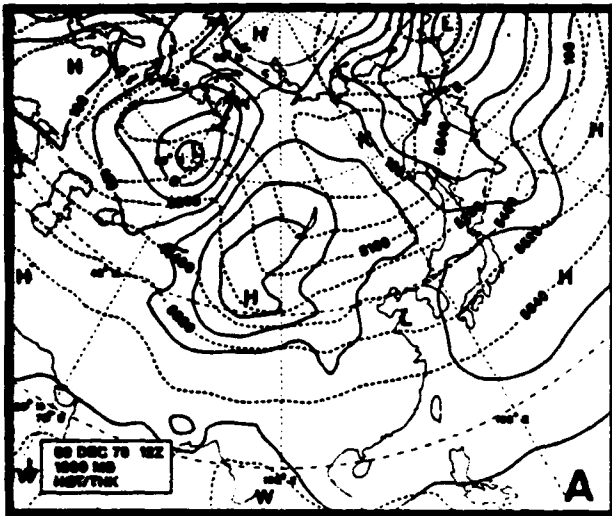


FIG. 10. As in Fig. 4 except for 1200 GMT 08 December 1978.

FIG. 11. As in Fig. 4 except for 1200 GMT 09 December 1978.

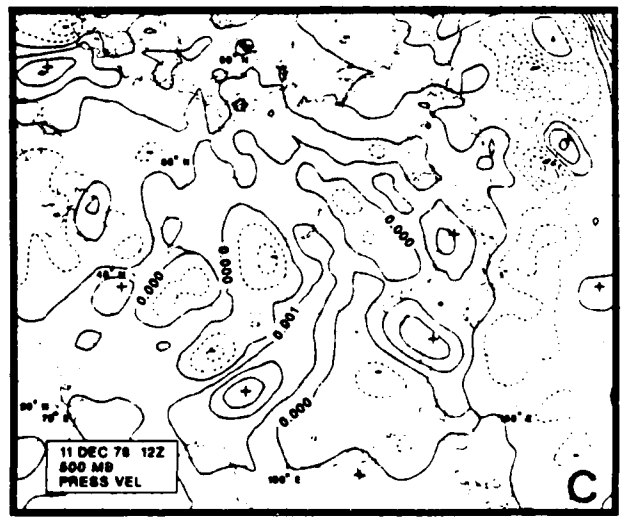
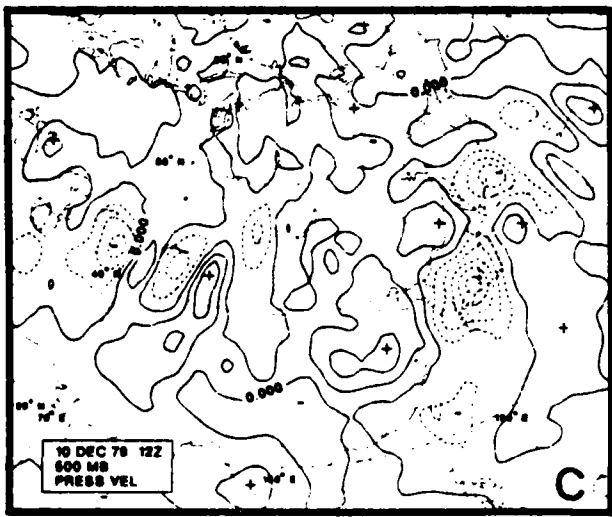
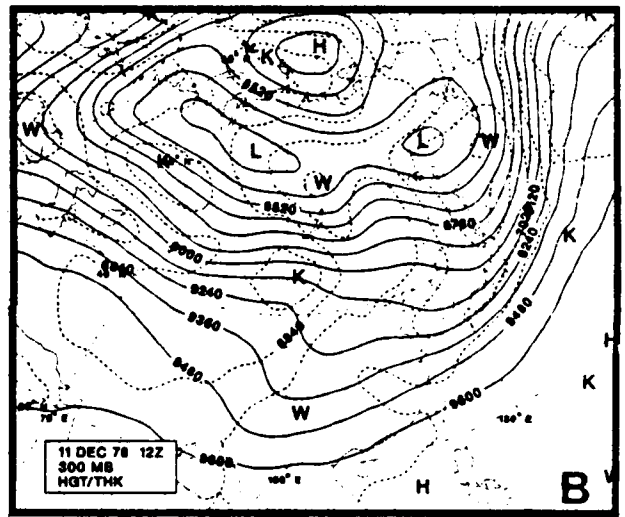
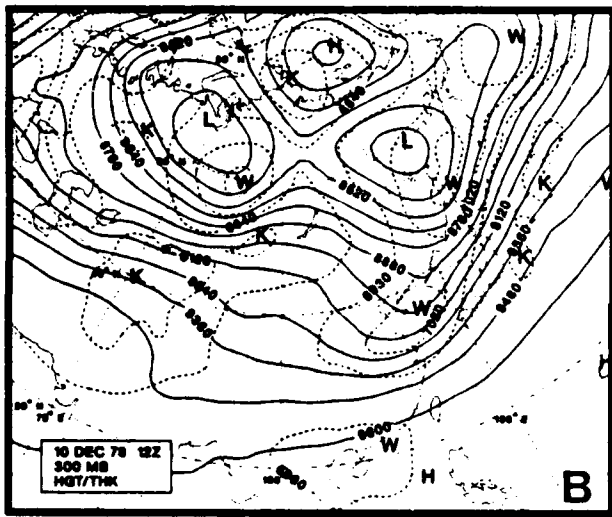
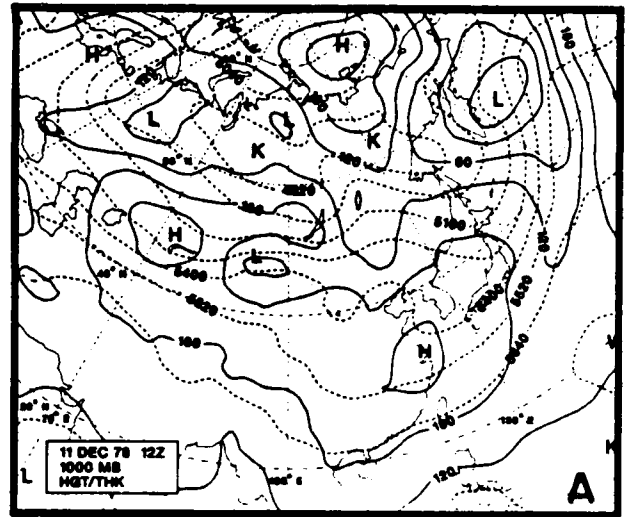
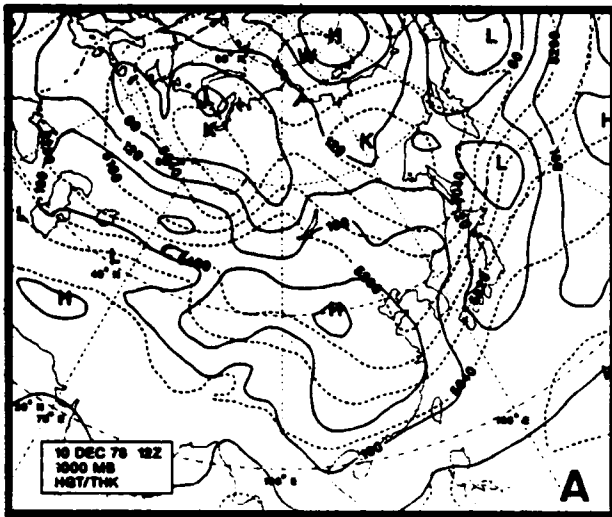


FIG. 12. As in Fig. 4 except for 0000 GMT 10 December 1978.

FIG. 13. As in Fig. 4 except for 0000 GMT 11 December 1978.

curing southeast of Lake Baikal. At  $35^{\circ}\text{N}$  there is ascent to the east and descent to the west of the short wave at 300 mb. A broad region of weak descent extends from the Kamchatka Peninsula southwestward to the Bay of Bengal.

By 1200 GMT 10 December 1978 the Siberian anticyclone has decreased in intensity from 358 m (1047 mb) to 318 m (1042 mb) while moving eastward, but the ridging has extended southward over China east of  $100^{\circ}\text{E}$ , and the 240 m contour has dropped southward. There is strong cold advection over the Yellow Sea and Sea of Japan. The thickness contours (e.g., 5640 m line) have also extended southward over China. At 300 mb the short wave has reached the coast and the long-wave trough there has become deeper in response to the short wave. There is upper-level cold advection southeast of Lake Baikal to Korea.

By 1200 GMT 11 December 1978 the 1000 mb anticyclone over China has diminished to 252 m (1034 mb). The 5640 m contour of thickness has moved slightly southward. The cyclone off the coast has developed and is now located off the Kamchatka Peninsula. The cold advection over the coastline has diminished. The 300 mb flow is somewhat more zonal as the trough along the coast has been reduced in intensity. West of the 300 mb trough there is a region of descent over the Yellow Sea and extending northward.

The surge in this case, as in December 1974, is triggered by a short wave propagating in northwesterly flow present to the west of the Asian coast. In December 1978 the larger-scale flow pattern favorable for the surge development only persists long enough for a single short wave to participate in the event. Thus the events in 1978 generally have a shorter time scale compared to 1974. Note also that the rapidly developing cyclone off the East Asian coast develops after the surge event is underway as in the 1974 case. This pattern is also similar to the composite fields of Lau and Lau (1984).

The  $Q$  vector field for 1200 GMT 10 December 1978 is shown in Fig. 14. The vectors imply that there is strong northerly ageostrophic flow along  $120^{\circ}\text{E}$  south of  $35^{\circ}\text{N}$ . There is a center of  $\nabla \cdot Q > 0$  (descent) about the location of Shanghai ( $31^{\circ}\text{N}$ ,  $121.5^{\circ}\text{E}$ ). The vectors have a strong cross isotherm component in southern China and off the coast implying quasi-geostrophic frontogenesis. The pattern is similar to that of Fig. 8 for December 1974.

## 2) DECEMBER 1978 CROSS SECTIONS

Figure 15 consists of cross sections taken from  $56^{\circ}$  to  $20^{\circ}\text{N}$ , along  $115^{\circ}\text{E}$ , of potential temperature, pressure velocity, the divergent and whole wind meridional component at 0000 GMT 10 December 1978. There is evidence for a thermally direct circulation within the plane of the section centered at about  $30^{\circ}\text{N}$ . There is brisk northerly flow by the whole wind ( $\sim 12 \text{ m s}^{-1}$ ) at 1000 mb over the South China Sea. Notice also that

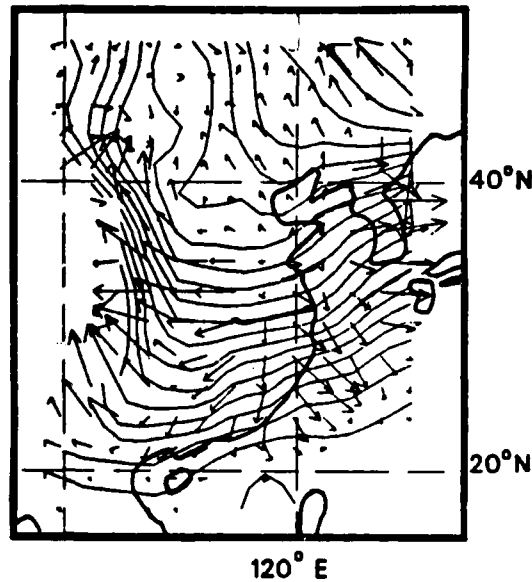


FIG. 14. As in Fig. 8 except for 0000 GMT 10 December 1978.

the baroclinic zone and the northerly winds are farther south in the December 1978 case as compared to December 1974. The divergent wind has a northerly maximum at 1000 mb at  $30^{\circ}\text{N}$ . This divergent component, while significant, is only  $3.5 \text{ m s}^{-1}$  at 1000 mb as compared to  $12 \text{ m s}^{-1}$  for the whole wind. The divergent meridional component is not as large a percentage of the whole meridional wind as in December 1974, perhaps due to the competition of stronger east-west divergent circulation. This east-west ageostrophic flow is indicated by the  $Q$  vector field of Fig. 14. There is a line of  $\nabla \cdot Q < 0$  southwest of Kyushu toward Taiwan implying ascent associated with incipient cyclogenesis. The weak ageostrophic flow along  $115^{\circ}\text{E}$  implied by Fig. 15d is in agreement with the low-level divergent flow implied in Fig. 14.

## 5. Discussion

Chu (1978) writes that ridging to the west and troughing to the east of Lake Baikal is a precursor condition to a surge occurring in Hong Kong in the subsequent twenty-four hours. The surges presented here conform to this rule, formulated at the Royal Observatory at Hong Kong. The establishment of northwesterly flow over Lake Baikal is seen to set up the larger scale flow upon which the shorter scale waves propagate toward the mean long-wave trough along the East Asian coast. The mechanisms initiating the cold surges of December 1974 and 1978 are quite similar in nature. The short waves passing through the long-wave trough position near the East Asian coast force a circulation that thrusts the cold air southward from the reservoir of the eastern Siberian cold pole. Figure 16 presents vertical cross sections along  $115^{\circ}\text{E}$

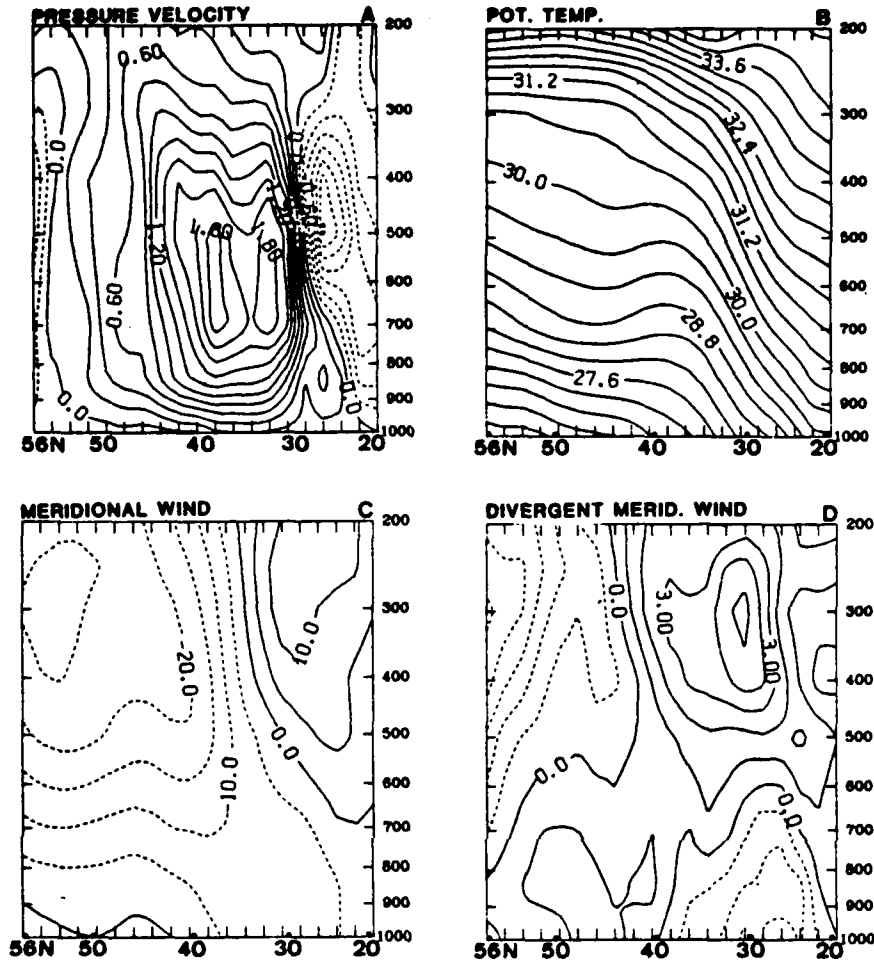


FIG. 15. As in Fig. 9 except for 0000 GMT 10 December 1978.

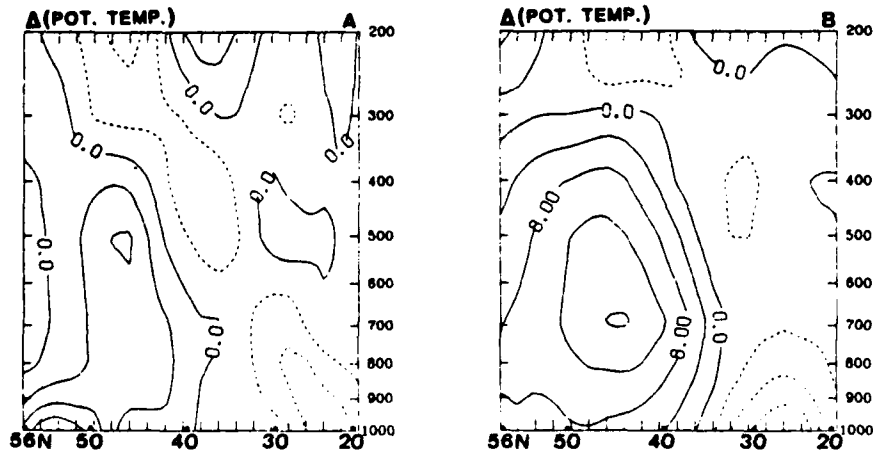


FIG. 16. (a) Latitude/height cross section of the change of potential temperature from 0000 GMT 17 December to 0000 GMT 20 December 1974. Solid contours are positive, dashed contours are negative values. Contour interval is 4 K. (b) As in (a) except for the period from 1200 GMT 9 December to 0000 GMT 11 December 1978.

from 56° to 20°N of the change in potential temperature computed from the peak to the trough of the temperature departures in Fig. 1 for the surges described above. For December 1974, surge III, the time period is three days, and for December 1978, surge II, the time period is 1.5 days. The patterns are similar with low latitude cooling and high latitude warming in the lower troposphere, with a tendency for the pattern to reverse in the upper levels (above 300 mb). The most intense cooling is at the lowest levels with most of the change taking place below 700 mb.

The difference in the time scale between the surges of the months appears to be governed by the larger scale flow. The peak to trough time of surge III of December 1974 is double that of surge II of December 1978 (Fig. 1). In December 1974 the low-index flow with blocking over Asia and deep troughing along the coast established northwesterly flow over Lake Baikal that persists for a number of days. In contrast, the high-index flow of December 1978 has the short waves moving rapidly through the more zonal current. The basic mechanism of short waves is the same in each month but in December 1974 the time scale is such that usually two such waves propagate through the northwesterly flow during the surge event. At least the first three of the surges in December 1974 have evidence of a double structure which illustrates this process. The surges of December 1978 are the result of a single wave.

The relative intensity of the cold air surge depends on the large scale conditions. The average flow over Asia for December 1974 and December 1978 presents a dramatic contrast with respect to ridging over the midcontinent. There is a major difference between December 1974 and December 1978 in the position and strength of the long waves. A ridge at 60°E was anomalously large in December 1974 and in December 1978 this ridge is absent. The East Asian trough was deep in December 1974 with a strong, sharp baroclinic zone below the strong jet. In December 1978 the East Asian trough was somewhat relaxed, and the jet weaker. The long waves act to organize the forcing and geographically focus the shorter-scale behavior. In December 1978 the long wave pattern has much less amplitude over Asia. The blocking pattern of December 1974 yields a coherent, stable pattern for anticyclonic development on the East Asian coast.

It is interesting to note that the mean fields of December 1974 and December 1978 (Figs. 2 and 3) strongly resemble the positive and negative polarities, respectively, of the Siberian and Chinese patterns of Hsu and Wallace (1985). Their data were five-day means and thus could not capture the details of the evolution of the surge events but it is significant that an entire month can be characterized according to their patterns and the intensity of the surge events of that month are consistent with that pattern.

The surge events are seen not to be the result of an expansion of the intensifying Siberian anticyclone but are a separate dynamic development to the east and southeast of the Siberian anticyclone position. Dynamic subsidence is initiated by the synoptic scale waves entering the highly baroclinic zone near the coast. The development of a descent center in the local direct circulation is explained by quasi-geostrophic dynamics. The onset of the surge is not directly the result of cyclonic development off the East Asian coast. Such cyclogenesis follows the surge initiation and is triggered by the same synoptic short wave which initiated the surge as the wave passes to the east of the long-wave trough position. There is substantial descent in the Yellow Sea region separate from the transient cyclone/anticyclone couplets which form off the coast and propagate to the northeast.

The cold air outbreaks off the East Asian coast described by Joung and Hitchman (1983) are extreme events with a great deal of very cold air flowing over Korea and the Sea of Japan. The scale of the waves they describe as forcing these events are of the order of the long wave present during December 1974. Evidently in their cases the wave which can be traced as it traverses a substantial portion of the globe forces a major rearrangement of the long-wave pattern over eastern Asia.

In contrast to the cold air outbreaks over North America, there is not a large north-south movement of a mobile cold air dome in East Asia. In the Asian situation cold air appears to be thrust southward in a thermally direct circulation. The cold air is shallow as it spreads to the latitude of Hong Kong (below 700 mb). Over North America the cold air domes generally undergo large excursions southward supported by wind asymmetries aloft (Palmen and Newton, 1951; Boyle and Bosart, 1983). These domes often then subside near the Gulf of Mexico coast. When the cold dome collapses the North American cold air also becomes shallow as it moves southward, at comparable latitude and with quite a similar pattern of surges on the East Asian coast. The East Asian pattern tends to release energy in a relatively small geographical region and results in a steady, intense jet. The North American processes appear to be less geographically focused with the energy being released over a wide area. This leads to more variability in time and space and thus a weaker mean jet. Apparently, the north-south orientation of the Rockies as opposed to the huge east-west extent of the Tibetan Plateau is a strong factor in determining the differences in the air mass movement of the two continents.

*Acknowledgements.* Professor C.-P. Chang supplied useful comments on the manuscript. This work was carried out while the author was a National Research Council Resident Research Associate at the Naval

Postgraduate School. The research was partially supported by the National Science Foundation under grant ATM-8020302. The computations were performed at the W. R. Church Computer Center at the Naval Postgraduate School.

## REFERENCES

- Bjerknes, J., 1951: Extratropical cyclones. *Compendium of Meteorology*, T. E. Malone, Ed., Amer. Meteor. Soc. 577-598.
- Bodurtha, F. T., 1952: An investigation of anticyclogenesis in Alaska. *J. Meteor.*, 9, 118-125.
- Boyle, J. S., 1986: Comparison of the synoptic conditions in mid-latitudes accompanying cold surges over eastern Asia for the months of December 1974 and 1978. Part II: Relation of surge events to features of the longer term mean circulation. *Mon. Wea. Rev.*, 114, 919-930.
- , and L. F. Bosart, 1983: A cyclone/anticyclone couplet over North America: An example of anticyclone evolution. *Mon. Wea. Rev.*, 111, 1025-1045.
- Chang, C.-P., and K. M. Lau, 1980: Northeasterly cold surges and near-equatorial disturbances over the winter MONEX area during December 1974. Part II: Planetary scale aspects. *Mon. Wea. Rev.*, 108, 298-312.
- , and —, 1982: Short-term planetary-scale interactions over the tropics and midlatitudes during northern winter. Part I: Contrast between active and inactive periods. *Mon. Wea. Rev.*, 110, 933-946.
- , and K. G. Lum, 1985: Tropical-midlatitude interactions over Asia and the Western Pacific Ocean during the 1983/84 northern winter. *Mon. Wea. Rev.*, 113, 1345-1358.
- , J. E. Erickson and K. M. Lau, 1979: Northeasterly cold surges and near-equatorial disturbances over the winter MONEX area during December 1974. Part I: Synoptic aspects. *Mon. Wea. Rev.*, 107, 812-829.
- Chen, T. C., J. C. Alpert and T. W. Schlatter, 1978: The effects of divergent and nondivergent winds on the kinetic energy budget of a midlatitude cyclone: A case study. *Mon. Wea. Rev.*, 106, 458-468.
- Chin, P. C., 1969: Cold surges over South China. Royal Observatory Tech. Note 28., Royal Observatory, Hong Kong, 22 pp.
- Chu, E. W. K., 1978: A method for forecasting the arrival of cold surges in Hong Kong. Royal Observatory Tech. Note 43, Royal Observatory, Hong Kong, 32 pp.
- Chu, P. S., and S. U. Park, 1984: Regional circulation characteristics associated with a cold surge event over East Asia during winter MONEX. *Mon. Wea. Rev.*, 112, 955-965.
- Crutcher, H. L., and J. M. Meserve, 1970: *Selected Level Heights, Temperatures and Dew Points for the Northern Hemisphere*. NAVAIR 50-1C-52. [Available from Naval Weather Service Command, Washington, DC 20772.]
- Danielsen, E. F., and F. P. Ho, 1969: An isentropic trajectory study of a strong northeast monsoon surge. Sci. Rep. 2, AFCRL-69-0036. Hawaii Institute of Geophysics, 13 pp. [Available from Dept. of Meteorology, University of Hawaii, Honolulu 96822.]
- Endlich, R. M., 1967: An iterative method for altering the kinematic properties of wind fields. *J. Appl. Meteor.*, 6, 837-844.
- Flangle, R. G., 1947: The fields of temperature, pressure and three dimensional motion in selected weather situations. *J. Meteor.*, 4, 165-185.
- Holton, J. R., 1979: *An Introduction to Dynamic Meteorology*, 2nd ed., Academic Press, 319 pp.
- Hoskins, B. J., and M. A. Pedder, 1980: The diagnosis of middle latitude synoptic development. *Q. J. Roy. Meteor. Soc.*, 106, 707-719.
- , I. D. Draghici and H. C. Davies, 1978: A new look at the omega equation. *Q. J. R. Meteor. Soc.*, 104, 31-38.
- Hsu, H.-H., and J. M. Wallace, 1985: Vertical structure of wintertime teleconnection patterns. *J. Atmos. Sci.*, 42, 1693-1710.
- Jenne, R., 1975: Data sets for meteorological research, NCAR Tech. Note NCAR-TN/1A-111, National Center for Atmospheric Research, Boulder CO 80307, 194 pp.
- Joung, C. H., and M. H. Hitchman, 1982: On the role of successive downstream development in East Asian polar air outbreaks. *Mon. Wea. Rev.*, 110, 1224-1237.
- Kung, E. C., and P. H. Chan, 1981: Energetics characteristics of the Asian winter monsoon in the source region. *Mon. Wea. Rev.*, 109, 854-870.
- , and H. Tanaka, 1983: Energetics analysis of the global circulation during the special observation periods of FGGE. *J. Atmos. Sci.*, 40, 2575-2592.
- Lau, K. M., C. P. Chang and P. H. Chan, 1983: Short term planetary-scale interactions over the tropics and midlatitudes during northern winter. Part II: Winter MONEX periods. *Mon. Wea. Rev.*, 111, 1372-1388.
- Lau, N.-C., 1978: On the three-dimensional structure of the observed transient eddy statistics of the northern hemisphere wintertime circulation. *J. Atmos. Sci.*, 35, 1900-1923.
- , 1984: A comparison of circulation statistics based on FGGE level III-B analyses produced by GFDL and ECMWF for the special observing periods. NOAA Data Rep. ERL GFDL-6, Geophysical Fluid Dynamics Laboratory, Princeton, NJ.
- , and K.-M. Lau, 1984: The structure and energetics of midlatitude disturbances accompanying cold air outbreaks over East Asia. *Mon. Wea. Rev.*, 112, 1309-1327.
- Lewis, J. M., and T. H. Grayson, 1972: The adjustment of surface wind and pressure by Sasaki's variational matching technique. *J. Appl. Meteor.*, 11, 586-597.
- Lorenc, A. C., 1981: A global three-dimensional multivariate statistical interpolation scheme. *Mon. Wea. Rev.*, 109, 701-721.
- McGinley, J., 1982: A diagnosis of Alpine lee cyclogenesis. *Mon. Wea. Rev.*, 110, 1271-1287.
- Murakami, T., 1979: Winter monsoonal surges over East and SouthEast Asia. *J. Meteor. Soc. Japan*, 57, 133-158.
- Palmen, E., and C. W. Newton, 1951: On the three-dimensional motions in an outbreak of polar air. *J. Meteor.*, 8, 25-39.
- , and —, 1969: *Atmospheric Circulation Systems*, Academic Press, 603 pp.
- Taubensee, R. E., 1975: Weather and circulation of December 1974—Continued warm across much of the country. *Mon. Wea. Rev.*, 103, 266-271.
- , 1979: Weather and circulation of December 1979—Record and near record cold in the West. *Mon. Wea. Rev.*, 107, 354-360.

## Comparison of the Synoptic Conditions in Midlatitudes Accompanying Cold Surges over Eastern Asia for the Months of December 1974 and 1978. Part II: Relation of Surge Events to Features of the Longer Term Mean Circulation

JAMES S. BOYLE

*Department of Meteorology, Naval Postgraduate School, Monterey, CA 93943*

(Manuscript received 29 September 1983, in final form 31 October 1985)

### ABSTRACT

This is the second of two papers dealing with midlatitude initiation of East Asian cold surges. The effects of individual cold surges on the circulation on the East Asian coast are studied for the months of December 1974 and December 1978. These months represent a contrast with respect to the strength of cold surges occurring in that month. The surges occurring in December 1978 were weak, those in 1974 were strong.

The circulation features and processes that were considered were: 1) the 200 mb zonal momentum budget, 2) the 400 mb frontogenesis forcing, 3) the low-level meridional eddy heat fluxes, and 4) the thermally direct circulation cell in the entrance region to the East Asian jet maximum. The times of the surge events are shown to be periods which dominate in computing the longer term monthly statistics of the aforementioned circulation features. The monthly mean features computed here are also typical of other studies using even much longer term winter averages. The implication is that surges also dominate these statistics, and long-term averages of the East Asian winter monsoon circulation at the midlatitudes and subtropics are dominated by the surge characteristics.

During the cold surge event the balance of the 200 mb zonal momentum budget is between the zonal advection of momentum and the coriolis acceleration. Between the events the balance is somewhat mixed, with no terms clearly dominating.

The climatological maximum in confluence at 400 mb (quasi-geostrophic frontogenesis) found over East Asia is seen to be, for the most part, the result of intensified confluence accompanying the surge event. This frontogenesis is necessary for the temperature field to remain in thermal-wind balance with the accelerating jet. There is also marked low-level frontogenesis taking place at lower levels as the cold air sweeps southward.

The low-level eddy heat fluxes, which have a large maxima on the East Asian coast, are shown by means of time-longitude plots to be largely the results of the surge circulation. Cold air is continuously moving southward in the Asian winter monsoon, but the surge fluxes are intense and are focused on the coast.

The thermally direct circulation cell in the entrance region to the East Asian jet maximum reaches its peak intensity during the cold surges.

The two months show very similar patterns, only the intensity of the circulation is somewhat reduced in the month of the weaker surges (December 1978). Evidently the same processes are at work during the surges of each month only at reduced levels in December 1978.

### 1. Introduction

This is the second of two papers dealing with cold surges over East Asia. The study of these surges and their relation to eastward moving waves in the baroclinic westerlies of midlatitudes was one of the major objectives of the Winter Monsoon Experiment (WMONEX) of the First Garp Global Experiment (FGGE). This and a companion paper, Boyle (1986, hereinafter B1), contrast the conditions occurring in December 1974 and December 1978 to describe the difference in the midlatitude forcing between the weak surges of 1978 and the strong surges of 1974. As described in B1, December 1974 was a month of well spaced, strong surges, while December 1978 had slightly more frequent but somewhat weaker surges. It was seen that the planetary scale flow of each month explained

these differences, but on an individual basis each surge is seen to have the same sequence of initiation forcing. A short wave propagating in the northwesterly flow initiates descent in the region of the East Asian coast. The divergent outflow from and circulation about this center thrust the cold air southward. This same short-wave feature usually then initiates rapid cyclogenesis in the highly baroclinic flow off the East Asian coast near Japan.

Individual case studies of surge events were presented in B1 to document this mechanism and to make clear the basic ingredients that make up each surge event. In this paper we will back away from the individual events and consider time series of various parameters, temperature, pressure velocity, quasi-geostrophic frontogenesis function (QGFF), momentum budgets, and eddy heat fluxes for selected regions to get a

monthly overview of the circulation features of the surge events and to contrast the forcing of the two months.

The structure of the paper is as follows. Section two describes the data handling and computational procedures. The monthly overview for December 1974 is presented in Section 3. In this section the results of the QGFF, 200 mb zonal momentum budgets and low-level heat flux computations will be given and discussed. Section 4 is the same as Section 3 except that the results will be those of December 1978. The final section will attempt to synthesize the pertinent results of the previous sections.

## 2. Data handling and computation procedures

### a. Datasets

The datasets were described in B1. Some germane characteristics of the data will be presented here for reference. The December 1974 data was taken from the operational analysis of the Navy's Fleet Numerical Oceanography Center (FNOC). The height and temperature fields were available at mandatory levels on a polar stereographic hemispheric grid with a grid length of 381 km at 60°N. The wind data were analyzed at the surface, 700, 400, 250 and 200 mb, on a mercator grid of grid length 257 km extending from 60°N to 40°S. The December 1978 data were the level III-B FGGE data from the European Center for Medium Range Weather Forecasts (ECMWF). All these data were available on the ECMWF global 1.875 degree grid at mandatory levels.

### b. Computations

In all calculations the appropriate map scale factor was taken into account although they may not be explicitly included in the equations presented.

For both datasets the rotational and divergent parts of the wind were computed from the analyzed wind fields using the technique of Endlich (1967). This is an iterative procedure which does not require any assumptions about the nature of the wind field at the grid boundaries. It has been successfully used in other synoptic studies. Chen et al. (1978).

On the polar stereographic grid, quasi-geostrophic pressure velocity ( $Dp/Dt$ ) was calculated using the omega equation (Holton, 1979, p. 180).

Quasi-geostrophic frontogenesis tendencies were computed using the following formulation from Hoskins and Pedder (1980):

$$\frac{D|\nabla\theta|^2}{Dt} = 2Q \cdot \nabla\theta \quad (1)$$

$$Q = \left( -\frac{\partial v_g}{\partial x} \cdot \nabla\theta, -\frac{\partial v_g}{\partial y} \cdot \nabla\theta \right) \quad (2)$$

where:  $V_g$  is the geostrophic wind, and  $\theta$  is the potential temperature.  $V_g$  was computed from the analyzed height fields,  $\theta$  from the temperature fields. Computing frontogenesis tendencies in this manner ignores the contributions by diabatic, vertical motion and ageostrophic effects. It is, essentially, considering only the geostrophic confluence mechanism (McGinley, 1982; Hoskins and Pedder, 1980). The quantity on the right hand side of (1) will be henceforth referred to as the quasi-geostrophic frontogenesis function (QGFF).

### 1) EDDY FLUX COMPUTATIONS

Two types of deviations from the mean flow were used in flux computations for fluxes of heat and momentum. The first deviation will be termed the eddy component defined by

$$\alpha^* = \alpha - [\alpha]$$

where:  $[\alpha]$  is the zonal average. The zonal average was taken on the FNOC mercator grid. It is not a global average but extends from 30°E to 172°E.

The other deviation will be termed the transient component defined by

$$\alpha' = \alpha - \bar{\alpha}$$

where  $\bar{\alpha}$  is the time average over the 62 synoptic times that comprise the month.

The transient flux computations are used in momentum budget calculations. Since the data we have analyzed includes only one month, the significance of decomposing the fields into transient and stationary components could be questioned. In this regard it should be noted that Rosen and Salstein (1982) have determined that a month is a sufficiently long enough period of time to effectively separate the transient and standing components of the general circulation.

### 2) MOMENTUM BUDGET

Budgets for the zonal momentum were computed using the equation:

$$\frac{\partial u}{\partial t} = -u \frac{\partial u}{\partial x} - v \frac{\partial u}{\partial y} + f v_a + \text{residual} \quad (3)$$

where:  $v_a = v - v_g$ , is the ageostrophic meridional wind.

In using this equation we have neglected the contributions due to vertical motion, curvature effects and friction. The residual is a term containing errors and also contributions by other terms not included in the computation. The time derivative was computed using a 24-hour centered difference. The budget terms were computed for every point on the mercator grid.

Budgets of the time mean zonal momentum were computed using the equation:

$$\frac{\partial \bar{u}}{\partial t} = -\bar{u} \frac{\partial \bar{u}}{\partial x} - \bar{v} \frac{\partial \bar{u}}{\partial y} - \frac{\partial}{\partial x} (u'u) - \frac{\partial}{\partial y} (u'v) + f\bar{v}_e + \text{residual.} \quad (4)$$

Notice that this equation also ignores the contributions due to vertical motion and curvature effects but explicitly includes the contributions by the transients to the momentum budget. Equation (4) yields just a single value for each term for each month of data, at each point. Monthly time series of sixty values can be constructed from the terms of (3), allowing some insight into the effect of the cold surges on the zonal momentum budget.

The computations described before make a number of demands upon the dataset. For example, the computation of the ageostrophic wind can be quite sensitive to errors in the data. In the first part of this study, Boyle (1986), it was mentioned that both the FNOC and ECMWF wind data yielded realistic monthly mean values of the ageostrophic flow. Furthermore, Chang and Lum (1985) have used the FNOC data and found them capable of describing day-to-day variations in the divergent component of the wind.

### 3. December 1974

#### Time series

In this section time series of deviations from the monthly mean values will be presented for various parameters at selected levels and locations. The locations and parameters were chosen in an attempt to describe the circulation changes in the region of East Asia that accompany cold surge events. Most of the modulations of the circulation could be anticipated and taken together form a picture of the midlatitude forcing of the surges.

Figure 1 consists of time series of departures from the monthly mean 1000 mb temperature at Hong Kong for December, 1978 and 1974. The times of the cold surges for the respective months are also indicated on the figure. In general the surges of December 1974 have a greater negative excursion in the temperature deviation and have a longer time scale than those of December 1978. The temperature in this region is often used as an indicator of cold surges in eastern Asia, Chang et al. (1981). There are four distinct cooling events in December 1974 depicted in Fig. 1 which are labeled according to the same nomenclature as in B1. This figure acts as a reference in determining the timing of the surge events.

Figure 2a is a time series of 500 mb pressure velocity for a position over the Yellow Sea (10° × 10 degree grid centered on 40°N, 123°E). This is the position of the monthly mean maximum subsidence over eastern Asia in December 1974. The correspondence between de-

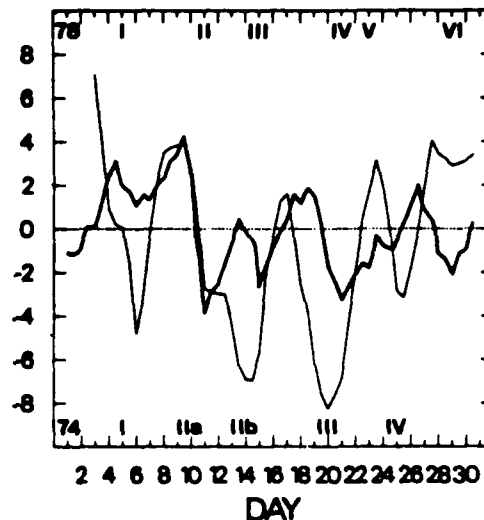


FIG. 1. Time series of deviations from the monthly mean temperature for a 5 × 5 degree, latitude, longitude grid centered on 24°N, 115°E (Hong Kong) for December 1974 (thin line) and December 1978 (thick line). The ticks on the bottom are 12 hours apart. The roman numerals (I, II etc.) designate cold surge events for the indicated year.

scent and the cold surge event in southern China is apparent. As described in B1 these quasi-geostrophic pressure velocity maxima are the result of the short waves entering the strong baroclinic zone around 40°N, 120°E and amplifying. In B1 it was pointed out that these short waves travel down the northwesterly flow downstream of a ridge near 60°E. Comparison of the thickness field and the vertical motion in this region indicates that the surges represent a strengthening of the thermally direct circulation in the entrance region of the East Asian jet maximum.

Figure 2b is a time series of the divergent component of the meridional wind at the surface and 200 mb for a 20 × 20 degree grid centered on 26.5°N, 115°E in southeast China. In B1 it was shown for surge III using Q vector analysis that there was an ageostrophic northerly wind in this region consistent with the quasi-geostrophic forcing. The events depicted in Fig. 2b give evidence that similar forcing is present for the surges throughout the month. Aloft at 200 mb the southerly component is also seen to oscillate quite strongly, approximately with the surges. If one makes the assumption that the divergent wind approximates the ageostrophic wind then these variations will affect the coriolis acceleration of the air entering the East Asian jet maximum. The circulation of Fig. 2b is the horizontal meridional component of the thermally direct circulation indicated by the vertical motion field. Figure 2c is the same as Fig. 2b only for the whole meridional wind. The whole wind northerly component is restricted mostly to the surface but occasionally extends

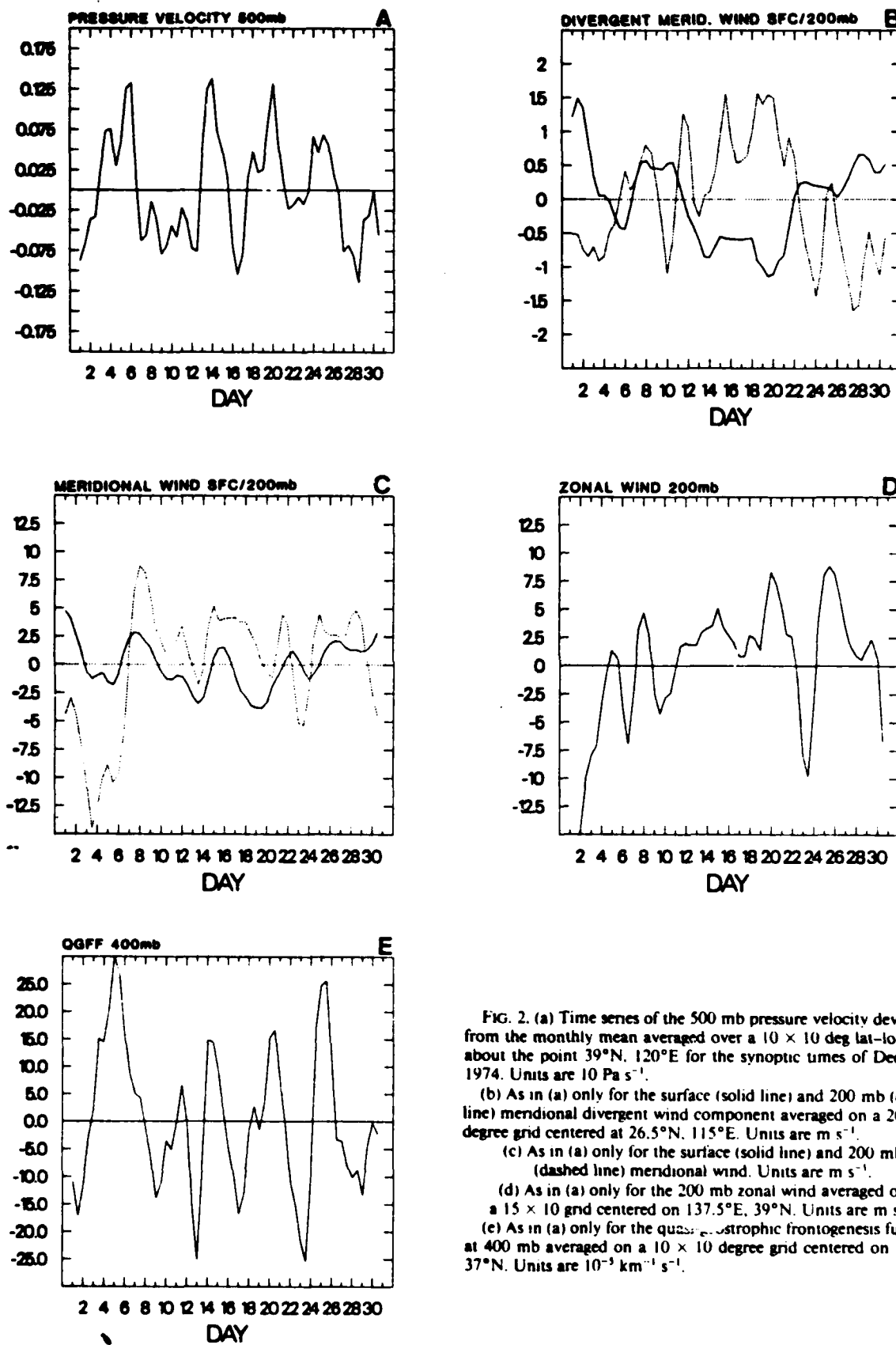


FIG. 2. (a) Time series of the 500 mb pressure velocity deviations from the monthly mean averaged over a  $10 \times 10$  deg lat-long grid about the point  $39^\circ\text{N}$ ,  $120^\circ\text{E}$  for the synoptic times of December 1974. Units are  $10 \text{ Pa s}^{-1}$ .

(b) As in (a) only for the surface (solid line) and 200 mb (dashed line) meridional divergent wind component averaged on a  $20 \times 20$  degree grid centered at  $26.5^\circ\text{N}$ ,  $115^\circ\text{E}$ . Units are  $\text{m s}^{-1}$ .

(c) As in (a) only for the surface (solid line) and 200 mb (dashed line) meridional wind. Units are  $\text{m s}^{-1}$ .

(d) As in (a) only for the 200 mb zonal wind averaged on a  $15 \times 10$  grid centered on  $137.5^\circ\text{E}$ ,  $39^\circ\text{N}$ . Units are  $\text{m s}^{-1}$ .

(e) As in (a) only for the quasi-geostrophic frontogenesis function at 400 mb averaged on a  $10 \times 10$  degree grid centered on  $125^\circ\text{E}$ ,  $37^\circ\text{N}$ . Units are  $10^{-3} \text{ km}^{-1} \text{ s}^{-1}$ .

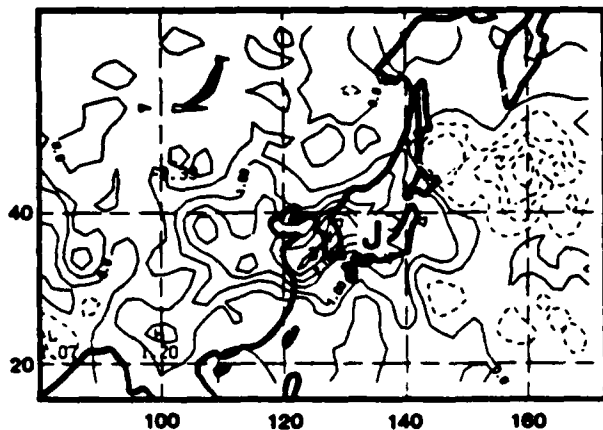


FIG. 3. The monthly average of the quasi-geostrophic frontogenesis function at 400 mb over eastern Asia for December 1974. Position of the mean jet maximum is indicated by the "J". Contour interval of  $5 \times 10^{-3} \text{ km}^{-1} \text{ s}^{-1}$ .

up to 700 mb. At the surface it is gratifying to see the correlation between an increase in the northerly divergent wind and the cold surge initiation since this freshening of the northerly wind is often taken as a definition of a surge event taking place. Figure 2d is the time series of the zonal component of the wind averaged over the mean position ( $15 \times 10$  degree grid centered on  $39^\circ\text{N}$ ,  $137.5^\circ\text{E}$  of the East Asian jet maximum at 200 mb. There is a definite increase in the jet maximum shortly after the onset of the cold surge event. This is consistent with the pattern of the meridional component of the divergent wind and the momentum budget in the next section.

Figure 2e presents the results of the QGFF calculations at 400 mb. The values are  $5 \times 5$  degree averages taken in the entrance region of the mean East Asian jet maximum ( $37^\circ\text{N}$ ,  $125^\circ\text{E}$ ; cf. Fig. 3a of B1). The correspondence between increased QGFF at 400 mb and the cold surges at Hong Kong is evident. The increased confluence indicated by the rise in the QGFF is a reflection of the tightening of the thermal gradient so that thermal wind balance is retained with the strengthening jet. Figure 3 is a chart of the monthly average values of the QGFF at 400 mb for December 1974. The monthly mean maximum of the QGFF field lies directly upstream of the East Asian jet maximum

at  $37^\circ\text{N}$ ,  $127^\circ\text{E}$  and there is a minimum in the jet maximum exit region. In the jet entrance region the QGFF is positive on the average (frontogenetic,  $3 \times 10^{-1} \text{ km}^{-1} \text{ s}^{-1}$ ). Large excursions ( $\sim$  one standard deviation) during the surge events result in this area having the maximum mean value of confluence over the entire computational grid. Namias and Clapp (1949) advocated the confluence mechanism as the process responsible for providing the strong thermal gradients needed to balance the jet maxima on the eastern flanks of the continents. Their work and more recent studies, Lau (1978), Blackmon et al. (1977), consider the wintertime mean values of confluence. Figure 2e shows the episodic nature that makes up the upper-level frontogenesis maxima over East Asia and its intimate connection with cold surges. This enhancement of confluence is due to the short waves passing through the mean trough position, increasing the mean confluence already present. Given this evidence one could anticipate that the values of the QGFF computed in the entrance region of the jet using forecast height fields might be useful in predicting surge onsets. The value of the QGFF does not appear to have any obvious relation to the magnitude of the temperature deviation in Hong Kong.

#### 1) MOMENTUM BUDGET—DECEMBER 1974

Momentum budgets were computed using (3) and (4) for December 1974 using the FNOC analyzed mercator grid winds. Table 1 gives the terms of the time averaged zonal momentum equation averaged spatially over the region from  $31^\circ$  to  $43^\circ\text{N}$  and  $105^\circ$  to  $135^\circ\text{E}$ . This is the mean position of the entrance region to the East Asian jet maximum at 200 mb. The balance is as described by Lau (1978), and Namias and Clapp (1949) for this region, in that the  $u(\partial u/\partial x)$  term nearly balances the coriolis acceleration, with the meridional advection being almost five times smaller than the zonal advection. Thus, it would appear that the December 1974 zonal momentum budget for the jet entrance is close to what is expected from past climatological work. The second line of Table 1 expresses the ratio of each term to the coriolis acceleration (the dominant term) as a percent (absolute value). In this case the transient contributions play a very minor role, their contribution

TABLE 1. Time average zonal momentum budget at 200 mb for December 1974. Units are  $10^{-4} \text{ m s}^{-2}$ .

$\partial \bar{u} / \partial t$	$\bar{u} \partial \bar{u} / \partial x$	$\bar{v} \partial \bar{u} / \partial y$	$f \bar{v}_a$	$\partial (\bar{u} \bar{u}) / \partial x$	$\partial (\bar{v} \bar{v}) / \partial y$	Residual
0.04	4.80	1.00	5.10	-0.07	-0.03	0.63
Each of the above terms divided by $f \bar{v}_a$ , expressed as a percent:						
0.8	96.0	20.0	100.0	1.4	0.6	15.0
2.0						

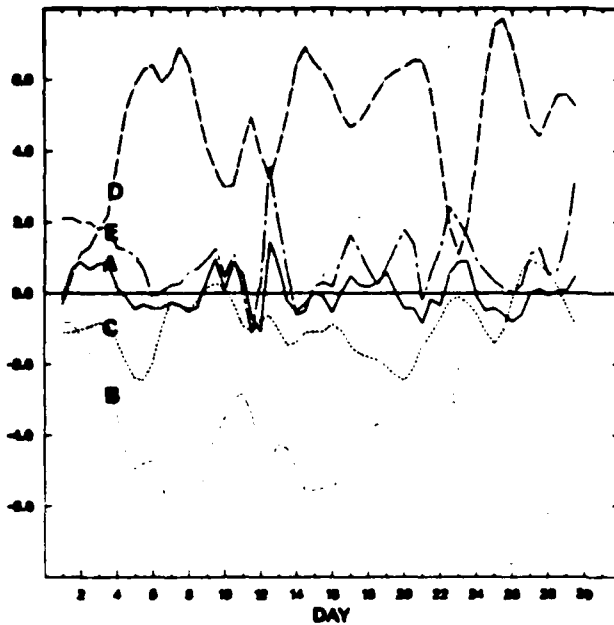


FIG. 4. Time series of the terms of the momentum budget equation for an average over a region from 31°N to 43°N, 105°E to 135°E. (a) Local time rate of change of zonal momentum ( $\partial u/\partial t$ ); (b) Zonal advection of zonal momentum ( $u\partial u/\partial x$ ); (c) Meridional advection of zonal momentum ( $v\partial u/\partial y$ ); (d) Coriolis acceleration ( $f\bar{v}_a$ ); (e) Residual term. Units are in  $m\ s^{-2}$ .

being less than that of the uncertainty expressed in the residual term. This is consistent with the strong confluence in this region and with the standard, classical picture of the balances in the region.

The balance is not as simple when the individual time periods are considered. Although there is considerable room for error in the values of the terms for single times especially in evaluating the ageostrophic wind component we feel that the patterns are consistent enough to bear examination. Figure 4 is the zonal momentum budget terms for the entire month of December 1974 using (3) in the entrance region of the East Asian jet maximum. There is a correlation between the surges at Hong Kong and an increase in the coriolis acceleration. It appears that the energy released by the thermally direct circulation which peaks during the surge provides energy for the accelerating jet.

The balance found by Blackmon et al. (1977) and Lau (1978), between the zonal advection and the coriolis torque is true for the entire month on the average. From Fig. 4 it can be seen that this balance [ $f\bar{v}_a \sim u\partial u/\partial x$ ] is dominant during the surge periods, however between the surges the balance can be rather mixed.

## 2) HEAT FLUXES—DECEMBER 1974

Figure 5 is the monthly average eddy ( $\overline{V^*T^*}$ ) heat fluxes at the surface for December 1974. There is a

very strong surface ( $\sim 100\ km\ s^{-1}$ ) flux maximum in Eastern China (27°N, 115°E) which represents the vigorous cold surges of the month. Actually, over a great deal of Eastern Asia the terrain heights make the surface values correspond to the 850 mb values in pressure coordinates. At 700 mb (not shown) the maximum moves farther to the north and east to 52°N, 123°E. The 700 mb fluxes are comparable to the standing wave fluxes at 850 mb of Blackmon et al. (1977) in location and strength.

Figures 6b and 6a are Hövmüller diagrams (longitude vs time) along 33° and 26.5°N, respectively, from 105° to 170°E of the eddy heat flux at the surface for the entire month of December 1974. The contours are of average values for a strip 2.5 degrees on either side of the indicated latitude. In December 1974 the position of the maximum mean heat flux value was at 26.5°N, while 33°N was the corresponding latitude in December 1978. The maxima in heat flux along the East Asian coast (position indicated on the figure) coincide with the cold surge events. Figure 6 illustrates the double nature of surges I, II and III which was noted previously in B1. The main flux maxima appear to be fixed along the coast with only a slight eastward extension. However, there are strong transient components which move eastward and develop in strength, these are especially evident at 33°N. These transient features are initiated almost simultaneously with the cold surge onset but move to the east rapidly and intensify. These features can be associated with the cyclones that are developed and maintained by the short waves which triggered the cold surge. The cyclones move to the east but the most intense cold air transport remains anchored to the coast. At the lower latitudes (Fig. 6a) the fluxes associated with the surge are stronger and farther inland. The eastward propagating disturbances are only weakly observable, thus the coastal thrust of cold air is by far the dominating feature in the monthly averages (Fig. 5).

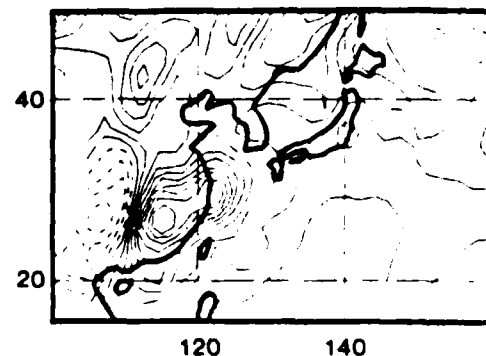


FIG. 5. The monthly average eddy heat fluxes ( $\overline{V^*T^*}$ ) for December 1974 at the surface. Contour interval is  $10\ km\ s^{-1}$ . Dashed contours indicate negative values.

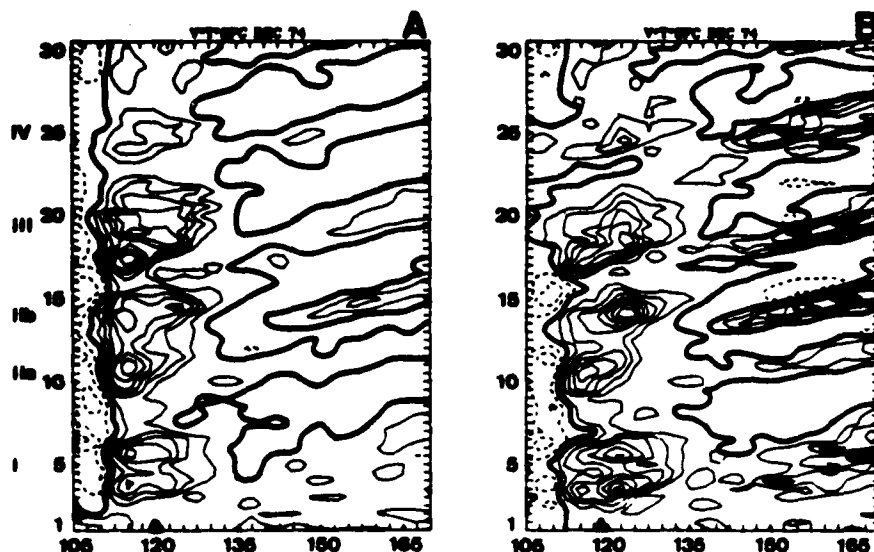


FIG. 6. (a) Hövmüller diagrams (time vs longitude) of the eddy heat flux along  $26.5^{\circ}\text{N}$  from  $105^{\circ}\text{E}$  to  $170^{\circ}\text{E}$ . The tick marks on the ordinate are 12-hours apart. The ticks on the abscissa are 2.5 degrees apart. The position of the coast is indicated by the solid triangle. Contour interval is  $25 \text{ km s}^{-1}$ . Surge events indicated by the roman numerals on the ordinate. Dashed contours indicate negative values. (b) As in (a) only for  $33^{\circ}\text{N}$ .

#### 4. December 1978 results

##### December 1978 time series

Figures 7a–c are time series of pressure velocity, meridional and zonal winds, divergent meridional wind and QGFF at the indicated pressure levels. The data are deviations from the monthly mean, averaged over a grid centered at the indicated latitude and longitude and at the given pressure level. The time of the surges for December 1978 are identified in the temperature deviation plot of Fig. 1.

The time series of the 500 mb pressure velocity (Fig. 7a) is centered on the point of the monthly average maximum descent on the East Asian coast ( $31^{\circ}\text{N}$ ,  $122^{\circ}\text{E}$ ). Although only 500 mb values are shown the descent maxima are observed to be at a lower level (700 mb as opposed to 500 mb) than those of December 1974. This could be the result of the December 1978 center being farther south compared to December 1974 ( $31^{\circ}\text{N}$  vs  $40^{\circ}\text{N}$ ). As in December 1974, the thermally direct circulation in the entrance region to the East Asian jet maximum is intensified during the surge event.

The divergent meridional component at Hong Kong (Fig. 7b) shows an increase in the northerly component during surges, with the maximum generally near the 1000 mb level, although the full extent of the northerlies can be quite deep (500 mb). There is a marked anticorrelation between the 1000 and 200 mb levels. Increased northerly flow at the 1000 mb level is accom-

panied by increased southerly flow at 200 mb and vice versa. December 1974 (Fig. 2b) did not display this obvious anticorrelation. The whole wind meridional component (Fig. 7c) has the lower-level northerly maxima at a slightly higher level ( $\sim 850$  mb, not shown) and it appears that the 1000 mb divergent component comprises about half of the magnitude in this region. This is a similar ratio as found in December 1974. The whole meridional wind does not display the strong anticorrelation that the divergent component did between 200 and 1000 mb. There is, as expected, a strong correlation between increased northerlies and colder air in southern China.

The time series of the zonal component of the wind, Fig. 7d, shows the passages of wind maxima associated with the synoptic waves into the entrance region of the jet. As in 1974 these accelerations are correlated with the surges and the meridional divergent component of the wind and with increases in the QGFF.

Figure 7e is a time series of the quasi-geostrophic frontogenesis function in the entrance region of the mean jet maximum. As in December 1974 there is a correlation between increased confluence at 400 mb and the cold surges. The values of the maximum being a good indication of short-wave passage through the region. The average value is positive ( $1.71 \times 10^{-5} \text{ m}^{-1} \text{ s}^{-1}$ ), and about one-half that of December 1974. The deviations were also of greater magnitude in 1974.

Figure 8 is a chart of the monthly mean value of the QGFF for December 1978. Comparing this to Fig. 3, the corresponding chart for December 1974, we can

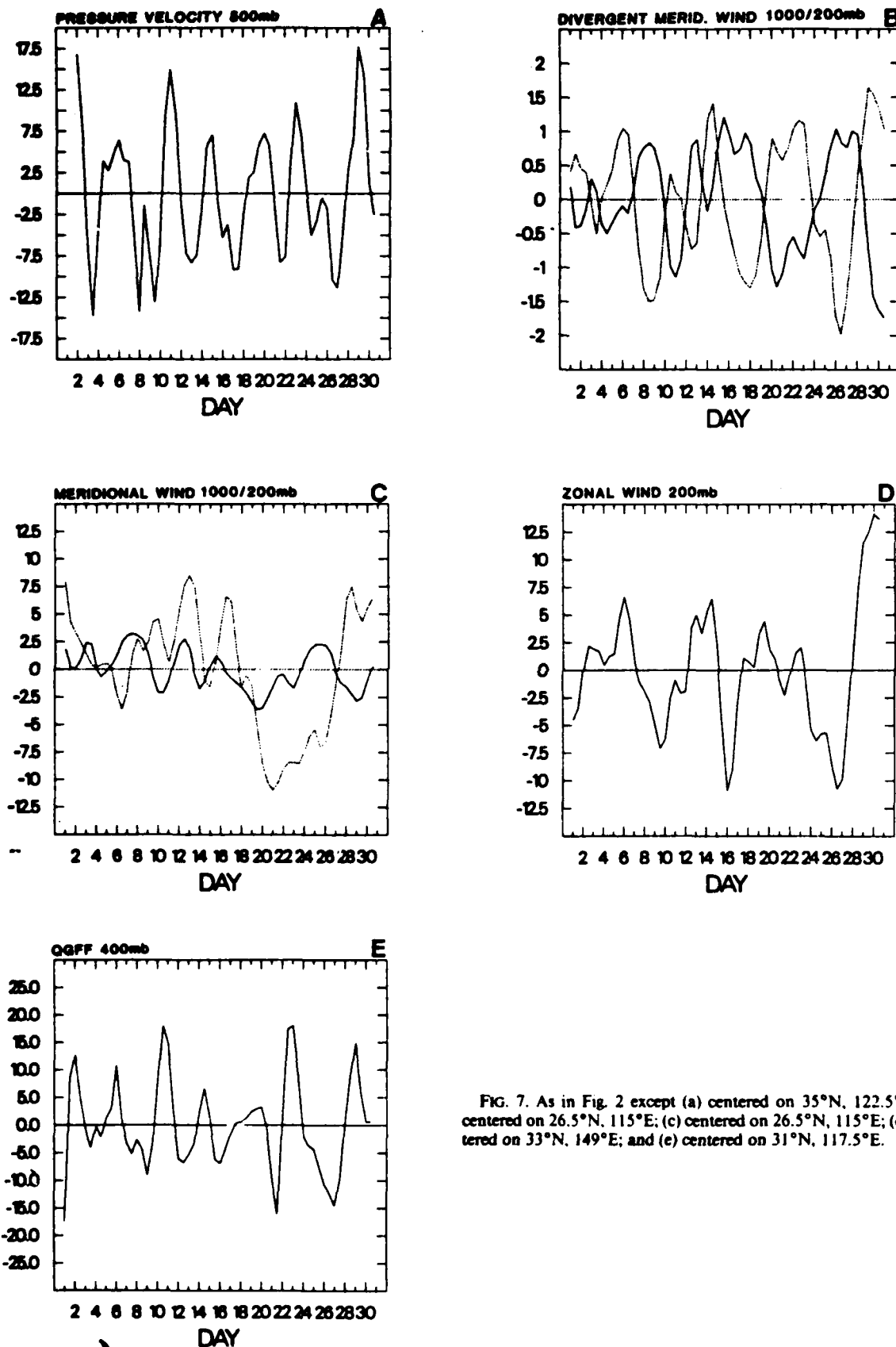


FIG. 7. As in Fig. 2 except (a) centered on 35°N, 122.5°E; (b) centered on 26.5°N, 115°E; (c) centered on 26.5°N, 115°E; (d) centered on 33°N, 149°E; and (e) centered on 31°N, 117.5°E.

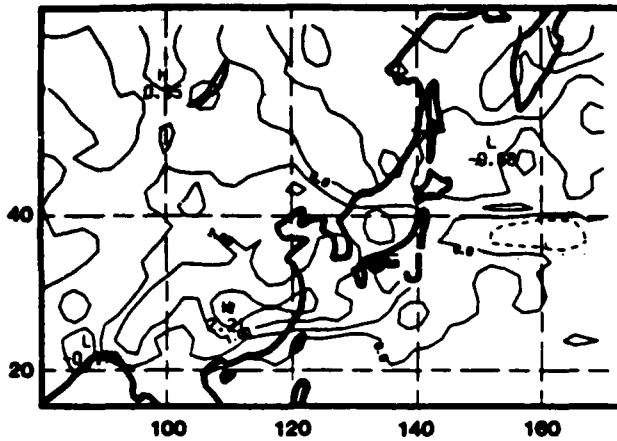


FIG. 8. As in Fig. 3 except for December 1978.

see that the maximum is more diffuse and farther south in 1978. The prominent negative/positive couplet about the EAJ maximum seen in 1974 is almost absent in 1978. This is consistent with the weaker, broader jet maximum in 1978.

1) MOMENTUM BUDGET DECEMBER 1978

Table 2 has the momentum budget for the time average zonal wind. These data are averages over an area bounded by 24°–37°N, 102.5°–132.5°E, the entrance region to the mean EAJ maximum for December 1978. The balance is essentially the same as in December 1974, but in this case the transients play a greater role. Although still relatively small the effect of the transients at least exceeds that of the residual term, and thus can be more confidently said to have an impact on the zonal flow.

The time series of the momentum budget at 200 mb for December 1978 is given in Fig. 9. Notice the scale difference of this figure and the corresponding one (Fig. 4) of December 1974. The dominant balance is between the  $u(\partial u/\partial x)$  term and the  $f\bar{v}_a$  term. There is a good correspondence between an increase (decrease) in the  $f\bar{v}_a$  term and the cold surge events as in December 1974. This can be interpreted as the direct circulation accel-

erating the jet due to the coriolis acceleration as indicated by Fig. 7d.

Comparison of the momentum budget of the entrance region to the jet maximum for December 1974 and December 1978 provides more evidence of the reduced intensity of the local circulation in December 1978. The magnitude of the average coriolis acceleration is reduced by a factor of about two, although the sense of the balance is the same in 1974 and 1978 with all the terms smaller in 1978. The circulation of December 1978 from the aspect of the momentum budget appears to be a scaled down version of December 1974. The same mechanisms are at work but the meridional and zonal circulations are weaker in December 1978. Notice that although event II is the strongest surge at Hong Kong the III and IV events yield slightly higher values of coriolis acceleration.

One must be cautious about assessing the results of the momentum budget using the ECMWF data. Kung and Tanaka (1983) have shown that on a global average the ECMWF data lean more toward geostrophic balance than the GFDL (Geophysical Fluid Dynamics Laboratory) analysis or the balance indicated by previous work. Lau (1984) also has demonstrated that the ECMWF data have a reduced Hadley circulation compared to that seen in the GFDL analysis. This problem of underestimating the divergent wind appears to be most severe in the tropics. Thus, the reduced values that are seen in Fig. 9 (compared to Fig. 4) could just be due to differences in the ECMWF and FNOC analysis procedures.

However, there is some evidence that the reduced magnitude of the December 1978 momentum budget terms might be real. First, the budget terms not involving the ageostrophic wind and presumably dominated by the rotational wind, such as  $u(\partial u/\partial x)$ , are also reduced in December 1978. Second, quantities computed using the height field only, such as the QGFF, also demonstrate the reduced intensity of the circulation. Thus, it is probable that the momentum budget in December 1978 is actually reduced in intensity, with respect to December 1974, but the actual amount reduced is obscured by the analyses differences. In any case the qualitative response of the momentum budget terms during the cold surge periods are quite similar in Figs. 4 and 9.

TABLE 2. Time average zonal momentum budget at 200 mb for December 1978. Units are  $10^{-4} \text{ m s}^{-2}$ .

$\partial \bar{u} / \partial t$	$\bar{u}(\partial \bar{u} / \partial x)$	$\bar{v}(\partial \bar{u} / \partial y)$	$f \bar{v}_a$	$\partial(\bar{u}^2) / \partial x$	$\partial(\bar{v}^2) / \partial y$	Residual
0.07	1.80	0.80	2.50	-0.12	0.18	0.17
Each of the above terms divided by $f \bar{v}_a$ , expressed as a percent:						
2.8	72.0	32.0	100.0	4.8	7.2	6.8
						2.4

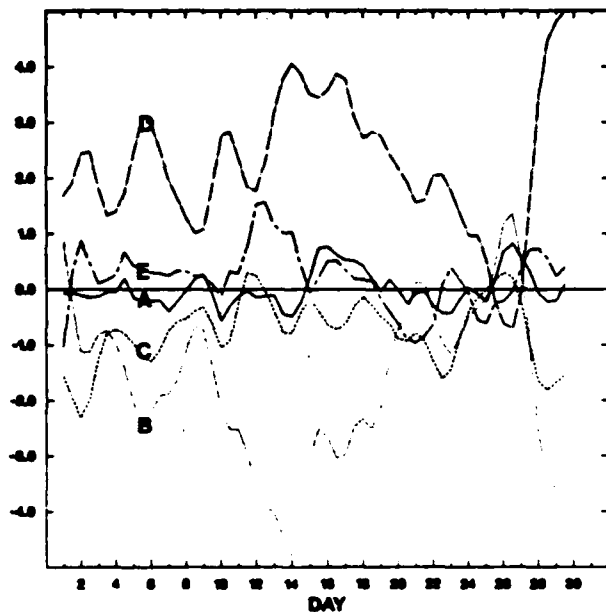


FIG. 9. As in Fig. 4 except for December 1978 and averaged over 24°-37°N, 102.5°-132.5°E.

## 2) HEAT FLUXES DECEMBER 1978

Considering the monthly averaged eddy heat fluxes ( $\overline{V^*T^*}$ ) for December 1978 (Fig. 10), the maximum at 1000 mb along the East Asian coast at 33°N, 120°E is about half the strength of the December 1974 surface value (Fig. 5), and located to the northeast of the December 1974 center. There is a second maximum over the Sea of Japan in December 1978. At 700 mb (not shown) the December 1978 maxima on the East Asian coast are weaker and farther north compared to the December 1974 fields. Cold air is being transported southward over the entire span of 80 to 30°E in December 1978.

Figures 11a and 11b are Hovmuller diagrams of the eddy heat fluxes ( $V^*T^*$ ) along 35° and 30°N at 1000 mb for December 1978. The pattern is similar to that of Fig. 6 for December 1974. The maxima along the coast are generally smaller than those of December 1974. Notice that 35°N is the latitude of the monthly average maximum in the flux while the December 1974 maximum was at 30°N. Again the pattern is of fluxes anchored to the coast and transient (eastward moving) fluxes developing to the east seen in December 1974 is repeated. The average duration of the positive fluxes along the coast is longer in December 1974, this is even more evident in the diagram at 26.5°N, which is through the December 1974 monthly mean maximum. There is not a great deal of difference in the transient components of the fluxes, and indeed the cyclones that developed off the East Asian coast in December 1978 appeared to be as robust as those in December 1974.

## 5. Discussion

The classical manner of considering the general circulation of the atmosphere was from a zonally averaged perspective. This viewpoint was well summarized by Lorenz in his 1967 monograph. Recently the study of the general circulation has expanded in scope to include the important longitudinal variations in the long term seasonal mean circulation. This work is exemplified by the study of Blackmon et al. (1977). Perhaps the next step in this progression would be to study the individual circulation patterns that are responsible for the longitudinal features of the long term fields. It would be of interest to determine if there are any specific circulation systems that dominate in making up a certain longitudinal feature. From the results presented here, it would appear that the East Asian cold surges play a dominant role in producing the circulation features on the Asian coast documented by Blackmon et al. (1977), and Lau (1978).

The circulation parameters studied here are those which comprise the processes occurring in the entrance region to the East Asian jet. Blackmon et al. (1977) present a schematic (their Fig. 15a) of the time mean circulation in the entrance region of a wintertime jet maximum on the east coast of a continent. The computations presented here demonstrates that this picture for East Asia is strongly influenced by the individual cold surge events.

The cold surge circulation has a clear effect on the zonal momentum budget in the vicinity of the East Asian jet maximum. The mean balance of the budgets of the zonal momentum at jet level in this region are dominated by the periods of the surge events. The circulation of December 1978 from the aspect of the momentum budget appears to be a scaled down version of December 1974. The same mechanisms are at work but the meridional and zonal circulations are weaker in December 1978.

The balance found by Blackmon et al. (1977) and Lau (1978), between the zonal advection and the coriolis acceleration is true for both months on the av-

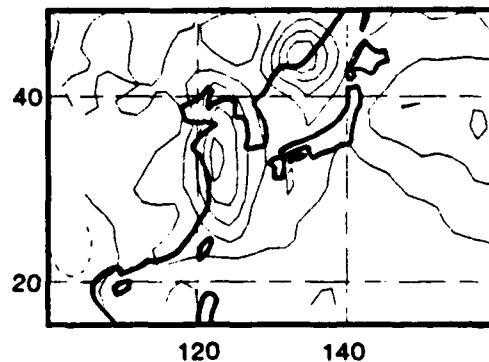


FIG. 10. As in Fig. 5 except for December 1978 and at 1000 mb.

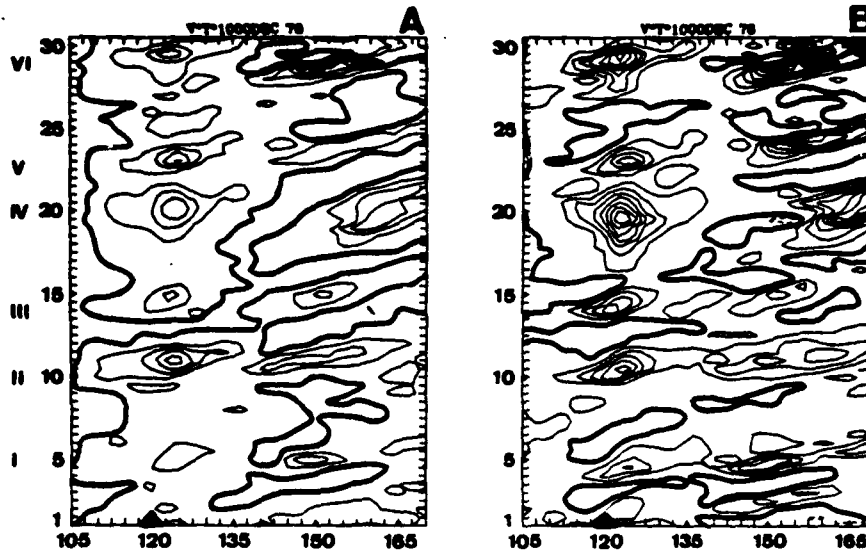


FIG. 11. As in Fig. 6 except for December 1978.

crage. From Figs. 4 and 9 it can be seen that this balance [ $f\bar{v}_a \sim u(\partial u/\partial x)$ ] is dominant during the surge periods, however between the surges the balance can be rather mixed.

The cold surge outbreaks are closely correlated to frontogenesis at upper levels in the East Asian jet region forced by confluent geostrophic deformation. This is a result of the short-wave passage through this region to the east. Computations indicate that the cold surge periods dominate the long term average confluence observed in this region, (Namias and Clapp, 1949). Thus the confluent geostrophic deformation is important in maintaining the thermal wind balance with the East Asian jet region.

The acceleration of the East Asian jet by the cold surge can provide a link of the cold surges to the global circulation by modulating the East Asian jet. Thus the surge circulation can then strongly feed back to the general circulation center of action in the North Pacific, Lau et al. (1984).

**Acknowledgments.** Prof. C.-P. Chang supplied useful comments on the manuscript. This work was carried out while the author was a National Research Council Resident Research Associate at the Naval Postgraduate School. The research was partially supported by the National Science Foundation under grant ATM-8020302. The computations were performed at the W. R. Church Computer Center at the Naval Postgraduate School.

#### REFERENCES

- Blackmon, M. L., J. M. Wallace, N.-C. Lau and S. L. Mullen, 1977: An observational study of the Northern Hemisphere wintertime circulation. *J. Atmos. Sci.*, **34**, 1040-1053.
- Boyle, J. S., 1986: Comparison of the synoptic conditions in mid-latitudes accompanying cold surges over Eastern Asia for the months of December 1974 and 1978. Part I: Monthly mean fields, individual events and composites. *Mon. Wea. Rev.*, **114**, 903-918.
- Chang, C.-P., and K. M. Lau, 1980: Northeasterly cold surges and near-equatorial disturbances over the winter MONEX area during December 1974. Part II: Planetary scale aspects. *Mon. Wea. Rev.*, **108**, 298-312.
- , J. E. Erickson and K. M. Lau, 1979: Northeasterly cold surges and near-equatorial disturbances over the winter MONEX area during December 1974. Part I: Synoptic aspects. *Mon. Wea. Rev.*, **107**, 812-829.
- Chen, T. C., J. C. Alpert and T. W. Schlatter, 1978: The effects of divergent and nondivergent winds on the kinetic energy budget of a midlatitude cyclone: A case study. *Mon. Wea. Rev.*, **106**, 458-468.
- Cressman, G. P., 1981: Circulations of the west Pacific jet stream. *Mon. Wea. Rev.*, **109**, 2450-2463.
- Endlich, R. M., 1967: An iterative method for altering the kinematic properties of wind fields. *J. Appl. Meteor.*, **6**, 837-844.
- Kung, E. C., and H. Tanaka, 1983: Energetics analysis of the global circulation during the special observation periods of FGGE. *J. Atmos. Sci.*, **40**, 2575-2592.
- Holton, J. R., 1979: *An Introduction to Dynamic Meteorology*, second ed., Academic Press, 319 pp.
- Hoskins, B. J., and M. A. Pedder, 1980: The diagnosis of middle latitude synoptic development. *Quart. J. Roy. Meteor. Soc.*, **106**, 707-719.
- Joung, C. H., and M. H. Hitchman, 1982: On the role of successive downstream development in East Asian polar air outbreaks. *Mon. Wea. Rev.*, **110**, 1224-1237.
- Lau, K. M., C. P. Chang and P. H. Chan, 1983: Short term planetary-scale interactions over the tropics and midlatitudes during northern winter. Part II: Winter MONEX periods. *Mon. Wea. Rev.*, **111**, 1372-1388.
- Lau, N.-C., 1978: On the three-dimensional structure of the observed transient eddy statistics of the northern hemisphere wintertime circulation. *J. Atmos. Sci.*, **35**, 1900-1923.
- , 1984: A comparison of circulation statistics based on FGGE level III-B analyses produced by GFDL and ECMWF for the

- special observing periods. NOAA Data Rep. ERL GFDL-6, Geophysical Fluid Dynamics Laboratory, Princeton, NJ.
- , and K.-M. Lau, 1984: The structure and energetics of midlatitude disturbances accompanying cold air outbreaks over East Asia. *Mon. Wea. Rev.*, 112, 1309–1327.
- Lorenz, E. N., 1967: *The Nature and Theory of the General Circulation of the Atmosphere*. WMO Publication No. 218, Tech. Pap. 115, World Meteorological Organization, Geneva, 161 pp.
- McGinley, J., 1982: A diagnosis of Alpine lee cyclogenesis. *Mon. Wea. Rev.*, 110, 1271–1287.
- Murakami, T., 1979: Winter monsoonal surges over East and Southeast Asia. *J. Meteor. Soc. Japan*, 57, 133–158.
- Namias, J., and P. F. Clapp, 1949: Confluence theory of the high tropospheric jet stream. *J. Meteor.*, 6, 330–336.
- Newell, R. E., J. W. Kidson, D. G. Vincent and G. J. Boer, 1974: *The General Circulation of the Tropical Atmosphere, Vol. 2*. Massachusetts Institute of Technology, 371 pp.
- Palmen, E., and C. W. Newton, 1951: On the three-dimensional motions in an outbreak of polar air. *J. Meteor.*, 8, 25–39.
- , and —, 1969: *Atmospheric Circulation Systems*, Academic Press, 603 pp.
- Rosen, R. D., and D. A. Salstein, 1982: General circulation statistics on short time scales. *Mon. Wea. Rev.*, 110, 683–698.
- Taubensee, R. E., 1975: Weather and circulation of December 1974—Continued warm across much of the country. *Mon. Wea. Rev.*, 103, 266–271.
- , 1979: Weather and circulation of December 1979—Record and near record cold in the West. *Mon. Wea. Rev.*, 107, 354–360.

## Analytical and Numerical Studies of the Beta-Effect in Tropical Cyclone Motion. Part I: Zero Mean Flow

JOHNNY C. L. CHAN\* AND R. T. WILLIAMS

Department of Meteorology, Naval Postgraduate School, Monterey, CA 93943

(Manuscript received 30 August 1985, in final form 10 November 1986)

### ABSTRACT

The  $\beta$ -effect on tropical cyclone motion is studied using an analytical as well as a numerical model in a nondivergent barotropic framework. The analytical model and the linear version of the numerical model give essentially the same result: the linear  $\beta$ -effect causes a westward stretching of the model vortex but no significant movement of the vortex center. An east-west asymmetry in the meridional wind field is also created. It is the inclusion of the nonlinear term that produces the northwestward movement of the vortex previously found by other investigators (e.g., Kitade, 1981). This northwestward movement increases with both the maximum wind speed and the radius of maximum wind in a constant-shape vortex. A wind maximum is also found to the northeast of the vortex, which appears to be consistent with the observational findings of Shea and Gray. This asymmetry plays an important role in the vortex motion.

### 1. Introduction

The study of the effect of the earth's rotation on the movement of a tropical cyclone dates back to the work of Rossby (1939, 1948). Since then, a number of theoretical and numerical studies have been conducted to examine this effect (see the review in Chan, 1982). Rossby suggested that the larger Coriolis force on the poleward side of a symmetric cyclonic vortex would produce a net force which would cause the cyclone to move poleward. On the other hand, Adem and Lezama (1960) and later Anthes and Hoke (1975) and others proposed that differential advection of the earth's vorticity to the west and east of the cyclone would cause it to move initially westward. A secondary circulation (in the horizontal) is then set up which advects the vortex northward (Holland, 1983). As a result, the cyclone tends to move towards the northwest. This has become known as the  $\beta$ -effect.

However, some questions regarding the physical processes associated with this main effect remain. For example, what is the mechanism that sets up the secondary circulation? How do the linear and nonlinear processes contribute to the movement of the cyclone? Is the  $\beta$ -effect independent of the intensity of the vortex? This study attempts to address these questions by solving the nondivergent barotropic vorticity equation. The numerical results of DeMaria (1983, 1985) suggest that cyclone movement is rather insensitive to the intensity of the cyclone. However, his results were obtained with the cyclone embedded in a basic flow. Ex-

clusion of any mean flow in this study will allow reexamination of the sensitivity of the cyclone movement to its intensity due to the beta effect. In Part II, the interaction between the vortex flow and different mean flows will be analyzed.

A simple analytical solution of the nondivergent barotropic vorticity equation is first sought to determine the effect of linear processes on the vortex movement. This effect is also demonstrated with a finite-difference numerical model, which indicates that the finite difference resolution is adequate to resolve the physical processes on the vortex scale. The numerical model is then used to study the nonlinear terms which cannot be easily included in the analytical model. Implications of these results on our understanding of the effect of the Coriolis parameter on both the motion and structure of the vortex will also be discussed.

### 2. Analytical model

#### a. Formulation

The nondivergent barotropic model used in this study can be formulated in terms of the conservation of absolute vorticity. The governing equation is

$$\frac{\partial \zeta}{\partial t} + \mathbf{V}_\psi \cdot \nabla(\zeta + f) = 0, \quad (2.1)$$

where  $\zeta$  is the vertical component of the relative vorticity,  $\mathbf{V}_\psi$  the nondivergent wind vector, and  $f$  the Coriolis parameter. A streamfunction  $\psi$  can be defined such that

$$\nabla^2 \psi = \zeta. \quad (2.2)$$

\* Present affiliation: Royal Observatory, Hong Kong.

The linearized version of (2.1) with no mean flow on an equatorial beta plane can then be written

$$\frac{\partial}{\partial t} \left( \frac{\partial^2 \psi}{\partial x^2} + \frac{\partial^2 \psi}{\partial y^2} \right) + \beta \frac{\partial \psi}{\partial x} = 0, \quad (2.3)$$

where  $\beta$  is the latitudinal variation of the Coriolis parameter.

Assuming periodic boundary conditions in both the  $x$  and  $y$  directions, the Fourier transform of (2.3) gives

$$\frac{\partial \Psi}{\partial t} - \frac{ik\beta}{(k^2 + l^2)} \Psi = 0, \quad (2.4)$$

where

$$\Psi(k, l, t) = \int_0^{2\pi} \int_0^{2\pi} \psi(x, y, t) e^{i(kx+ly)} dx dy, \quad (2.5)$$

and  $k, l$  are the wavenumbers in the  $x$  and  $y$  directions, respectively. If the function  $\Psi$  is separable in time and the temporal part is oscillatory, then it can be written as

$$\Psi(k, l, t) = A(k, l) e^{-i\omega t}. \quad (2.6)$$

Substituting (2.6) into (2.4) yields

$$A(k, l) = \Psi(k, l, 0) \quad (2.7)$$

and

$$\omega = -\frac{k\beta}{k^2 + l^2}. \quad (2.8)$$

The streamfunction at any time  $t$  is then given by the inverse transform of  $\Psi(k, l, t)$  as

$$\psi(x, y, t) = \frac{1}{2\pi} \sum_k \sum_l A(k, l) e^{-i(kx+ly+\omega t)}. \quad (2.9)$$

Given the initial conditions  $\psi(x, y, 0)$ , we can then solve for  $\psi(x, y, t)$  using (2.5) and (2.7)–(2.9). Note that since the wavenumber  $l$  in the  $y$ -direction only appears as  $l^2$  in (2.8), the solution will be symmetric about the  $x$ -axis.

The cyclonic vortex used in this part of the study has a tangential wind  $V(r)$  profile of

$$V(r) = V_m \left( \frac{r}{r_m} \right) \exp \left\{ \frac{1}{b} \left[ 1 - \left( \frac{r}{r_m} \right)^b \right] \right\}, \quad (2.10)$$

where  $r$  is the radius,  $V_m$  the value of  $V(r)$  at the radius of maximum wind  $r_m$  and  $b$  is a factor that determines the shape of the vortex. Examples of this profile can be found in Fig. 1 for different values of  $V_m$ . The corresponding vorticity ( $\zeta$ ) profile is given by

$$\zeta(r) = \frac{2V_m}{r_m} \left[ 1 - \frac{1}{2} \left( \frac{r}{r_m} \right)^b \right] \exp \left\{ \frac{1}{b} \left[ 1 - \left( \frac{r}{r_m} \right)^b \right] \right\}. \quad (2.11)$$

One method to initialize the model just described is to solve for  $\psi$  from (2.2) and (2.11). However, a simpler method is to use the  $\zeta(r)$  profile directly by first noting the equality

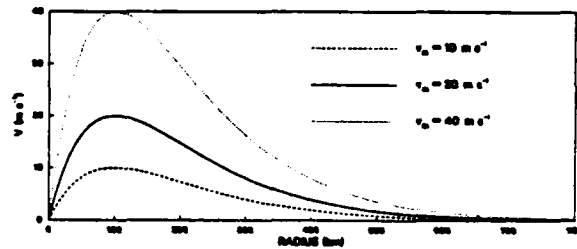


FIG. 1. Tangential wind profiles as defined in (2.10) for different values of  $V_m$ .

$$\begin{aligned} \int_0^{2\pi} \int_0^{2\pi} [\nabla^2 \psi(x, y, 0)] e^{i(kx+ly)} dx dy \\ = -(k^2 + l^2) \int_0^{2\pi} \int_0^{2\pi} \psi(x, y, 0) e^{i(kx+ly)} dx dy \end{aligned}$$

so that

$$A(k, l) = -\frac{1}{(k^2 + l^2)} \int_0^{2\pi} \int_0^{2\pi} \zeta(x, y, 0) e^{i(kx+ly)} dx dy. \quad (2.12)$$

The streamfunction at any time  $t$  is then obtained by solving (2.9), with the spectral amplitude  $A(k, l)$  of the initial conditions given by (2.12). In the following, solutions of (2.9) using a grid size of 20 km and 101 grid points in both the  $x$  and  $y$  directions will be presented. Beta is evaluated at  $10^\circ$  latitude.

### b. Results

The streamfunction fields at selected times for a vortex given by (2.10) with  $V_m = 40 \text{ m s}^{-1}$ ,  $r_m = 100 \text{ km}$  and  $b = 1.0$  are shown in Fig. 2. The vortex is seen to elongate westward with time as a result of the dispersive effects of Rossby waves. The dispersion relation given by (2.8) implies that longer waves have larger westward phase speeds than shorter waves. Since the waves representing the outer circulation have lower wavenumbers than those representing the inner circulation, the outer part of the vortex propagates westward faster than the inner part, which results in a stretching of the vortex westward. Such a dispersion of linear Rossby waves has also been studied for ocean vortices (e.g., Flierl, 1977; McWilliams and Flierl, 1979; Mied and Lindemann, 1979).

The time variations of the relative vorticity fields are similar to those of the streamfunction and therefore will not be shown. However, it must be noted that in solving for  $\zeta$  from (2.2) and (2.9), the amplitudes of the spectral coefficients  $A(k, l)$  are reduced by a factor  $(k^2 + l^2)$  so that the westward propagation of shorter waves (representing the inner circulation) will be further decreased. As a result, even though the  $\psi$  and  $\zeta$  fields are initially concentric, the  $\beta$ -effect produces an intersection of the two fields, as illustrated in Fig. 3.

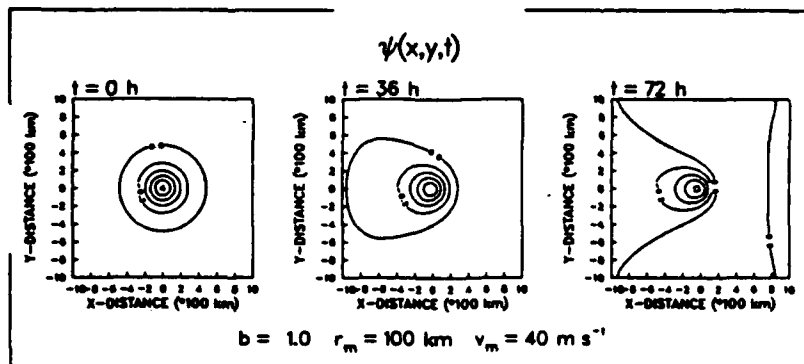


FIG. 2. Streamfunction fields ( $\psi$ ) at 0, 36 and 72 h for the analytical model using the vortex profile in (2.10) with  $V_m = 40 \text{ m s}^{-1}$ ,  $r_m = 100 \text{ km}$  and  $b = 1.0$ . The contour interval is  $0.2 \times 10^6 \text{ m}^2 \text{ s}^{-1}$ .

Notice that the intersection of the  $\psi$  and  $\zeta$  isolines occurs near the center of the vortex where not much movement of the vorticity maximum occurs. Since the streamfunction represents the flow field, such an intersection between the two fields becomes important when the effect of relative vorticity advection (not considered in this formulation) is included.

The asymmetry in the  $\psi$  field (Fig. 2) also implies an asymmetry in the wind fields. Since the streamfunction is symmetric about the  $x$ -axis, the wind asymmetry is only in the meridional ( $v$ ) component (Fig. 4) and results in a wind maximum to the east of the vortex. Note also that the speed differential between the east and west sides of the vortex increases with time.

The large east-west wind asymmetry may be explained as follows. Advection of the earth vorticity produces an increase (decrease) in relative vorticity to the west (east) of the vortex. Since the governing equation (2.3) implicitly assumes an instantane-

ous adjustment of the winds, these changes in relative vorticity will increase the southerly flow near, and northerly flow at distances both east and west of, the vortex center. This southerly flow was first identified by Anthes and Hoke (1975) and termed the "secondary circulation" by Holland (1983). Because the winds are initially northerly to the west and southerly to the east of the vortex, this secondary circulation will produce an east-west asymmetry in the  $v$ -component. As only linear effects are included in the model, this asymmetry cannot be removed through self-advective (nonlinear) processes. At the same time, the increase in southerly flow further decreases the relative vorticity near and to the east of center through the advection of the earth's vorticity. The asymmetry in the wind field therefore increases with time.

If the rate of decay of the tangential wind with radius is decreased (that is, the value of  $b$  is reduced in Eq. 2.10), the center of the vortex (where the stream func-

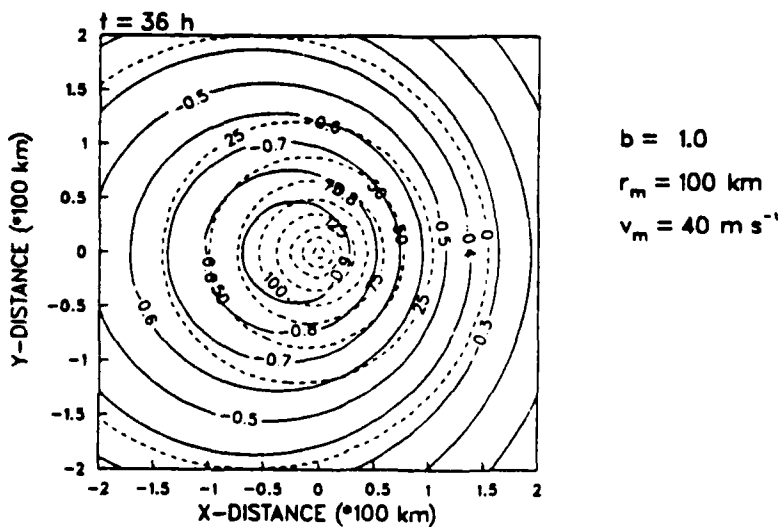


FIG. 3. As in Fig. 2 except for the streamfunction (solid,  $10^6 \text{ m}^2 \text{ s}^{-1}$ ) and relative vorticity (dashed,  $10^{-3} \text{ s}^{-1}$ ) fields at 36 h.

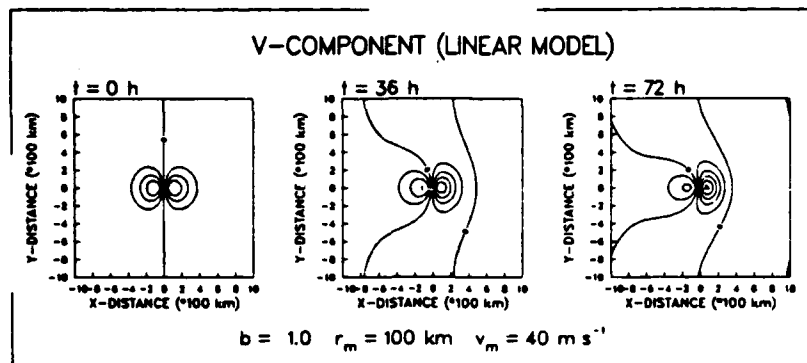


FIG. 4. Meridional ( $v$ ) wind component at 0, 36 and 72 h derived from the solutions in Fig. 2. The contour interval is  $10 \text{ m s}^{-1}$ .

tion is a minimum) is found to have a slightly larger westward displacement (not shown). This results from the longer waves associated with a larger vortex having a larger amplitude so that the westward phase speed is enhanced. For the same reason, a constant-shape vortex with a larger radius of maximum wind ( $r_m$  in Eq. 2.10) will move westward faster than one with a smaller  $r_m$ . However, varying the magnitude of the maximum wind ( $V_m$ ) does not have an effect on the vortex movement. An increase in the value of  $V_m$  simply increases the amplitudes of the spectral coefficients  $A(k, l)$  by the same amount for all wavenumbers (see Eq. 2.12). This results in the values of  $\psi(x, y, t)$  obtained by solving (2.9) being multiplied by a larger factor but the location of the relative minimum in the streamfunction remains unchanged.

To summarize, the linear  $\beta$ -effect elongates a symmetric vortex westward with very little displacement of the center of the vortex (as given by the maximum of relative vorticity or minimum in streamfunction). The wind field also becomes highly asymmetric in the east-west direction with stronger (weaker) winds to the east (west).

### 3. The numerical model

#### a. Formulation

The nondivergent barotropic model developed by Tupaz (1977) to study barotropic instabilities associated with an easterly jet (Tupaz et al., 1978) is utilized. The governing equation with no mean flow can be written as

$$\frac{\partial}{\partial t} \nabla^2 \psi = -J(\psi, \nabla^2 \psi) - \beta \frac{\partial \psi}{\partial x}, \quad (3.1)$$

where the symbols are as in section 2. The Jacobian  $J(\psi, \nabla^2 \psi)$  represents the nonlinear effect that is excluded in section 2. The domain is an east-west channel with cyclic boundary conditions in the zonal direction. That is,

$$\psi = 0 \quad \text{at} \quad y = \pm D, \quad (3.2)$$

where the meridional domain is defined by

$$-D \leq y \leq D.$$

Eq. (3.1) is solved using the leapfrog time-differencing scheme. The Jacobian is evaluated using the finite difference form developed by Arakawa (1966). At the north-south boundaries, the values of  $\nabla^2 \psi$  are extrapolated from the first interior points. The direct method described by Sweet (1973) is used to solve for  $\partial \psi / \partial t$  in (3.1) and to derive the initial streamfunction field from the vorticity profile defined in (2.11).

The linear [with  $J(\psi, \nabla^2 \psi)$  set to zero] solutions to (3.1) are found to be very similar to those from the analytical model. The similarity of the results from the two models provides an indication that the truncation errors in the numerical solutions are small.

#### b. Results

The nonlinear solutions to (3.1) for the same vortex used in section 2 are shown in Fig. 5. Contrary to the linear solution (Fig. 2), the inner part of the vortex remains rather symmetric. At the same time, the outer part of the vortex maintains a westward stretching as a result of the linear  $\beta$ -effect. The vortex center is now displaced to the northwest. An acceleration in the movement of the vortex can also be identified from its track (Fig. 6), with its translation speed increasing from  $0.8 \text{ m s}^{-1}$  in the first 12 h to  $2.8 \text{ m s}^{-1}$  by 60 h. Notice also a slight oscillation in the vortex track.

Such a northwestward displacement and acceleration of the vortex as well as the oscillation in the track are consistent with results obtained by other researchers (e.g., Kitade, 1981). This movement can be explained by considering the east-west asymmetry induced by the  $\beta$ -effect discussed in section 2. Since the nonlinear term (advection of vortex vorticity) is now included, the crossing of the  $\psi$  and  $\zeta$  isolines shown in Fig. 3 implies an advection of the vortex vorticity by the

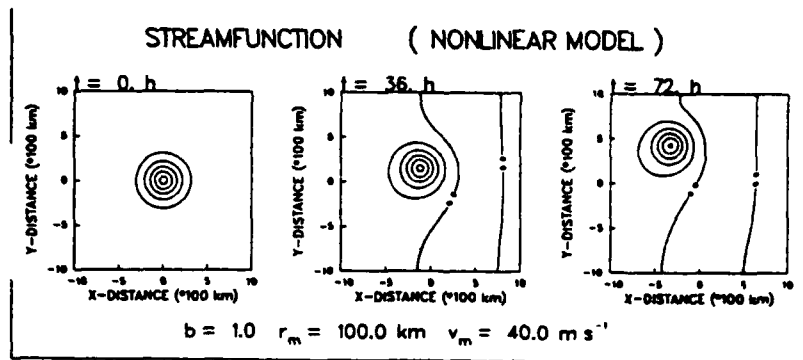


FIG. 5. As in Fig. 2 except for the nonlinear numerical simulations. The contour interval is  $0.1 \times 10^6 \text{ m}^2 \text{ s}^{-1}$ .

asymmetric flow represented by the streamfunction  $\psi$ . This advection leads to an increase of vorticity to the north of the vortex and a decrease to the south. These changes in vorticity depend on the crossing angle between the  $\psi$  and  $\zeta$  isolines. Near the vortex center, the crossing angle and the speed are large and thus a strong advective (nonlinear) effect results. In the outer region, the two fields do not intersect significantly so that this part of the vortex continues its westward elongation while the inner region moves northward. Consequently, the asymmetry in the streamfunction field is no longer east-west but rather along a southwest-northeast direction (Fig. 5).

The physical explanation given here of the northwestward vortex displacement due to the  $\beta$ -effect is somewhat different from that schematically portrayed by Holland (1983). According to Holland (1983), the vortex first moves west due to the beta effect. Then the vorticity changes lead to a secondary circulation which is directed to the north over the vortex center, which combined with the beta effect causes the vortex to move to the northwest. In the present study the early northward motion is caused by relative vorticity advection which results from the Rossby wave distortion of the vortex. At a later stage when the wind asymmetry is developed (Fig. 7), the asymmetry has associated with it a flow component across the center in the direction of movement. This is generally consistent with Holland's view of the role of the secondary circulation.

Because of the orientation of the streamfunction asymmetry (Fig. 5), the maximum wind speed is now to the northeast of the vortex (Fig. 7). Notice also an oscillation of the  $40 \text{ m s}^{-1}$  isotach around the northeastern quadrant of the vortex. The maximum wind increases from  $41.6 \text{ m s}^{-1}$  at 12 h to  $43.5 \text{ m s}^{-1}$  at 48 h. If the translation speed is subtracted, a residual asymmetry still remains. Therefore, this wind asymmetry cannot be explained simply by the translation of the vortex. Adjustments of the wind field to the increase in relative vorticity to the northwest of the vortex (due to the nonlinear effect) tends to produce a wind maximum in this region but the (linear)  $\beta$ -effect induces

a wind maximum to the east of the vortex. A combination of these two effects therefore causes a continuous adjustment between the  $\psi$  and  $\zeta$  fields, which leads to the wind asymmetry and the associated oscillations. The oscillation in the vortex track can also be explained in a similar manner as the vortex tries to move along a "constant phase" line which balances the linear and the nonlinear effects. Part of this oscillation may be due to difficulty in finding the center between grid points, but the increase in speed is well defined.

The existence of an asymmetry in the tangential winds in tropical cyclones after the motion of the cyclone is removed has been observed by several researchers (e.g., Jordan, et al., 1960; Shea and Gray, 1973; George and Gray, 1976). The asymmetry is usually to the right of the cyclone (facing downstream along the direction of cyclone motion). Most tropical cyclones (in the Northern Hemisphere) move westward or northwestward. Thus, this asymmetry would be in the northeast quadrant, which is consistent with the numerical result presented here. Therefore, the combination of the beta (linear) and the nonlinear effects may offer an explanation of such an observed asymmetry.

To summarize, it is the combination of the linear and nonlinear effects that leads to a northwestward displacement of the vortex. The continuous distortion of the streamfunction and relative vorticity fields by the  $\beta$ -effect causes an adjustment between these two fields to occur when nonlinear (horizontal advection of vortex vorticity) effects are included. A modification of either effect will therefore lead to a change in the vortex movement, as will be seen in section 4.

#### 4. Sensitivity tests with vortex strength and scale

In this Section, results are presented from integrations with different values of  $r_m$  and  $l_m$  in the initial vortex (2.10), but with the original value  $b = 1$ . The following grid sizes are used for each value of the radius of maximum wind:  $r_m = 50 \text{ km}$ ,  $\Delta x = \Delta y = 10 \text{ km}$ ;  $r_m = 100 \text{ km}$ ,  $\Delta x = \Delta y = 20 \text{ km}$ ;  $r_m = 200 \text{ km}$  and  $\Delta x = \Delta y = 40 \text{ km}$ . All experiments use a domain size

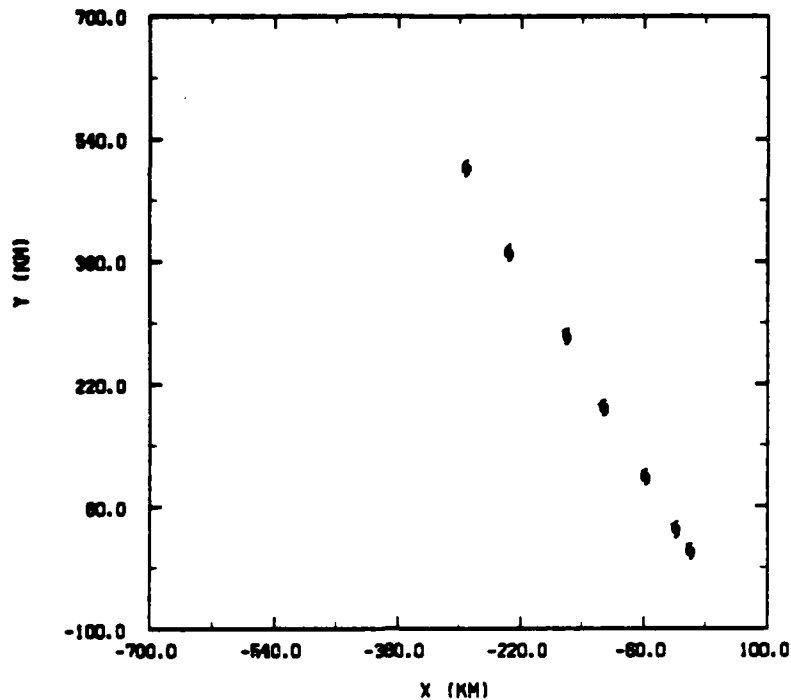


FIG. 6. The 0-72 h track of the vortex with  $r_m = 100$  km,  $V_m = 40$  m s<sup>-1</sup>. The symbols along the track are 12 h apart.

of  $201 \times 201$  which insures that the boundaries do not affect even the fastest moving vortex over 72 hours. In each experiment the form of the vortex trajectory is similar to that shown in Fig. 6 for  $r_m = 100$  km and  $V_m = 40$  m s<sup>-1</sup>. All results presented in this section are averages from  $t = 48$  hours to  $t = 72$  hours. The directions of motion for the various experiments are given in Table 1. They have a monotonic variation from  $315^\circ$  to  $335^\circ$ . For a fixed  $r_m$ , the angle increases with increasing  $V_m$ , and the angle decreases for increasing  $r_m$  when  $V_m$  is fixed. The curves in Fig. 8 give the speed of movement as a function of  $V_m$  for each of the three

values of  $r_m$ . The curves imply a linear behavior as a function of  $V_m$  for  $V_m \leq 20$  m s<sup>-1</sup>, but note that the curves do not extrapolate to the origin as  $V_m \rightarrow 0$ . This may be related to the vastly different structure type in the highly distorted Rossby wave solution ( $V_m = 0$ ) as compared with the nearly circular solution when  $V_m$  is small, but not zero. This strongly suggests that one cannot get the proper solution by expanding about the linear solution. Figure 9 contains movement curves as a function of  $r_m$  for three values of  $V_m$ . In this case, the portions of the curves which satisfy  $r_m \leq 100$  km do appear to extrapolate to zero as  $r_m \rightarrow 0$ . Figure 10

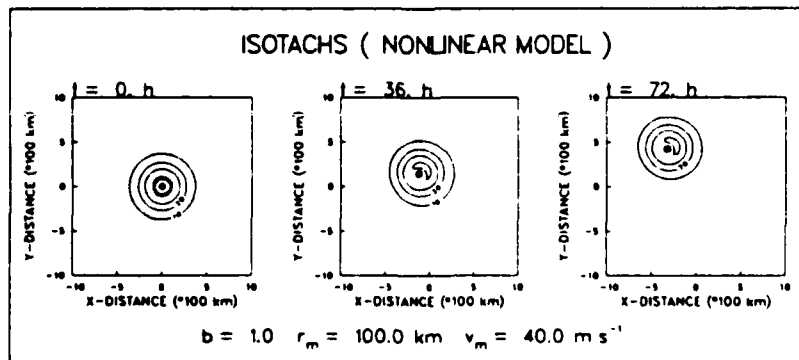


FIG. 7. Isotachs derived from the nonlinear numerical simulation given in Fig. 5. The contour interval is  $10$  m s<sup>-1</sup>.

TABLE 1. Directions of movement averaged from 48 to 72 h for each experiment.

$V_m$ ( $\text{m s}^{-1}$ )	$r_m$ (km)		
	50	100	200
2.5		321.1°	
5.0		321.7°	
10.0	330.3°	324.8°	314.4°
20.0	332.2°	328.9°	318.6°
40.0	333.9°	329.3°	325.9°
80.0		334.1°	

contains contours of the speed of movement as a function of  $r_m$  and  $V_m$ . The curves are roughly hyperbolic, which would be expected since the curves in Figs. 8 and 9 have approximately linear variations.

These results show that the speed of movement of the vortex increases with  $V_m$  and  $r_m$ , although the direction changes only slowly. If the "angular momentum",  $r_m V_m$ , is held constant in Fig. 10, it can be seen that the speed of movement is nearly constant (since the isolines in Fig. 10 are nearly hyperbolas). This suggests that a tropical cyclone track would be unaffected by changes in intensity provided that  $r_m V_m$  were conserved. Holland (1984) states that "no track changes accompany oscillations in central pressure or maximum winds in hurricanes". However, it is not known whether or not  $r_m V_m$  is conserved in these cases. Our solutions (see especially Fig. 9) indicate that the winds in the outer region have more influence on the vortex motion than winds closer to the center. In fact DeMaria (results presented by Holland, 1984) showed that increasing the wind in the inner part of the vortex ( $r$

< 100 km) had no effect on vortex motion while changes in the outer region had a direct effect. DeMaria (1983, 1985) found similar results in a model which included horizontal wind shear as well as the beta effect.

### 5. Discussion and conclusion

The results from this study can be summarized as follows. The linear  $\beta$ -effect, though incapable of significantly displacing the central core of the vortex, provides a necessary environment for vortex movement. It creates an east-west asymmetry in the meridional wind field which then interacts with the vortex vorticity when nonlinear effects are included. Advection of the vortex vorticity then gives rise to a northwestward displacement of the vortex. This nonlinear process depends on the strength of the meridional wind field created by the linear effect and the relative vorticity gradient within the vortex. An increase in the tangential winds at all radii causes an increase in the northwestward movement although the linear  $\beta$ -effect remains unchanged. Increasing the size of the vortex with the shape held fixed enhances the meridional flow through the linear dispersion of Rossby waves and leads to a larger northwestward displacement. The solutions show that the speed of movement is nearly constant for vortices which have the same characteristic "angular momentum"  $r_m V_m$ . The results of this paper agree with the previous conclusion (Holland, 1983, 1984 and DeMaria, 1983, 1985) that the vortex motion is insensitive to the wind structure in the inner region.

Another consequence of the combination of the (linear)  $\beta$ -effect and the nonlinear effect is the creation of a wind maximum to the northeast of the vortex. It

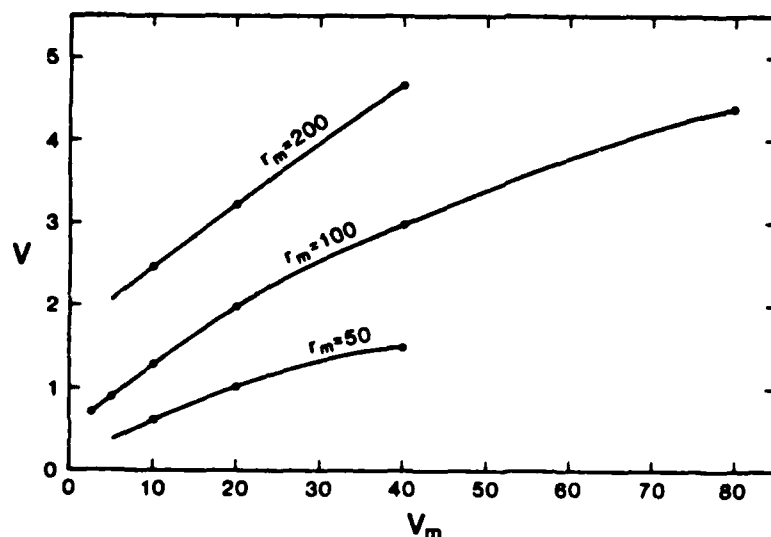


FIG. 8. The speed of movement  $V$  ( $\text{m s}^{-1}$ ) as a function of  $V_m$  ( $\text{m s}^{-1}$ ) for three values of  $r_m$  (km).

appears that this asymmetry plays an important role in the vortex motion. Such an across-the-vortex wind asymmetry has been found from aircraft observations of hurricanes (Shea and Gray, 1973). The  $\beta$ -effect may therefore offer an explanation of this observed asymmetry.

From the fluid dynamical point of view, this study shows how dispersion (linear) and vorticity advection (nonlinear) effects can combine to move the vorticity center even though neither process can significantly move the vortex by itself. It is very important to obtain a more complete understanding of this process.

No mean flow is included in these experiments in order to isolate the  $\beta$ -effect. As is discussed in section 4, incorporation of a basic flow significantly complicates the problem. DeMaria (1985) has pointed out the importance of the vorticity gradient associated with the basic flow. The linear advection of the vortex by a spatially nonuniform basic flow will also modify the vortex movement. In addition, the dispersion of Rossby waves can occur with this basic flow. Nonlinear interactions between the vortex circulation and the basic flow can also alter the movement of the vortex. All these effects will be presented in Part II of this study.

**Acknowledgments.** The authors would like to thank Mr. M. Fiorino for performing all of the numerical integrations which are presented in section 4, and especially for finding a critical error in the original com-

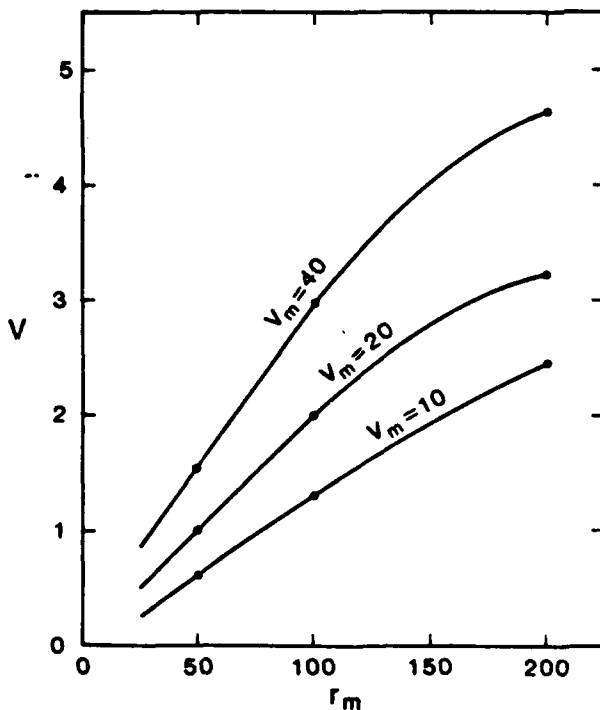


FIG. 9. The speed of movement  $V$  ( $m s^{-1}$ ) as a function of  $r_m$  (km) for three values of  $V_m$  ( $m s^{-1}$ ).

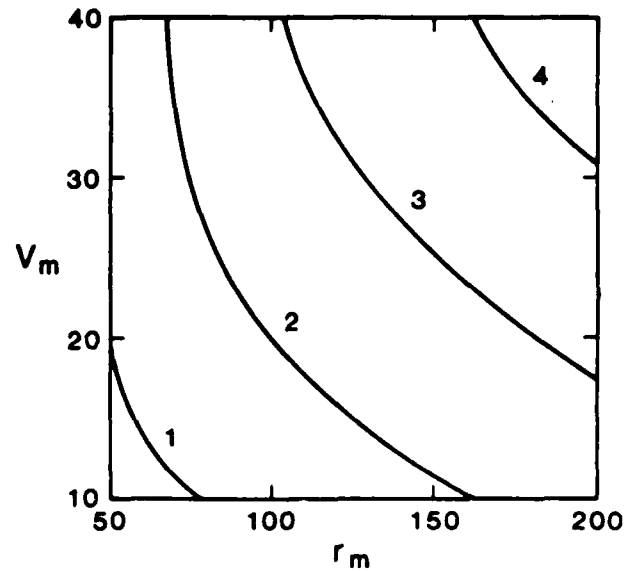


FIG. 10. Isolines of the speed of movement  $V$  ( $m s^{-1}$ ) as functions of  $V_m$  ( $m s^{-1}$ ) and  $r_m$  (km).

puter code. The authors would also like to thank Professor R. L. Elsberry, Dr. Greg Holland and Dr. Mark DeMaria for helpful comments on the manuscript. Mrs. Penny Jones carefully typed the manuscript and Mr. Mike McDermet drafted some of the figures. This research was supported by the National Science Foundation Global Atmospheric Research Program under Grant ATM 8315175 and the Naval Air Systems Command through the Naval Environmental Prediction Research Facility.

#### REFERENCES

- Adem, J., and P. Lezama, 1960: On the motion of a cyclone embedded in a uniform flow. *Tellus*, **12**, 255-258.
- Anthes, R. A., 1982: Tropical Cyclones: their evolution, structure and effects. *Meteor. Monographs*, Vol. 19, No. 41, Amer. Meteor. Soc., 208 pp.
- , and J. A. Hoke, 1975: The effect of horizontal divergence and the latitudinal variation of the Coriolis parameter on the drift of a model hurricane. *Mon. Wea. Rev.*, **103**, 757-763.
- Arakawa, A., 1966: Computational design for long-term numerical integration of the equations of atmospheric motion. *J. Comput. Physics*, **1**, 119-143.
- Chan, J. C.-L., 1982: On the physical processes responsible for tropical cyclone motion. *Atmos. Sci. Paper No. 358*, Department of Atmospheric Science, Colorado State University, Fort Collins, CO, 200 pp.
- DeMaria, M., 1983: Experiments with a spectral tropical cyclone model. *Atmos. Sci. Paper No. 371*, Department of Atmospheric Science, Colorado State University, Fort Collins, CO, 224 pp.
- , 1985: Tropical cyclone motion in a nondivergent barotropic model. *Mon. Wea. Rev.*, **113**, 1199-1210.
- Flierl, G. R., 1977: The application of linear quasi-geostrophic dynamics to Gulf Stream rings. *J. Phys. Oceanogr.*, **7**, 365-379.
- George, J. E., and W. M. Gray, 1976: Tropical cyclone motion and

- surrounding parameter relationships. *J. Appl. Meteor.*, 15, 1252-1264.
- Holland, G. J., 1983: Tropical cyclone motion: Environmental interaction plus a beta effect. *J. Atmos. Sci.*, 40, 328-342.
- , 1984: Tropical cyclone motion: A comparison of theory and observation. *J. Atmos. Sci.*, 41, 68-75.
- Jordan, C. L., D. A. Hurt and C. A. Lowry, 1960: On the structure of Hurricane Daisy of 27 August 1958. *J. Meteor.*, 17, 337-348.
- Kitade, T., 1981: A numerical study of the vortex motion with barotropic models. *J. Meteor. Soc. Japan*, 59, 801-807.
- McWilliams, J. C., and G. R. Flierl, 1979: On the evolution of isolated, nonlinear vortices. *J. Phys. Oceanogr.*, 9, 1155-1182.
- Mied, R. P., and G. J. Lindemann, 1979: The propagation and evolution of cyclonic Gulf Stream rings. *J. Phys. Oceanogr.*, 9, 1183-1206.
- Rossby, C. G., 1939: Relation between variations in the intensity of the zonal circulation of the atmosphere and the displacements of the semi-permanent centers of action. *J. Marine Res.*, 2, 38-55.
- , 1948: On displacements and intensity changes of atmospheric vortices. *J. Marine Res.*, 7, 157-187.
- Shea, D. J., and W. M. Gray, 1973: The hurricane's inner-core region. I: symmetric and asymmetric structure. *J. Atmos. Sci.*, 30, 1544-1564.
- Sweet, R. A., 1973: A generalized cyclic reduction algorithm. *SIAM J. Num. Anal.*, 10, 506-520.
- Tupaz, J. B., 1977: A numerical study of barotropic instability of a zonally varying easterly jet. Ph.D. Thesis, Naval Postgraduate School, Monterey, CA, 107 pp.
- , R. T. Williams and C.-P. Chang, 1978: A numerical study of barotropic instability in a zonally varying easterly jet. *J. Atmos. Sci.*, 35, 1265-1280.

## Tropical-Midlatitude Interactions over Asia and the Western Pacific Ocean during the 1983/84 Northern Winter

C.-P. CHANG

*Department of Meteorology, Naval Postgraduate School, Monterey, CA 93943*

K. G. LUM

*Malaysian Meteorological Service, Petaling Jaya, Selangor, Malaysia*

(Manuscript received 6 October 1984, in final form 24 April 1985)

### ABSTRACT

Previous studies of cold surges during the northern winter monsoon suggested a short-term midlatitude-tropical interaction such that the variations of the midlatitude jet over East Asia correspond to variations in tropical convection. However, because cold surges occur during periods of intensified baroclinicity, it is possible that the strengthening of the jet may be due entirely to midlatitude baroclinic development rather than the enhanced local Hadley circulation forced by the increase in tropical convection. In this study objectively analyzed 200 mb wind data for the 1983/84 winter are examined to address the problem of determining cause and effect in short-term midlatitude-tropical interactions.

Significant positive correlation between the midlatitude jet acceleration and tropical divergence was found in several regions in the Asia-Pacific-Indian Ocean region. Among six major intensifications of the East Asian jet streak maximum during December 1983, three were related to tropical cyclone activity and two to cold surges. The tropical cyclone cases led to the conclusion that the midlatitude jet can be influenced effectively by tropical convective activity on a day-to-day basis. This result has possible implications for midlatitude weather forecasting. The study also confirmed the downstream propagation of the strengthened jet streaks, which is probably due to self-advection, and the existence of thermally indirect circulations at the exit region of the jet, both in the time-mean and in the transient motion fields.

### 1. Introduction

The zonal asymmetry of the time-mean, thermally direct meridional (Hadley) circulation linking the tropics and midlatitudes has been the subject of many studies in the last decade or so. While some work used kinematically computed divergence fields to discuss this time-mean structure (e.g., Krishnamurti *et al.*, 1973), others obtained important, although implicit, results from the geopotential height or rotational component of the wind in the midlatitudes using the principles of quasi-geostrophic jet dynamics (e.g., Blackmon *et al.*, 1977). When combined, the evidence is mounting that the wintertime jet streaks over the east coast of continents and west part of oceans are associated with a thermally direct meridional circulation at the jet entrance region and an indirect circulation at the exit region.

Blackmon *et al.* (1977) derived their results from the consideration that the Coriolis torque of these time-mean meridional circulations is necessary for the maintenance of the spatial acceleration and deceleration of the jets. In recent studies of the northern winter monsoon, short-term variation of the East Asian jet was observed to be correlated with that of the local Hadley circulation (Chang and Lau, 1980, 1982; Lau

*et al.*, 1983). The upward branch of the local Hadley circulation is located over the tropical convection region of the maritime continent downstream from the low-level northeasterlies. From time to time these northeasterlies intensify and surge equatorward, producing a cold surge which causes an enhancement of the tropical convection (Ramage, 1971; Chang *et al.*, 1979). A similar phenomenon has also been observed by Bosart (1973) in the Caribbean Sea region. Along with a strengthening of the equatorial Walker circulations, the local Hadley circulation is strengthened with the upper tropospheric return flow exerting an increased ageostrophic Coriolis torque resulting in a temporal acceleration of the jet. Thus the role of the meridional circulation in the time-mean jet dynamics as elucidated by Blackmon *et al.* (1977) may be applicable in a similar way to the transient motions, with the important implication that during cold surges significant interactions exist between the day-to-day weather changes in the midlatitudes and those in the tropics.

However, the cause-effect relationship of the observed transient interactions remains somewhat unclear. Since a cold surge occurs as a consequence of the enhanced midlatitude baroclinicity (Chang and Lau, 1982), a strengthening of the jet can occur without

increased tropical convection. The lack of discernible time lags between the increases in tropical convection and the jet acceleration makes the forcing-response relationship difficult to identify. Furthermore, in the jet entrance region a thermally direct secondary circulation can be induced solely due to the conservation of total energy for parcels entering the jet (Palmen and Newton, 1969; Uccellini and Johnson, 1979). These parcels move to the cyclonic (poleward) side of the jet so that their potential energy decreases to compensate for the increasing kinetic energy. Chang and Lau (1982) showed that the resultant secondary circulation is unlikely to be the main process responsible for the observed acceleration, because the upper-level poleward divergent flow originated from the equatorial region far away from the jet latitude. Nevertheless, more direct evidence is required to ascertain the validity of this interpretation.

The purpose of this study is to examine the transient interaction between the upper-level tropical divergent outflow and the midlatitude jet stream, using the 1983/84 winter data. These data are the most recently available operationally analyzed data for the northern winter and, due to the incorporation of upper-level satellite winds over East Asia and the western Pacific, represent a considerable improvement over the data used in previous studies.<sup>1</sup>

## 2. Data

The basic data used in this study are the 200 mb winds for December 1983–February 1984 from the Fleet Numerical Oceanographic Center's (FNOC) Global Band objective analysis. Although the analysis uses a variational approach to integrate temperature and winds in the vertical, the 200 mb level is the top boundary of the analysis and is analyzed strictly with a two-dimensional successive correction method without the influence of temperature or wind fields from other levels. The analysis incorporates all available real time data using 6 h persistence as the first guess and is not used as input to a numerical weather prediction model. In regions of adequate data coverage, the analyzed data may be more suitable than other operationally produced analyses (especially for the purpose of studying tropical divergence) for two reasons. First, it is the only operational analysis not using model forecast as the first guess and therefore not influenced by the model-forecasted tropical divergence whose representativeness is subject to debate. Second, it does not have the bias of some operational centers' optimum interpolation schemes that use midlatitude-determined

structure functions which tend to suppress synoptic-scale divergence in the tropics. Due to the available geostationary satellite-derived winds and aircraft data, the 200 mb data coverage over the tropical Pacific and Indian Ocean was relatively adequate during the period of study.

The data are analyzed twice daily on a tropical global band from 40°S to 60°N having a grid resolution of approximately 2.5° × 2.5°. Divergence ( $\chi$ ) and velocity potential ( $\delta$ ) are computed from the horizontal wind components  $u$ ,  $v$  according to the following formula<sup>2</sup>:

$$\nabla^2 \chi = -\delta = -\left(\frac{\partial u}{\partial x} + \frac{\partial v \cos \phi}{\cos \phi \partial y}\right) \sec \phi,$$

$$\chi = 0 \quad \text{at } 40^\circ\text{S and } 60^\circ\text{N},$$

where the horizontal coordinates in the Mercator projection are

$$x = a\lambda, \quad y = a \ln\left(\frac{1 + \sin \phi}{\cos \phi}\right).$$

Here  $a$  is the radius of the earth, and  $\lambda$  and  $\phi$  are longitude and latitude, respectively.

The velocity potential near the north and south boundaries is significantly influenced by this boundary condition. Comparison with the National Meteorological Center's (NMC) monthly mean final analyses shows that velocity potential pattern differences attributable to the boundary influences are noticeable only north of 40°N and south of 30°S. Since only tropical velocity potential patterns will be discussed, the boundary effects are not considered important.

## 3. Time-mean fields

The winter seasonal mean (December 1983–February 1984) horizontal wind and velocity potential fields at 200 mb are shown in Fig. 1. Because the December 1983 data will be discussed extensively, its monthly means are shown in Fig. 2.

The seasonal mean wind (Fig. 1a) shows the well-known structure of two jet stream maxima in the Northern Hemisphere between 25 and 40°N: the East Asia jet and the North American jet. The former is clearly the dominant one, with a jet core of 60 m s<sup>-1</sup> or higher winds extending from 90°E to the dateline. The area enclosed by the 40 m s<sup>-1</sup> isotach of this jet covers an approximately 180° longitudinal span (the entire Eastern Hemisphere), compared to the North American jet whose core as delineated by the 40 m s<sup>-1</sup> isotach covers only the southeastern United States, about 30° in longitude. In the December mean (Fig.

<sup>1</sup> The operational winter MONEX data used by Chang and Lau (1982) and Lau *et al.* (1983) did not contain the GMS-1 satellite-derived wind vectors because of a problem in determining the level in the operational algorithm used by the Japan Meteorological Agency during 1978/79.

<sup>2</sup> The sign convention of  $\chi$  is chosen so that positive  $\chi$  is correlated with positive divergence. This is opposite to the convention used in Haltiner and Williams (1980).

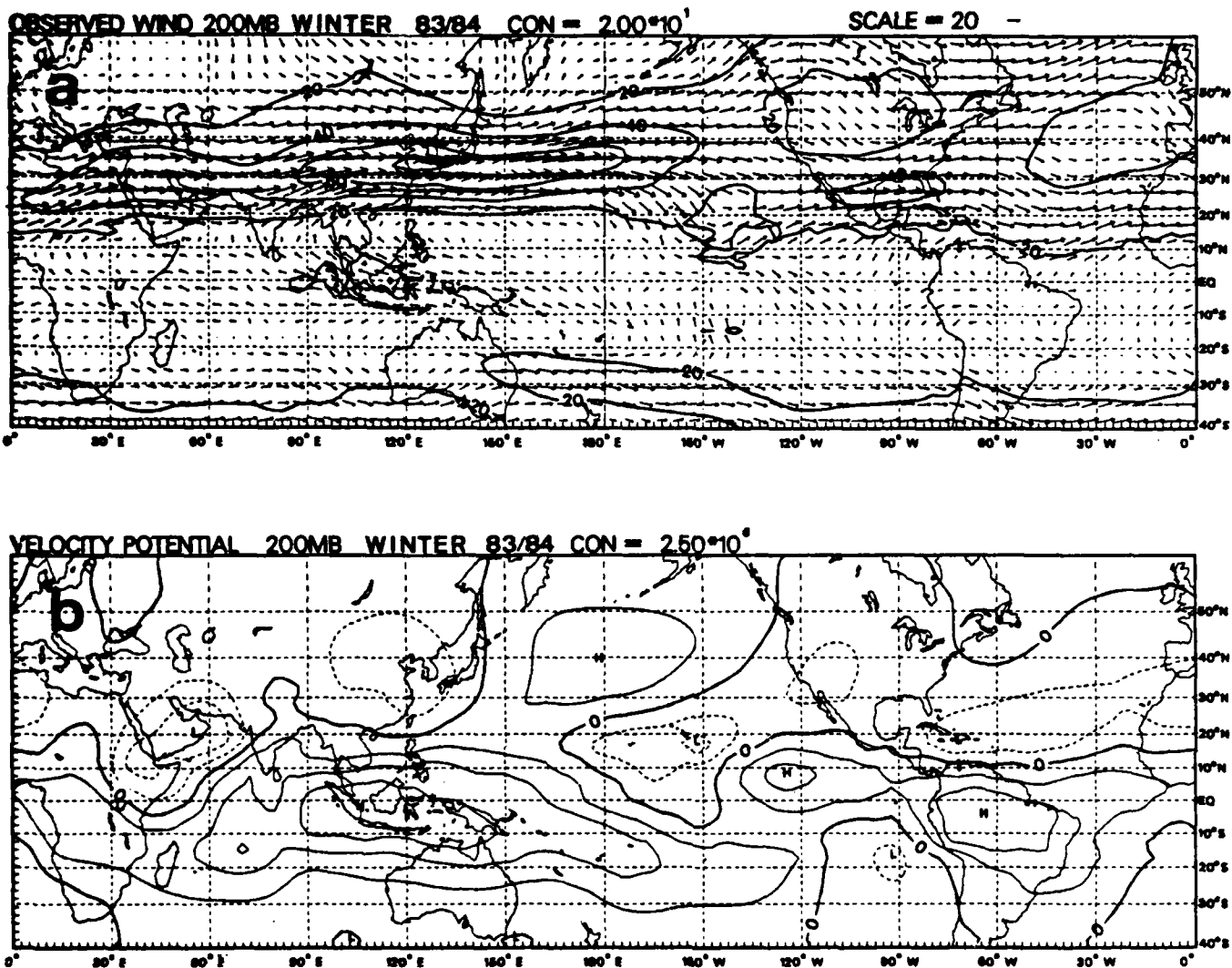


FIG. 1. The seasonal (December 1983–February 1984) mean 200 mb horizontal wind vectors with (a) isotachs ( $\text{m s}^{-1}$ ); and (b) velocity potential (isopleth interval  $2.5 \times 10^2 \text{ m}^2 \text{ s}^{-1}$ ).

2a), the Asian jet still dominates, although its strength is somewhat weaker than the seasonal mean, while the American jet is somewhat expanded. The latter may reflect the fact that the American jet is less stationary and may show a stronger presence when averaged over a shorter period.

The seasonal mean velocity potential (Fig. 1b) shows a vast area of tropical divergent flow centered over the east–west oriented maritime continent, extending longitudinally in both directions. To the east–southeast, the central axis extends deeply into the tropical southeastern Pacific, representing the outflow of the South Pacific Convergence Zone (SPCZ). To the west and west–southwest, it extends to tropical south Africa covering the equatorial Indian Ocean. In the December mean (Fig. 2b), this tropical velocity maximum is broken into two centers, one over the western part of the maritime continent from Sumatra to western Borneo,

and the other is in the SPCZ. Compared to the long-term mean of the immediate past decade (1973/74–1982–83) produced by Boyle and Chang (1984), the structure of this equatorial Indian Ocean–Pacific divergence area is close to normal, both for the winter seasonal mean and for the December mean. Since the axis of the divergence center is parallel to, and almost entirely to the south of, the East Asia jet axis, the northward divergent velocity ( $v_x$ ) between the two axes shall be used to represent the local Hadley circulation in the discussion of the midlatitude–tropical interaction over East Asia.

Another feature in the velocity potential distribution worth noting is the minimum  $\chi$  center in the central Pacific between 15 and 20°N. This center implies a thermally indirect, reversed local Hadley circulation north of it, where the deceleration of the East Asia jet is found. This supports Blackmon *et al.*'s (1977) de-

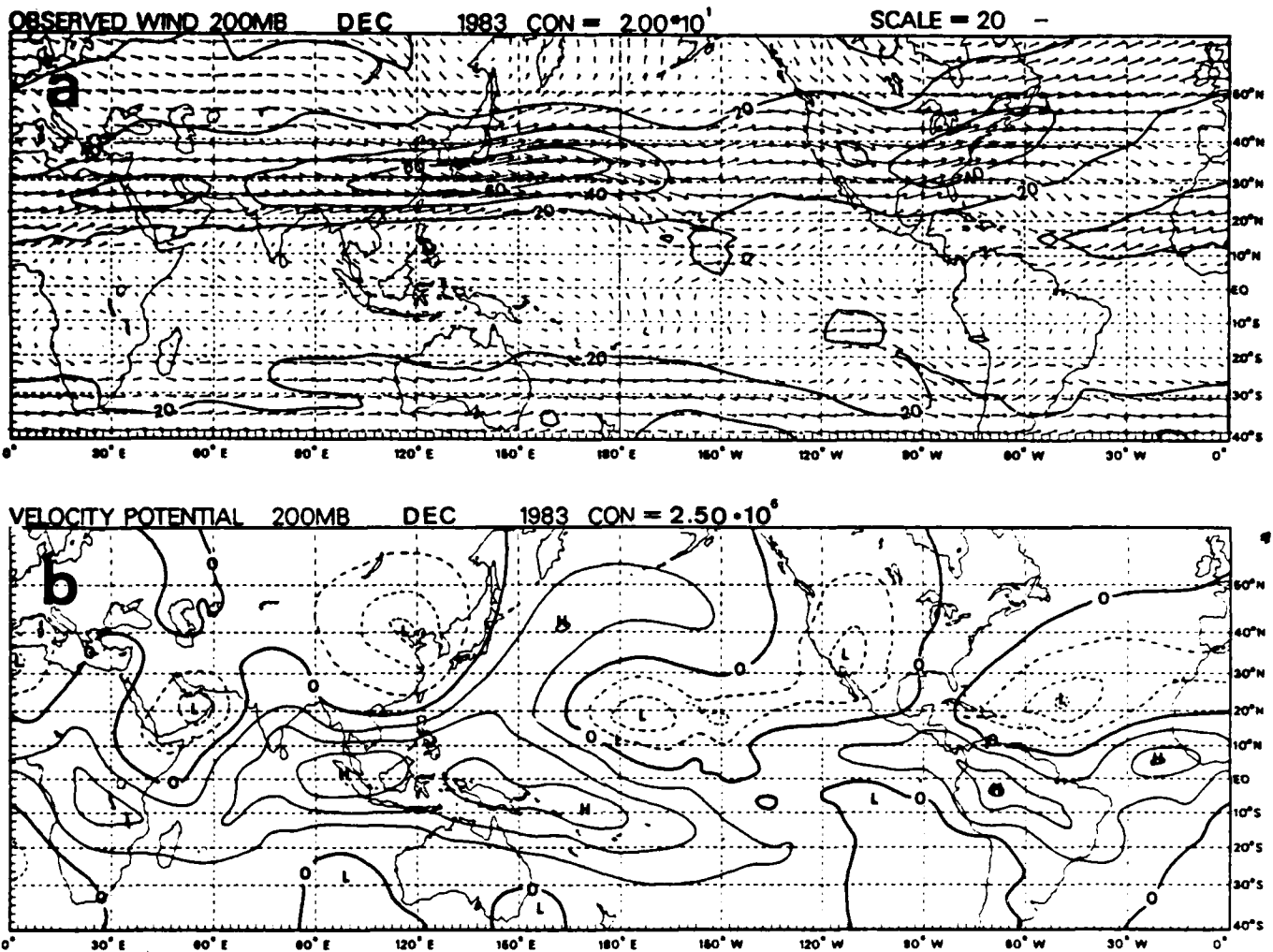


FIG 2. As in Fig. 1 but for the December 1983 mean.

duction of the existence of such an indirect circulation based on quasi-geostrophic theory. A local meridional circulation south of this center, with rising air from the SPCZ, is also implied.

#### 4. Day-to-day variations in December 1983

##### a. Time-longitude sections

Figures 3a and 3b show the time-longitude sections of the midlatitude jet and the tropical velocity potential from  $40^{\circ}\text{E}$  to  $100^{\circ}\text{W}$  for December 1983, respectively. The midlatitude jet (Fig. 3a) is represented by a latitudinal mean zonal velocity averaged over  $25^{\circ}\text{--}40^{\circ}\text{N}$  at each longitude. An eastward propagation pattern in many parts of the diagram is observed, with an averaged speed of approximately  $10^{\circ}$  longitude per day. This eastward propagation is similar to that observed by Chang and Lau (1982) and Lau *et al.* (1983) following the intensification of the East Asian jet during cold surges. Their analysis of the zonal momentum equation

suggests that the propagation is mainly due to the self-advective effect of the jet streak.

In Fig. 3a, the temporary maxima of the East Asian jet as defined by the shape of the  $60$  and  $70 \text{ m s}^{-1}$  mean isotachs are marked by heavy solid lines. The temporary minima downstream of the jet are marked by heavy dashed lines. These lines are also plotted in Fig. 3b, which shows the velocity potential averaged over the equator- $18^{\circ}\text{N}$  latitude band at each longitude. In Fig. 3b, the maximum regions ( $\chi \geq 7.5 \times 10^2 \text{ m}^2 \text{ s}^{-1}$ ) in the Asia-west Pacific sectors are shaded. Here it is obvious that although the  $\chi$  patterns do not show much east-west propagation, the maximum  $\chi$  regions, each of which last several days, tend to occur upstream of each episode of jet acceleration.

To verify this apparent correspondence between tropical divergence and jet acceleration in Figs. 3a and 3b, the time-longitude section of the midlatitude meridional divergent wind component,  $v_x$ , is shown in Fig. 3c. The highlighted areas of maximum velocity

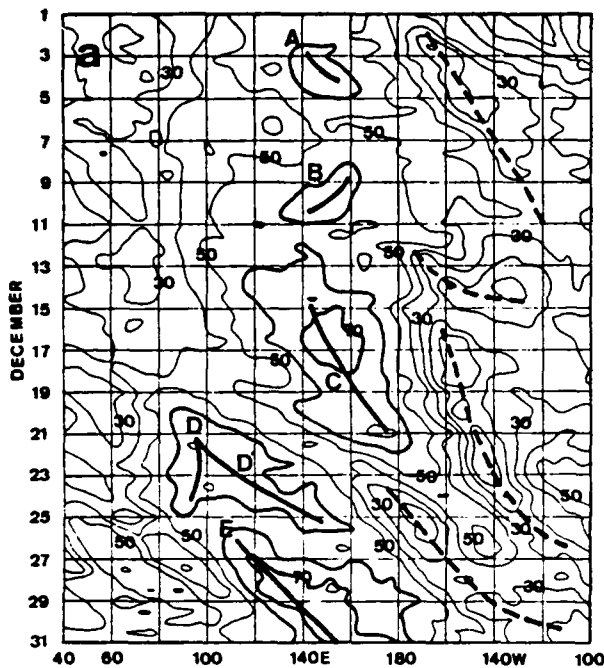


FIG. 3a. Longitude-time section of midlatitude zonal velocity (interval  $10 \text{ m s}^{-1}$ ) averaged over  $25\text{--}40^\circ\text{N}$  for December 1983, with isotachs of  $60$  and  $70 \text{ m s}^{-1}$  labeled by solid lines. The axes of maximum and minimum speed are delineated by dark solid lines and dashed lines, respectively. Letters A, B, C, D, D' and E identify significant events of jet strengthening. See text for details.

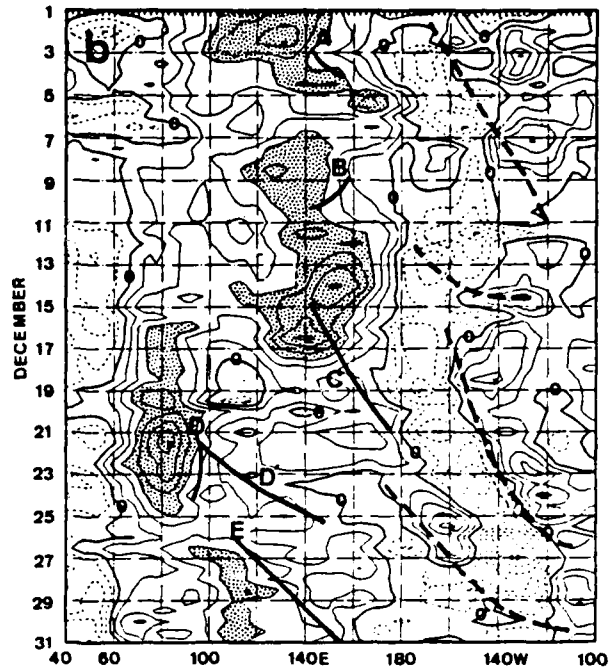


FIG. 3b. Longitude-time section of tropical velocity potential (interval  $2.5 \times 10^2 \text{ m}^2 \text{ s}^{-1}$ ) averaged over  $0^\circ\text{--}18^\circ\text{N}$  for December 1983, with areas  $\geq 7.5 \times 10^2 \text{ m}^2 \text{ s}^{-1}$  shaded by stippling. Dark solid lines and dashed lines, indicating the axes of jet maximum and minimum, respectively, are copied from Fig. 3a.

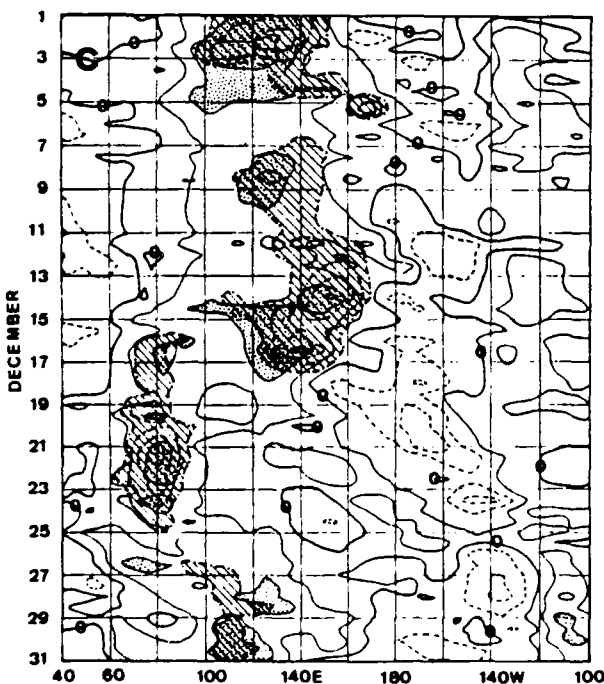


FIG. 3c. Longitude-time section of the meridional component of the divergent wind (interval  $2 \text{ m s}^{-1}$ ) averaged over  $25\text{--}40^\circ\text{N}$ , for December 1983, with areas  $\geq 4 \text{ m s}^{-1}$  shaded by stippling. Areas shaded by hatching are maximum tropical velocity potential areas highlighted in Fig. 3b.

potential from Fig. 3b are also indicated here. As expected, the maxima of the two fields are highly correlated, lending support to the possibility that the tropical divergence forces the strengthening of the jet through increased  $v_x$  in the entrance region of the jet streak.

A total of five episodes of jet strengthening can be identified in Fig. 3. They are labeled by the letters A (2–5 December), B (8–11 December), C (13–20 December), D (20–25 December), and E (26 December–beginning of January), respectively, in Figs. 3a and 3b. Episode D also branches into two axes, one remaining stationary between  $90$  and  $95^\circ\text{E}$  and the other, labeled D', propagating eastward to about  $150^\circ\text{E}$ . These episodes will be referred to in the ensuing discussion.

As expected, the minimum  $\chi$  in the zone of  $180\text{--}140^\circ\text{E}$  occurs in the longitudes of the jet deceleration regions.

*b. Examination of selected regions*

To study in detail the apparent transient interaction between the tropical divergence and the midlatitude jet, the  $200 \text{ mb}$  horizontal wind and velocity potential distribution averaged over shorter periods, as well as time series of area-averaged tropical divergence and midlatitude zonal velocity over selected regions, are examined to focus on the individual episodes identified in Fig. 3. Since D is the only event which indicates

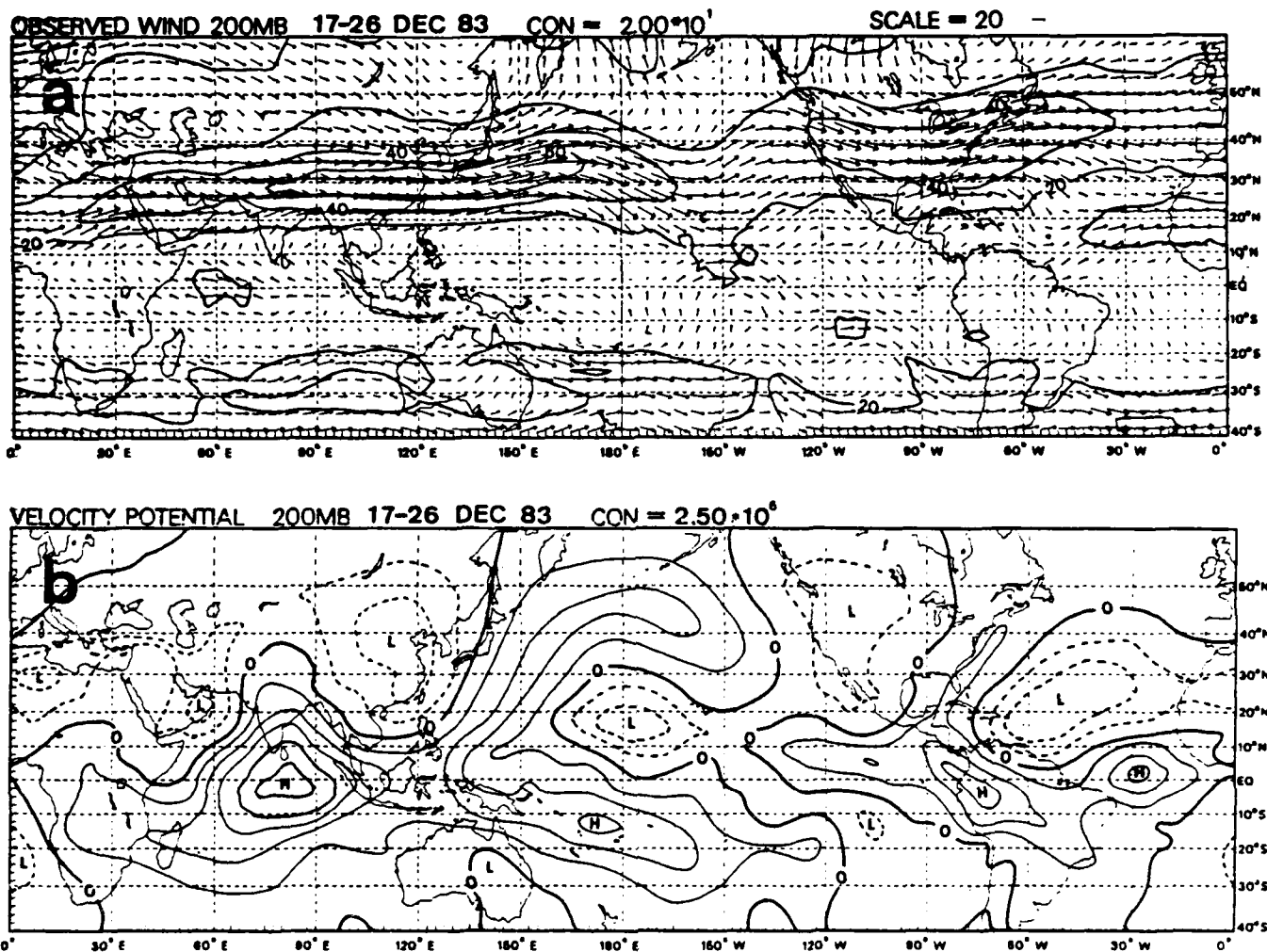


FIG. 4. As in Fig. 1 but only for the period 17-26 December 1983.

enhanced upper level divergence over the Indian Ocean, the global band 200 mb wind and the velocity potential for the period 17-26 December are first averaged and shown in Fig. 4. Compared to monthly means (Fig. 2), it is clear that the East Asian jet core (as defined by the  $60 \text{ m s}^{-1}$  isotach) is stretched westward by about  $25^\circ$  longitude to cover the Tibetan Plateau. This corresponds to a westward shift of the tropical  $\chi$  center from its December mean position to the central and eastern equatorial Indian Ocean. As a consequence of the latter the northeastward divergent circulation may be viewed as the main East Asian local Hadley cell during this 10-day period.

Figure 5 compares the time series of the western side of the jet core, as represented by the zonal velocity averaged over  $80\text{--}110^\circ\text{E}$ ,  $25\text{--}40^\circ\text{N}$ , and that of the equatorial Indian Ocean divergence, averaged over  $70\text{--}90^\circ\text{E}$ ,  $5^\circ\text{S}\text{--}10^\circ\text{N}$ . These areas are outlined in the respective locations of Fig. 4. The zonal velocity series shows a major peak from 16-27 December, corresponding to episode D in Fig. 3. An overall agreement

can be readily seen in the divergence series, whose value is significantly higher than zero only during this period. To understand this increased divergence, we examined the surface weather maps during the same period produced by NMC and FNOC, both of which show an active equatorial trough in the equatorial Indian Ocean box with a developed tropical depression between 20-24 December. Figure 6 is a plot of the minimum surface pressure observed in this box which reflects this tropical depression. (The dip on 1200 GMT 7 December is due to the activity of a tropical depression in the southwestern Indian Ocean which briefly moved to the western edge of the averaging box.) Inspection of satellite imagery further confirms that the enhanced divergence associated with episode D corresponds to the convection of the active equatorial trough and the tropical depression.<sup>3</sup>

<sup>3</sup> The maximum divergence of  $\sim 10^{-5} \text{ s}^{-1}$  shown in Fig. 5 is larger than the normally expected value for the domain size. However, this

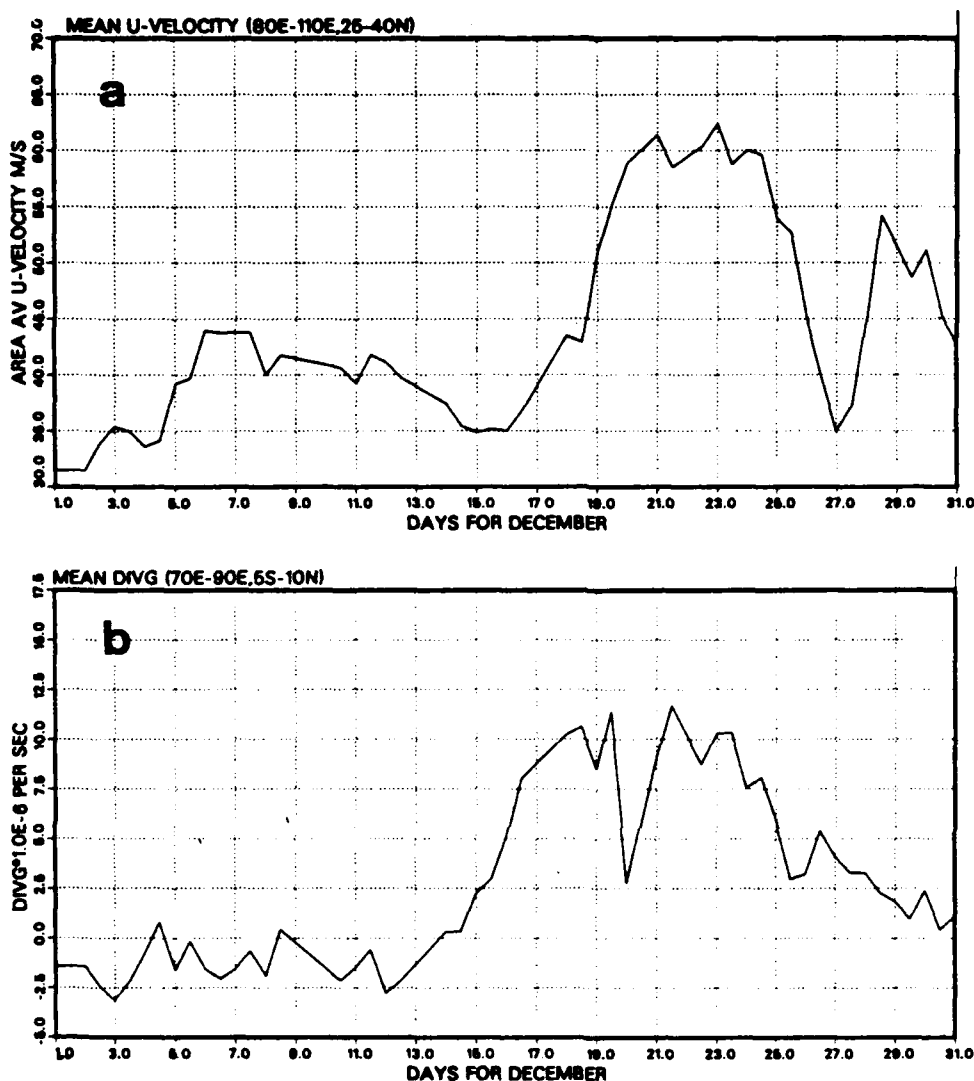


FIG. 5a. Time series of area-averaged zonal velocity for the Tibetan Plateau region (80–110°E, 25–40°N).

FIG. 5b. Time series of area-averaged horizontal divergence for the equatorial Indian Ocean region (70–90°E, 5°S–10°N).

During episode D, in addition to the acceleration of the zonal wind over the Tibetan Plateau, the strengthening of the midlatitude jet also propagates eastward for several days into the region of the monthly-mean jet core (corresponding to episode D' in Fig. 3).

Figure 7 shows the comparison between the zonal wind averaged over area of 110–114°E, 25–40°N, and the divergence averaged over 90–115°E, 5°S–10°N. As outlined in Fig. 2, the former area covers the western half of the December-mean East Asia jet core, and the latter area covers the December-mean velocity poten-

tial center over the maritime continent. Both time series show three major periods of oscillations, with the same peak dates: 3, 14 and 24 December. There was no tropical cyclone activity in the maritime continent divergence center region during December, but an examination of surface wind data over the South China Sea indicated that a major (and the only one of the month) cold surge occurred for the last ten days of December. This cold surge actually has two impulses. The first one started on 20 December and continued through 24 December. The freshening of the surface wind was then relaxed somewhat and picked up again in a second push on 26 December for about three more days. Previous cold surge studies by Chang and Lau (1980, 1982) indicated that such surge events usually cause an enhancement of tropical convection over the maritime-continent, and that convection may be sustained for a

magnitude is still reasonable since the seasonal mean divergence over a similar-sized area of the maritime continent, where the equatorial trough is usually situated during winter, is about half of this value. Also a typical tropical cyclone has a  $10^{-5} \text{ s}^{-1}$  averaged divergence at 200 mb over a 8° diameter (Anthes, 1982, Fig. 2.5).

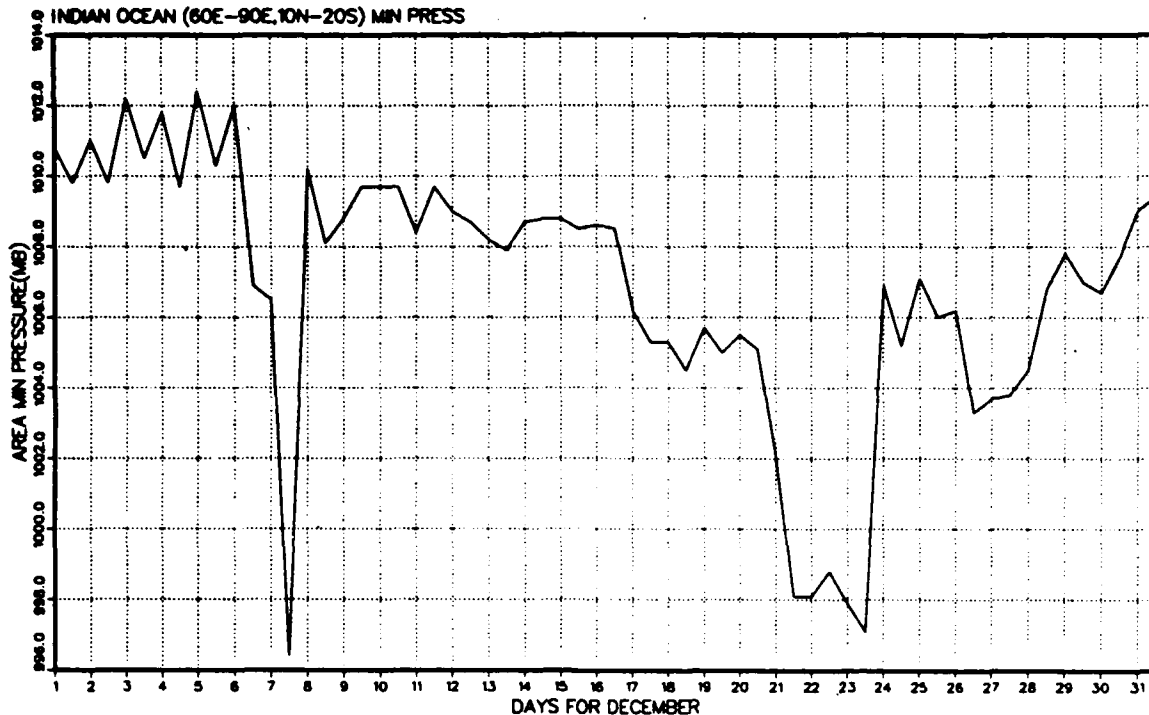


FIG. 6. The minimum surface pressure reported on each 12-h period during December 1983 in the Indian Ocean region of 60°E–90°E, 20°S–10°N.

few days after the surge onset. The increase in divergence shown in Fig. 7b starting 20 December may be attributed to the forcing of the cold surge. The first surge impulse occurred during the period when the divergence center was shifted to the eastern Indian Ocean (episode D) due to the tropical depression activity, but the second surge impulse can be clearly identified as episode E in Fig. 3b.<sup>4</sup> The increase in the jet velocity during the last ten days of December shown in Fig. 7a agrees well with the two-impulse cold surge. The first part (21–25 December) of this period is also influenced by the downstream propagation of the jet maximum (episode D' in Fig. 3).

The jet intensification identified as episodes A, B and C in Fig. 3a occurred over the eastern half of the December-mean jet core. Figure 3b suggests that episodes A and C are the two major divergence events associated with the jet intensification. These two episodes coincide with the periods when two typhoons, Sperry and Thelma, respectively, were active in the western tropical Pacific. Their tracks are shown in Fig. 8. Both of them moved slowly for a few days before recurving northeastward out of the region.

<sup>4</sup> The difference in the relative magnitudes of the time variations between Fig. 3b and 7b over the maritime continent region is mostly due to the different latitudinal bands. The higher intensity of  $\chi$  for episode E in Fig. 3b relative to the rest of the December reflects the fact that the surge-enhanced divergence during the second impulse is mainly concentrated over 10–20°N, outside of the area chosen for Fig. 7b.

Figure 9 shows the horizontal wind and velocity potential distribution averaged over 14–18 December, the period of the maximum divergence during episode C, which coincides with the appearance of Typhoon Thelma in the region. This is also the maximum divergence period over the western Pacific for the entire month (Fig. 3b). Consistent with the typhoon activity, the major tropical velocity potential center is shifted east of Philippines, considerably different from both Figs. 2b and 4b. The jet core also assumes a different pattern than that shown in Figs. 2a and 4a, with a shorter longitudinal domain but stronger maximum velocity ( $>80 \text{ m s}^{-1}$ ) centered at 150°E. Furthermore, the relatively short-wave anticyclonic circulation south of the jet core resembles the pattern of a Rossby mode response to a tropical heat source in the region of the observed tropical divergence center, as predicted by linear equatorial wave theories (e.g., Lim and Chang, 1983). This structure strongly indicates that Typhoon Thelma exerts a significant transient influence on the midlatitude flow. In fact, the amplified midlatitude wave pattern eastward of the East Asia (western Pacific) jet may even suggest some of the downstream effect of the tropical heating predicted by the theories.

##### 5. Variations during January and February 1984

Figures 10a and 10b, which are continuations of Figs. 3a and 3b, respectively, show the time-longitude sections of the midlatitude jet and the tropical velocity potential from 40°E–100°W for January 1984. Four

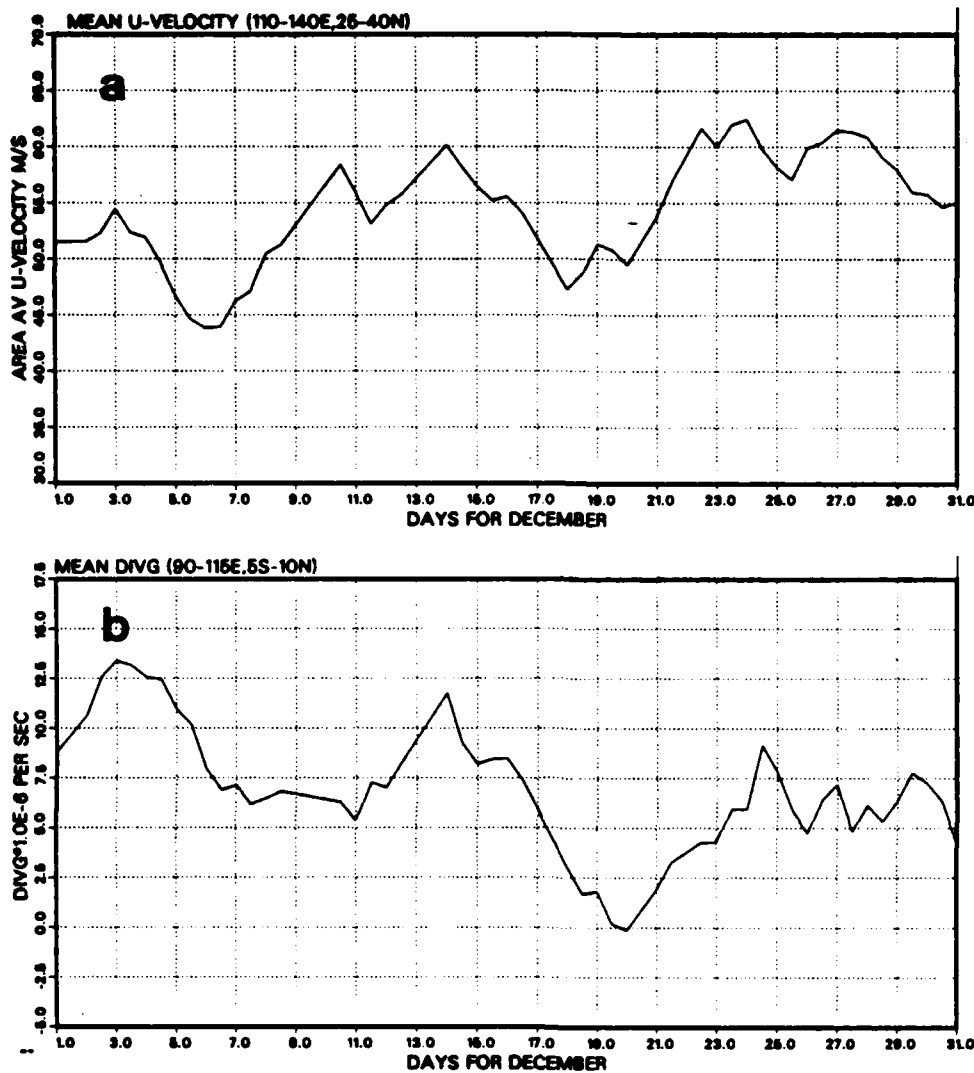


FIG. 7a. As in Fig. 5a but for the East Asia-western Pacific region (110-140°E, 25-40°N).  
 FIG. 7b. As in Fig. 5b but for the maritime continent region (90-115°E, 5°S-10°N).

major episodes (labeled F, G, H and I) of jet acceleration with sustained eastward propagation over the East Asian region are identified in Fig. 10a, and four prominent maximum velocity potential centers are identified in Fig. 10b. Again each of the episodes of jet intensification occurs immediately downstream of a velocity potential maximum.

Time-longitude sections for February 1984 (not shown) indicate a much weaker and less organized tropical divergence pattern compared to December 1983 and January 1984. In the entire eastern hemisphere, ten very small regions of  $\chi \geq 7.5 \times 10^2 \text{ m}^2 \text{ s}^{-1}$  are found in the 29-day time section. Seven of these last for only 12 h and the other three last for about one day or so. Furthermore, except for a single time on 0000 GMT 28 February over two longitudinal grid points (5°), none of the velocity potential maximum reaches  $10 \times 10^2 \text{ m}^2 \text{ s}^{-1}$  (one isopleth inside the high-

lighted area). So the significant tropical divergence events observed in the previous two months did not occur in February 1984. The time-longitude section of the midlatitude jet also exhibits less eastward propagation and less organized strengthening-weakening activity over the Asia-Pacific region. In view of the lack of significant tropical events in this month, this relative inactivity of the midlatitude jet streak may be considered as another, although indirect, evidence of the effect of tropical convection on the midlatitude jet.

#### 6. Correlations between tropical $\chi$ and midlatitude jet acceleration

Since the correspondence between the variations of the midlatitude zonal wind and the tropical velocity potential is very good over several regions over Asia and the western Pacific, it is interesting to calculate the

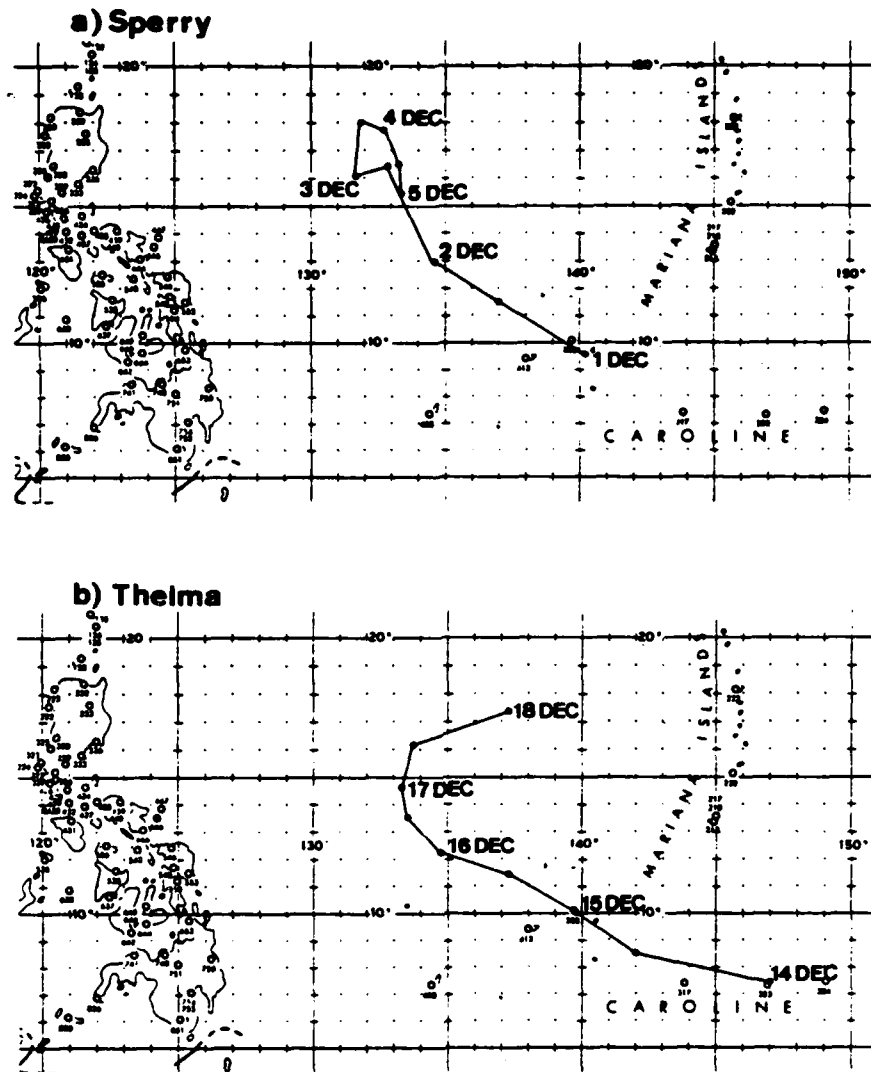


FIG. 8. Typhoon tracks for (a) Sperry and (b) Thelma, 1983.

correlation coefficients between the two variables at all longitudes. Figure 11 shows the correlation coefficients as a function of time lag at each longitude between the tropical  $\chi$  averaged over  $0-18^\circ\text{N}$ , and  $du/dt$  averaged over  $25-40^\circ\text{N}$  for the period December 1983–February 1984. The total time rate of change of  $u$  is used because, assuming negligible meridional and vertical advection,

$$\frac{du}{dt} \approx \frac{\partial u}{\partial t} + u \frac{\partial u}{\partial x} \approx fv_x$$

where  $f$  is the Coriolis parameter and  $v_x$  the divergent (ageostrophic) meridional wind. This equation shows that if the Coriolis torque of the 200 mb return flow of the local Hadley circulation is playing a role in the change of the midlatitude jet, the best correlation can be found between  $v_x$  and  $du/dt$ , rather than  $\partial u/\partial t$ , at the same location. Since the boundary conditions for  $\chi$  are fixed, changes in tropical  $\chi$  basically represent

changes in large-scale tropical divergence. We therefore use tropical  $\chi$  instead of the midlatitude  $v_x$ , so that a good correlation implies that the expected correlation between  $v_x$  and  $du/dt$  is due to the influence of the tropical divergence.

In Fig. 11 nearly all of the correlations are positive, and the most significant correlations are more or less symmetric with the zero lag line, indicating no discernible time lag in the correlation. Based on an estimated degree of freedom of 45 (one fourth of the data points) a correlation coefficient of 0.3 is significant at the 96% level and one of 0.4 is significant at the 99% level. Correlations with 96% significance or higher are found in several general areas. While these coefficients on the order of 0.3–0.4 are far from perfect, they are considered significant because the day-to-day changes of the midlatitude zonal wind are normally expected to be governed mainly by midlatitude rather than tropical events. In such a case there would be no significant

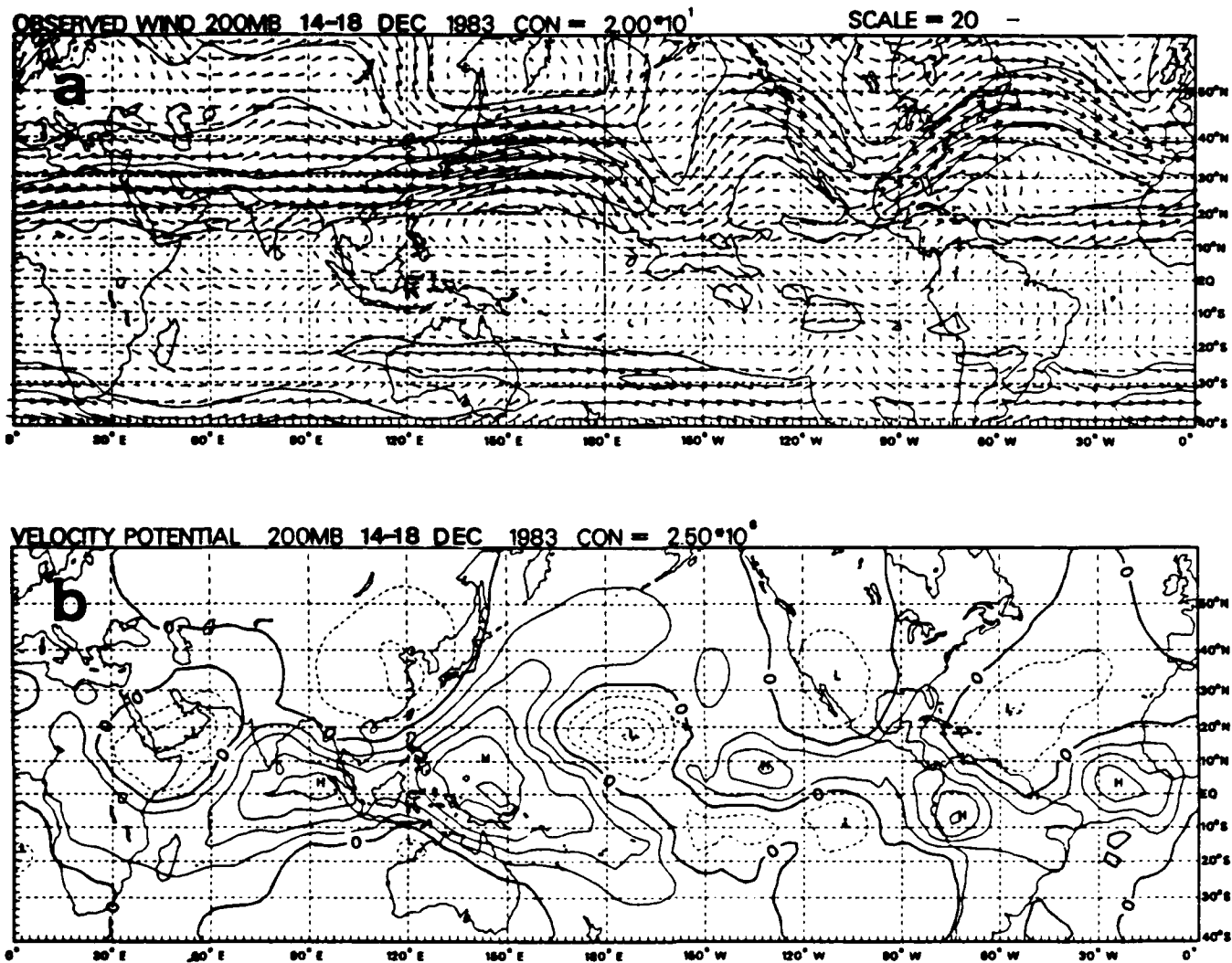


FIG. 9. As in Fig. 1 but for the period 14-18 December 1984.

correlations at all. It takes several periods of tropical influence with consistent effects on the jet to produce these correlations.

From left to right in Fig. 11, the first general area of significant correlation is from about  $50$  to  $120^\circ\text{E}$ , covering the longitudes of the Indian Ocean and the maritime continent. This is the jet entrance region for the East Asian jet, and the good correlation is apparently a result of the Coriolis torque of the northward divergent flow induced by tropical convection as discussed in the preceding section. The correlations, however, fall below the 96% significance level in a narrow longitudinal zone near  $90^\circ\text{E}$ . To understand this, individual monthly correlation coefficients are calculated (not shown). It is found that within the general region the maximum correlations for the three months occur in different longitudes, apparently reflecting the variable locations of the strong tropical convection. This variation, of course, causes a lower correlation for the seasonal statistics.

The second area of maximum correlation is from the dateline eastward to about  $150^\circ\text{W}$ . This is the exit region of the East Asian jet, and its location appears to be more or less stationary for all three individual months. The mechanism of an indirect circulation induced by the spatial deceleration of the jet is likely the reason for the correlation.

The remaining areas of maximum correlation are from approximately  $140$  to  $100^\circ\text{W}$ , and in the narrow bands  $90$ - $80^\circ\text{W}$ , and  $70$ - $60^\circ\text{W}$ . The former is the general area of the entrance region of the North American jet, and the last two probably represent the exit region. This narrower separation of the entrance and exit region (compared to the East Asian jet) is consistent with the seasonally averaged North American jet pattern shown in Fig. 1a.

Figure 12 is a southern hemispheric image of Fig. 11. Here the lag correlation coefficients between the tropical  $\chi$  (averaged over  $0$ - $18^\circ\text{S}$ ) and midlatitude  $du/dt$  (averaged over  $25$ - $40^\circ\text{S}$ ) for the three-month winter

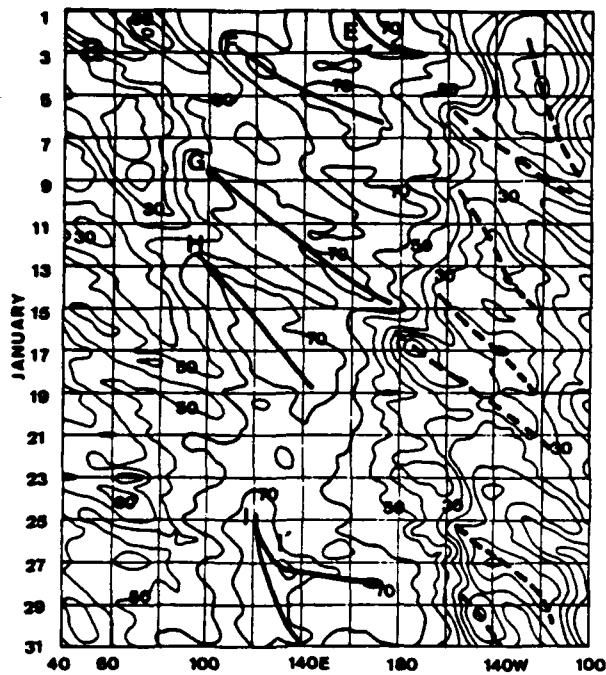


FIG. 10a. As in Fig. 3a but for January 1984. Letters E, F, G, H, I and J identify significant events of jet strengthening initiated in the East Asian region.

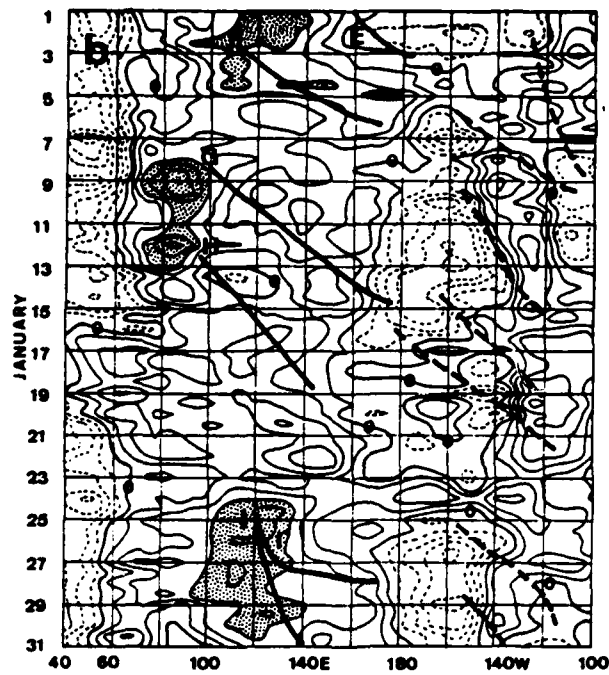


FIG. 10b. As in Fig. 3b but for January 1984. Letters E, F, G, H, I and J identify significant events of jet strengthening initiated in the East Asian region.

period are displayed. Positive correlation is still evident throughout the domain, but the correlation coefficients are considerably smaller in general. This is consistent with the notion that during northern winter the Hadley circulation is much stronger in the winter hemisphere than in the summer hemisphere.

7. Concluding remarks

We have shown that a correlation between the enhancement of tropical divergence and the strengthening

of the midlatitude jet to the north of it existed in the winter of 1983/84. As a consequence, the large scale tropical convective events in regions outside of the normal centers, such as in the Indian Ocean, can bring about a significant longitudinal displacement of the East Asian jet streak. This correlation is consistent with the momentum budget calculation of the East Asian jet by Lau *et al.* (1983) which suggests that the Coriolis torque of the poleward outflow of the tropical convection is responsible for the jet streak strengthening during cold surges. As was found previously, each occur-

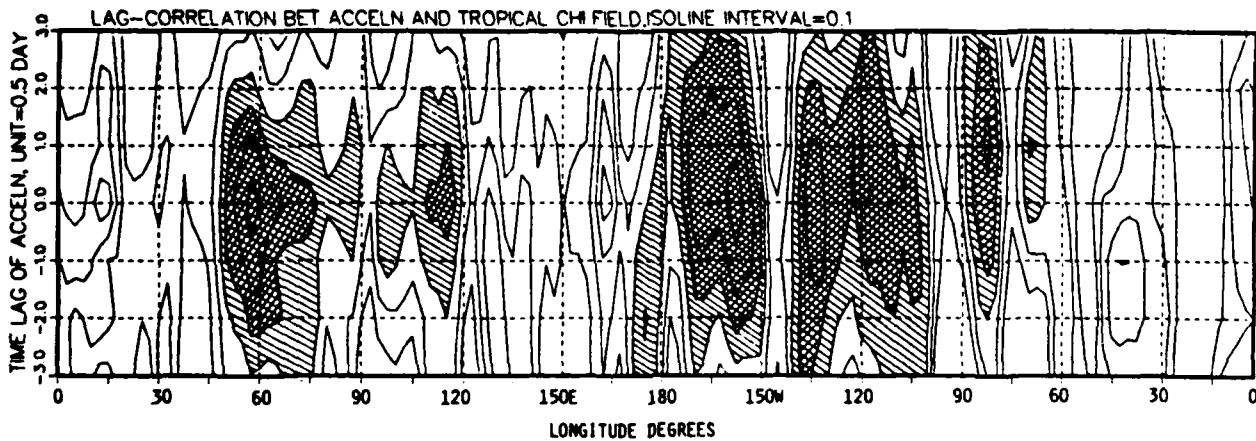


FIG. 11. Time-lag correlation coefficients ( $r$ ) between tropical  $\chi$  (averaged over 0–18°N) and midlatitude jet acceleration  $du/dt$  (averaged over 25–40°N) at the same longitude for the 1983/84 winter. Interval of isoplethes is 0.1. Lag interval is 12 h. Positive lag indicates midlatitude leading. Areas enclosed by  $r = 0.3$  (significant levels > 96%) are shaded by hatching and those enclosed by  $r = 0.4$  (significant level > 99%) are shaded by cross-hatching.

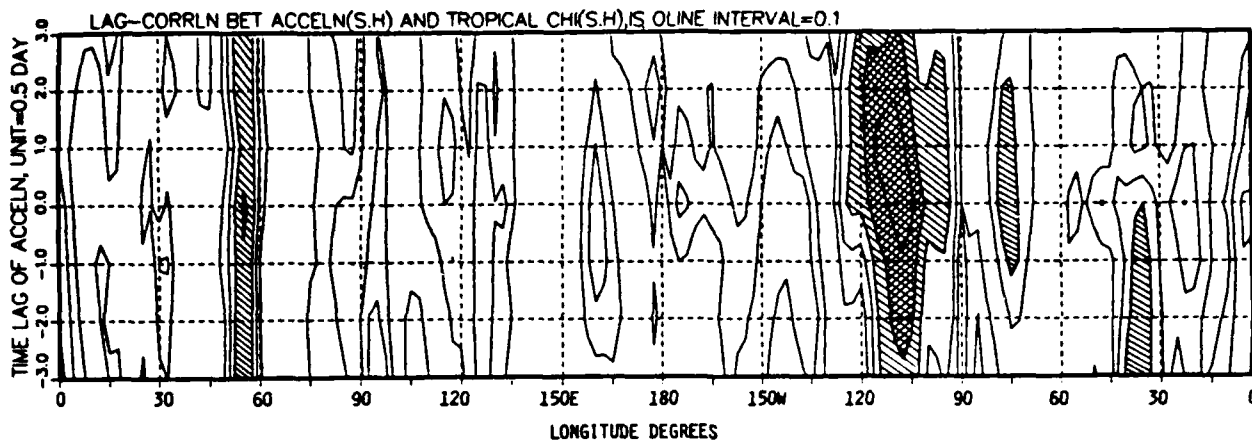


FIG. 12. As in Fig. 11 but for the Southern Hemisphere ( $0-18^{\circ}\text{S}$  for  $\chi$  and  $25-40^{\circ}\text{S}$  for  $du/dt$ ).

rence of the strengthening is usually followed by a downstream propagation, which apparently is a result of the self-advection of the zonal wind, since the tropical divergence center does not move significantly during each episode.

The lack of discernible time lag in the correlations seems to make it difficult to sort out the cause and effect in the tropical-midlatitude interactions. However, the detailed examination of the December 1983 cases provided useful information on this regard. Although the synoptic causes of some of the enhanced 200 mb divergence events (such as the first two peaks shown in Fig. 7b and episode B in Fig. 3b) are not identified, causes for most major events of tropical divergence increases during this month have been found. Episodes A, C and D are due to the activity of tropical cyclones, and episode E (and D', in part) are due to cold surges. Since tropical cyclones are mature storms that should be considered tropical—instead of midlatitude—forced systems when they are already developed, episodes A, C and D led us to believe that the intensifications of the midlatitude jet are more likely the result, rather than the cause, of the tropical-midlatitude interaction. This finding also supports the two-way interaction mechanism during cold surges suggested by Chang and Lau (1980, 1982). This interaction is such that, in addition to an initial strengthening due to a baroclinically induced secondary circulation in its immediate vicinity, the jet is also strengthened due to the feedback effect of the enhanced tropical convection, which is itself a consequence of the midlatitude cold surges. The lack of a clear time lead or lag does not necessarily conflict with this conclusion, because an increase in the tropical velocity potential would simultaneously lead to an increase of the velocity potential gradient and therefore the divergent meridional wind in the jet latitude without any delay, provided the velocity potential is invariant poleward of the jet latitude.

A general tendency of 200 mb tropical convergence in the vicinity of the jet deceleration regions is also

found, but no definitive conclusion on the cause-effect relationship of the midlatitude-tropical interaction can be drawn in these regions. Lacking any evidence to the contrary, it is quite possible that the observed correlation in these regions is due to the indirect circulation induced by the spatial deceleration of the jet (e.g., Palmen and Newton, 1969; Cressman, 1981).

As the jet acceleration represents intensified baroclinicity which is likely to lead to disturbance activity, the short-term forcing of midlatitude jet acceleration by the large-scale tropical convection may have useful implications for midlatitude weather forecasting.

*Acknowledgments.* Drs. J. S. Boyle, H. Lim and G. T. Chen provided valuable assistance and suggestions in various phases of this work. The second author (KGL) wishes to thank the support of the Director General, Malaysian Meteorological Service, and the World Meteorological Organization Fellowship Program for a one-year study leave at the Naval Postgraduate School. This research was supported in parts by the National Science Foundation under Grants ATM-8315175 and INT-8119982, and by the National Oceanic and Atmospheric Administration under Contract NA83AAG03828.

#### REFERENCES

- Anthes, R. A., 1982: *Tropical Cyclones—Their Evolution, Structure and Effects*. Meteor. Monogr., No. 41, Amer. Meteor. Soc., 208 pp.
- Blackmon, M. L., J. M. Wallace, N. C. Lau and S. M. Mullen, 1977: On observation study of the Northern Hemisphere winter time circulation. *J. Atmos. Sci.*, **34**, 1040–1053.
- Bosart, L. F., 1973: A synoptic investigation of anomalous warmth in the mid and upper troposphere during February 1964. *J. Appl. Meteor.*, **12**, 3–11.
- Boyle, J. S., and C.-P. Chang, 1984: Monthly and seasonal climatology over the global tropics and subtropics for the decade 1973 to 1983. Vol. 1: 200 mb winds. Tech. Rep. NPS-63-84-006, Dept. of Meteorology, Naval Postgraduate School, Monterey, CA 93943, 172 pp.
- Chang, C.-P., and K. M. Lau, 1980: Northeasterly cold surges and

- near-equatorial disturbances over the winter MONEX area during December 1974. Part II: Planetary scale aspects. *Mon. Wea. Rev.*, **108**, 298-312.
- , and —, 1982: Short-term planetary-scale interactions over the tropics and midlatitude during northern winter. Part I: Contrasts between active and inactive periods. *Mon. Wea. Rev.*, **110**, 933-946.
- , J. E. Erickson and K. M. Lau, 1979: Northeasterly cold surges and near-equatorial disturbances over the winter MONEX area during December 1974. Part I: Synoptic aspects. *Mon. Wea. Rev.*, **107**, 812-829.
- Cressman, G. P., 1981: Circulation of the West Pacific jet stream. *Mon. Wea. Rev.*, **109**, 2450-2463.
- Haltiner, G. J., and R. T. Williams, 1980: *Numerical Prediction of Dynamic Meteorology*. Wiley and Sons, 477 pp.
- Krishnamurti, T. N., M. Kanamitsu, W. J. Koss and J. D. Lee, 1973: Tropical east-west circulations during the northern winter. *J. Atmos. Sci.*, **30**, 780-787.
- Lau, K. M., C.-P. Chang and P. H. Chan, 1983: Short-term planetary-scale interactions over the tropics and midlatitudes. Part II: Winter-MONEX period. *Mon. Wea. Rev.*, **111**, 1372-1388.
- Lim, H., and C.-P. Chang, 1983: Dynamics of teleconnections and Walker circulations forced by equatorial heating. *J. Atmos. Sci.*, **40**, 1897-1915.
- Palmen, E., and C. W. Newton, 1969: *Atmospheric Circulation Systems*. Academic Press, 603 pp.
- Ramage, C. S., 1971: *Monsoon Meteorology*. Academic Press, 296 pp.
- Uccellini, L. W., and D. R. Johnson, 1979: The coupling of upper and lower tropospheric jet streaks and implications for the development of severe convective storms. *Mon. Wea. Rev.*, **107**, 682-703.

## Large-Scale Features of the Summer Monsoon Fronts over China<sup>1</sup>

C.-P. Chang and M. S. Peng  
Department of Meteorology  
Naval Postgraduate School  
Monterey, CA 93943 USA

Based on a nine-year (1975-1983) operational objective analysis data set produced by the U.S. Navy's Fleet Numerical Oceanographic Center, this work studies the large-scale features of fronts over China during the summer monsoon season of May, June and July. The emphasis is on the Mei-Yu fronts that occur over southeast China in June and July. These fronts often produce heavy precipitation and are a major component of the East Asian summer monsoon. Because the operational data analysis smoothes out sharp temperature gradients and contains no moisture data, the location of a front is determined by identifying a surface wind shear line that is imbedded in a sea-level pressure trough.

The early season fronts (those occurring prior to late May or early June) behave quite differently from those occur in midseason. In early May, fronts that originate north of the Tibetan Plateau propagate southeastward more or less continuously out of the Chinese mainland into the western Pacific. At the later stage these fronts sometimes slow down or even become near stationary for a few days and affect an elongated belt which extends from the southern coast of China to Taiwan and northeastward to southern Japan (Fig. 1). Scientists from Taiwan (Tsay and Chen, 1980) have identified this situation as the "Taiwan Mei-Yu." Even though the fronts themselves have a

---

<sup>1</sup> Extended abstract for the 2nd U.S.-P.R.C. Workshop on Monsoon Research, Monterey, CA. 10-13 June 1985.

mixed midlatitude-tropical structure of modest horizontal temperature gradient and strong horizontal shear (Chen and Chang, 1980) over Taiwan, the large-scale flow structure is similar to those associated with polar fronts during winter. Consistent with this structure the movement of the fronts basically follows the eastward progression of a 500 mb short wave trough.

From early June to mid July, the 500 mb jet stream and short wave activities are reduced and displaced northward to  $50^{\circ}\text{N} \sim 60^{\circ}\text{N}$ . As a consequence, low-level fronts originating in northwestern China no longer migrate. The fronts are usually oriented northeast-southwest, connecting northeastern China with the heat low region over India. The western segment of each front may either stay at the same location north of the Tibetan Plateau for several days before disappearing, or jump abruptly southward across the Plateau to become the quasi-stationary Mei-Yu front in the Yantze River (Changjiang) valley. The duration for each Mei-Yu front to persist can be relatively long, up to a week or more. Sometimes the fronts appear to jump back and forth between these two locations (Fig. 2). Also during this period a quasi-stationary subsynoptic scale surface anticyclonic circulation often develops over the eastern part of the Tibetan Plateau. This localized anticyclone, which is also seen as a high in the sea level pressure field and the 850 mb geopotential, appears to correlate with the existence of the Mei-Yu front such that the latter is blocked from moving northward. The prevailing wind to the north of the anticyclone region is northerly most of the time, which suggests an orographic mechanism of producing an anticyclonic flow over the mountain. Fig. 3a,b are the time series of the maximum surface velocity that is normal to the smoothed terrain contours in the area  $40\text{--}44^{\circ}\text{N}$ ,  $90\text{--}110^{\circ}\text{E}$  which is north of the eastern Tibetan Plateau, for the summers of 1979 and 1980. Also shown are the periods when the localized anticyclone is observed.

The reason that this anticyclone is not pronounced in the early season is because during May the whole area is under the influence of the broad Mongolian high which either encompasses this region or moves southeastward through it and overwhelms the local feature.

To understand the frontogenesis processes for both the fronts north of the Tibetan Plateau and the Mei-Yu fronts, Q-vectors as formulated by Hoskin et al. (1978) and Hoskin and Pedder (1980) are calculated at the 700 mb and 900 mb levels based on geostrophic winds. The Q-vector is defined as the time rate of change of potential temperature gradient moving with the geostrophic velocity. It is directed in the direction of the low level ageostrophic flow and toward ascending air. It is proportional to the low-level ageostrophic wind that is required to restore geostrophic balance. The distribution of  $\vec{Q} \cdot \nabla \theta$  provides an estimate of the packing of the potential temperature gradient by the ageostrophic wind. The quasi-geostrophic frontogenesis on an *f*-plane,  $\frac{D|\nabla\theta|^2}{Dt} = 2 \vec{Q} \cdot \nabla \theta$ , corresponds well with the occurrences of the fronts at both locations (examples shown in Figs. 4 and 5), indicating that the large-scale geostrophic dynamics is probably adequate to account for the frontogenesis at both locations. Vertical velocity induced by topography is therefore not necessarily required to explain the occurrence of the fronts.

To further elucidate the frontogenesis mechanism at both locations, the deformation field with the contraction axis in the north-south direction (Deformation 1) and that in the northwest-southeast direction (Deformation 2) are also calculated using the 900 mb geostrophic winds. Deformation 2 shows a good degree of correspondence with the occurrence of the Mei-Yu front but not with the front to the north of the Tibetan Plateau. Deformation 1 shows little correspondence with either front occurrences. The fact that

Deformation 2 is likely the major mechanism responsible for the Mei-Yu front further suggests that the localized anticyclone over the eastern Tibetan Plateau plays an important role, because the geometry of the flow around the eastern peripheral of this anticyclone tends to provide a northwest-southeast oriented contraction. On the other hand, the frontogenesis north of the Tibetan Plateau is a result of the horizontal shear between the northeasterlies from the north and the southwesterly monsoon winds from the south. Any deformation field that may be induced by topographical influence on the windward side is apparently not important.

#### Summary

- 1) In May and early June the southern China front (Taiwan Mei-Yu) is basically a cold front that is modified by subtropical influences and moves slowly southeastward under a 500 mb short-wave trough.
- 2) In June and July the southwest monsoon winds penetrate to the interior of China, where the basic flow has become less baroclinic, and meet the northerly flow from the north to form a near-stationary front whose western segment jumps back and forth between two preferred locations: i) the Yantze River valley over southeastern China (Mei-Yu front), and ii) north of the Tibetan Plateau.
- 3) The Mei-Yu front is established when a localized anticyclone is formed over the eastern half of the Tibetan Plateau to block the southwesterly winds. This anticyclone is a result of the northerly flow over the plateau and appears frequently during most of the mid-summer. The associated large-scale deformation field provides the basic frontogenesis to maintain the location of the Mei-Yu front (Fig. 6).
- 4) When the localized anticyclone over the eastern Tibetan Plateau weakens or disappears, the front is formed to the north of the Tibetan Plateau

where the main frontogenesis mechanism is due to horizontal shear rather than deformation (Fig. 7).

- 5) Even though latent heat release, which is not studied here, no doubt plays an important role in maintaining the strength of the summer monsoon fronts over China, the main development mechanism appears to be the quasi-geostrophic frontogenesis whose location depends mainly on the occurrence of the topographically-induced eastern Tibetan anticyclone. Topographically-induced vertical motion and deformation fields do not appear to be important mechanisms.

Fig. 1 Schematic diagram of 12-hourly positions of fronts in May.

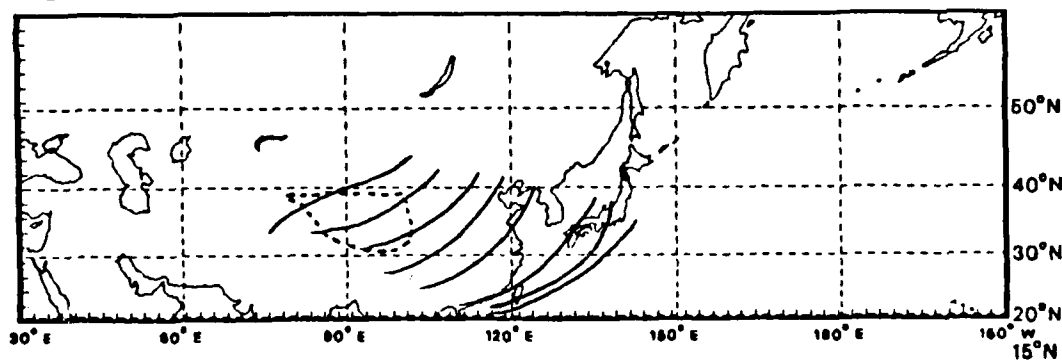


Fig. 2 Schematic diagram of the preferred positions of fronts in June-July.

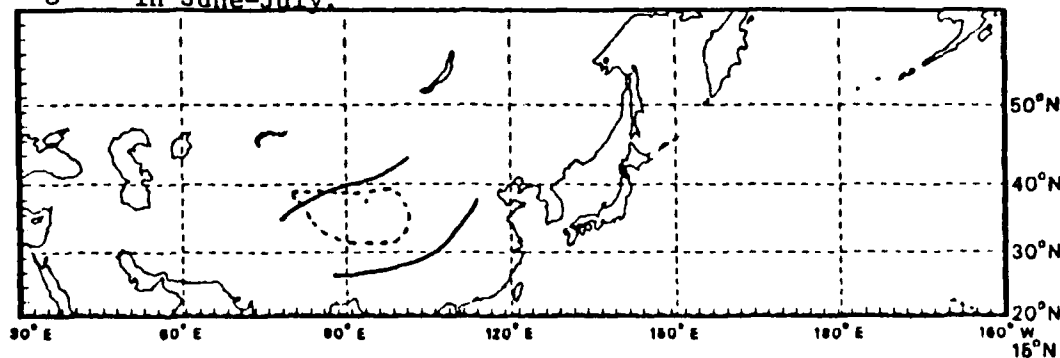


Fig. 3a

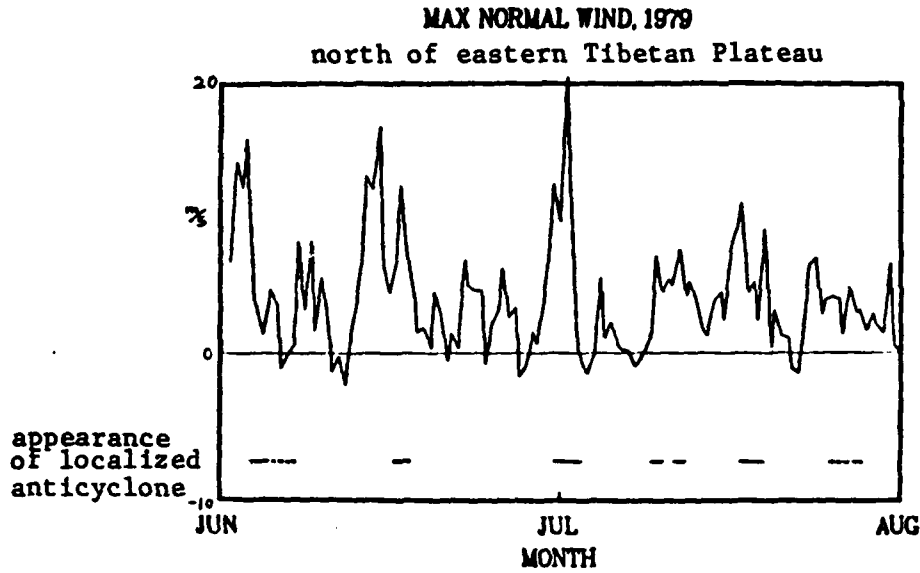


Fig. 3b

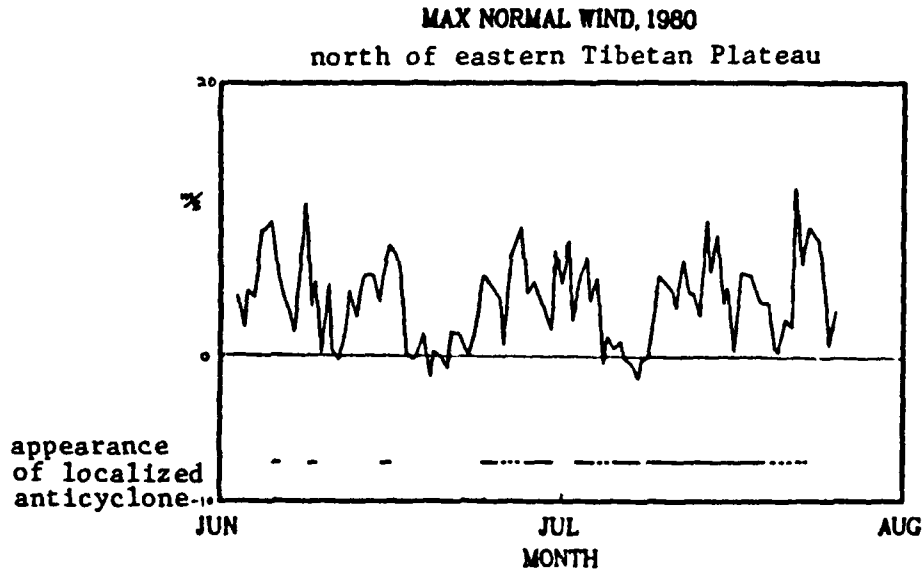


Fig. 4

FRONTOGENESIS 900MB 4 JUL 0 HR 1981 CON =  $1.78 \cdot 10^{-10}$

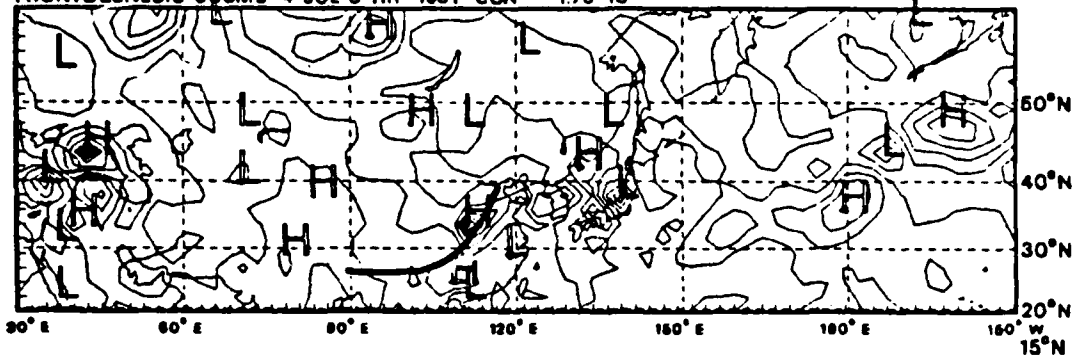


Fig. 5

FRONTOGENESIS 900MB 24 JUL 12 HR 1981 CON =  $7.11 \cdot 10^{-10}$

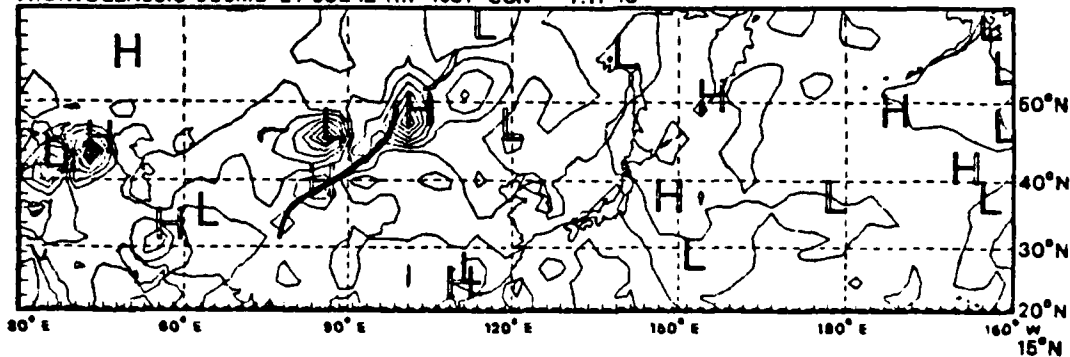


Fig. 6 Schematic diagram of flow pattern associated with the Mei-Yu front and the localized anticyclone.

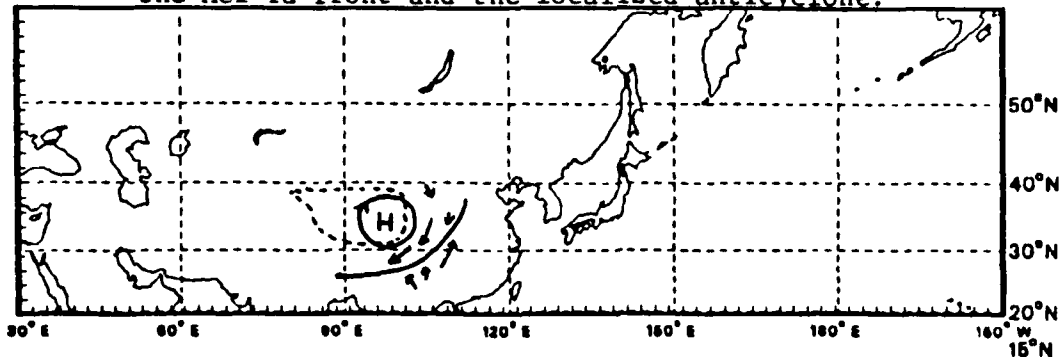
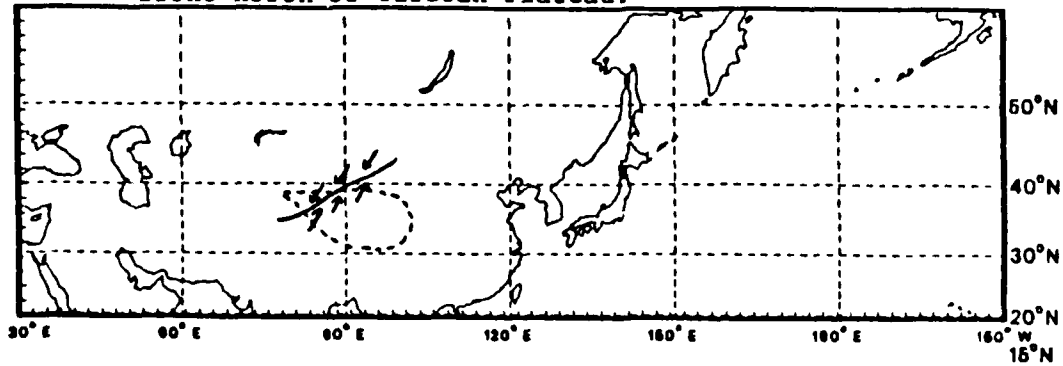


Fig. 7 Schematic diagram of flow pattern associated with the front north of Tibetan Plateau.



## Evaluation of the Surface Prognoses of Cyclones and Anticyclones of the JMA and FNOC Models over East Asia and the Western Pacific during the 1983 Mei-Yu Season\*

G. T. J. CHEN AND Y. J. WANG

*Department of Atmospheric Sciences, National Taiwan University, Taipei, China*

C.-P. CHANG

*Department of Meteorology, Naval Postgraduate School, Monterey, CA 93943*

(Manuscript received 20 April 1986, in final form 19 July 1986)

### ABSTRACT

This study compares the systematic errors of 36-h surface cyclone and anticyclone forecasts for two operational numerical weather prediction models over East Asia and the western North Pacific Ocean: the U.S. Navy's Operational Global Atmospheric Prediction System (NOGAPS), and Japan Meteorological Agency's Fine-mesh Limited Area Model (JFLM). The study is carried out for the 1983 Mei-Yu season (May–July), which is the wettest season over East Asia based on nontyphoon-produced rainfall. All available 0000 and 1200 GMT forecast runs are evaluated against an independent dataset of subjective analysis produced operationally by the Central Weather Bureau, Taipei. The mean position errors, mean central pressure errors and forecast skill indices for both cyclones and anticyclones in the NOGAPS and JFLM models are examined.

Both NOGAPS and JFLM models are more likely to underforecast than to overforecast the existence and/or genesis of both cyclones and anticyclones. However, over the Tibetan Plateau and its vicinity, both models tend to overforecast the existence and/or genesis of cyclones. They also forecast both cyclones and anticyclones too slow and too far to the north.

Diurnal variations in central pressure errors suggest that the error source is the lack of radiation processes in the JFLM and too strong a diurnal cycle of radiation processes in NOGAPS. Also, the failure to treat adequately the bulk effects of cumulus convection seems to be primarily responsible for the poor forecasts of oceanic cyclone development.

### 1. Introduction

Systematic errors in Numerical Weather Prediction (NWP) are repetitive errors in the prognoses of a model due to imperfect physical and mathematical modeling of the atmosphere. In discussing the performance of NWP models the term "systematic error" has been used in two rather different contexts. Fawcett (1969), Hollingsworth et al. (1980) and Wallace and Woessner (1981) have used systematic error to describe differences between the mean fields generated by a forecast model and those of the verification analyses based on the observations. On the other hand, Leary (1971), Colucci and Bosart (1979) and Silberberg and Bosart (1982) have used the term to describe the tendency of a model to show a bias in forecasting specific kinds of synoptic weather systems such as cyclones, anticyclones, troughs or ridges. In the present study we will focus on systematic errors as used in the second context.

Nearly all of the systematic error studies published in the open literature were concerned with National

Meteorological Center (NMC) models over North America and its immediate vicinity during the cool season (e.g., Leary, 1971; Colucci and Bosart, 1979; Silberberg and Bosart, 1982). One exception is the recent study by Toll and Clune (1985) who evaluated the 48-h surface pressure forecasts of extratropical cyclones of the Navy's Operational Global Atmospheric Prediction System (NOGAPS) for the 1983 winter season in the North Pacific and North Atlantic Ocean areas. Due to the incomplete representation of atmospheric processes it is reasonable to expect that the model systematic errors in synoptic weather systems are functions of both space and time. Therefore, it is interesting from both operational and research points of view to investigate the NWP performance at different geographical areas and in different seasons for different operational models. The purpose of this paper is to identify systematic errors of operational NWP models in the surface prognoses of cyclones and anticyclones over East Asia and the western North Pacific Ocean during the period of May–July 1983. The mean geopotential at 1000 mb based on the U.S. Navy's climatology file is displayed in Fig. 1. This is the season of "Mei-Yu" (plum rain) which represents the development of the summer monsoon trough over East Asia

\* JMA—Japan Meteorological Agency. FNOC—Fleet Numerical Oceanographic Center.

with a heavy rainfall belt progressing from the subtropics to northern China (e.g., Chen, 1983). This season usually produces the maximum monthly rainfall for East Asia with the exception of the typhoon season. Two established NWP operational centers are concerned with the day-to-day weather forecast in this region: the Japan Meteorological Agency (JMA) and the Fleet Numerical Oceanographic Center (FNOC). At JMA, a 10-layer Fine-mesh Limited area Model (JFLM), embedded in a northern hemispheric spectral model, has been in operation since March 1982. At FNOC, a 6-layer, rather coarse NOGAPS has been in operation since August 1982<sup>1</sup>. A brief comparison of the two models is given in Table 1. More detailed aspects of these models can be found in Nitta and Yamagishi (1979), Tatsumi (1982), and Rosmond (1981). Even though their application over the East Asia-western North Pacific Ocean region are very similar, the two models are very different in their domains, resolutions and representation of physical processes, so a comparison of their performance may be especially interesting. In this work we evaluate the 36 h forecasts of sea-level cyclones and anticyclones of both models using the methodology of Silberberg and Bosart (1982). The choice of 36-h forecasts is due to the availability of the operational NWP products.

In section 2 the procedure of data analysis and certain important definitions are given. The results of error computations are described, in sections 3-6, but intermodel comparisons are saved for section 7. Section 8 provides a summary and some concluding remarks.

## 2. Procedures

The prognoses evaluated in this study cover the period 0000 GMT 1 May through 1200 GMT 31 July 1983. The 0000 and 1200 GMT watch runs are analyzed separately because of the possible differences that may arise due to diurnal variations in the atmosphere and in the availability of data. The evaluation area is from 20° to 50°N and from 90° to 160°E as shown in Fig. 1.

Cyclones and anticyclones are first identified on both the observed and forecast maps. Then their center positions and central pressures are extracted. Each cyclone/anticyclone is included in the sample if it possesses at least one closed isobar on the observed or forecast maps. On the NOGAPS forecast maps, center position and central pressure to a tenth of a mb are routinely plotted. The central pressure is read directly and the latitude and longitude of the cyclone center are located to a tenth of a degree. On the JFLM forecast maps, isobars are analyzed at 4 mb intervals and center positions are not routinely plotted. Consequently each

TABLE 1. Summary of operational JMA and FNOC models.

Features	Model	
	JFLM	NOGAPS (Version 1.0)
Grid distance	127 km	$\Delta\lambda = 3^\circ$ ; $\Delta\phi = 2.4^\circ$
Vertical resolution	10 layers	6 layers
Cumulus parameterization	Moist convective adjustment	Arakawa-Schubert & moist convective adjustment (Arakawa and Schubert, 1974)
Planetary boundary layer	Bulk-aerodynamic stability dependent $C_D$ , diagnostic	Randall-Deardorff well-mixed layer, prognostic interactive with cumulus (Randall, 1976)
Radiation	No	Explicit calculations, short and long waves interactive with clouds
Objective analysis	Optimum interpolation	Barnes successive correction
Initialization	Balance equation	Variational nonlinear balance equation

central pressure, subject to an estimated error of  $\pm 1$  mb, and the latitude and longitude of the cyclone center to tenths of a degree are estimated at the geometrical center of the innermost closed isobar. On occasion the JFLM model forecasts no well-defined central pressure and a poorly defined circulation. In these cases a procedure consistent with the one used by Silberberg and Bosart (1982) is employed. In this procedure the entire forecast run is reexamined to determine the time evolution of the cyclone/anticyclone. If the cyclone/anticyclone is observed at verification time, the forecast case is included. The location and central pressure are then subjectively determined from the orientation and spacing of the forecast isobars. The errors for these cases are estimated to be at most  $\pm 2-3$  mb. If all cases for each watch are subject to such a large random error, the fractional error will be approximately 0.2 mb for each watch or 0.1 mb when cases for both watches are combined, based on the formula given by Kurihara (1961).

The following four types of forecast errors are determined from an independent verification dataset: the operational subjective analysis of the Central Weather Bureau, Taipei.

1) *Position.* Errors in forecasting position are computed only for values greater than  $0.5^\circ$  of latitude or longitude.

2) *Central pressure.* Errors in the mean sea-level central pressure are computed by the forecast-minus-observed convention. A negative (positive) error implies overforecasting (underforecasting) for cyclones and underforecasting (overforecasting) for anticyclones.

<sup>1</sup> In December 1983 FNOC has implemented a 9-layer version of NOGAPS.

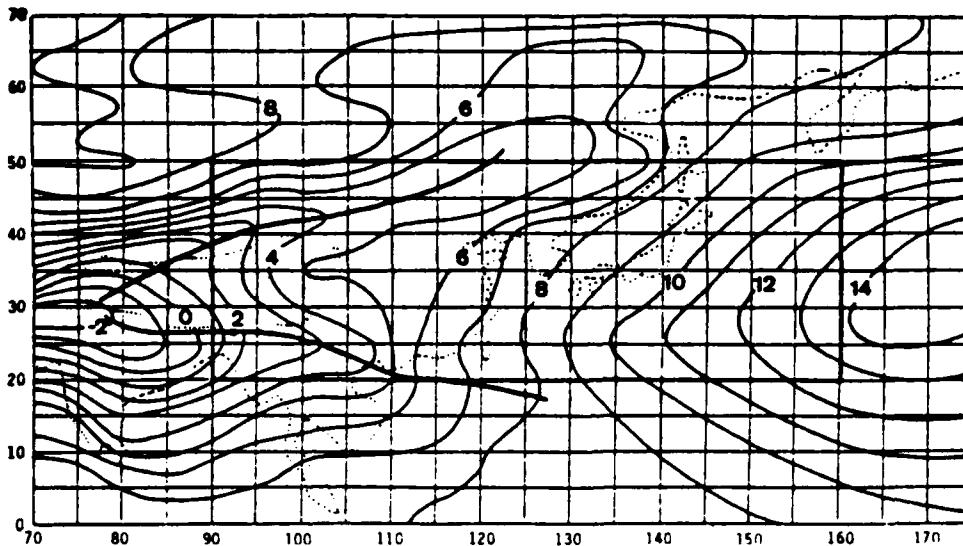


FIG. 1. May-July mean of 1000 mb geopotential over Asia and the western Pacific. The central rectangle delineates the evaluation area for NOGAPS and JFLM 36-h forecasts. The Tibetan Plateau is outlined by a dotted line.

Individual central pressure errors are tabulated in  $5^\circ \times 5^\circ$  latitude-longitude quadrangles according to the observed location of the cyclone/anticyclone center at verification time. The individual errors for each quadrangle are then averaged to yield the mean pressure error assigned to the center of the quadrangle. A cyclone/anticyclone that verifies on a quadrangle boundary is recorded as belonging to the north and/or the west adjacent box(es), consistent with the scheme used by Leary (1971) and Silberberg and Bosart (1982).

3) *Occurrence*. Cyclones/anticyclones that are forecast to occur but not observed are called NOBS and are recorded in the quadrangle where they are forecast. Those that are observed but not forecast in the box are called NFCST and are recorded in the box where they are observed. A forecast is defined as successful if a center is forecast and verified, regardless of the position error of the center. When two closed circulation centers are observed (forecast) but only one is forecast (observed), the one closer to the forecast (observed) center is recorded as verified and the other one is taken as not being forecast (observed).

4) *Deepening rate*. The forecast deepening rate of each cyclone/anticyclone is computed by taking the forecast central pressure at verifying time minus the initial observed central pressure. The observed deepening rate is defined as the difference between the final and initial observed central pressures.

The cyclone and anticyclone centers over the Tibetan region (Fig. 1) are largely results of the process of pressure reduction. Information of the procedures used in the two models, which could be different, is not available. Since one purpose of this study is to document the difference of the performance of the two

operational models, data over this region is also shown, but should be viewed with caution.

### 3. Overall forecast capability

#### a. Occurrence error

The number of cyclone and anticyclone cases, including the successful occurrence forecasts, those forecast but not observed (NOBS), and those observed but not forecast (NFCST), are given in Table 2. In general, there are more cyclone cases than anticyclone cases and there are comparable number of cases for the JFLM and the NOGAPS. The difference in the total number of cases used between NOGAPS and JFLM is due to the availability of forecast data. NOGAPS has a slightly larger percentage of successful occurrence forecasts than the JFLM for anticyclone cases, whereas for cyclone cases the reverse is true.

Even though the evaluation area is about evenly divided between land and ocean (Fig. 1), there are more NFCST cyclone cases over land than over ocean for both models. The total number of NFCST cyclones is comparable for both models, 332 for NOGAPS and 321 for JFLM. This is also true for the NFCST anticyclone cases, 136 for NOGAPS and 140 for JFLM.

The total cases of NOBS cyclones are remarkably less than the NFCST ones for both models. JFLM has 78 versus 321 while NOGAPS has 61 versus 332. There are much less NOBS cases over ocean than over land for both models. This indicates that these models are more likely to underforecast the existence and/or genesis over land than over ocean for both models.

Similar to the cyclone cases, the total number of NOBS anticyclones is significantly less than the NFCST

TABLE 2. Total numbers of cyclone/anticyclone occurrence verification cases, numbers of successful occurrence forecast, forecast but not observed (NOBS), and observed but not forecast (NFCST).

Cases	Models			
	Cyclone		Anticyclone	
	NOGAPS	JFLM	NOGAPS	JFLM
0000 GMT runs				
Total cases (a) = (b) + (c) + (d)				
Successful forecast (b)	448	455	226	220
NOBS (c)	251	249	128	126
NFCST (d)	29	36	30	24
(b)/(b + d) (%)	168	170	68	70
	59.9	59.4	65.3	64.3
1200 GMT runs				
Total cases (a) = (b) + (c) + (d)				
Successful forecast (b)	440	450	226	227
NOBS (c)	244	257	128	126
NFCST (d)	32	42	30	31
(b)/(b + d) (%)	164	151	68	70
	59.8	63.0	65.3	64.3
Total (0000 and 1200 GMT)				
Total cases (a) = (b) + (c) + (d)				
Cases of successful forecast (b)	888	905	465	447
NOBS (c)	495	506	269	252
NFCST (d)	61	78	60	55
(b)/(b + d) (%)	332	321	136	140
	59.9	61.2	66.4	64.3

ones for both models, 55 versus 140 for JFLM and 60 versus 136 for NOGAPS. In other words, both models are more likely to underforecast the existence and/or genesis of synoptic-scale systems. Similar to the cyclone cases, there are less NOBS anticyclone cases over ocean than over land for both models.

#### b. Position error

The mean position errors and rms errors of cyclones and anticyclones are shown in Table 3. The 0000 GMT and 1200 GMT data are combined because there is no significant difference. The NOGAPS mean position errors are 11% greater than those of the JFLM for cyclone

cases, apparently due to the coarser horizontal grid of NOGAPS as shown in Table 1. Although this is also true for anticyclone cases, the error difference is reduced. The rms errors are comparable for both models in the cyclone and anticyclone cases with NOGAPS actually having slightly smaller errors. These error characteristics indicate that JFLM has a wider range of position errors than the NOGAPS. In other words, JFLM is more likely to have an extreme position error for synoptic-scale systems than NOGAPS does.

Furthermore, for all three months, mean position and rms errors for both models are greater for anticyclones than for cyclones except for the rms errors of NOGAPS in June. The differences average to about 10% for both models. This seems to be consistent with the fact that, compared to cyclones, anticyclone center positions are usually less well defined.

#### c. Central pressure error

Table 4 shows the mean and rms central pressure errors. For cyclones, the two models have similar rms errors for all months with both seasonal averages being essentially the same (~5.3 mb). This value is somewhat smaller compared to the rms errors of NMC LFM-II during the 1978/79 cool season over North America, which are 5.5 and 8.4 mb, respectively, for the 24-h and 48-h forecasts (Silberberg and Bosart, 1982). On the other hand, the mean central pressure errors of the two models are quite different. The JFLM tends to underforecast the central pressure in all three months with a seasonal average of +1.9 mb. This error may be compared to the +1.3 mb mean error for the NMC LFM-II 24-h and 48-h forecasts as obtained by Silberberg and Bosart (1982). The NOGAPS mean central pressure errors are much smaller than those of JFLM in all three months with a seasonal average of +0.2 mb as compared to +1.9 mb of JFLM.

For the anticyclones, the NOGAPS and JFLM again have comparable rms errors, but the mean errors of NOGAPS are considerably smaller than those of JFLM. In general, JFLM tends to underforecast both cyclones and anticyclones while NOGAPS appears to have a very small systematic error in the central pressure forecasts.

TABLE 3. 36-h mean position error and rms error of cyclone/anticyclone forecasts for all 0000 and 1200 GMT model runs

Month	Cyclone case						Anticyclone case					
	Number		Mean error (km)		rms error (km)		Number		Mean error (km)		rms error (km)	
	NOGAPS	JFLM	NOGAPS	JFLM	NOGAPS	JFLM	NOGAPS	JFLM	NOGAPS	JFLM	NOGAPS	JFLM
May	145	148	361	326	444	443	99	97	490	406	571	530
June	167	191	355	335	442	472	95	86	368	404	434	503
July	183	167	389	337	461	448	75	69	399	370	488	502
Seasonal mean	495	506	369	333	450	456	269	252	422	396	503	513

TABLE 4. 36-h mean error and rms error of mean sea level cyclone/anticyclone central pressure forecasts for all 0000 and 1200 GMT model runs.

Month	Cyclone case						Anticyclone case					
	Number		Mean error (mb)		rms error (mb)		Number		Mean error (mb)		rms error (mb)	
	NOGAPS	JFLM	NOGAPS	JFLM	NOGAPS	JFLM	NOGAPS	JFLM	NOGAPS	JFLM	NOGAPS	JFLM
May	145	148	0.9	4.0	6.1	6.9	99	97	-0.1	-0.3	3.5	3.5
June	167	191	-0.2	1.1	5.3	5.2	95	86	0.3	-1.3	3.4	3.0
July	183	167	-0.1	1.0	4.2	4.7	75	69	0	-2.5	3.0	3.6
Seasonal mean	495	506	0.2	1.9	5.2	5.3	269	252	0.1	-1.3	3.3	3.4

d. Occurrence skill indices

To better represent the model capability in forecasting the occurrence of cyclones and anticyclones, three indices are defined as follows:

- 1) Bias =  $F/O$  = number of events forecast/number of events observed.
- 2) False alarm rate =  $NO/F$  = number of NOBS/number of events forecast.
- 3) No-hit rate =  $NF/O$  = number of NFCST/number of events observed.

It is clear that the best occurrence skill is represented by a bias of 1 and 0 values of false alarm rate and no-hit rate. A bias greater than 1 means the model overforecast the number of events and vice versa. False alarm rate gives the percentage about the events erroneously forecast whereas no-hit rate indicates the percentage of observed events not forecast.

Latitudinal distribution of skill indices for the NOGAPS cyclone forecasts over land and over ocean is

shown in Fig. 2. The false alarm rate is much smaller than the no-hit rate for both land and oceanic cyclone forecasts at all latitudinal belts. This is also reflected in considerably fewer cases of NOBS compared to the NFCST as shown in Table 2. Latitudinal distribution of skill indices for the JFLM cyclone forecasts over land and ocean is shown in Fig. 3. In general, occurrence skills are comparable for both models at almost all latitudinal belts for both land and oceanic cyclone forecasts. The exception is over subtropical ( $20^{\circ}$ - $30^{\circ}$ N) ocean, where NOGAPS, apparently due to the advantage of its global domain, has greater skill than JFLM. The no-hit rate increases from high to low latitudes for both models over ocean. The large bias, false alarm rate and no-hit rate in the  $30^{\circ}$ - $40^{\circ}$ N zone over land indicate the tendency for both models to overforecast the occurrence of cyclones to the lee of the Tibetan Plateau.

Figure 4 shows the latitudinal distribution of skill indices for the NOGAPS anticyclone forecasts over land and over ocean. Forecast skill for oceanic anti-

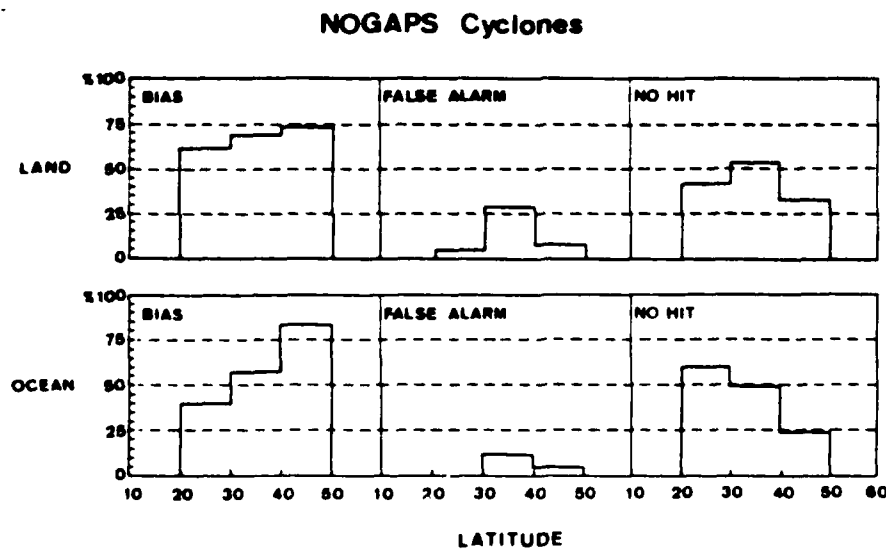


FIG. 2. Latitudinal distribution of (a) bias, (b) false alarm rate, (c) no-hit rate indices for NOGAPS cyclone forecasts over land and (d) bias, (e) false alarm rate, (f) no-hit rate indices for NOGAPS cyclone forecasts over ocean. Abcissa is latitude (deg) and ordinate is index (%).

## JFLM Cyclones

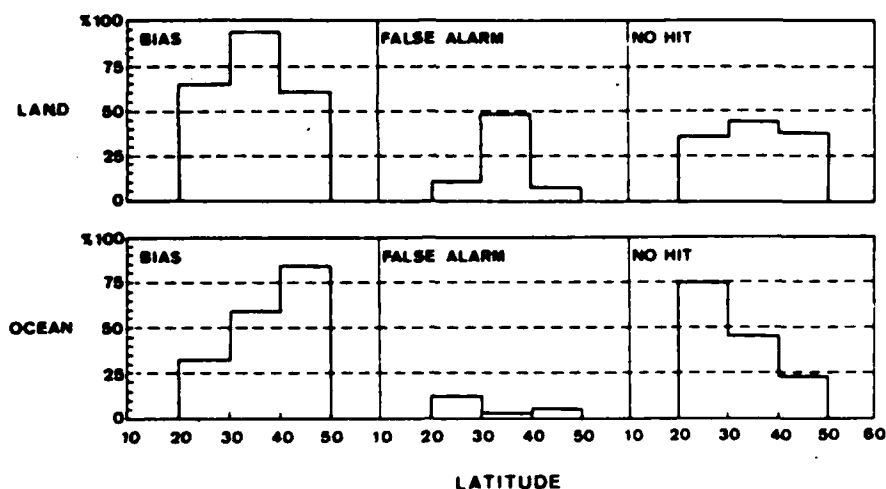


FIG. 3. As in Fig. 2 but for JFLM forecasts.

cyclones is apparently greater than for land anticyclones. Figure 5 shows the latitudinal distribution of skill indices for the JFLM anticyclone forecasts over land and over ocean. In general, both models have comparable skills for the land forecasts and the JFLM is slightly less skillful than the NOGAPS for oceanic forecasts. This is also reflected in Table 2 as the successful occurrence forecast is 64.3% and 66.4% for the JFLM and NOGAPS, respectively.

Over the ocean, both models have a better skill for forecasting the occurrence of anticyclones than for cyclones. The reverse is true over land, except in the 30°–40°N belt.

## 4. Geographical distribution of central pressure error

## a. Cyclones

Figure 6 shows the error distribution of cyclone central pressure for NOGAPS forecasts. For the 0000 GMT runs, the model underforecasts central pressure (positive error) over ocean especially near Japan (+3 mb), and overforecasts (negative error) over land especially in the regions of northwestern China, Tibet and southern China (–3 mb). For the 1200 GMT runs, positive errors over the vicinity of Japan and negative errors over southern China remain similar to the 0000 GMT runs. Over northwestern China and Tibet, however,

## NOGAPS Anticyclones

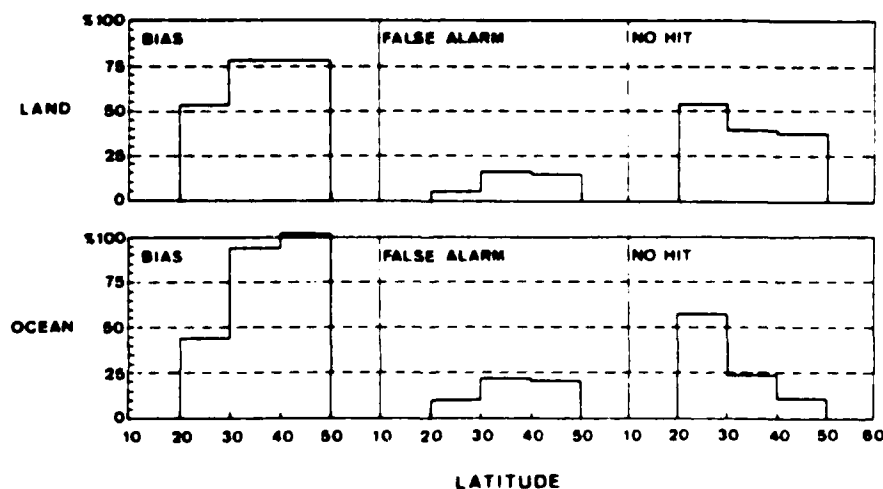


FIG. 4. As in Fig. 2 but for NOGAPS anticyclone forecasts

JFLM Anticyclones

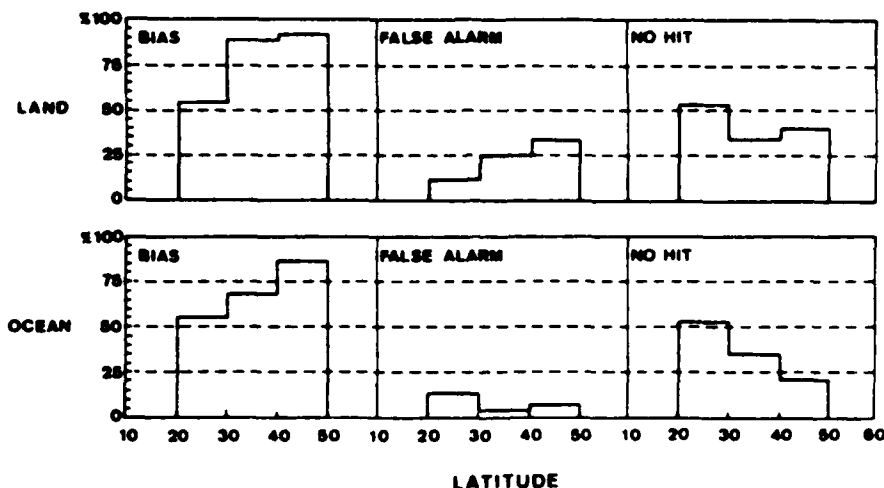


FIG. 5. As in Fig. 2 but for JFLM 36-h anticyclone forecasts.

the errors change sign from their 0000 GMT runs. In other words, over these regions the diurnal variation in the error field is evident and the model tends to overforecast the cyclone central pressure at 0000 GMT run and underforecast at 1200 GMT run.

The cyclone central pressure error for JFLM forecasts is shown in Fig. 7. It is interesting to note that over several areas NOGAPS and JFLM have opposite errors. For 0000 GMT runs, the model underforecasts the central pressure over most of the area especially over northwestern China (+9 mb), Japan and the nearby ocean (+3 mb). For 1200 GMT runs, the error over northwestern China changes sign to become mostly negative. Over central Tibet and its southern slope, weak negative error for 0000 GMT runs is replaced by maximum negative error (-6 mb) for 1200 GMT runs. Positive error again dominates over ocean especially to the east of Japan except with a greater magnitude (+6 mb). It is clear that the diurnal variations in the error field are more evident over land than over ocean for both the JFLM and NOGAPS runs.

*b. Anticyclones*

The anticyclone central pressure error for NOGAPS forecasts is shown in Fig. 8. No significant diurnal variation is observed over the ocean. Over land, however, diurnal variation in the error field is obvious especially over Mongolia and northwestern China, where a maximum negative error of -3 mb for 0000 GMT runs and a maximum positive error of +6 mb for 1200 GMT runs are observed.

The anticyclone central pressure error for the JFLM forecasts is shown in Fig. 9. Unlike the NOGAPS forecasts over ocean, the JFLM possess a substantial error to the east of Japan with diurnal variation. Diurnal

variations in the error field is evident over the area of Mongolia and northern China. The sign is roughly opposite to that of NOGAPS forecasts, however, with positive error in 0000 GMT runs and negative error in 1200 GMT runs.

5. Movement error

Errors in the model forecasts of surface cyclone/anticyclone position are shown in plots of the observed position of a particular cyclone/anticyclone relative to its forecast position. Figures 10 and 11 show the position error for the NOGAPS and JFLM forecasts, respectively. A perfect forecast is assumed to fall in the central box which includes all cases with a position error less than 0.5° of latitude and longitude. A model whose zonal phase speed is too slow (fast) would have the majority of its cyclone/anticyclone located in the NE, E and SE (NW, W and SW) boxes. For example, 19% or 92 of the 495 NOGAPS cyclones tabulated verify to the northeast of their forecast position (Fig. 10a), i.e., they were forecast too slow and too far to the south and west. A separate stratification of the data by the 0000 and 1200 GMT runs failed to disclose any important differences for either NOGAPS or JFLM.

For NOGAPS forecasts, both cyclones and anticyclones are forecast too slow and too far to the north and west. For cyclone cases, 58% are forecast too slow (NE, E and SE) and only 29% too fast (NW, W and SW). For anticyclone cases, 67% are forecast too slow and only 23% forecast too fast. For both cyclone and anticyclone forecasts, 50% of the cases are forecast too far to the north versus 30% forecast too far to the south.

The JFLM also forecast too slow and too far to the west and north for both cyclones and anticyclones. For

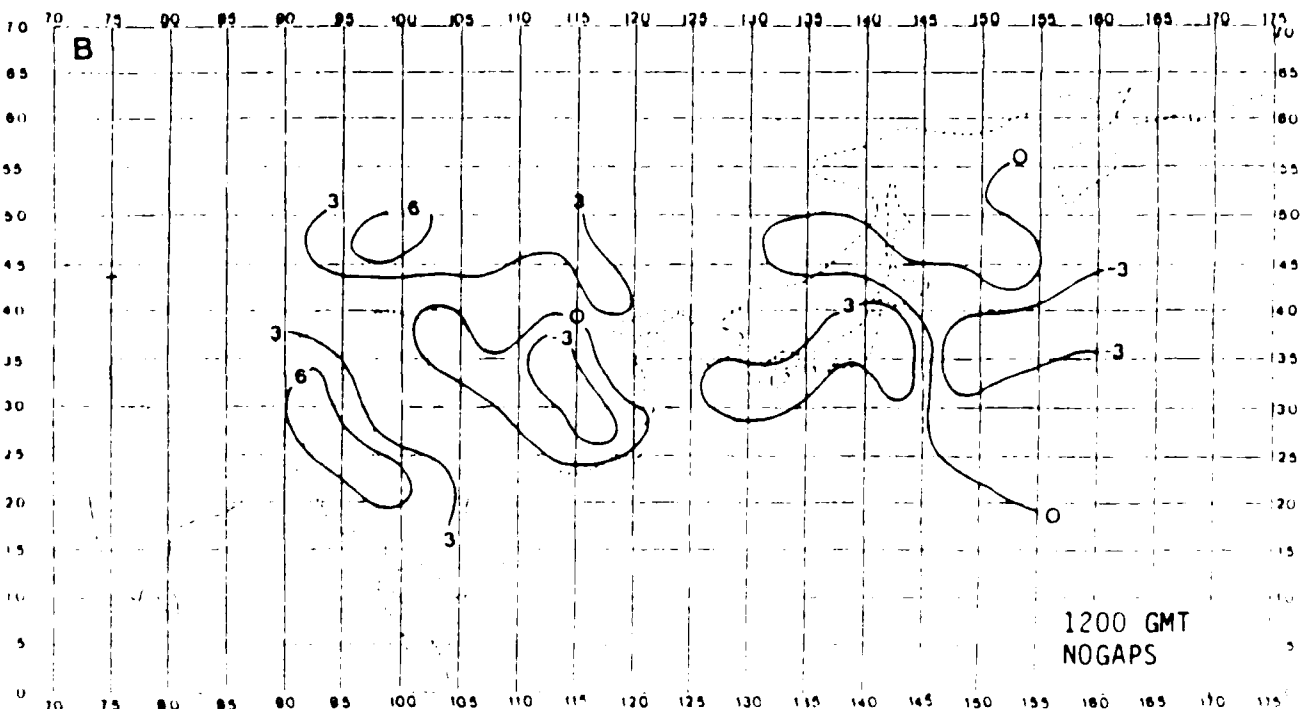
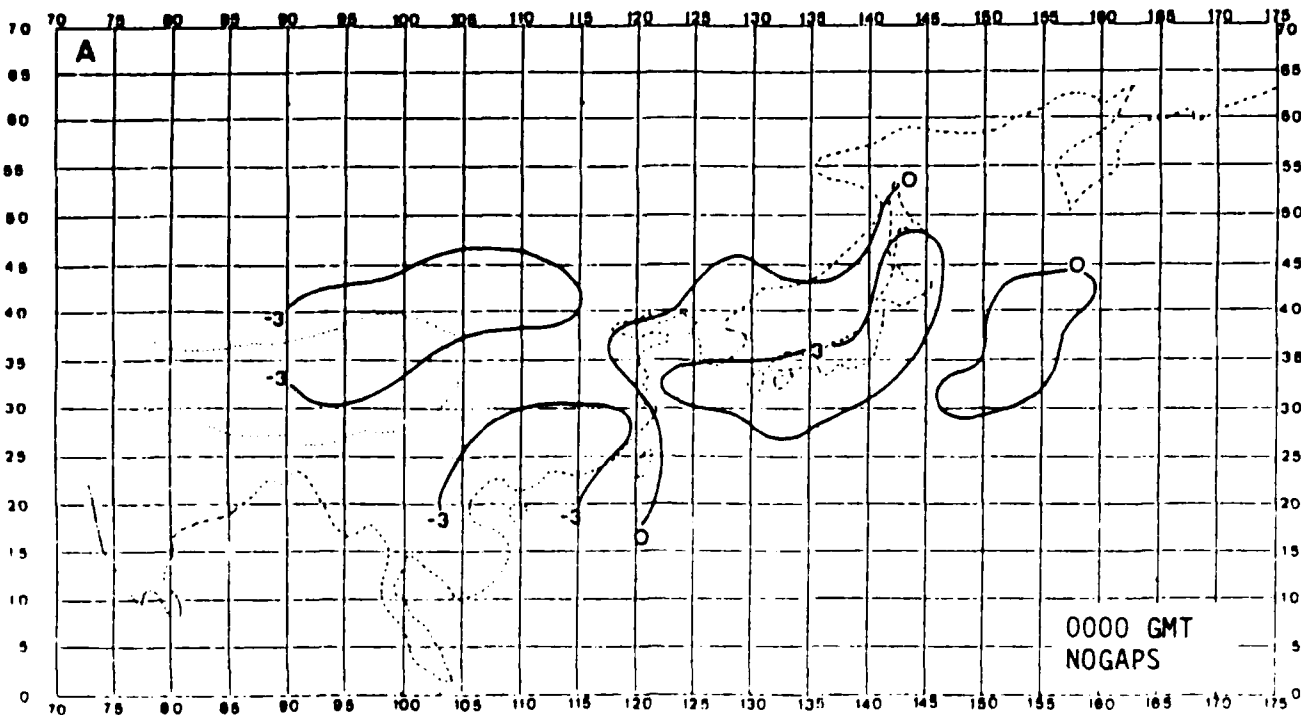


FIG. 6. Cyclone central pressure error for NOGAPS forecasts at (a) 0000 GMT and (b) 1200 GMT runs.

cyclone cases, 52% are forecast too slow and 34% too fast. For anticyclone cases, 57% are forecast too slow and 29% too fast. The ratios of forecasts too far to the north over those too far to the south are 44%/35% and 50%/33%, respectively, for cyclones and anticyclones.

6. Deepening rate error

The forecast deepening rate is the forecast central pressure minus the initial observed central pressure whereas the observed deepening rate is the difference

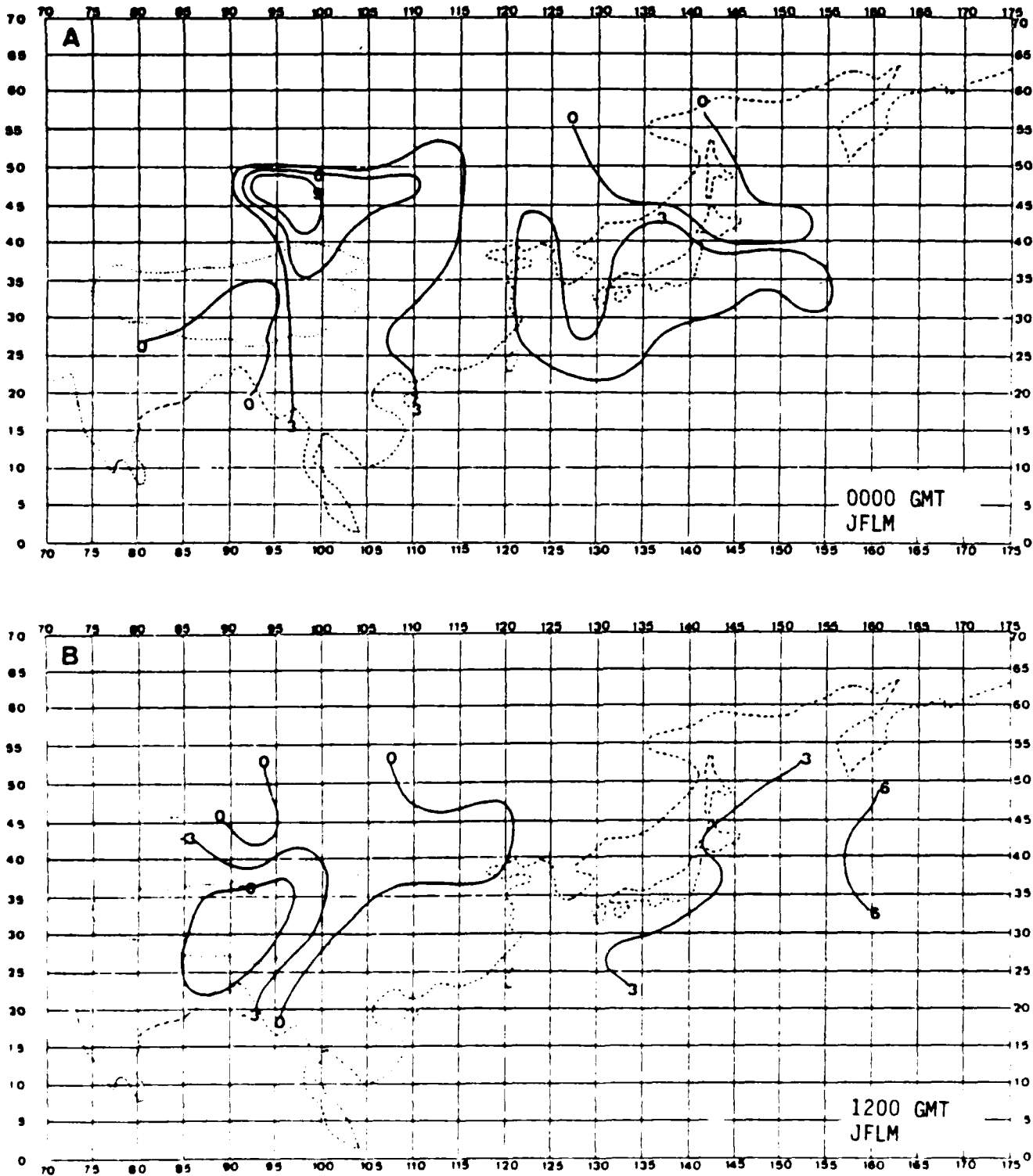


FIG. 7 As in Fig. 6 but for JFLM forecasts.

between the final and initial observed central pressure. Absolute central pressure errors have been given in Table 4. In this section the discussion will focus on the tendency of over (under) forecasting stratified accord-

ing to intensifying and weakening highs and lows. A positive (negative) deepening rate ( $\Delta p$ ) means filling (deepening) for cyclones and building (weakening) for anticyclones.

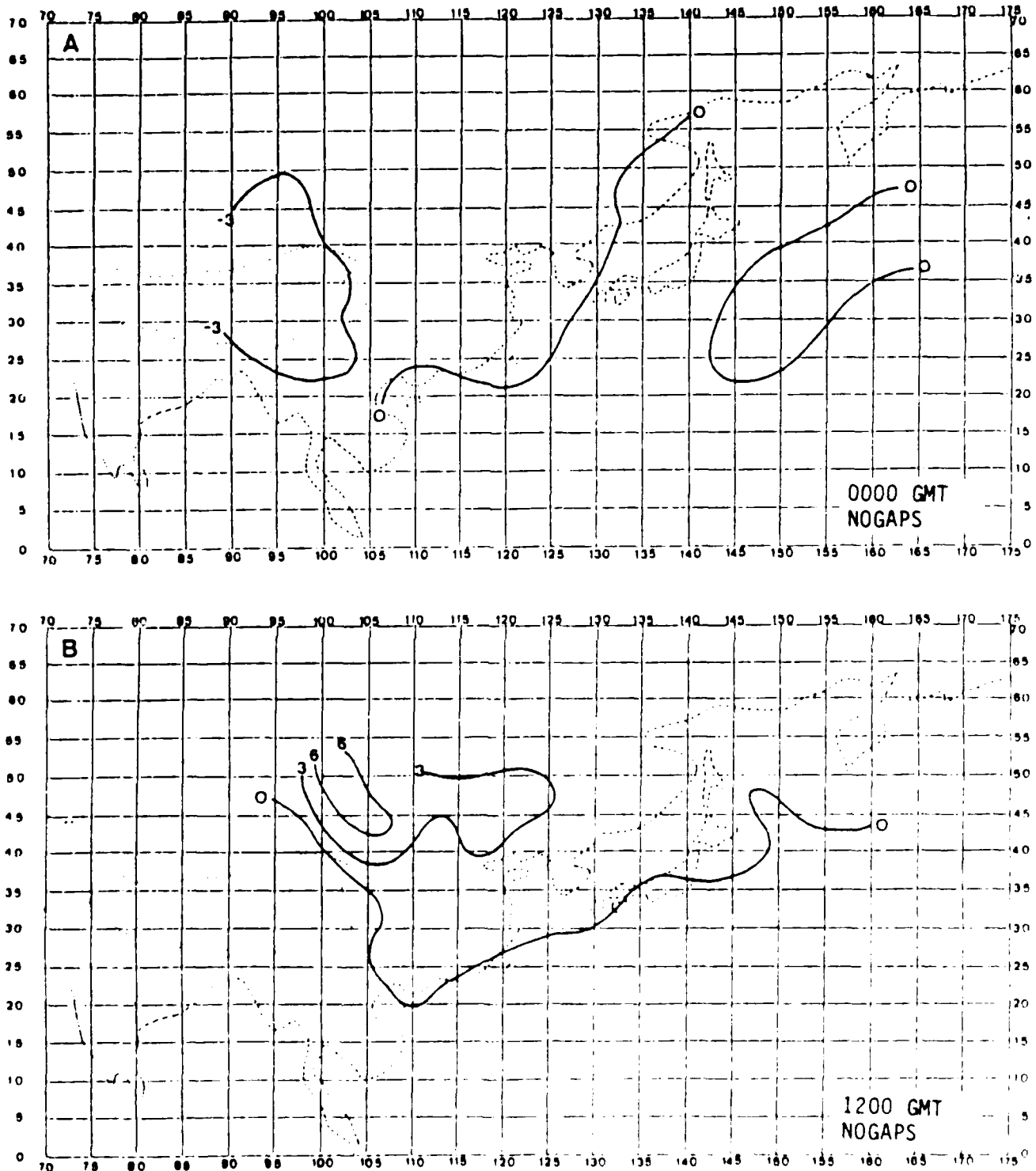


FIG. 8 Anticyclone central pressure error for NOGAPS forecasts at (a) 0000 GMT and (b) 1200 GMT runs

*a Cyclones*

Figure 12 shows the NOGAPS forecast versus observed deepening rate of cyclones over land and over ocean. The distribution is rather scattered over both

sides of the perfect forecast line (forecast equals observed deepening rate) The percentage of correct forecast sign of the deepening rate is somewhat higher for land cyclones versus oceanic cyclones (72% and 67%, respectively). The cases of correct/incorrect forecast in

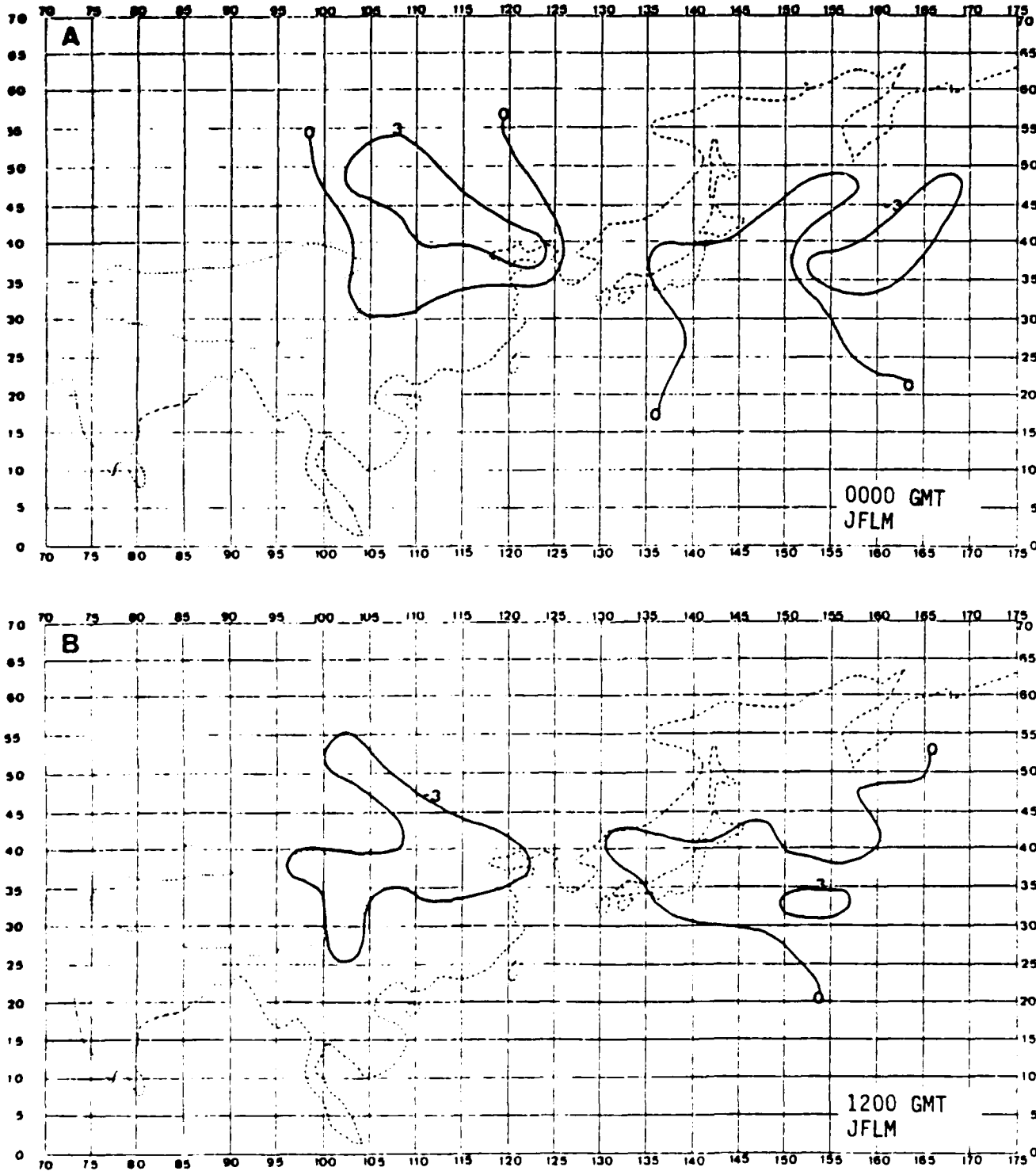


FIG. 9. As in Fig. 8 but for JFLM forecasts.

sign are 89/34 and 51/25 for cyclones over land and over ocean, respectively. For those cases of correct sign forecast over land, NOGAPS has a tendency of underforecasting both deepening and filling rate. The cases of underforecast/overforecast in the correct sign fore-

cast category are 28/22 and 27/12 for filling and deepening cyclones, respectively. For cyclone cases of correct sign forecast over ocean, however, NOGAPS has a tendency of overforecasting both of the deepening and filling cyclones. The exception is that in the two

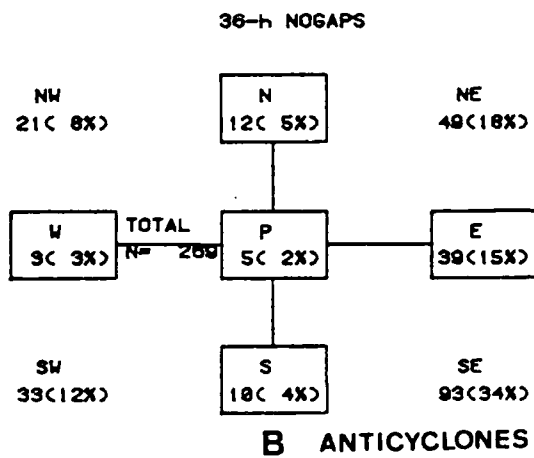
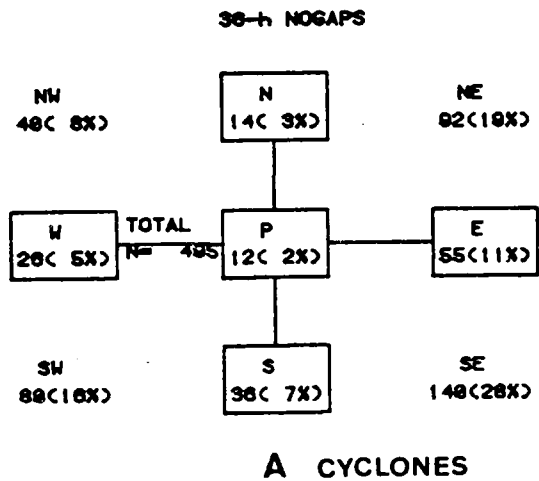


FIG. 10. NOGAPS forecast position error showing observed positions of (a) cyclones, (b) anticyclones relative to the forecast position. Number of events are given for each compass direction with the percentage contribution to the entire sample in parenthesis.

extreme cases when the deepening rate exceeds 16 mb/36 h, NOGAPS underforecasts.

In contrast with the randomness of NOGAPS errors, JFLM shows a clear bias in cyclone deepening rate over both land and ocean (Fig. 13). Wrong sign forecasts occur almost exclusively for deepening cyclones only. For correct sign forecasts, JFLM tends to overforecast the filling cyclones and underforecast the deepening ones, both over land and over ocean (Fig. 13).

*b. Anticyclones*

Figure 14 shows the NOGAPS forecast versus observed building/weakening rate of anticyclones over land and ocean. The percentage of correct forecast in sign is higher for anticyclones than for cyclones both over land (84%) and over ocean (90%). For those few cases of correct sign forecast over land, NOGAPS has

a tendency of overforecasting the extreme building anticyclones (> +8 mb/36 h) and underforecasting the extreme weakening ones (< -8 mb/36 h). For the cases of correct sign forecast over ocean, however, NOGAPS has only a slight tendency of overforecasting the building anticyclones and no systematic bias for the weakening ones. The JFLM forecasts have a tendency of underforecasting the building anticyclones and overforecasting the weakening ones both over land and over ocean (Fig. 15).

**7. Discussion**

As pointed out by Silberberg and Bosart (1982), NWP error sources may be classified into three categories: 1) initial analysis uncertainties, 2) incomplete model physics and 3) numerical effects. However, it is difficult to assess quantitatively the relative contributions of these errors as direct evidence is hard to obtain. Sometimes, even a qualitative assessment of the error sources is a difficult task. On the other hand, comparison with another model's performance may provide a useful measure of the model forecasts. Silberberg and Bosart (1982) have obtained systematic cyclone forecast

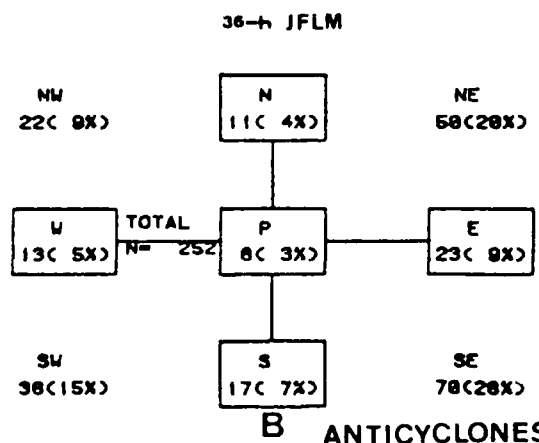
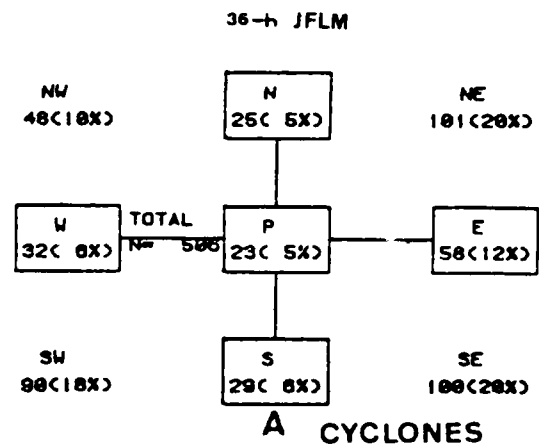


FIG. 11. As in Fig. 10 but for JFLM forecasts.

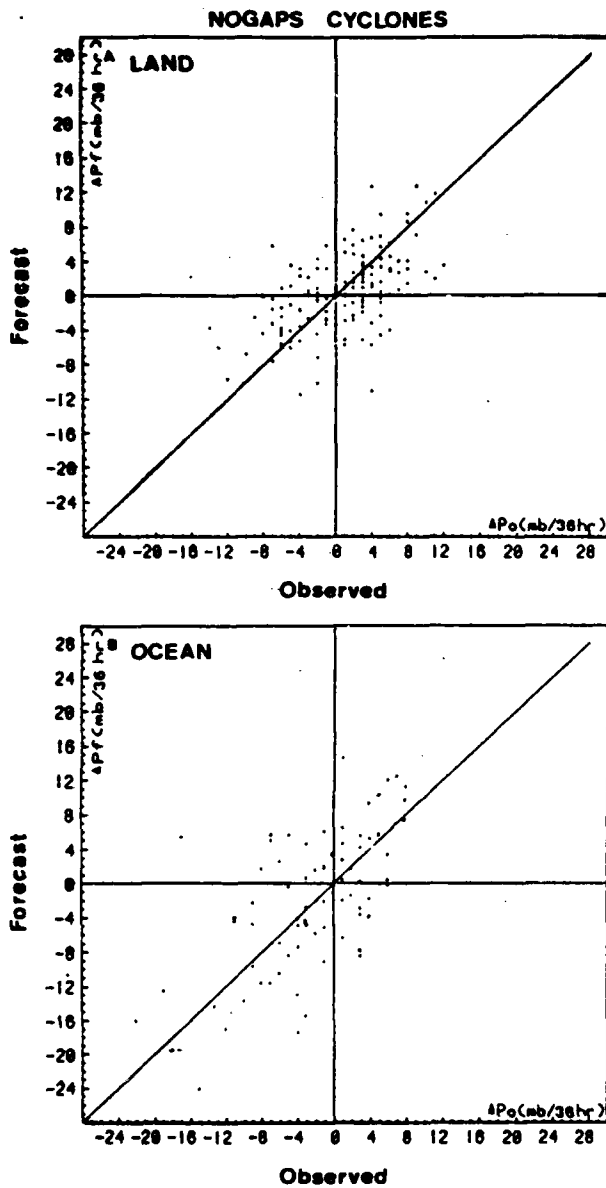


FIG. 12. NOGAPS forecast (y axis) vs observed (x axis) deepening rate for cyclones initially observed (a) over land and (b) over ocean. Unit in mb/36 h.

errors in the NMC Limited Fine Mesh Model II (LFM-II) for the winter of 1978/79, and Colucci and Bosart (1979) have obtained anticyclone forecast errors in earlier versions of NMC models for the winter of 1969/70. These errors are for winter-season North American forecasts, therefore they may contain inherent different characteristics compared to the spring-to-summer transition season of Mei-Yu over East Asia. Nevertheless they may serve as useful references in evaluating the JFLM and the NOGAPS errors obtained here.

Position errors shown in Table 3 are related to the movement errors shown in Figs. 10 and 11, which will be discussed later. Comparing the seasonal mean po-

sition errors for NOGAPS and JFLM forecast cyclones and anticyclones, it is found that NOGAPS has greater errors in both cyclone and anticyclone forecasts. This is apparently due to the higher resolution of the horizontal grid of JFLM. Both models perform better when compared with the position errors of the NMC models in winter. The cyclone mean absolute error of 366 km in the NMC LFM-II during the 1978/79 cool season is greater than the mean position error of 333 km in the JMA JFLM and comparable to the error of 369 km NOGAPS for the 36-h forecasts. The mean displacement error of 517 km for 36-h anticyclone forecasts in the NMC 6-layer Primitive Equation (6L-PE)

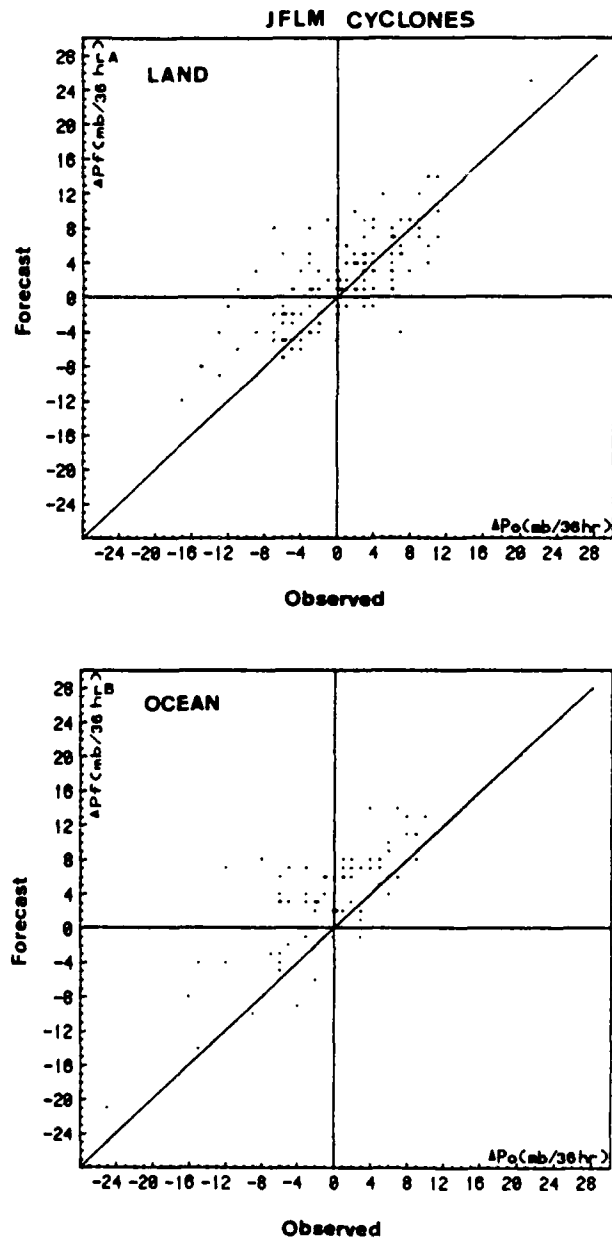


FIG. 13. As in Fig. 12 but for JFLM.

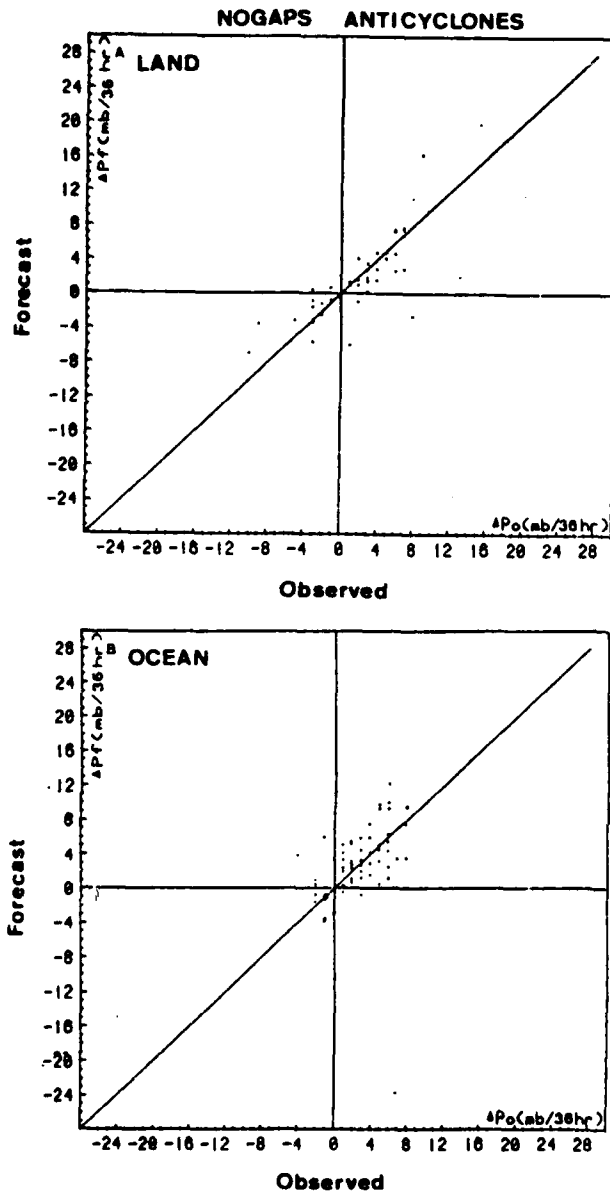


FIG. 14. As in Fig. 12 but for anticyclones.

model during the 1969/70 winter season is much greater than the 422 km error in NOGAPS and the 396 km error in JFLM forecasts. However, caution must be exercised in using these comparisons, because the usually faster system movements in winter seasons may lead to larger forecast errors.

Both NOGAPS and JFLM forecasts are too slow and too far to the west and north for cyclones and anticyclones. A similar behavior for the early winter cyclones was also observed in the NMC LFM-II. On the other hand, the behavior is somewhat different for anticyclone movements. In Colucci and Bosart's (1979) study, the NMC model anticyclones in winter season are too slow and tend to move to the right of the observed track (i.e., forecast too far to the south).

The overall mean central pressure errors of 36-h cyclone and anticyclone forecasts (Table 4) show that JFLM has a greater tendency to underforecast both cyclones and anticyclones than NOGAPS. The rms error of about 5.3 mb for both NOGAPS and JFLM cyclone central pressure forecasts is much smaller than the 6.95 mb error of the NMC LFM II cyclone forecasts during the 1978/79 cool season. Again, the difference in season may explain part of the differences.

The percentage of correct occurrence is slightly lower for cyclones and higher for anticyclones for NOGAPS as compared to JFLM at 36-h forecast time interval. For cyclones it is 59.9%/61.2% while for anticyclones

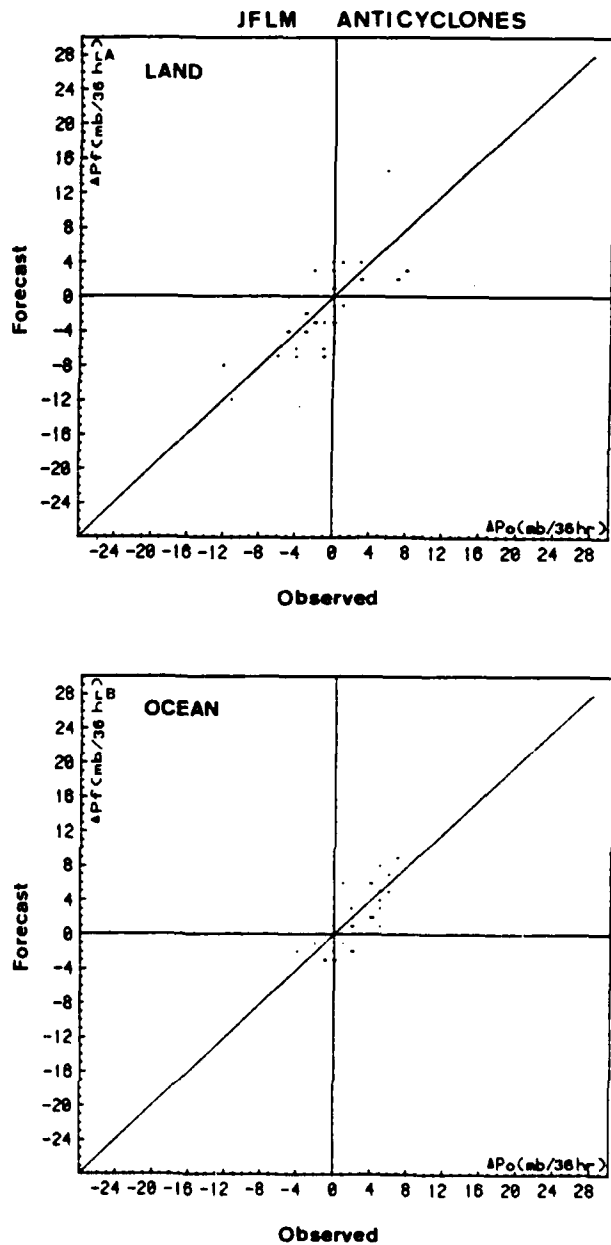


FIG. 15. As in Fig. 14 but for JFLM.

66.4%/64.3% in NOGAPS/JFLM forecasts. The better score for JFLM in the cyclone forecast is again probably due to its higher resolution. The greater capability of NOGAPS in forecasting the anticyclones appears to be due to two reasons: 1) The anticyclones are larger in scale therefore the effect of coarse resolution is less, and 2) NOGAPS is a global model which handles the subtropical anticyclones better than JFLM. Skill indices in terms of bias, false alarm rate and no hit rate at 36-h forecast time interval (Figs. 2-5) show that the NOGAPS has greater occurrence forecast skill than the JFLM for both land and oceanic cyclones and anticyclones. The cases of NFCST cyclones are more than those of NOBS for both JFLM and NOGAPS, indicating that both models have a greater tendency of missing, rather than artificially generating, cyclones. This is consistent with the underforecast of cyclone central pressure in both models. Comparing the NFCST and NOBS cyclones and anticyclones (Table 2), it is found that NOBS cases are much less than NFCST cases for both models. Thus both models are more likely to underforecast than to overforecast the existence and/or genesis of both cyclones and anticyclones. The false alarm rate for cyclone forecasts in JFLM reaches maximum (i.e., greatest probability to overforecast the existence and/or genesis of cyclones) in the 30°-40°N belt over land (Fig. 3). This is also true for NOGAPS but the value is smaller (Fig. 2). The 30°-40°N latitudinal belt is the region where the Tibetan Plateau is located. A similar result was obtained by Silberberg and Bosart (1982), who found that the NMC LFM-II tends to overforecast the continental cyclones to the lee of major mountain barriers.

Geographical distribution of central pressure errors (Figs. 6-9) shows a clear diurnal variation over northwestern China and Mongolia in both NOGAPS and JFLM forecasts. This is a vast desert area and the diurnal variation of radiation processes is expected to be important in controlling the temperature and pressure in the lower troposphere. No radiation processes are included in the JFLM model. Thus, it is expected that the model atmosphere may be too cold and the surface pressure too high in these areas for the 0000 GMT (0700 LST) runs, since the actual atmosphere goes through daytime heating twice and nighttime cooling only once for the 36-h forecasts. The reverse is expected for the 1200 GMT runs. This is indeed observed in the JFLM forecasts for both cyclone and anticyclone central pressures (Figs. 7, 9), with a positive error for 0000 GMT runs and negative error for 1200 GMT runs. A parameterization scheme of short and long wave radiation processes interacting with clouds exists in NOGAPS. Thus, the diurnal variation of central pressure error as observed in JFLM model should not occur if this parameterization scheme describes reasonably well actual radiation processes. However, in NOGAPS forecasts a diurnal variation is still evident over the same desert area except the sign is reversed, being negative for the 0000 GMT runs and positive for 1200

GMT runs for both cyclones and anticyclones (Figs. 6 and 8). This suggests that the model process of the diurnal cycle of radiation in NOGAPS may be too strong.

Over the ocean, while there are no systematic errors for anticyclones, positive cyclone central pressure errors are generally observed for both NOGAPS and JFLM models (Figs. 6, 7). The maximum positive error is observed over the area to the east of Japan and to the south of Kamchatka where cyclones usually deepen along their northeast track in the May-July period from synoptic experience. As observed by Chen and Chang (1980), cumulus heating plays a crucial role in maintaining the low-level Mei-Yu trough and its cyclonic vorticity. An examination of the GMS satellite infrared photos over Japan (not shown) during the period of study confirms that mesoscale convective systems always exist near the cyclone centers, similar to those observed in other years (e.g., Akiyama, 1978). Therefore, the effect of cumulus convection is probably quite important in the development of cyclonic disturbances in the Mei-Yu trough. Since the air-sea temperature difference is small and the relative humidity is generally high (Chen and Tsay, 1977), the bulk effects of boundary-layer sensible and latent heat fluxes within the local area are probably not important factors for cyclogenesis. Therefore, a positive error of cyclone central pressure may be due to the inability of the cumulus parameterization scheme in producing sufficient heating in the cyclone center. Similar central pressure errors were also found for NMC models by Leary (1971) and Silberberg and Bosart (1982) for the winter cyclones over the western Atlantic Ocean.

Over the Tibetan Plateau and its immediate vicinity, JFLM tends to overforecast the cyclone central pressure. The errors are most likely due to the unrealistic treatment of mountain effects. The NOGAPS cyclone forecasts also contain errors with a diurnal variation similar to that over the desert area to the north. This is again indicative of too strong a diurnal cycle of radiation processes in NOGAPS.

## 8. Summary and conclusions

This work studies the systematic errors of 36-h forecasts of surface cyclones and anticyclones in the FNOC six-layer NOGAPS and the JMA ten-layer JFLM, for the 1983 Mei-Yu season (May to July) over East Asia and the western North Pacific Ocean. The principal findings are as follows:

- 1) The seasonal mean position errors are somewhat greater for NOGAPS as compared to the JFLM for both cyclone and anticyclone forecasts probably due to its coarser resolutions. Both NOGAPS and JFLM models forecast too slow and too far to the west and north for cyclones and anticyclones.

- 2) JFLM has a tendency to underforecast both cyclones and anticyclones, while the deepening rate errors for NOGAPS are more random.

3) The overall occurrence forecast skill for cyclones and anticyclones for NOGAPS is somewhat greater than for JFLM.

4) Both NOGAPS and JFLM are more likely to underforecast than to overforecast the existence and/or genesis for both cyclones and anticyclones.

5) Over the mountainous area of Tibet and its immediate vicinity, JFLM model is more likely to overforecast the existence and/or genesis of cyclones than any other latitudinal belts. NOGAPS also has a similar tendency but to a lesser degree.

6) Diurnal variations of the central pressure errors exist for both cyclone and anticyclone forecasts in both models over the desert areas of northwestern China and Mongolia. This is apparently due to the lack of radiation processes in JFLM and too strong a diurnal cycle of radiation processes in NOGAPS.

7) Both NOGAPS and JFLM show positive cyclone central pressure errors and underforecast the more rapidly deepening cyclones over ocean. Failure to treat the bulk effects of cumulus convection properly seems to be the primary cause.

*Acknowledgments.* We wish to thank Prof. C. H. Wash for reading the manuscript and offering helpful suggestions. The NOGAPS data are provided by the Fleet Numerical Oceanographic Center, Monterey. Other data are provided by the Central Weather Bureau, Taipei, China. This work is supported in part by the Naval Environmental Prediction Research Facility, and by the AIT-CCNAA Cooperative Science Program which is funded by the National Science Foundation (Grants ATM8315175 and INT8506450) and the National Science Council in Taipei (Grant NSC740202M00208)

#### REFERENCES

- Akiyama, T., 1978: Mesoscale pulsation of convective rain in medium-scale disturbances developed in Baiu front. *J. Meteor. Soc. Japan*, **56**, 267-273.
- Arakawa, A., and W. H. Schubert, 1974: Interaction of a cumulus cloud ensemble with the large-scale environment, Part I. *J. Atmos. Sci.*, **31**, 674-701.
- Chen, G. T. J., 1983: Observational aspects of the Mei-Yu phenomenon over subtropical China. *J. Meteor. Soc. Japan*, **61**, 306-312.
- , and C. Y. Tsay, 1977: A detailed analysis of a case of Mei-Yu system in the vicinity of Taiwan. Tech. Rep. Mei-Yu-001. 249 pp. [Available from Dept. of Atmos. Sci., National Taiwan University, Taipei, Taiwan, R.O.C. 107.]
- , and C.-P. Chang, 1980: The structure and vorticity budget of an early summer monsoon trough (Mei-Yu) over southeastern China and Japan. *Mon. Wea. Rev.*, **108**, 942-953.
- Colucci, S. J., and L. F. Bosart, 1979: Surface anticyclone behavior in NMC prediction models. *Mon. Wea. Rev.*, **107**, 377-394.
- Fawcett, E. B., 1969: Systematic errors in operational baroclinic prognoses at the National Meteorological Center. *Mon. Wea. Rev.*, **97**, 670-682.
- Hollingsworth, A. K. Arpe, M. Tiedtke, M. Capaldo and H. Savijarvi, 1980: The performance of a medium-range forecast model in winter—impact of physical parameterizations. *Mon. Wea. Rev.*, **108**, 1736-1773.
- Kurihara, Y., 1961: Accuracy of wind-aloft data and estimation of error in numerical analysis of atmospheric motions. *J. Meteor. Soc. Japan*, **39**, 331-345.
- Leary, C., 1971: Systematic errors in operational National Meteorological Center primitive equation surface prognoses. *Mon. Wea. Rev.*, **99**, 409-413.
- Nitta, T., and Y. Yamagishi, 1979: Operational performance of a regional numerical weather prediction model. *J. Meteor. Soc. Japan*, **57**, 308-330.
- Randall, D. A., 1976: The interaction of the planetary boundary layer with large-scale circulations. Ph.D. thesis, The University of California, Los Angeles. 247 pp.
- Rosmond, T. E., 1981: NOGAPS: Navy Operational Global Atmospheric Prediction System. *Fifth Conf. Numerical Weather Prediction*, Monterey, Amer. Meteor. Soc., 74-79.
- Silberberg, S. R., and L. F. Bosart, 1982: An analysis of systematic cyclone errors in the NMC LFM-II model during the 1978-79 cool season. *Mon. Wea. Rev.*, **110**, 254-271.
- Tatsumi, Y., 1982: On the operational fine mesh limited area model (10L-FLM) at JMA. 14 pp. [Available from Electronic Computational Center, Japan Meteorological Agency.]
- Toll, R. F., and W. M. Clune, 1985: An operational evaluation of the Navy Operational Global Atmospheric Prediction System (NOGAPS) 48-hour surface pressure forecasts. *Mon. Wea. Rev.*, **111**, 1433-1440.
- Wallace, J. M., and J. K. Woessner, 1981: An analysis of forecast error in the NMC hemispheric primitive equation model. *Mon. Wea. Rev.*, **109**, 2444-2450.

**Structural Variations of the Synoptic-Scale Cyclonic Disturbances  
Near Borneo during the WMONEX Period**

George Tai-Jen Chen

*Department of Atmospheric Sciences  
National Taiwan University  
Taipei, R. O. C.*

and

T. E. Gerish and C.-P. Chang

*Department of Meteorology  
Naval Postgraduate School  
Monterey, CA 93943*

**ABSTRACT**

Five cases of cold surges over the South China Sea are selected from the December 1978 Winter MONEX data set to study the effects of the cold surges on the quasi-stationary cyclonic disturbances near Borneo. The differences between disturbances situated in the equatorial South China Sea and those over the western Pacific are also studied using the same data set.

It is found that cold surge enhances the low-level disturbances which in turn enhances the convective activities and reduces the vertical tilt of disturbance center. As the dry air surges into the cyclonic circulation in the boundary layer 24 h after the maximum surge, it helps to weaken the 850 mb disturbance. Analyses of the temperature anomalies at 300, 500, 850 mb, IR cloudiness, and 200 mb divergence suggest that large-scale subsidence suppresses the convection and causes warming. About 40–50% decrease in IR cloudiness, 200 mb divergence, and 850 mb vorticity is found as the disturbance moves from the western Pacific into the South China Sea. This is probably due to the combined effect of the cold sea surface over the South China Sea and the large-scale subsidence from north.

**1. Introduction**

During northern winter the equatorial "maritime continent" is a major convective area and serves as a significant heat source to the planetary scale cir-

ulation (Ramage, 1971). In early winter (December) the deep convection is often centered over or near Borneo, and is frequently associated with synoptic scale disturbances which may be quasi-stationary or westward propagating

(Cheang, 1977; Chang et al., 1979). Although the principal convection structure is of the mesoscale and strongly influenced by a diurnal oscillation due to the land-sea breeze (Houze et al., 1981; Johnson and Priegnitz, 1981; Johnson, 1982), the convection is significantly modulated by the northeasterly cold air surges off the southern China coast (Chang et al., 1979; Chang and Lau, 1980, 1982; Johnson and Priegnitz, 1981; Lau et al., 1983). As the surges can be traced backward in time for about 1-2 days to midlatitude development (Chang et al., 1983) the surges can not be viewed as a response to the tropical convection. In a pre-MONEX study, Chang et al. (1979) reported three cases of such interactions between the cold surges and the structure of the convection-associated synoptic-scale cyclonic disturbances near Borneo. This paper is a further investigation of the structure variations of these cyclonic disturbances near Borneo, using the December 1978 Winter MONEX data set. We will focus on the effects of the cold surges on these disturbances as well as on the difference between disturbances situated in the equatorial South China Sea and those further east, from which many of the propagating systems appear to originate.

## 2. Data and Procedure

Data used in this study are from the following sources: 1) The subjectively analyzed Winter MONEX wind atlas prepared by Chang et al. (1981), which was used to digitize winds at the gradient, 850, 700 and 500 mb levels. 2) The objective analyses of zonal and

meridional wind components, vorticity and divergence at 850 and 200 mb produced by Murakami et al. (1981) at 2.5° latitude-longitude grids. 3) Subjectively analyzed temperature at 850, 500 and 300 mb and dew point at the surface. The temperature data, however, are sparse and less reliable than the wind observations. 4) The GMS-1 infrared imagery was subjectively digitized to obtain the deep convective cloud amount using a method analogous to that of Payne and McGarry (1977).

Since the disturbances often appear as vortices in the lower tropospheric wind field with a diameter of 10-15°, a polar grid coordinate movable with the center of disturbance was used to digitize the wind and satellite cloud fields. The subjectively analyzed winds were digitized using radial grid points at 1.5° (latitude), 3°, 4.5°, 6.5°, and 8.5° away from the center. They have the best data base and contains finer features. For the objectively analyzed winds and the convective cloud amount the same radial grid distances were used. The temperature and the dew point fields were digitized on a constant 2° x 2° square grid, as finer resolution near the center cannot be supported by the quality of the data.

For different categories of disturbances, the data were composited in a quasi-Lagrangian framework (i.e., following a system rather than an air parcel) with respect to the 850 mb disturbance center. The disturbance center at each level is defined by the center of cyclonic circulation in the streamline analysis with the help of GMS-1 cloud imageries especially over the data sparse area. Admittedly the regular upper air data are

relatively sparse over the area of interest, however with the additional WMONEX aircraft, ship reports and satellite derived winds it is usually possible to reasonably well define a disturbance center. Fig. 1 is an example of the streamline analysis with two cyclonic disturbances. The choice of categories was based on different stages of a cold surge and on the geographical locations of the disturbances.

### 3. Composite according to cold surges

A cold surge is defined when 1) there is an increase in the area-averaged surface northerly wind component over the northern South China Sea ( $15\text{--}20^\circ\text{N}$ ,  $110\text{--}115^\circ\text{E}$ ) to over  $8\text{ ms}^{-1}$  and 2) a surface pressure differential between Hong Kong and a location at  $30^\circ\text{N}$ ,  $115^\circ\text{E}$  not less than 8 mb 0-24 hr before 1) is satisfied. Five events in December 1978 satisfy these criteria (Lau et al., 1983) and are selected for compositing. Each event is thus categorized into 7 stages with 12 h intervals, from -36 to 36 h, where 0 h represents the time of maximum surge wind in the northern South China Sea and -24 h or -36 h usually corresponds to the onset time of surge in that region (Lau et al., 1983). A cyclonic disturbance is included in the compositing of a stage if it is located directly downstream of the surge (i.e., between  $0\text{--}6^\circ\text{N}$  and  $105\text{--}116^\circ\text{E}$ ). The number of cases selected for each stage for the five surge events is listed in Table 1. Noted that the cyclonic disturbances in the chosen area were picked up at each synoptic map analyzed at 12 h intervals from 48 h before to 48 h after the surge time (0 h). To eliminate the

Table 1. Number of cases selected for each stage of a cold surge.

stage	-36h	-24h	-12h	0h	12h	24h	36h
number	16	17	14	12	11	13	14

short period variations, a 3-point running mean was applied to the time sequence of each cold surge event before compositing. The nonhomogeneous case number shown in Table 1 is due to the fact that within the chosen area some vortices were moving in and out and occasionally two vortices were observed. The geographic area of interest and the locations of different types of observational stations are also shown in Fig. 1.

Fig. 2 shows the composite disturbance center at different stages. The disturbance is well defined as a closed cyclonic circulation from the gradient level to 700 mb, with its center tilted vertically towards the southwest which is hydrostatically consistent with the 850-500 mb layer mean temperature as the cold air is located to the southwest of the center (not shown). The tilt is reduced from about  $3^\circ$  latitude at the surge onset to  $1^\circ$  after the surge reaches maximum. The lower tropospheric vorticity of the disturbance also increases following the surge onset. At 850 mb the maximum vorticity increases from  $2 \times 10^{-5}\text{ s}^{-1}$  at -24 hr to  $2.5 \times 10^{-5}\text{ s}^{-1}$  at -12h. Fig. 3 shows the continued increases as evidenced by the expansion of the area enclosed by the  $2.5 \times 10^{-5}\text{ s}^{-1}$  isopleth at 0 h, reaching maximum at 24 h. The vorticity increase is a direct result of the land sea distribution and the surge, with a freshening of the northeasterlies occurring in the

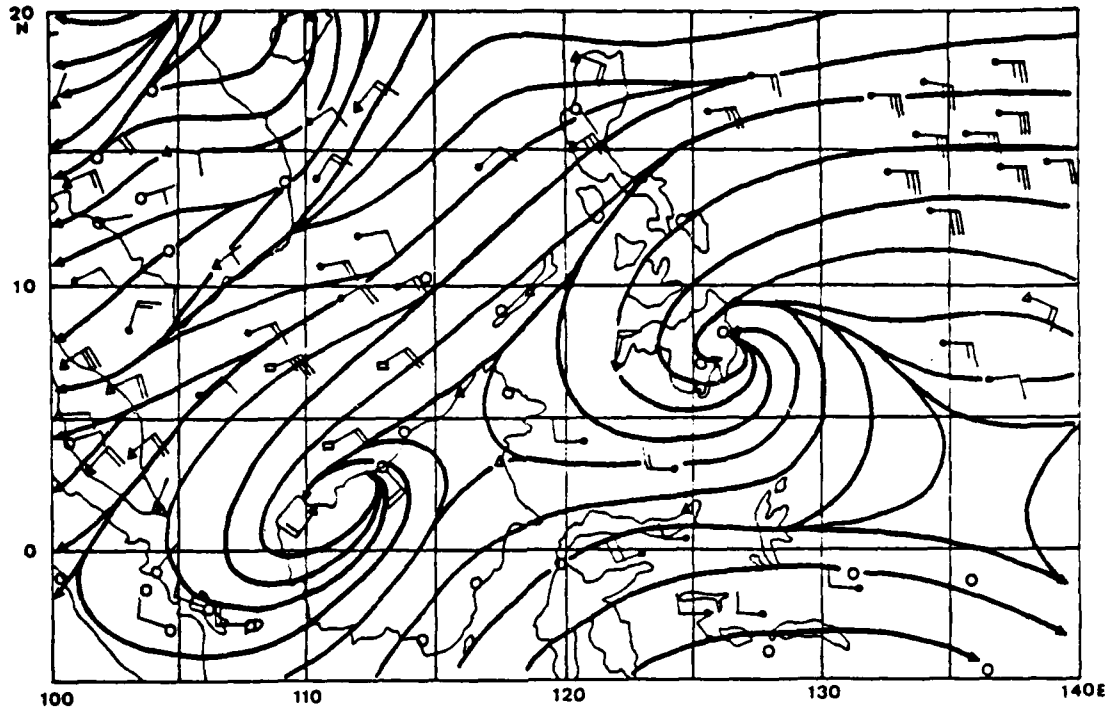


Fig. 1 Geographic area of interest and the locations of stations. Triangles, circles, and squares represent radiosonde stations, pibal stations, and Russian ships, respectively. Solid circles are satellite derived winds. The 00Z 13 December 1978 streamline analysis at 850 mb with two cyclonic centers are shown.

South China Sea where the northwestern quadrant of the disturbance is located.

Table 2 shows the area-averaged IR cloudiness (tenths) over a  $8.5^\circ$  radius centered on the disturbance. It is clear that the convective cloudiness activity has a general trend of increase after the surge onset with about 35% increase from  $-36$  h to 0 h. Fig. 4 shows the IR

Table 2. Area-averaged convective cloudiness (tenths) over a  $8.5^\circ$  radius.

stage	-36h	-24h	-12h	0h	12h	24h	36h
cloudiness	3.2	3.3	3.7	4.3	4.2	4.0	3.6

cloudiness distribution at different stages. The maximum cloudiness remains in the northwestern quadrant and increases steadily from  $-36$  h to reach maximum at 0 h. At the northern edge the cloudiness is 1 before 0 h and increases to 3 at and after 0 h. At the southwestern edge the convection remains rather active throughout all stages.

Fig. 5 shows the 200 mb divergence. Prior to 0 h there is a strong convergence in the northern edge suggesting downward motions, and divergence in the southwestern quadrant. At  $-12$ h, which is about one day after the surge onset, a

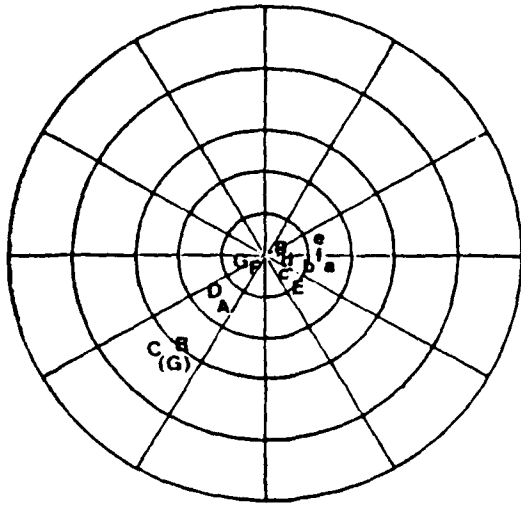


Fig. 2 Disturbance centers at gradient level (small letter), 700 mb (capital), and 500 mb (parenthetic) with respect to 850 mb center at -36 h (a, A), -24 h (b, B), -12 h (c, C), 0 h (d, D; maximum surge time), 12 h (e, E), 24 h (f, F), 36 h (g, G). Radial grid points are at 1.5° (latitude), 3°, 4.5°, 6.5°, and 8.5° away from the center.

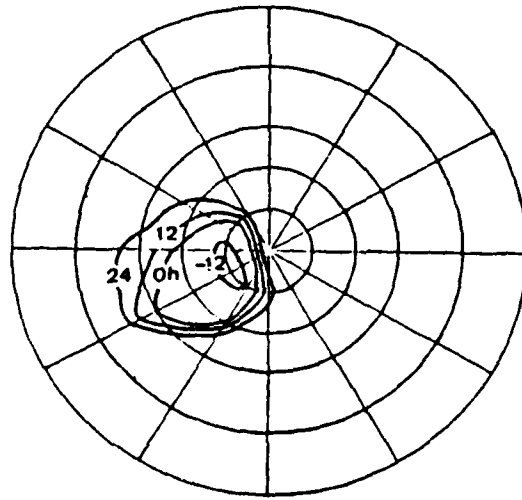
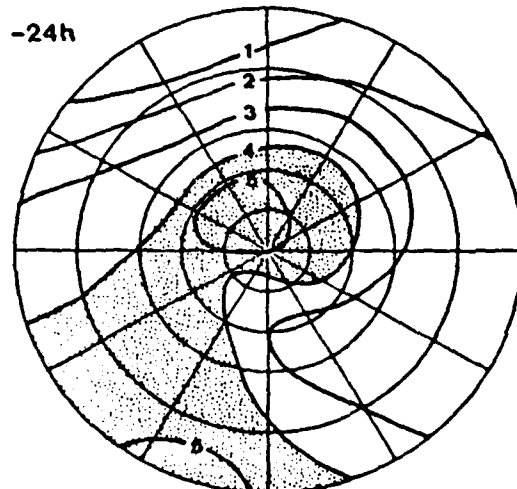
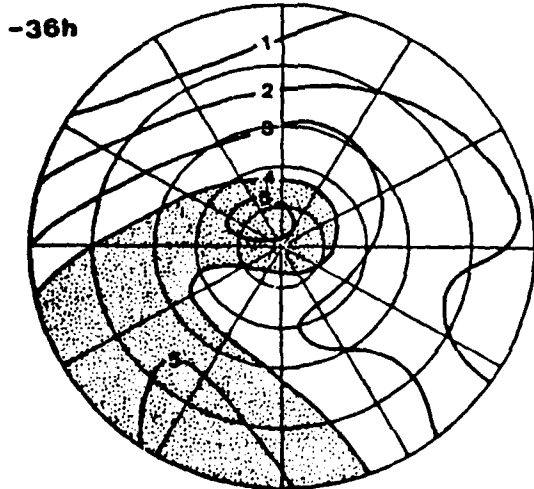


Fig. 3. Isolines of vorticity with a value of  $2.5 \times 10^{-5} \text{ s}^{-1}$  at 850 mb.



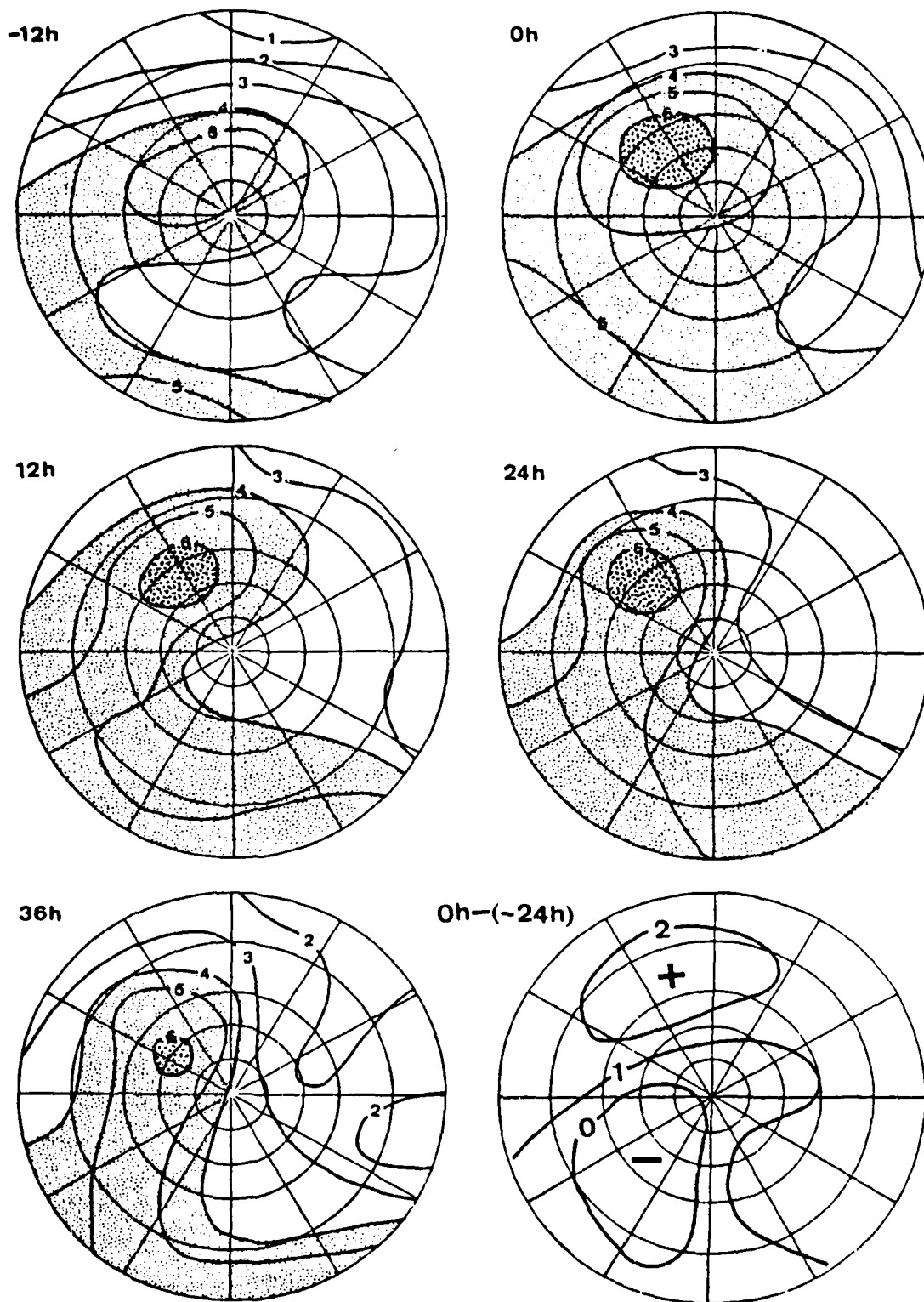
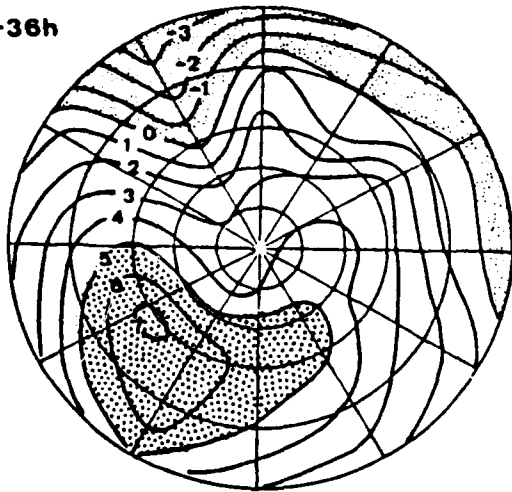


Fig. 4. IR cloudiness (tenths) at different stages of surge and its tendency from -24 h to 0 h. 0 h is the time of maximum surge. Light shading is greater than 4 unit, dark shading is greater than 6 unit.

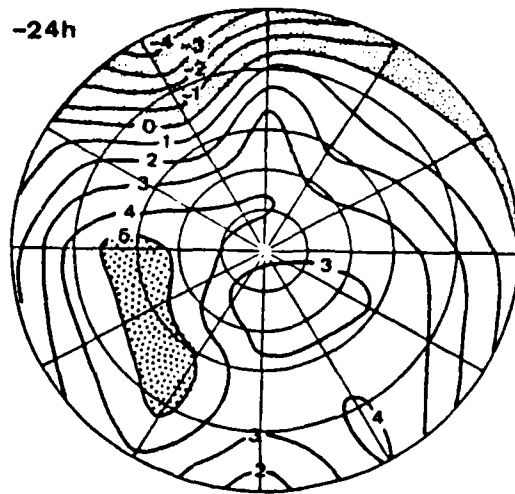
divergence center develops about  $3^{\circ}$  latitude north of the disturbance center, reaching maximum at 0 h and persists through 24 h. This development of the divergence center is in good agreement with the enhanced IR cloudiness after the surge onset, especially in view of the rather crude data base and the usual

error involved in the divergence calculation. The correspondence between the IR cloudiness and the divergence is much clearer in the tendency fields. For example, the tendency from  $-24$  h to 0 h shows an area of maximum increases in both the cloudiness and divergence in the north and northwestern quadrants

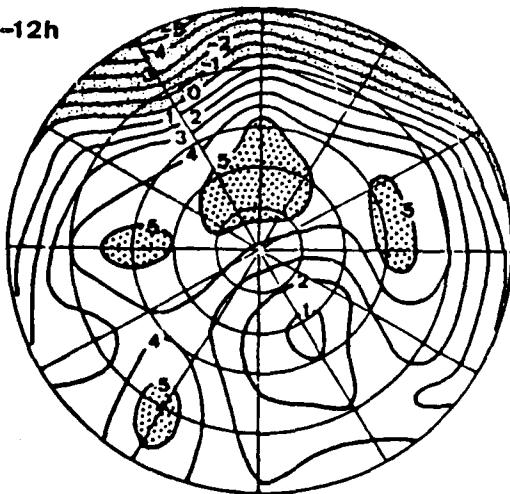
-36h



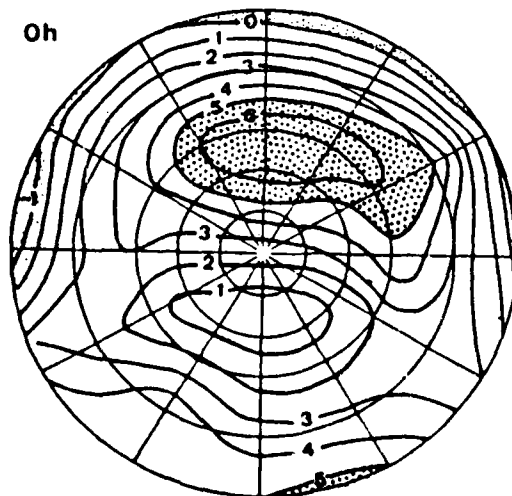
-24h



-12h



0h



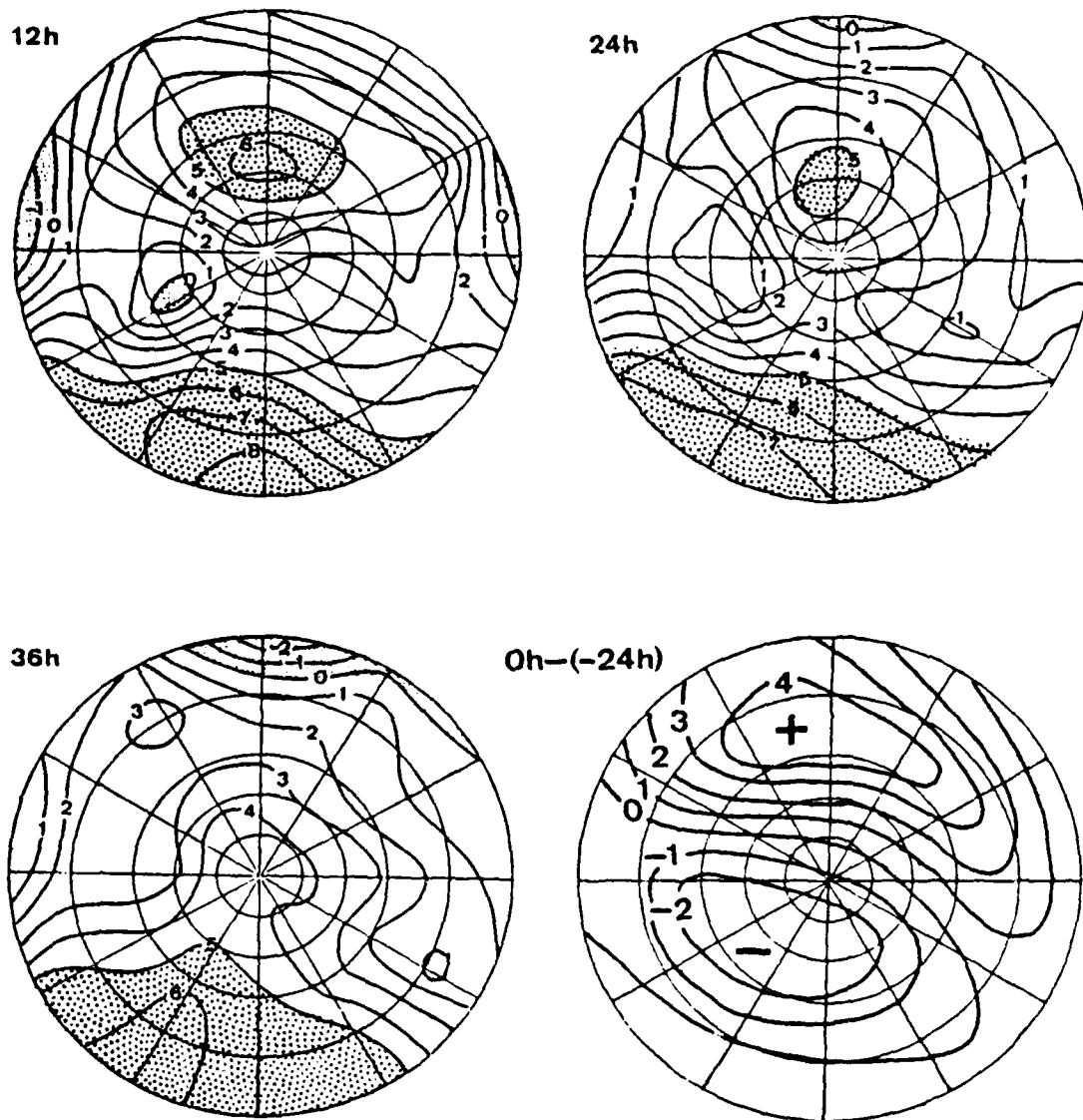


Fig. 5. Same as Fig. 4, except for 200 mb divergence ( $10^{-6} \text{ s}^{-1}$ ). Light shading is convergence and dark shading is greater than 5 unit.

(Figs. 4, 5).

Throughout all stages the 200 mb vorticity (not shown) is basically anti-cyclonic in the northern half and cyclonic in the southern half, indicating an easterly jet in the latitude of disturbance center in consistency with the composite wind field. This is also in good agreement with the temperature field (not shown) at 500 and 300 mb which shows the warm air to the north and cold air to the south with maximum temperature gradient over the disturbance center. No significant variations can be found between the different stages.

Due to the fact that the horizontal variations in both the temperature and dew point are relatively small in the tropics, the anomaly fields were analyzed. The anomaly is defined here as the departure from time mean during surge periods over the selected area between  $0^{\circ}$ – $6^{\circ}$ N and  $105^{\circ}$ – $116^{\circ}$ E. Fig. 6 shows the surface dew point anomaly. Starting from  $-36$  h a dry tongue penetrates cyclonically into the circulations from the northwest. It moves around the south of the disturbance center at 0 h then turns northeastward and northward from 12 to 36 h. Figs 7-9 show the temperature anomaly from time mean over the same area as that for the dew point at 300, 500 and 850 mb, respectively. In general, warming starts from the northwest prior to the surge and progresses towards the center at all three levels. At 300 mb the temperature anomaly for the disturbance domain becomes maximum at 0 h, while at 500 mb and 850 mb the warming continues through 36 h. It is a well known fact that in the tropics the troposphere

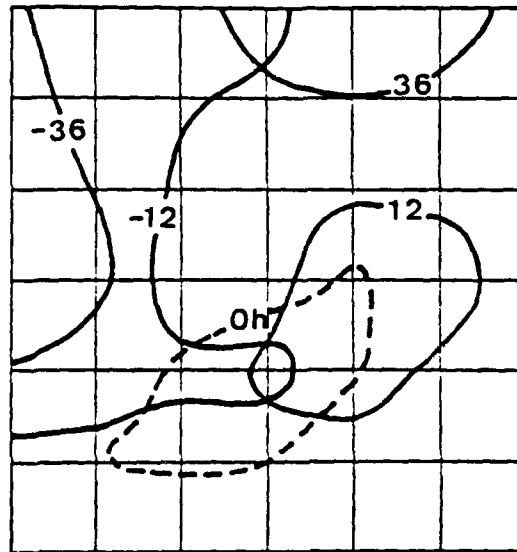


Fig. 6. Isolines of  $-0.4^{\circ}\text{C}$  surface dew point anomaly from the time mean at different stages. 0 h is the time of maximum surge and grid interval is at  $2^{\circ}$  latitude.

experiences warming due to convection mainly as a consequence of compensating dry adiabatic sinking motion (e.g., Gray, 1973; Frank, 1980). In the present case, however, 300 mb temperature anomaly pattern with a warm maximum north and a cold maximum south is opposite to the cloudiness distribution shown in Fig. 4. This distribution excludes the possibility of the latent heating over the region of maximum warmth. Lacking any other indication of a different warming mechanism, the pattern appears to suggest that the warming north of the disturbance center is due to large scale subsidence from the southeastward moving jet. The warming pattern is similar to that of the surge period.

AD-A188 387

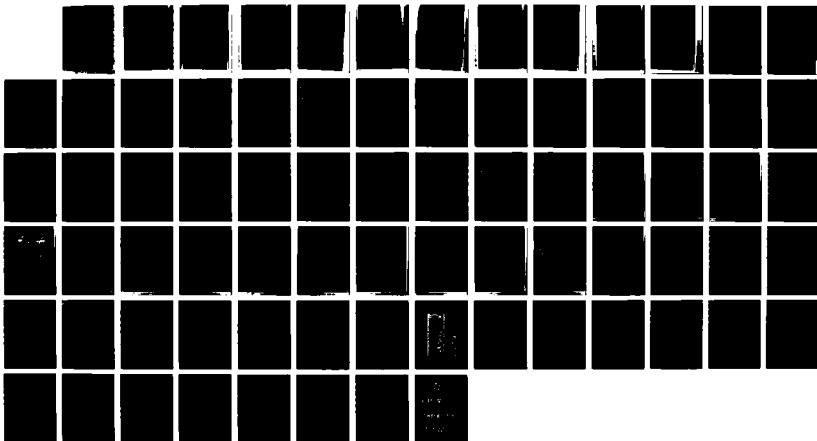
TROPICAL AND MONSOONAL STUDIES(U) NAVAL POSTGRADUATE SCHOOL MONTEREY CA C CHANG ET AL. JAN 88 NPS-63-88-001 2/2

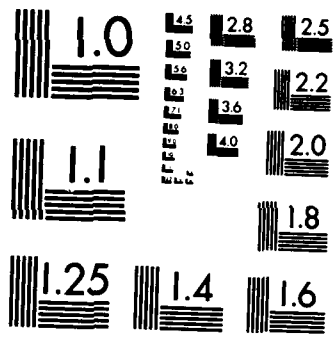
NSF-ATM83-15175

UNCLASSIFIED

F/G 4/4

NL





MICROCOPY RESOLUTION TEST CHART  
 NATIONAL BUREAU OF STANDARDS-1963-A

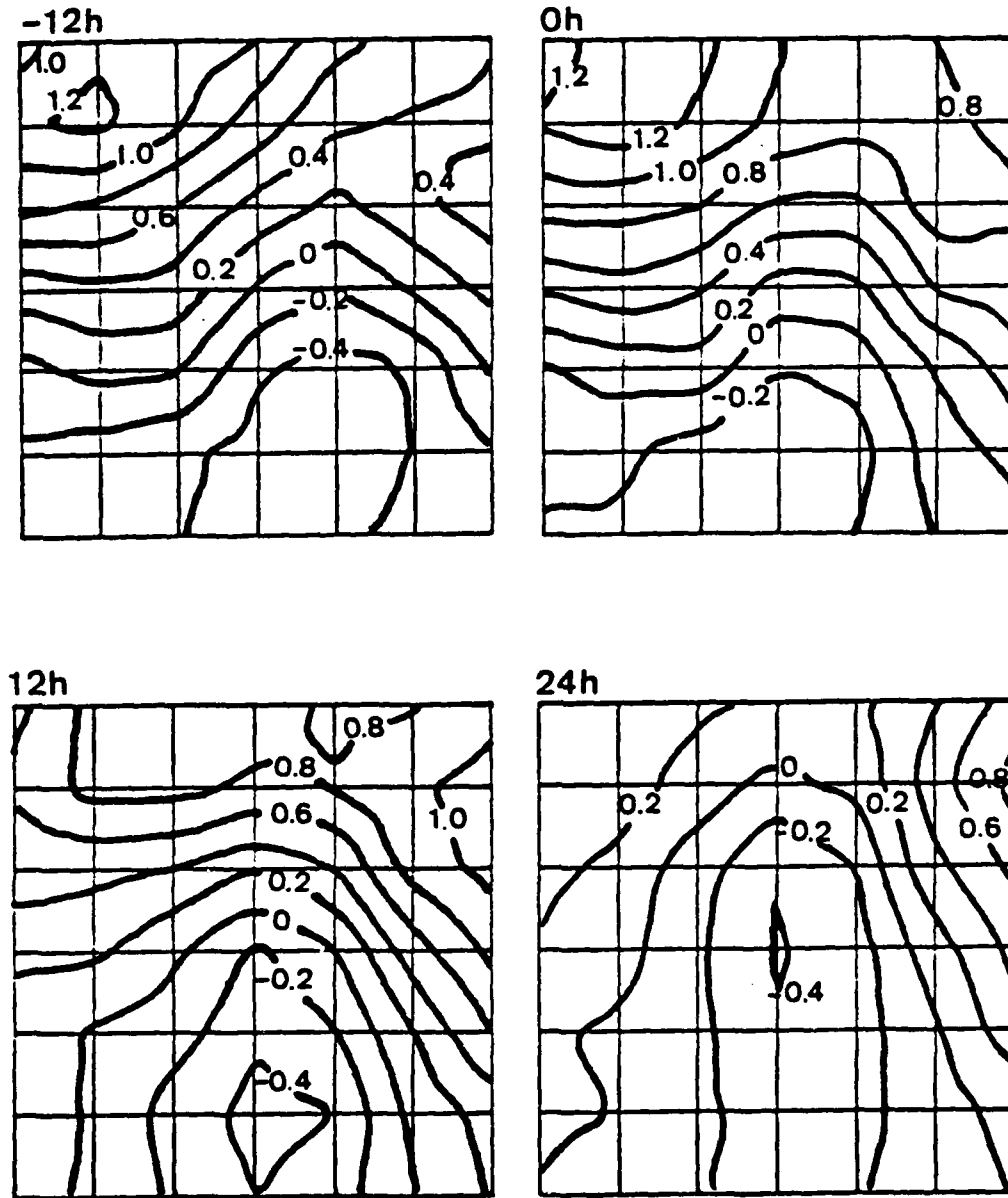


Fig. 7. 300 mb temperature anomaly from the time mean at different stages of surge. 0 h is the time of maximum surge and grid interval is at 2° latitude.

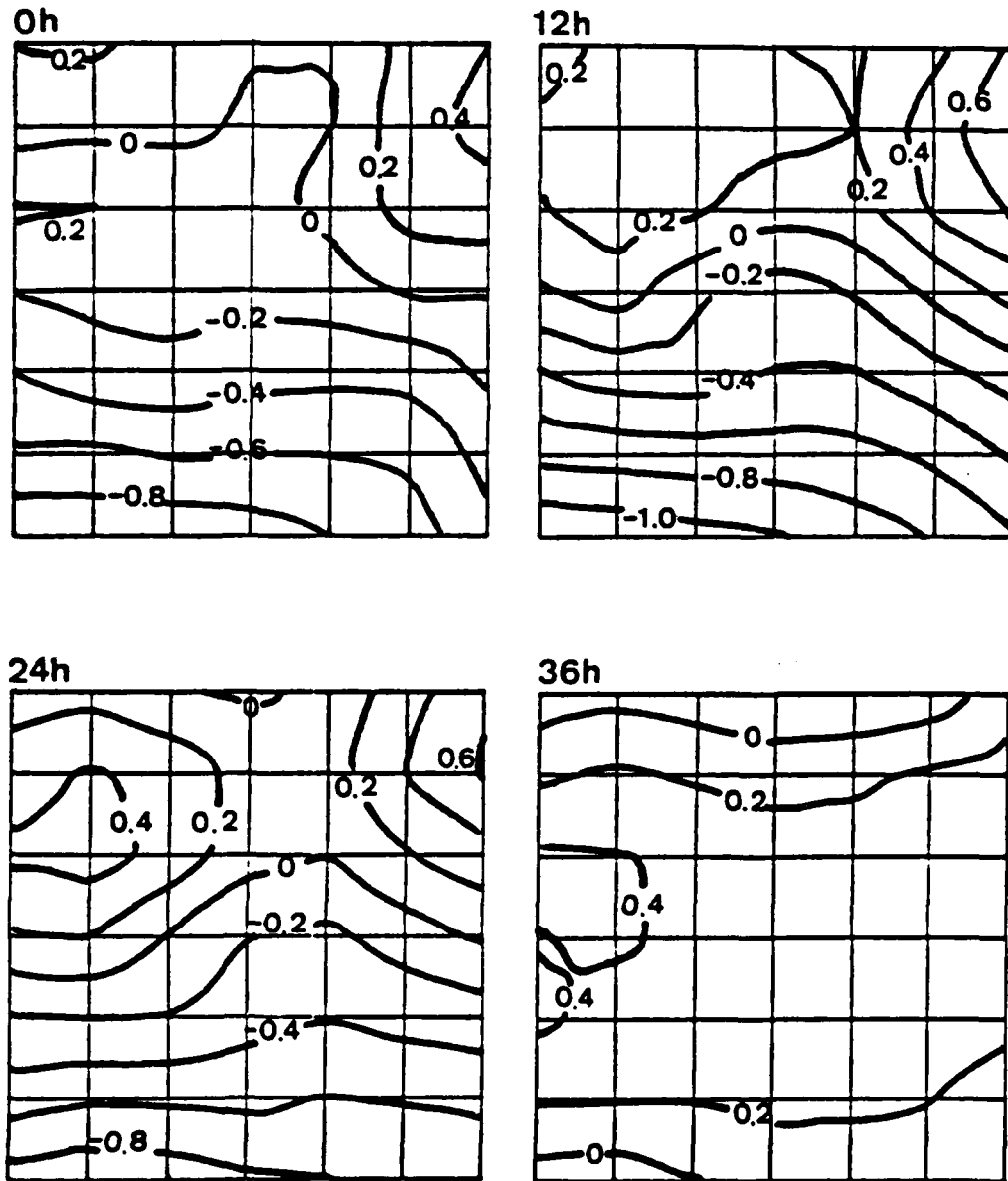


Fig. 8. Same as Fig. 7, except at 500 mb.

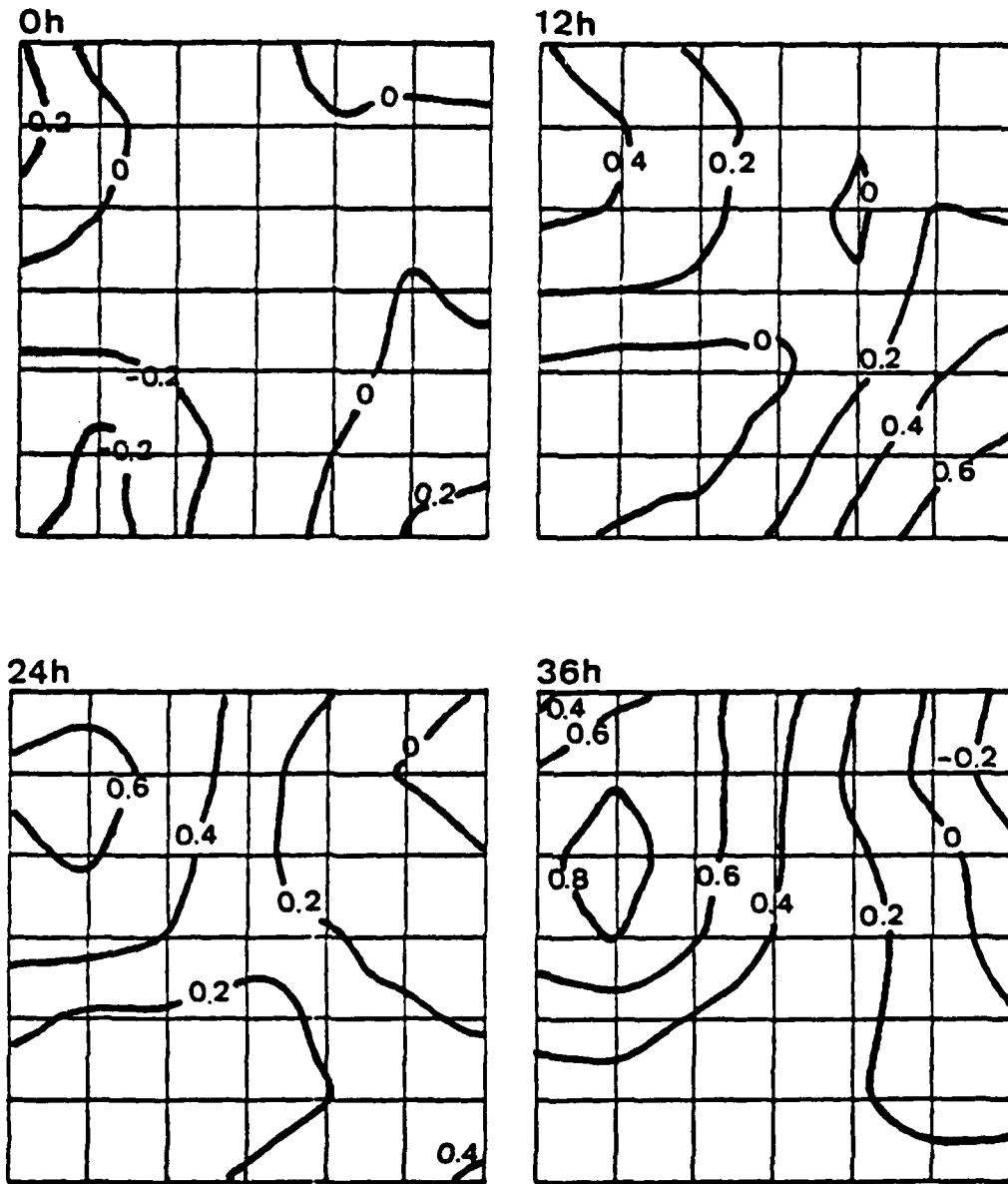


Fig. 9. Same as Fig. 7, except at 850 mb.

(  
c  
d  
th  
in  
tu  
wi  
sta  
or  
aft  
nur

just a result of the increased tropical convection. Convergence in the north side before 0 h as shown in Fig. 5 is also consistent with the existence of such subsidence. Based on this interpretation, Figs. 7–9 suggest that the warming at all levels is due to large-scale environmental subsidence rather than the disturbance motion or latent heating, and that the subsidence expands southward at lower levels.

#### 4. Structure variation of the westward propagating disturbance

In the previous section we considered the effect of the surges for all cyclonic disturbances downstream in the South China Sea near Borneo, without considering their origins. These disturbances may be separated into two categories, those developed *in situ* and those propagated into the South China Sea from the Western Pacific. Regarding the latter system, there has been extensive studies of easterly waves in the Western Pacific to the east of 155°E (e.g., Wallace, 1971; Reed and Recker, 1971), but little is known about the disturbances over the area to the west of 140°E and after they enter the South China Sea. In this section we will compare the structure of the propagating disturbances before and after they enter the South China Sea, as well as with the *in situ* developed, quasi-stationary disturbances. To avoid ambiguity, we will not include systems that become stationary after a period of propagation, or systems that become propagating after a period of being stationary.

A disturbance may include a number of cases depending upon the

number of times it appears on the twice-daily analysis. By examining the twice-daily low-level analysis maps during December 1978, we can select 26 consistently westward propagating cases and 35 consistently quasi-stationary cases. The former is further divided into the Western Pacific (WP) type where the disturbances are observed between 120–140°E, 0–10°N, and the South China Sea (SCS) type, where the disturbances are observed between 105–120°E, 0–10°N. There are 13 cases in each of these two types. Only one of the 13 cases coincides with a case selected for the surge onset (0 h) category, thus the SCS type basically represents disturbances not influenced by the cold surge. The stationary type and each of the two propagating types are composited within each type to find their averaged structure.

The composite structures (not shown) indicate that the stationary type disturbance is quite shallow with its cyclonic center defined only at 850 and 700 mb. The WP type is well defined at all levels from gradient level to 500 mb, whereas the SCS type is confined at and below 700 mb. Fig. 10 shows the relative vorticity at 850 mb, which is generally cyclonic for all types. For the WP type, the maximum cyclonic vorticity is located near the disturbance center to the northeastern quadrant, not much different from the structure of a typical easterly wave in the Atlantic observed by Reed et al. (1977) in which the maximum cyclonic vorticity is right over the wave trough. As the disturbance moves into the South China Sea and becomes the SCS type, a 40% decrease in maximum cyclonic vorticity is

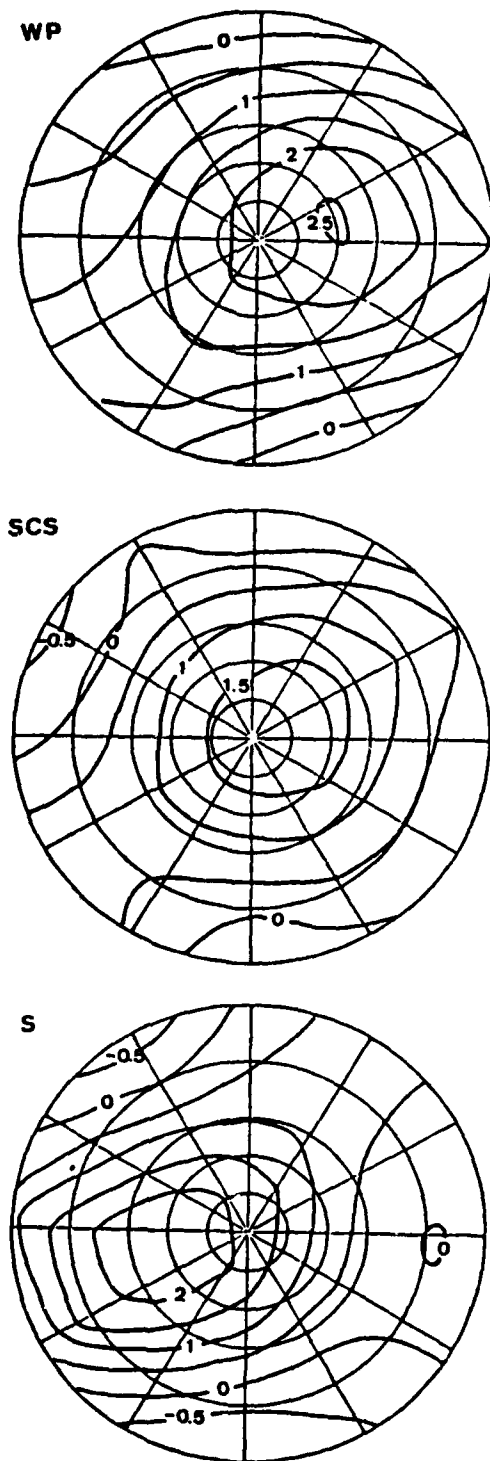


Fig. 10. 850 mb vorticity ( $10^{-4} \text{ s}^{-1}$ ) for Western Pacific (WP), South China Sea (SCS), and stationary (S) types.

observed over the same region. In contrast to both of the propagating types, the maximum cyclonic vorticity for the stationary disturbance is located to the west-southwestern side of the center.

Fig. 11 shows the IR cloudiness distribution. For the WP type, the maximum cloudiness of 7 occurred to the north and northeast of the center. As the disturbance moves into the South China Sea and becomes the SCS type, cloudiness over the same area, although still a relative maximum, decreases by  $>50\%$ . This is in good agreement with the decrease in the intensity of the disturbance shown in the 850 mb vorticity (Fig. 10). Different from the propagating disturbances, the stationary type has the maximum cloudiness in the southwestern quadrant of the disturbance, which is over the northwestern coast of Borneo. Since the stationary disturbances stay in the same place for a longer period of time, the influence of the local topography is likely to be important. It therefore seems that the surface convergence due to the land-sea differential frictional effect may be the main cause for the cloudiness distribution.

Fig. 12 shows the 200 mb divergence. Overall, the 200 mb divergence is positively correlated with the IR cloudiness, with the area of maximum cloudiness being roughly coincided with the area of maximum divergence for each of the three types. For the stationary type, the maximum divergence occurs in the southwestern quadrant where the maximum convective cloudiness is observed. For the WP type, the

Fig

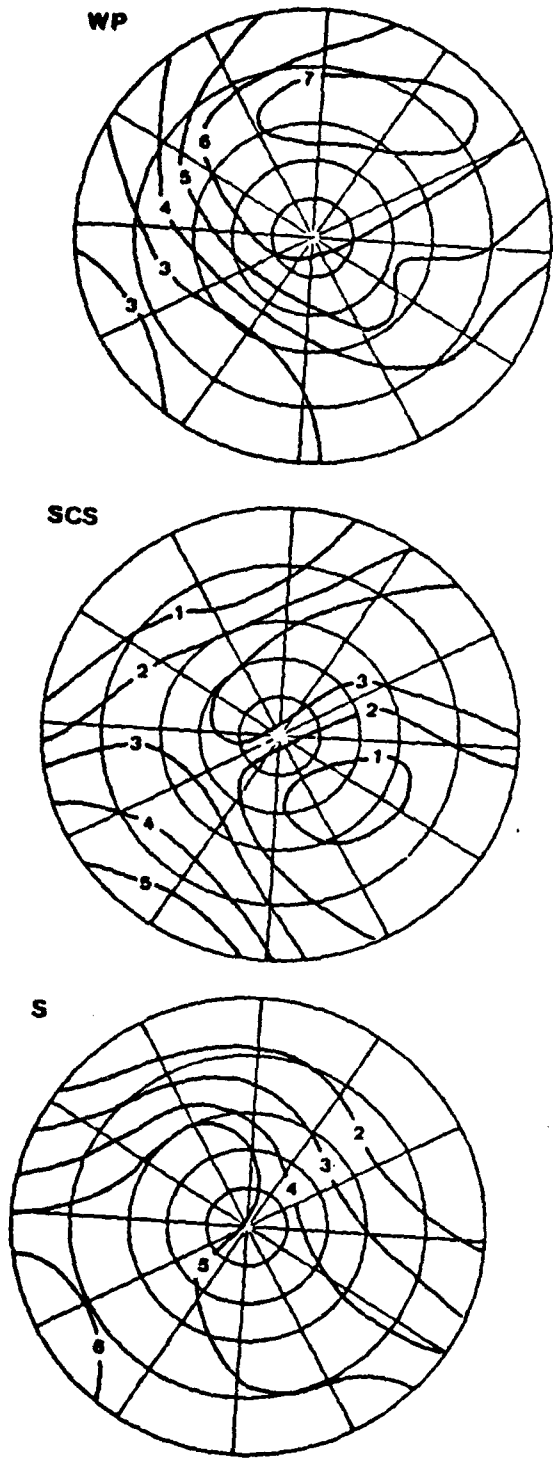


Fig. 11. IR cloudiness (tenths) for Western Pacific (WP), South China Sea (SCS), and stationary (S) types.

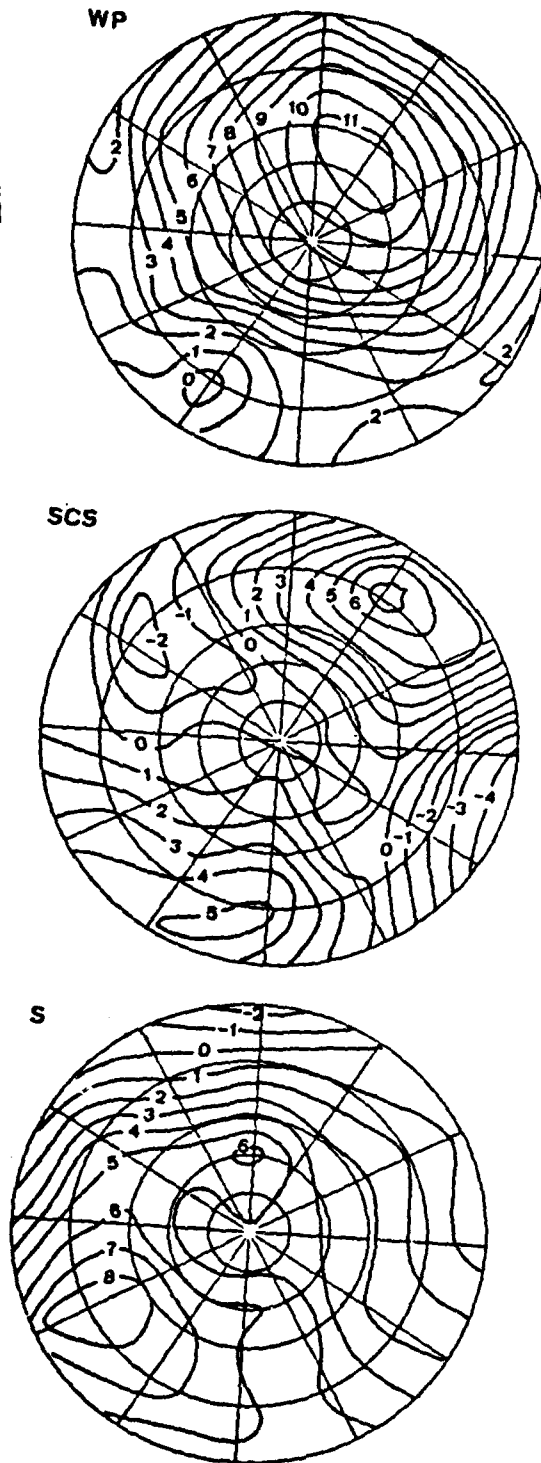


Fig. 12. 200 mb divergence ( $10^{-6} s^{-1}$ ) for Western Pacific (WP), South China Sea (SCS), and stationary (S) types.

center of maximum divergence is found in the northeastern quadrant. This distribution is somewhat different from the structure of a typical easterly wave in the Atlantic where the maximum divergence is located just ahead of the disturbance center (Reed et al., 1977). It is also different from the wave disturbances in the equatorial Western Pacific to the east of 155°E as observed by Reed and Recker (1971) in which the maximum divergence is right over the disturbance center. A decrease of 40% in the maximum divergence in the northeastern quadrant is observed as the disturbance moves into the South China Sea and becomes the SCS type. This weakening of the divergence center is again in good agreement with the suppressed IR cloudiness after the disturbance moves into the South China Sea. For both the WP and the SCS types, an easterly jet streak of the basic flow at 200 mb is located to the immediate south of the disturbance center (not shown). The typical divergence pattern associated with such a jet streak, namely divergence in the entrance (exit) region to the right (left) and convergence in the entrance (exit) region to the left (right), is consistent with the observed divergence patterns. The maximum anticyclonic vorticity at 200 mb (not shown) is found over the area of maximum divergence and convective cloudiness in the northeastern quadrant for both propagating types. This together with the existence of a basic flow jet streak indicates that deep convection is probably organized by the upper-level outflow associated with the large-scale motions. After the disturbance moves into the South China Sea, the 200 mb

anticyclonic vorticity and divergence weaken just as the IR cloudiness over the same area.

##### 5. Summary and concluding remarks

Chang and Lau (1980) suggested that cold surges cause low-level convergence which may in turn enhance convection. Lim and Chang (1981), in a theoretical study of the surge motions, showed that cyclogenesis occurring in the equatorial trough region downstream of the surge forcing is a result of a Rossby wave group response. In the real tropical atmosphere, this cyclogenesis can be expected to be associated with enhanced convective activities because of the presence of conditional instability almost everywhere, except when drier air penetrates into the lower levels. In the present composite study (section 3) the lower tropospheric vorticity of the cyclonic disturbance downstream of the cold surge increases following the surge onset, mainly due to the freshening of the northeasterlies which increases the cyclonic shear. Apparently due to the sparsity of data over the area of study, the computed 850 mb divergence were not capable of showing an organized pattern. On the other hand, since the 850 mb vorticity maximum increases during the surge period (Fig. 3) to the west of the disturbance center, the increase in convergence upstream of the vorticity maximum in the northwestern quadrant may be expected from the conservation of potential vorticity argument. Thus, surge enhances vorticity which in turn causes the convergence to increase. As a result, IR cloudiness to the northwest of the center increases

in concurrent with the strengthening of the 850 mb cyclonic vorticity after the surge onset.

The development of the divergence center at 200 mb is in good agreement with the enhanced IR cloudiness after the surge onset. Thus the cold surge enhances the disturbance and reduces the vertical tilt, probably through the increased organized deep convection. The slight decrease in IR cloudiness after the time of maximum surge (0 h) and the slight weakening of the 850 mb vorticity 24 h after the maximum surge are likely due to the dry air surge into the cyclonic circulation in the boundary layer as evidenced by the surface negative dew point anomaly. It seems legitimate to argue that the convection would die down as the surge dies down since the convection is a response to the dynamic forcing of the surge. However, due to the fact that the tropical air is highly conditionally unstable and the large-scale dynamic forcing of the surge is the triggering mechanism, the convection is not necessary to die down as the surge dies down. The dry surge air appears to reduce the moisture supply for the deep convection and helps to weaken the disturbance. The good agreement among the 200 mb convergence, temperature anomalies at 200, 500, 850 mb, and reduced IR cloudiness over the northwestern border of disturbance suggests that large-scale subsidence suppresses the convection and causes warming. The large-scale subsidence over the central South China Sea was observed by Chu and Park (1984) in their time-mean meridional mass circulation between 100 and 126°E for the surge case during 9-13 December 1978.

This large-scale thermal change seems to mask any temperature change that may result from the disturbance-scale motion.

One of the basic differences between the quasi-stationary and westward propagating disturbances is the distribution of the IR cloudiness. For the propagating type, the maximum cloudiness occurs to the north and northeast of the disturbance center. For stationary type, on the other hand, the maximum cloudiness is found, in the southwestern quadrant, apparently due to the differential friction effect of the northwestern coast of Borneo. The weakening of the westward propagating disturbances (most of them are not influenced by surge in this study), when they move into the South China Sea, is evidenced by the 40-50% decrease of IR cloudiness, 200 mb divergence and 850 mb vorticity. It is probably a result of the combined effect of the cold sea surface over the South China Sea and the large-scale subsidence from north.

From the foregoing discussion, the response of the synoptic-scale disturbance and the accompanied convection to the cold surge in the South China Sea region is quite clear. This is an important link in the wintertime midlatitude-tropical interactions in view of the recent findings of the planetary-scale response to the enhanced South China Sea convection during the cold surge (Chang and Lau, 1982; Lau et al., 1983). Only some preliminary structure variations of these equatorial disturbances during the winter monsoon is reported here. To further study the dynamic and thermodynamic effects involved in these disturbances, quantitative computations

with better data, especially temperature and humidity data, are required.

#### ACKNOWLEDGEMENTS

We wish to thank Dr. J. Boyle for reading the manuscript and Dr. H. Lim and Mr. L. C. Chou for assistance in data processing. The first author (GTJC) wishes to acknowledge the support provided by the National Science Council of ROC under Gant NSC 76-0202-M002-04. This research was supported in part by National Science Foundation AIT-CCNAA cooperative program INT 8506450.

#### REFERENCES

- Chang, C.-P., B. K. Cheang and G.T.J. Chen, et al., 1981: Regional synoptic analysis during Phase I of Winter MONEX. Tech. Rept., Dept. of Meteorology, Naval Postgraduate School, Monterey, CA 93943, 285 pp.
- \_\_\_\_\_, J.E. Erickson and K.M. Lau, 1979: Northeasterly cold surges and near-equatorial disturbances over the Winter MONEX area during December 1974. Part I: Synoptic aspects. *Mon. Wea. Rev.*, 107, 812-829.
- \_\_\_\_\_, and K.M. Lau, 1980: Northeasterly cold surges and near-equatorial disturbances over the Winter MONEX area during December 1974: Part II: Planetary-scale aspects. *Mon. Wea. Rev.*, 108, 298-312.
- \_\_\_\_\_, and K.M. Lau, 1982: Short-term planetary-scale interactions over the tropics and midlatitudes during northern winter. Part I: Contrasts between active and inactive periods. *Mon. Wea. Rev.*, 110, 933-946.
- \_\_\_\_\_, J.E. Millard and G.T.J. Chen, 1983: Gravitational character of cold surges during Winter MONEX. *Mon. Wea. Rev.*, 111, 293-307.
- Cheang, B.K., 1977: Synoptic features and structures of some equatorial vortices over the South China Sea in the Malaysia region during the winter monsoon, December 1973. *Pure Appl. Geophys.*, 115, 1303-1334.
- Chu, P.S. and S.U. Park, 1984: Regional circulation characteristics associated with a cold surge event over East Asia during Winter MONEX. *Mon. Wea. Rev.*, 112, 955-965.
- Frank, W.M., 1980: Modulations of the net tropospheric temperature during GATE. *J. Atmos. Sci.*, 37, 1056-1064.
- Gray, W.M., 1973: Cumulus convection and large-scale circulations. Part I: Broad-scale and mesoscale considerations. *Mon. Wea. Rev.*, 101, 839-853.
- Houze, R.A. Jr., S.G. Geotis, F.D. Marks and A.K. West, 1981: Winter monsoon convection in the vicinity of North Borneo. Part I: Structure and time variation of the clouds and precipitation. *Mon. Wea. Rev.*, 109, 1595-1614.
- Johnson, R.H., 1982: Vertical motion in near-equatorial winter monsoon convection. *J. Meteor. Soc. Japan*, 60, 682-690.
- \_\_\_\_\_, and D.L. Priegnitz, 1981: Winter monsoon convection in the vicinity of North Borneo. Part II: Effects of large-scale fields. *Mon. Wea. Rev.*, 109, 1615-1682.
- Lau, K.M., C.-P. Chang and P.H. Chan, 1983: Short-term planetary scale interactions over the tropics and midlatitudes. Part II: Winter MONEX periods. *Mon. Wea. Rev.*, 111, 1372-1388.
- Lim, H. and C.-P. Chang, 1981: A theory for midlatitude forcing of tropical motions during winter monsoon. *J. Atmos. Sci.*, 38, 2377-2392.
- Murakami, T., A. Sumi, S.W. Lyons, L.Y.C. Ho and L.K. Oda, 1981: Daily 200 and 850 mb wind fields over the greater WMONEX region. UHMET81-04, Dept. of Meteor., Univ. of Hawaii, Honolulu 96822, 192 pp.
- Payne, S.W., and M.M. McGarry, 1977: The relationship of satellite infrared convective activity to easterly waves over west

- Africa and the adjacent ocean during Phase III of GATE. *Mon. Wea. Rev.*, 105, 413-420.
- Ramage, C.S., 1971: *Monsoon Meteorology*, Academic Press, 296pp.
- Reed, R.J., D.C. Norquist and E.E. Recker, 1977: The structure and properties of African wave disturbances as observed during Phase III of GATE. *Mon. Wea. Rev.*, 105, 317-333.
- \_\_\_\_\_, and E.E. Recker, 1971: Structure and properties of synoptic-scale wave disturbances in the equatorial Western Pacific. *J. Atmos. Sci.*, 28, 1117-1133.
- Wallace, J.M., 1971: Spectral studies of tropospheric wave disturbances in the tropical Western Pacific. *Rev. Geophys. Space Phys.*, 9, 557-612.

Chou, Lang C., Ph.D. Thesis, 1986  
A Numerical Simulation of the Mei-Yu Front and the Associated Low-level Jet

#### ABSTRACT

The Mei-Yu front is a quasi-stationary belt of heavy precipitation imbedded in the summer monsoon trough over East Asia. This work used a two dimensional frontogenesis model to study the Mei-Yu front, especially its associated low-level jet (LLJ) which often occurs during intense convection. Several numerical experiments were carried out to simulate the quasi-steady frontal structures in different environments. The results resemble many observed features, such as the stronger temperature and moisture gradients in the midlatitude fronts and the stronger horizontal shear and LLJ in the subtropical fronts. The LLJ is most conspicuous in the subtropical simulation when high humidity and surface fluxes are included. The results further suggest that the LLJ is developed through the Coriolis torque that is exerted by the low-level poleward branch of a "reversed Hadley cell" equatorward of the front. This thermally direct cell is different from the normal cross-frontal secondary circulation. Its development depends on the occurrence of intense convection.

Reprinted from *JOURNAL OF THE ATMOSPHERIC SCIENCES*, Vol. 43, No. 9, 1 May 1986  
American Meteorological Society

**Generation of Internal- and External-Mode Motions from Internal Heating:  
Effects of Vertical Shear and Damping**

H. LIM AND C.-P. CHANG

## Generation of Internal- and External-Mode Motions from Internal Heating: Effects of Vertical Shear and Damping

H. LIM\* AND C.-P. CHANG

*Department of Meteorology, Naval Postgraduate School, Monterey, CA 93943*

(Manuscript received 5 February 1985, in final form 15 December 1985)

### ABSTRACT

Tropical heating due to latent heat release has been proposed as a source that may influence midlatitude weather through teleconnection patterns. However, such heating is usually internal (with the maximum in the midtroposphere) and, by itself, inefficient in exciting external, barotropic-type responses, which are necessary for the teleconnection mechanism. To study this problem, a simple two-level model is used to investigate the effects of vertical shear, differential damping and the planetary boundary layer on the characteristics of the atmospheric response to internal heating.

All three effects are found to enable a transfer of energy from the internal-mode motions, which are directly forced by the internal heating, to external-mode motions. To generate external-mode divergent motions, it is necessary to have a planetary boundary layer or other equivalent effects that force vertical motion at the bottom of the atmosphere. The efficiency of generation increases with the horizontal scale. On the other hand, vertical shear is normally the main effect for generating external-mode rotational motions, and the efficiency of generation decreases with the horizontal scale. In addition, this efficiency depends strongly on the *relative* vertical shear (vertical shear divided by vertical-mean wind). When the relative vertical shear is greater than unity, the external mode finally attains an amplitude larger than that of the internal mode.

The solution of an initial-value problem shows that in tropical regions, the process of energy transfer from internal to external-mode motions takes about two weeks to complete. This rather slow rate of energy transfer to external-mode motions implies that in a given vertical wind shear, the responses to a transient heating lasting for only a few days will have stronger internal mode (more baroclinic) structure than those to a steady-state heating.

### 1. Introduction

Several numerical studies (e.g., Hoskins and Karoly, 1981; Webster, 1981, 1982) have modeled the tropical-midlatitude teleconnection patterns observed by Horel and Wallace (1981). In these models, purely internal (zero at top and bottom boundary and maximum in the middle level) heating in the tropics was used to force prominent external-mode Rossby wave responses whose influence covered a large latitudinal and longitudinal span. The predicted structure resembles the observed teleconnection patterns. However, Lim and Chang (1983) pointed out that in the absence of other factors, it is very difficult for internal heating to excite directly external mode responses. A similar conclusion was also implied in the theoretical analyses of Chang (1976) and Kasahara (1984) who both found rather small external responses to internal heating. Thus the interpretation of the aforementioned numerical studies may need to be reexamined.

Based on physical arguments, Lim and Chang (1983) further pointed out that vertical mean wind shear, surface boundary layer effects or differential damping in the vertical, some or all are present in the various numerical models, may be the main reason for the excitation of the external Rossby responses in these models. The purpose of this paper is to check these physical arguments by carrying out an analysis of the effects of the above factors using a simple two-level model. In section 2, Lim and Chang's (1983) point on the relationship between internal heating and the external mode response will be reviewed and illustrated with a 20-level calculation. In section 3 the two-level model equations will be presented and analyzed to offer some insight on the transfer of energy first from the heat source to the internal mode and then to the external mode. In section 4 an initial-value problem of the model response to switch-on heating is solved. From the solutions for the adjustment phase, a time scale for the transfer of energy to the external mode is obtained in section 5, where the implications of this time scale for the establishment process of the teleconnection patterns observed by Horel and Wallace (1981) are also discussed. The conclusions are given in section 6.

\* Permanent address: National University of Singapore, Republic of Singapore.

**2. Vertical structure of atmospheric response to internal heating**

In an atmospheric model with a constant mean wind and a constant damping coefficient, motion may be resolved into vertical eigenmodes (Matsuno, 1966). Lim and Chang (1983) showed that in such an atmosphere, the characteristics of the response to heating depend very strongly on the equivalent depth of the vertical mode excited. The external mode and deep internal modes with the free gravity-wave speed larger than  $120 \text{ m s}^{-1}$  give rise to "barotropic" responses, while shallow internal modes with the free gravity-wave speed between  $30$  and  $50 \text{ m s}^{-1}$  give rise to "baroclinic" responses.

They further pointed out that, from the vertical eigenmode point of view, an internal heating is expected to excite essentially only baroclinic motions. This is because the amplitude,  $A$ , of a vertical mode with profile  $V(p)$  excited by a heat source  $Q(p)$  is determined by

$$A = - \int_0^{p_0} V(p) \frac{\partial}{\partial p} \left[ \frac{RQ(p)}{c_p p \sigma} \right] dp,$$

where  $R$ ,  $c_p$ ,  $\sigma$ ,  $p_0$  are the gas constant, specific heat at constant pressure, static stability parameter, and surface pressure, respectively. For the external mode and deep internal modes,  $V(p)$  is nearly constant in the troposphere. If  $Q(p)$  is negligible above the troposphere, the amplitude is given approximately by

$$A \approx - \left[ V(p) \frac{RQ(p)}{c_p p \sigma} \right]_0^{p_0} = - V(p_0) \frac{R}{c_p p_0 \sigma(p_0)} Q(p_0).$$

Therefore if there is no surface heating, i.e.,  $Q(p_0) = 0$ , the excitation of these large equivalent depth modes is negligible.

To further illustrate this point, we show in Fig. 1 the vertical structures of a deep internal mode which may be considered as a near-barotropic vertical eigenmode and a typical "baroclinic" vertical eigenmode computed using a 20-level model. Taking the equatorial tropopause to be at about 100 mb, the near-barotropic mode with  $c = 164.72 \text{ m s}^{-1}$  shows a nearly constant structure within the troposphere while the baroclinic mode with  $c = 45.12 \text{ m s}^{-1}$  shows a typical phase reversal at midtroposphere. Beside each of these eigenmodes, the special heating profile  $Q(p)$  that will excite only that particular mode is shown. It can be seen that the near-barotropic mode is forced mainly by stratospheric heating and is insensitive to tropospheric heating. A purely external barotropic mode, such as that found by Hoskins and Karoly (1981) and Webster (1981, 1982), would be even more insensitive to tropospheric heating. The baroclinic mode, on the other hand, is forced by a heating that has a prominent maximum near the midtroposphere. Therefore, the deep teleconnection patterns prominent in the numerical

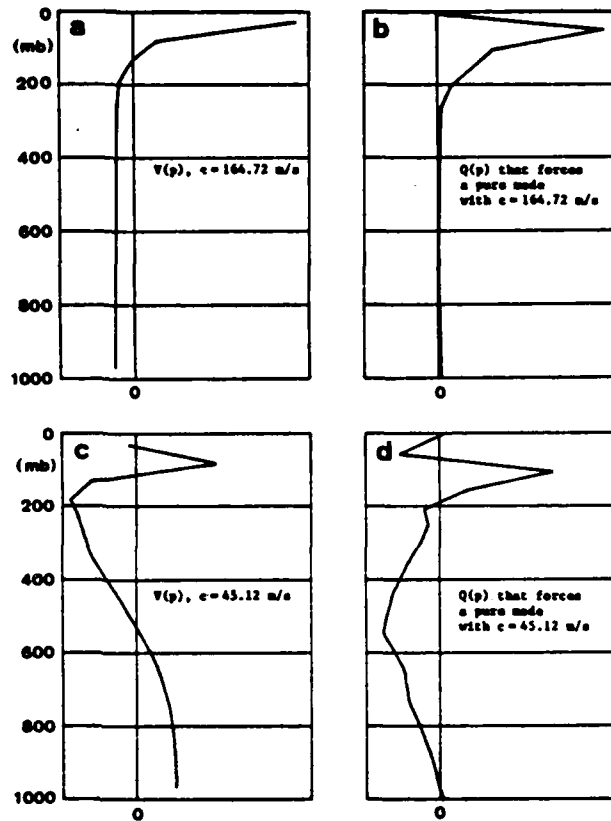


FIG. 1. (a) The vertical structure,  $V(p)$ , of a near-barotropic deep internal mode with the free gravity-wave speed  $c = 164.72 \text{ m s}^{-1}$ . (b) The special heating profile,  $Q(p)$ , that excites only the vertical eigenmode shown in (a). (c) and (d) Same as in (a) and (b), respectively, except that they are for a typical baroclinic shallow internal mode with  $c = 45.12 \text{ m s}^{-1}$ .

models cannot be considered to be directly forced by the prescribed internal heating. Other factors must be present to transfer energy from the more efficiently excited internal, baroclinic modes to the barotropic modes.

**3. Model and equations**

The model for our study is a simple two-level model (Fig. 2) with the zonal velocity  $u$ , meridional velocity  $v$ , and geopotential height  $\phi$  specified at 250 and 750 mb, respectively, and the vertical pressure velocity  $\omega$  specified at 500 and 1000 mb. At the top of the atmosphere ( $p = 0$ ),  $\omega$  is always zero. At 1000 mb,  $\omega$  is assumed to be forced by Ekman pumping in the planetary boundary layer. All variables are assumed to be functions of  $x$  and  $t$  only, so that all  $u$ -velocities are associated with divergent motions and all  $v$ -velocities with rotational motions.

The equations describing the motions are

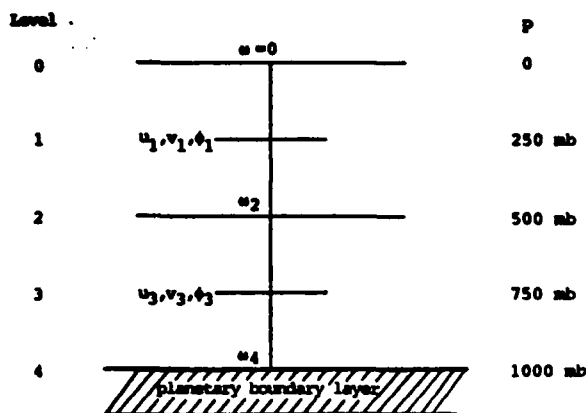


FIG. 2. Structure of the simple two-level model used in this study.

$$\frac{\partial u_1}{\partial t} + U_1 \frac{\partial u_1}{\partial x} + \omega_1 \frac{U_3 - U_1}{\Delta p} = f v_1 - \frac{\partial \phi_1}{\partial x} - D_1 u_1,$$

$$\frac{\partial u_3}{\partial t} + U_3 \frac{\partial u_3}{\partial x} + \omega_3 \frac{U_3 - U_1}{\Delta p} = f v_3 - \frac{\partial \phi_3}{\partial x} - D_3 u_3,$$

$$\frac{\partial v_1}{\partial t} + U_1 \frac{\partial v_1}{\partial x} = -f u_1 - D_1 v_1,$$

$$\frac{\partial v_3}{\partial t} + U_3 \frac{\partial v_3}{\partial x} = -f u_3 - D_3 v_3,$$

$$\frac{\partial}{\partial t} \phi_- + U_2 \frac{\partial}{\partial x} \phi_- + \kappa \phi_- - f(U_3 - U_1) \times \left( \frac{v_3 + v_1}{2} \right) + \Delta p \sigma_2 \omega_2 = - \frac{R \Delta p}{c_p p_2} Q_2,$$

$$\frac{\partial u_1}{\partial x} + \frac{\omega_2}{\Delta p} = 0, \quad \frac{\partial u_3}{\partial x} + \frac{\omega_4 - \omega_2}{\Delta p} = 0,$$

$$\omega_4 = -\rho_0 g \left( \frac{\nu}{2f} \right)^{1/2} \frac{\partial v_3}{\partial x} = -\alpha \Delta p \frac{\partial v_3}{\partial x}$$

$$\omega_1 = \frac{1}{8} (6\omega_2 - \omega_4), \quad \omega_3 = \frac{3}{8} (\omega_4 + 2\omega_2),$$

$$U_2 = \frac{1}{2} (U_3 + U_1)$$

(1)

Here subscripts 1, 2, 3, 4 denote values at 250, 500, 750 and 1000 mb, respectively;  $D_1, D_3$  and  $\nu$  are the linear frictional coefficients at levels 1 and 3 and within the surface boundary layer;  $\kappa$  is the Newtonian cooling constant;  $f, g, \rho_0$ , and  $\sigma_2$  are the Coriolis parameter, gravitational acceleration, density of air in the surface boundary layer, and the static stability parameter, respectively. The mean zonal wind  $U$  is assumed to vary linearly with  $p$ . The values  $\omega_1, \omega_3$  are determined from  $\omega_2, \omega_4$  assuming that  $\omega$  is a quadratic function of  $p$ .

In the simple case of no mean-wind shear ( $U_1 = U_3$ ), equal damping coefficients ( $D_1 = D_3 = \kappa$ ), and rigid-lid lower boundary condition ( $\omega_4 = 0$ ), the model equations may be separated into two vertical modes:

- (i) an external mode with free gravity-wave speed  $c \rightarrow \infty$  and flow variables  $u_+ = u_3 + v_1, \phi_+ = \phi_3 + \phi_1$ ;
- (ii) an internal mode with  $c \approx 65 \text{ m s}^{-1}$  and flow variables  $u_- = u_3 - u_1, v_- = v_3 - v_1, \phi_- = \phi_3 - \phi_1$ .

In the presence of a mean wind shear, differential damping, or surface boundary layer, Eq. (1) is no longer separable and, strictly speaking, the external mode and the internal mode no longer exist as eigenmodes. However, the concept of vertical eigenmode is still very useful for a physical understanding of the mathematical solutions and for interpretation of observed atmospheric motion. This is demonstrated by the success of the normal mode initialization techniques used in numerical weather prediction. We may also draw an analogy from the common linear studies where advection terms such as  $u \partial u / \partial x$  are neglected. All the free-wave modes of such linear analyses become similarly nonexistent as soon as the advection terms are restored. However, except in some fully nonlinear motions such as solitons and hydraulic jumps, the concept of linear free-wave modes remains useful in the analysis and description of motions. The nonlinear effect of the advection terms may be regarded as interaction mechanisms through which the linear wave modes exchange energy. In this study, we shall use the concept of vertical eigenmodes in a similar manner and regard wind shear, differential damping, etc., as effects through which vertical eigenmodes exchange energy.

Therefore, in terms of the external- and internal-mode flow variables, (1) may be rewritten as two groups of equations. The first group, which describes the changes of the external mode, is

$$\left. \begin{aligned} \left( \frac{\partial}{\partial t} + u_2 \frac{\partial}{\partial x} + D_2 \right) u_+ - f v_+ + \frac{\partial \phi_+}{\partial x} &= - \frac{1}{2} \\ \times \left( \Delta U \frac{\partial}{\partial x} + \Delta D \right) u_- - \frac{3}{2} \frac{\Delta U}{\Delta p} \omega_2 - \frac{1}{4} \frac{\Delta U}{\Delta p} \omega_4 \\ \left( \frac{\partial}{\partial t} + U_2 \frac{\partial}{\partial x} + D_2 \right) v_+ + f u_+ & \\ &= - \frac{1}{2} \left( \Delta U \frac{\partial}{\partial x} + \Delta D \right) v_- \\ \frac{\partial u_+}{\partial x} &= - \frac{\omega_4}{\Delta p} \end{aligned} \right\} \quad (2a)$$

The second group, which describes the change of the internal mode, is

$$\begin{aligned}
 & \left( \frac{\partial}{\partial t} + U_2 \frac{\partial}{\partial x} + D_2 \right) u_- - f v_- + \frac{\partial \phi_-}{\partial x} \\
 & \quad = \frac{1}{2} \left( \Delta U \frac{\partial}{\partial x} + \Delta D \right) u_+ - \frac{1}{2} \frac{\Delta U}{\Delta p} \omega_4 \\
 & \left( \frac{\partial}{\partial t} + U_2 \frac{\partial}{\partial x} + D_2 \right) v_- + f u_- \\
 & \quad = - \frac{1}{2} \left( \Delta U \frac{\partial}{\partial x} + \Delta D \right) v_+ \\
 & \left( \frac{\partial}{\partial t} + U_2 \frac{\partial}{\partial x} + \kappa \right) \phi_- + \Delta p \sigma_2 \omega_2 \\
 & \quad = f \frac{\Delta U}{2} v_+ - \frac{R \Delta p}{c_p P_2} Q_2 \\
 & \frac{\partial u_-}{\partial x} - \frac{2 \omega_2}{\Delta p} = - \frac{\omega_4}{\Delta p}
 \end{aligned} \tag{2b}$$

In both (2a) and (2b),

$$\begin{aligned}
 U_2 &= (U_3 + U_1)/2, & \Delta U &= U_3 - U_1, \\
 D_2 &= (D_3 + D_1)/2, & \Delta D &= D_3 - D_1.
 \end{aligned}$$

When mean wind shear, differential damping, and surface forcing are absent (i.e.,  $\Delta U = 0$ ,  $\Delta D = 0$ ,  $\omega_4 = 0$ ), (2a) and (2b) become decoupled. An internal heating represented by  $Q_2$  clearly can only force a response in the internal mode. On the other hand, (2a) shows that if any of these effects is present, an external mode response is excited. The external mode response may be excited directly by surface forcing ( $\omega_4$ ) or may gain energy from the internal mode through wind shear or differential-damping effects. The complete path of energy flow from the heat source to the external mode may be summarized in Fig. 3.

Beginning from  $Q_2$  in Fig. 3 the heating of an atmospheric column at its midlevel increases its thickness,  $\phi_-$ , which in turn leads to a divergent flow at the

upper level and a convergent flow at the lower level. This internal-mode divergent flow shows up in  $u_-$  and  $\omega_2$ . The  $u_-$  flow gives rise to a stretching of the lower atmospheric column and a compression of the upper atmospheric column. Conservation of potential vorticity implies that an internal-mode rotational flow ( $v_-$ ) is generated. At the same time, the vorticity field of this internal-mode rotational flow induces a vertical motion ( $\omega_4$ ) at the top of the planetary boundary layer through the Ekman pumping effect.

The external-mode divergent flow ( $u_+$ ) obtains energy from the internal-mode divergent flow through the action of wind shear and differential damping effects. It is also directly forced by the lower-boundary vertical motion ( $\omega_4$ ). The external-mode rotational flow ( $v_+$ ) finally receives energy from the internal-mode rotational flow through the action of wind shear and differential damping effects and also from the external-mode divergent flow through the stretching effect. An analogy of the last step may be drawn from the familiar two-level quasi-geostrophic model where advection of the internal baroclinic vorticity by the mean thermal wind will cause a change of the barotropic component of the vorticity.

#### 4. Solutions for a switch-on heating function

We shall specify a switch-on heating function as follows:

$$Q_2(x, t) = \begin{cases} Q(x)[1 - e^{-t/\tau}], & \text{for } t \geq 0 \\ 0, & \text{for } t < 0 \end{cases}$$

and obtain solutions for (1) with the atmosphere starting from an initial state of no perturbation.

Carrying out a Laplace transformation with respect to  $t$ :

$$(\bar{\quad}) = \int_0^\infty e^{-st} (\quad) dt,$$

and considering only one wave component  $e^{-ikx}$ , (1) is reduced to

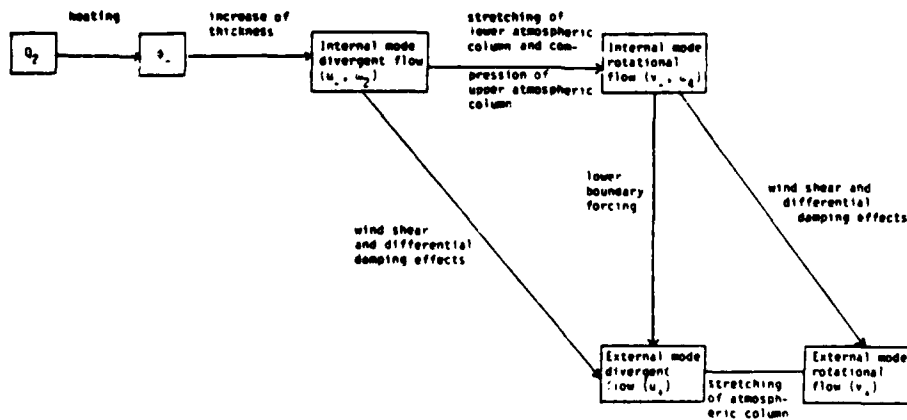


FIG. 3. Schematic diagram of the transfer of energy from heating to internal mode to external mode.

$$\begin{pmatrix} s - ikU_3 + D_3 + \frac{f\alpha}{2} & \frac{f\alpha}{2} & 0 & 0 \\ \frac{\Delta D}{2} - \frac{f}{\alpha} & s - ikU_2 + D_2 & f & -ik \\ \frac{f}{2} & -\frac{f}{2} & s - ikU_1 + D_1 & 0 \\ ik \frac{\Delta p^2 \sigma_2}{2} - \frac{f\Delta U}{2\alpha} & \frac{-ik\Delta p^2 \sigma_2}{2} & \frac{-f\Delta U}{2} & s - ikU_2 + \kappa \end{pmatrix} \begin{pmatrix} \tilde{u}_+ \\ \tilde{u}_- \\ \tilde{v}_1 \\ \tilde{\phi}_- \end{pmatrix} = \begin{pmatrix} 0 \\ 0 \\ 0 \\ \frac{R\Delta p}{c_p p_2} \frac{Q(k)}{s(1+s\tau)} \end{pmatrix}, \quad (3)$$

with

$$\tilde{v}_3 = \frac{\tilde{u}_+}{\alpha}, \quad \tilde{\omega}_2 = ik\Delta p(\tilde{u}_+ - \tilde{u}_-), \quad \tilde{\omega}_4 = ik\Delta p\tilde{u}_+,$$

$$Q(x) = \int_{-\infty}^{+\infty} Q(k)e^{-ikx}dk.$$

After solving the linear equation (3) for expressions of  $\tilde{u}_+$ , etc., and carrying out the inverse Laplace transforms, we obtain the following solutions:

$$u_+(k) = \frac{R\Delta p}{c_p p_2} \frac{Q(k)}{\tau} \frac{ikf\alpha}{2} \left\{ \frac{(-ikU_1 + D_1)\tau}{\prod_{j=1}^4 s_j} + \frac{(1 + ikU_1\tau - D_1\tau)e^{-U_1\tau}}{\prod_{j=1}^4 \left(\frac{1}{\tau} + s_j\right)} + \sum_{j=1}^4 \frac{(s_j - ikU_1 + D_1)e^{s_j\tau}}{s_j \left(s_j + \frac{1}{\tau}\right) \prod_{l=1, l \neq j}^4 (s_j - s_l)} \right\}, \quad (4a)$$

$$u_-(k) = -\frac{R\Delta p}{c_p p_2} \frac{Q(k)}{\tau} ik \left\{ \frac{\left(-ikU_3 + D_3 + \frac{f\alpha}{2}\right)(-ikU_1 + D_1)\tau}{\prod_{j=1}^4 s_j} + \frac{(1 + ikU_1\tau - D_1\tau)\left(-\frac{1}{\tau} ikU_3 + D_3 + \frac{f\alpha}{2}\right)}{\prod_{j=1}^4 \left(\frac{1}{\tau} + s_j\right)} e^{-U_1\tau} + \sum_{j=1}^4 \frac{\left(s_j - ikU_3 + D_3 + \frac{f\alpha}{2}\right)(s_j - ikU_1 + D_1)e^{s_j\tau}}{s_j \left(s_j + \frac{1}{\tau}\right) \prod_{l=1, l \neq j}^4 (s_j - s_l)} \right\}, \quad (4b)$$

$$v_+(k) = \frac{R\Delta p}{c_p p_2} \frac{Q(k)}{\tau} \frac{ikf}{2} (ik\Delta U - \Delta D - f\alpha) \left\{ \frac{\tau}{\prod_{j=1}^4 s_j} - \frac{\tau e^{-U_1\tau}}{\prod_{j=1}^4 \left(\frac{1}{\tau} + s_j\right)} + \sum_{j=1}^4 \frac{e^{s_j\tau}}{s_j \left(s_j + \frac{1}{\tau}\right) \prod_{l=1, l \neq j}^4 (s_j - s_l)} \right\}, \quad (4c)$$

$$v_-(k) = -\frac{R\Delta p}{c_p p_2} \frac{Q(k)}{\tau} ikf \left\{ \frac{\left(-ikU_2 + D_2 + \frac{f\alpha}{2}\right)\tau}{\prod_{j=1}^4 s_j} + \frac{\left(1 + ikU_2\tau - D_2\tau - \frac{f\alpha}{2}\tau\right)e^{-U_2\tau}}{\prod_{j=1}^4 \left(\frac{1}{\tau} + s_j\right)} + \sum_{j=1}^4 \frac{\left(s_j - ikU_2 + D_2 + \frac{f\alpha}{2}\right)e^{s_j\tau}}{s_j \left(s_j + \frac{1}{\tau}\right) \prod_{l=1, l \neq j}^4 (s_j - s_l)} \right\}, \quad (4d)$$

where  $s_j$ ,  $j = 1, 2, 3, 4$ , are the roots of the equation obtained by setting the determinant of the coefficient matrix of (3) equal to zero. The solutions (4a-d) consist of terms representing steady-state responses, transient responses ( $e^{-st}$  terms), and wave responses ( $e^{st}$  terms). In general,  $s_j$  are complex. Most wave responses have  $\text{Re}(s_j) < 0$  and the wave amplitudes are damped with time. However, when the vertical wind shear is strong enough, there also exist wave responses with  $\text{Re}(s_j) > 0$ . These represent the unstable baroclinic waves observed in the midlatitudes.

Consistent with our discussion of energy transfer mechanisms based on (2a) and (2b), solution (4) shows that while the internal mode components  $u_-$  and  $v_-$  depend on mean flow parameters such as  $U_1$ ,  $U_2$  and  $U_3$ , the external mode components  $u_+$  and  $v_+$  contain factors  $f\alpha$  and  $(ik\Delta U - \Delta D - f\alpha)$ , respectively. The magnitude of the external mode therefore increases approximately linearly with the mean-wind shear, the boundary layer Ekman-pumping effect, and the differential damping between the vertical levels. This conclusion is valid irrespective of the existence of unstable baroclinic wave responses.

In the tropical region, no unstable baroclinic wave response exists for moderate values of wind shear. After sufficiently long time, the solutions converge to a steady-state response. The amplitude of the external and the internal mode velocity components of the steady-state response are in the following proportions:

$$u_+ : u_- = \frac{f\alpha}{2} \left( ikU_3 - D_3 - \frac{f\alpha}{2} \right), \quad (5a)$$

$$v_+ : v_- = (ik\Delta U - \Delta D - f\alpha) : (ikU_2 + D_2 + f\alpha). \quad (5b)$$

Equation (5a) shows that when there is no lower boundary layer (i.e.,  $\alpha = 0$ ),  $u_+$  vanishes. Since  $u$  is the divergent flow component, we see that excitation of the external-mode divergent flow requires some mechanism to force vertical motion at the lower boundary of the atmosphere. Unless the low-level mean wind,  $U_3$ , is very weak, there is also a scale dependence with the excitation of the long-wave divergent motion being more efficient. On the other hand, (5b) shows that the external-mode rotational flow component  $v_+$  is always excited when a wind shear, differential damping, or a lower boundary layer is present. Of the three effects, we may expect  $\Delta D$  to be normally very small, and a calculation will readily show that, except for very long planetary-scale waves, the wind shear effect dominates over the boundary layer effect. As a consequence, for the external-mode rotational motions, shorter waves are more efficiently generated. This scale dependence is more prominent as the vertically averaged mean wind,  $U_2$ , becomes smaller. In such a case the excitation is in general more efficient, with the shorter-scale waves converting almost all of their heat-generated energy into external modes. For a stronger  $U_2$ ,  $v_+ : v_- \sim \Delta U /$

$U_2$ , which means the excitation efficiency is determined almost entirely by the relative wind shear ( $\Delta U / U_2$ ) with very little scale dependence. These results can clearly be seen in Figs. 4 and 5. Figure 4 shows the magnitude of the ratio of  $v_+ : v_-$  as a function of  $U_2$  and zonal wavenumber, with  $\Delta D = 0$ ,  $D_2 = 1.16 \times 10^{-6} \text{ s}^{-1}$ ,  $\rho_0 = 1.17 \text{ kg m}^{-3}$ ,  $U = 5 \text{ m}^2 \text{ s}^{-1}$  (these values show that the  $f\alpha$  terms are basically inconsequential in generating the external-mode rotational motions), for  $\Delta U = 5 \text{ m s}^{-1}$ . Figure 5 shows the same magnitude as a function of  $U_2$  and  $\Delta U$  for zonal wavenumber six. Here it can be seen that the line of  $v_+ / v_- = 1$  is very close to the line of  $\Delta U / U_2 = 1$ , so that, to a first order approximation, excitation of the external-mode rotational motions exceeds that of the internal-mode rotational motions if  $\Delta U > U_2$ .

Equation (5b) also indicates that  $v_+$  and  $v_-$  will be more in phase when  $U_2$  is large, especially for shorter waves. This means the upper-level vorticity patterns of the two modes will be in phase. On the other hand, when  $U_2$  is small and especially for planetary-scale waves, the external-mode rotational flow will be closer to  $90^\circ$  out of phase from the internal-mode rotational flow. The phase relationship between  $v_+$  and  $v_-$  for the same parameter values as those used in Fig. 4 is shown in Fig. 6. Since in the tropical Pacific during northern winter the typical mean wind is weak westerly in the upper troposphere and weak easterly in the lower troposphere (i.e.,  $\Delta U < 0$ ,  $U_2 \sim 0$ ), we may expect a large-scale heat source to excite an external-mode response with its vorticity field shifted westward by about a  $45^\circ$ - $90^\circ$  phase difference from that of the internal mode response.

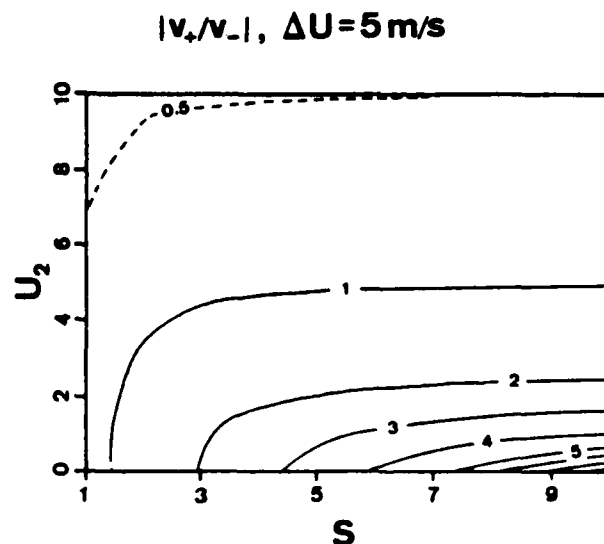


FIG. 4. Magnitude of the ratio of external-mode rotational velocity,  $v_+$ , and the internal-mode rotational velocity,  $v_-$ , as a function of the vertical-mean wind  $U_2$ , and zonal wavenumber  $S$ .  $S = ak$  where  $a$  is the radius of the earth. The vertical shear ( $\Delta U$ ) is  $5 \text{ m s}^{-1}$ .

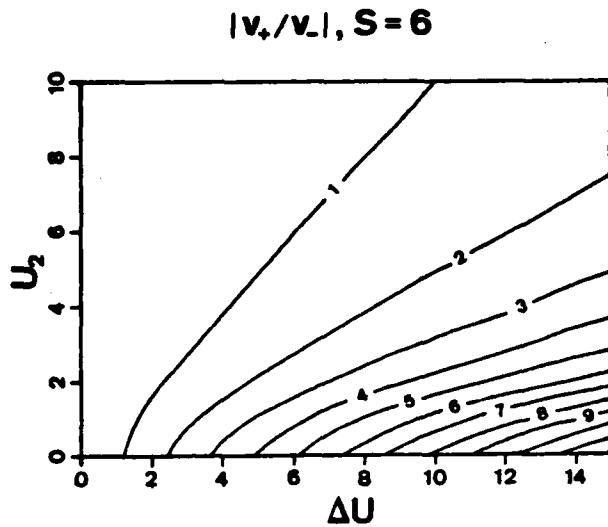


FIG. 5. As in Fig. 4 except as a function of  $U_2$  and  $\Delta U$  for zonal wavenumber  $S = 6$ .

5. Transfer of energy from the internal mode to the external mode

In this section some specific examples of solutions (4a-d) are evaluated to highlight the process of energy transfer between the vertical eigenmodes. While mid-latitude atmospheric motions are dominated by baroclinic processes, the response to latent heat forcing appears to give an adequate account for many important tropical flow patterns. We shall therefore adopt for our calculations the following parameter values which are appropriate for tropical regions:

$$\begin{aligned}
 f &= 2.5 \times 10^{-5} \text{ s}^{-1}, \\
 \sigma_2 &= 2.78 \times 10^{-6} \text{ kg}^{-2} \text{ m}^4 \text{ s}^2, \\
 \nu &= 5 \text{ m}^2 \text{ sm}^{-1}, \\
 \rho_0 &= 1.17 \text{ kg m}^{-3}, \\
 g &= 9.8 \text{ m s}^{-2}, \\
 D_1 = D_3 = \kappa &= 1.16 \times 10^{-6} \text{ s}^{-1} \text{ (i.e., } 1/10 \text{ day}^{-1}).
 \end{aligned}$$

The heating function  $Q(x)$  is chosen to have a Gaussian profile with a half-width equal to  $2.5^\circ$  latitude. The  $e$ -folding time scale  $\tau$  is specified to be one day.

To highlight the energy transfer between the vertical eigenmodes, we split the total kinetic energy  $E_t$  into two parts,  $E_x$  due to the external mode motion and  $E_i$  due to the internal mode motion:

$$\begin{aligned}
 E_t &= \int_0^L \frac{1}{2} (u_1^2 + v_1^2 + u_3^2 + v_3^2) dx, \\
 &= \int_0^L \frac{1}{4} (u_+^2 + v_+^2) dx + \int_0^L \frac{1}{4} (u_-^2 + v_-^2) dx, \\
 &= E_x + E_i.
 \end{aligned}$$

the  $x$ -domain being taken to be cyclic with a cycle length  $L$  equal to the circumference of the earth.

Figure 7 shows the evolution of the ratio  $E_x/E_t$  for two mean-flow structures: (a) a westerly  $U_1$  overlies an easterly  $U_3$  with  $U_1 = -3U_3$  and (b) an easterly  $U_1$  and  $U_3$  with  $U_1 = 3U_3$ . The (a) cases are more typical of the vertical wind shear during northern winter when teleconnection patterns are often observed. The rise of the heating function is shown in (c). The three curves in each of (a) and (b) are for values of  $\Delta U = 20, 10,$  and  $5 \text{ m s}^{-1}$ , respectively.

We note that  $E_x/E_t$  rises gradually from zero, indicating negligible external mode motions just after the heating is switched on. The curves for the two smaller values of  $\Delta U$  show that  $E_x/E_t$  has a growth time scale of about one week during the near-exponential increase period, and takes about two weeks to reach its steady-state value.

The curves for  $\Delta U = 20 \text{ m s}^{-1}$  show signs of baroclinic instability. In (b), a sinusoidal variation becomes prominent after about day 15. In (a), the instability is mild and is detectable only in a slight steepening of the curve after Day 24. Notwithstanding baroclinic instability, the  $E_x/E_t$  curves exhibit a growth similar to those of smaller  $U$  for the period before the baroclinic waves develop to large amplitude.

This result supports our physical argument that internal heating directly forces mainly internal-mode motions. The presence of wind shear, differential damping, or lower boundary layer then enables a transfer of the internal mode energy to the external mode. Even though the heating is switched on with a time scale of one day, the process of completing the energy transfer from the internal mode to the external mode has a much longer time scale of about two weeks. This means that for short transient forcings that last

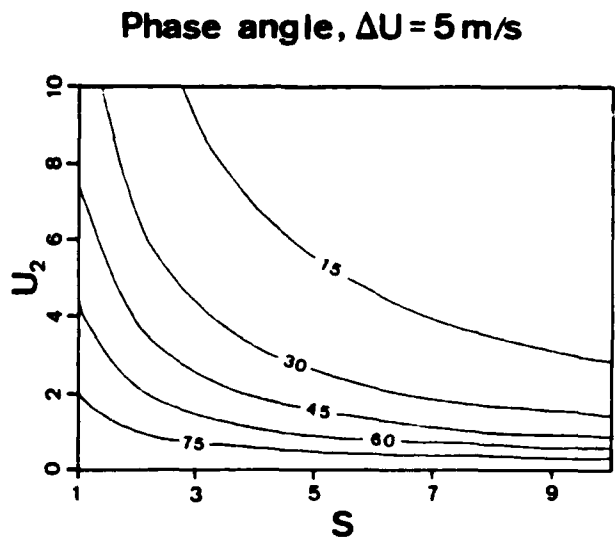


FIG. 6. As in Fig. 4 except for the phase difference (degree) between  $v_+$  and  $v_-$ . Positive values indicate  $v_+$  is shifted to the west of  $v_-$ .

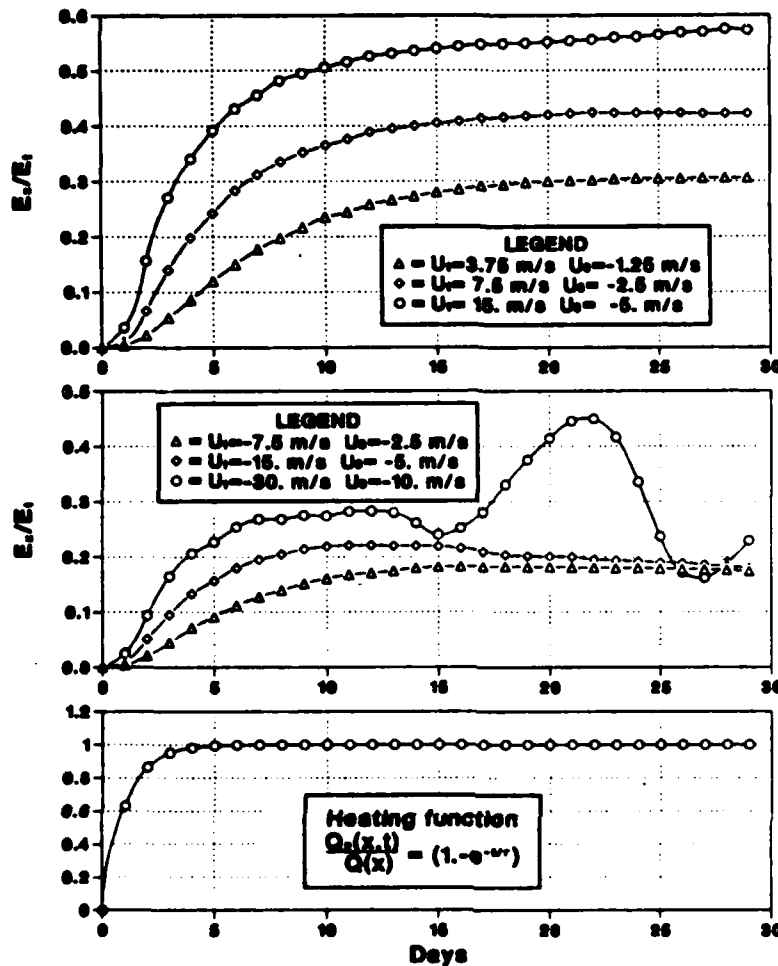


FIG. 7. The evolution of the ratio of the external-mode kinetic energy,  $E_e$ , to the total kinetic energy,  $E_t$ , of the atmospheric response to a switch-on internal heating function,  $Qz$ .

for, say, less than three days, the wind shear, differential damping, and lower boundary layer effects are rather ineffective in forcing the external mode. Atmospheric response to transient forcings may therefore exhibit even stronger internal-mode characteristics (i.e., baroclinic in structure) than one would infer from a knowledge of the mean winds alone.

## 6. Discussion and conclusions

Our analysis of the response of a simple two-level model to an internal heating allows us to draw the following conclusions:

1) Internal heating directly forces mainly internal-mode (baroclinic) motions. Vertical shear in the mean wind, differential damping between the vertical levels, and Ekman pumping in the planetary boundary layer serve as mechanisms through which the energy of internal-mode motions is transferred to external-mode (barotropic) motions. This conclusion is in agreement with Lim and Chang (1983).

2) To force external-mode divergent flow, it is necessary to have a mechanism to force a vertical motion at the lower boundary of the atmosphere. This mechanism was provided by Ekman pumping in our analysis. However, Lim and Chang (1983) showed by vertical eigenmode argument that surface heating may be just as effective.

3) External-mode rotational motions are generated when vertical wind shear, differential damping, or lower boundary layer is present. Of the three effects, we may expect the differential damping to be negligible ( $\Delta D \approx 0$ ) under normal circumstances. In the tropics, the boundary-layer effect is also small compared with the wind shear effect except for very long wavelength (wavenumber one or two) responses. We may therefore state that external-mode rotational motions are mainly generated through the vertical wind shear effect. The physical mechanism involved is essentially the differential vorticity advection effect discussed in Lim and Chang (1983).

4) The efficiency of generating the external-mode responses increases with horizontal wavelength for divergent motions and decreases with horizontal wavelength for rotational motions.

5) For rotational motions this efficiency also depends strongly on the relative vertical shear. For most relevant parameter ranges, the response amplitudes of the two modes are about equal if  $\Delta U/U = 1$ , and the external-mode amplitude becomes larger if  $\Delta U/U > 1$ . The two modes are nearly in phase for stronger mean winds and shorter waves, and nearly  $90^\circ$  out of phase for weaker mean winds and longer waves.

6) The process of energy transfer from internal-mode motions to external-mode motions has a growth time scale of about one week and takes about two weeks to reach a steady state.

Based on these conclusions, we may make some conjectures that may have important implications. First, we note that for transient heat sources that last for only a few days, the energy transfer mechanism may be ineffective. Responses to transient forcings may therefore be more baroclinic than one would infer from the vertical mean wind profile alone.

Second, this energy transfer time scale may also be an important factor in the establishment time scale of the teleconnection patterns observed by Horel and Wallace (1981). The establishment process of teleconnection patterns may be conceptually divided into two phases: a phase of energy transfer from internal-mode motions forced directly by heating to external-mode motions, followed by a phase of the propagation of the external-mode motions to higher latitudes. The latter phase proceeds with a typical meridional group velocity of about  $15 \text{ m s}^{-1}$  (Lau and Lim, 1984) and hence will take about five days. The total establishment time for the teleconnection patterns may therefore be expected to be about 20 days, most of the time being required to effect the transfer of energy from the internal mode to the external mode. For a winter season with a sea surface temperature (SST) anomaly forcing lasting two to three months, we may expect steady-state teleconnection patterns to develop and persist as a prominent feature of the atmospheric circulation. On the other hand, depending mainly on the vertical shear, if the forcing lasts for less than one month teleconnection patterns may make only a brief and relatively weak appearance.

Another possible implication of our results is in the area of medium-range numerical weather prediction. Parameterization of cumulus convection, especially in the tropics, has often been considered as an area of significant problems which may contribute to large errors in the forecast of midlatitude deep planetary-scale waves. Our results on the efficiency and the time scale of the generation of external-mode rotational motions suggest that the errors due to improper cumulus heating, which is basically internal, may be not as significant

and would depend on the relative vertical shear of the basic flow.

The above conclusions and conjectures are based on the results of a simple two-level model. Their applicability to multilevel numerical models and the real atmosphere needs to be further investigated.

For numerical models with a rigid-lid upper boundary, the conclusions may be expected to be qualitatively correct. As demonstrated by the success of the normal-mode initialization schemes in numerical weather prediction, motions in such models can be adequately represented in terms of vertical normal modes. Our arguments about the response amplitudes of the various modes remains valid and an internal heating will be much more efficient in directly forcing the internal modes than the external mode. Wind shear and other effects will again help to transfer energy from the internal modes to the external modes. However, the energy transfer rate and efficiency have to be recomputed. If no significant difference from the two-level model values is found, then our conclusions and conjectures will be applicable to such multilevel models.

The use of an  $f$ -plane rather than a  $\beta$ -plane or a global model does not affect our discussion of the vertical modes and energy transfer among them. This is due to the fact that the structures of the vertical modes depend only on the mean-state temperature profile and not at all on the geometry of the model. Our results give basically the partition of energy between the vertical modes in response to a tropical forcing, and the results are not expected to change qualitatively when the geometry of the model is changed. It is obvious that horizontal propagation of the response cannot be discussed in an  $f$ -plane model. However, in the context of linear models, we may still apply our results to a discussion of the qualitative characteristics of response on a globe by associating a correct relative amplitude with each of the corresponding global vertical modes.

For more "realistic" models of the atmosphere, the upper rigid-lid condition is replaced by a radiation condition. With the extension of the upper boundary to infinity, the internal modes merge into a continuous spectrum. However, this change in the mathematical representation would not by itself lead to a qualitative change in the structure of the response. The solution in the region of a synoptic scale forcing is still dominated by the particular integral which has a distinct baroclinic structure of the internal modes. Differences in the far field response may appear as some of the motion may now propagate upward instead of horizontally away from the forcing. The degree of the difference may be expected to depend on the ratio of the energy propagated upward to the total of the energy propagated horizontally and dissipated by damping effects. When this ratio is large, significant differences in the results of rigid-lid and radiation condition models may be expected. Whereas when this ratio is small, the differences may be expected to be insignificant. How-

ever, it is well known that in the presence of a vertical wind shear, vertical propagation is often severely restricted by the critical level effect. This implies that when the external mode response is expected to have a large amplitude, its horizontal propagation behavior is probably not seriously affected by the vertical propagation effect. This fortunate coincidence suggests that results obtained with rigid-lid models, which include practically all numerical-model studies of teleconnection patterns carried out so far, are probably applicable to the real atmosphere despite the lack of a mechanism for upward energy propagation. Nevertheless, this important issue requires a careful investigation which has yet to be carried out.

*Acknowledgments.* We wish to thank Professor R. T. Williams for reading the manuscript and for valuable discussion. This work was supported by the National Science Foundation, Global Atmospheric Research Program, under Grant ATM 8315175.

## REFERENCES

- Chang, C.-P., 1976: Forcing of stratospheric Kelvin waves by tropospheric heat sources. *J. Atmos. Sci.*, **33**, 740-744.
- Horel, J. D., and J. M. Wallace, 1981: Planetary-scale atmospheric phenomena associated with the Southern Oscillation. *Mon. Wea. Rev.*, **109**, 813-829.
- Hoskins, B. J., and D. Karoly, 1981: The steady linear response of a spherical atmosphere to thermal and orographic forcing. *J. Atmos. Sci.*, **38**, 1179-1196.
- Kasahara, A., 1984: The linear response of a stratified global atmosphere to tropical thermal forcing. *J. Atmos. Sci.*, **41**, 2217-2237.
- Lau, K.-M., and H. Lim, 1984: On the dynamics of equatorial forcing of climate teleconnections. *J. Atmos. Sci.*, **41**, 161-176.
- Lim, H., and C.-P. Chang, 1983: Dynamics of teleconnections and Walker circulations forced by equatorial heating. *J. Atmos. Sci.*, **40**, 1897-1915.
- Matsumo, T., 1966: Quasi-geostrophic motions in the equatorial area. *J. Meteor. Soc. Japan*, **44**, 25-43.
- Webster, P. J., 1981: Mechanisms determining the atmospheric response to sea surface temperature anomalies. *J. Atmos. Sci.*, **38**, 554-571.
- , 1982: Seasonality in the local and remote atmospheric response to sea surface temperature anomalies. *J. Atmos. Sci.*, **39**, 41-52.

Reprinted from JOURNAL OF THE ATMOSPHERIC SCIENCES, Vol. 43, No. 21, 1 November 1986  
American Meteorological Society

**Spatial Instability of the Barotropic Jet with Slow Streamwise Variation**

MELINDA S. PENG AND R. T. WILLIAMS

## Spatial Instability of the Barotropic Jet with Slow Streamwise Variation

MELINDA S. PENG AND R. T. WILLIAMS

*Department of Meteorology, Naval Postgraduate School, Monterey, CA 93943*

(Manuscript received 23 October 1985, in final form 8 May 1986)

### ABSTRACT

A two-scale expansion technique is used to study the barotropic instability of basic flows with slow streamwise variation. Disturbances in nonparallel flow possess properties that differ from those calculated from parallel flow theory. The difference, which is obtained at higher order in the parameter that measures the nonparallelism, depends on the first derivative of the parallel flow properties with respect to the streamwise direction. This higher order correction shifts the spatial growth rate profile for the nonparallel flow downstream relative to the spatial growth rate profile for parallel flow. These results are compared with a previous numerical study by Tupaz, Williams and Chang, and some of their conclusions are modified.

Physically, the difference in the spatial instability for parallel and nonparallel flow is subject to two combined effects. The first is the lag effect discussed by Tupaz et al., which causes the disturbance structure to lag the parallel-flow solution structure in regions where the mean flow changes rapidly downstream. This causes the downstream shifting of the nonparallel growth rate profile. The second is related to the phase speed difference between the parallel and nonparallel flows. If the disturbance propagates faster than predicted by the parallel flow theory, the local spatial growth rate will be smaller than that calculated by the parallel flow and vice versa.

### 1. Introduction

Barotropic and baroclinic instabilities that are characterized by horizontal shear and vertical shear, respectively, are the principal instabilities of large-scale atmospheric flows. Conventionally, the instability of a sheared flow is studied by assuming that the mean flow is uniform (parallel) in the streamwise direction. Yet, in reality the mean flows are frequently nonparallel. An example is the subtropical jet stream, which has much stronger baroclinic shear near Japan and much weaker shear to the west and east (Krishnamurti, 1961). It is common to predict the linear growth rate of the synoptic scale waves based on the temporal instability of the parallel flow without considering the influence of the streamwise variation. Therefore, the regions with strongest shear are expected to be the most unstable and to be the most favorable places for the disturbances to grow. However, if the disturbances propagate with a relatively fast speed, the local instability may not be achieved as the disturbances propagate through a spatially varying mean flow. Tupaz et al. (1978; hereafter referred to as TWC) and Williams et al. (1984) found the spatial-growth approach to be very attractive for the study of barotropic jets with streamwise variation. With this approach it is assumed that a train of waves of constant amplitude move into the region of interest from the upstream side. This is equivalent to having a periodic forcing on the upwind boundary as was employed by TWC. As the waves move into the region of interest they grow spatially in response to the stream-

wise changes in the mean flow. (Their time variation is periodic.) If the temporal instability approach is used, cyclic boundary conditions are required and a single temporal growth rate is obtained. In order to get the effects of streamwise mean flow variations, the streamwise variations in the eigensolution must be analyzed. With the spatial growth approach, variations in spatial growth rate can be directly related to variations in the mean flow. The amplifying modes have been regarded since the early 1960s as physically superior to unstable modes in describing the shear instabilities. For example, the eigenvalue problem solved for amplifying waves in a shear flow by Michalke (1965) gave better agreement with experimental observations. Later, this approach was successfully extended to strong nonlinear developments. A discussion of relevant literature can be found in Merkin (1977).

TWC used a numerical model to study the nonparallel linear barotropic instability. The basic flow was a Bickley jet that roughly simulates the easterly jet observed south of the Tibetan high near 200 mb during Northern Hemispheric summer. Two major results were obtained by them. First, it was found that the maximum spatial growth rate for nonparallel flow was about 25% larger than that calculated from the parallel flow theory. Second, the location of the maximum growth rate region was shifted downstream from where the parallel flow predicted the local maximum. This downstream shifting corresponds to the lag of the spatial structure of the disturbance in nonparallel flow that was discussed by TWC. The maximum of the wave-

packet is further shifted downstream of the maximum shear region where the spatial growth rate vanishes. In a similar numerical study for weakly nonparallel barotropic flow with a localized potential vorticity source, Merkin and Balgovind (1983) also observed the downstream shifting of the maximum wavepacket.

From observations, the variation of the basic flow in the streamwise direction is usually much slower than the variation in the cross current direction. This suggests that the variation of the basic flow can be separated into different scales in space so that an analytical formulation will be tractable. The purpose of the present study is to examine the effect of the downstream variation of a jet on its stability properties using a multiple-scale expansion technique. Benney and Rosenblat (1964) developed the procedure for the analytical formulation for the stability of spatially varying and time-dependent flows, and a similar approach was used by Drazin (1974) for several model studies. Their ideas and those of Nayfeh et al. (1974) and Saric and Nayfeh (1975) will be used in the present study.

The basic model is described in section 2, and the mathematical formulations for the multiple-scale expansion are developed in section 3. In section 4, the relationship between temporal and spatial growth rate is discussed and some of the conclusions from TWC are modified. The results are presented in section 5. Section 6 contains the concluding remarks.

2. The model

The model treats the barotropic instability of a zonal jet confined within a channel in the east-west direction. As in TWC, the nondivergent barotropic vorticity equation is used. In a linearized nondimensional form, this equation can be written as

$$\frac{\partial}{\partial t} \nabla^2 \psi' - \frac{\partial \bar{\psi}}{\partial y} \frac{\partial}{\partial x} \nabla^2 \psi' + \frac{\partial \bar{\psi}}{\partial x} \frac{\partial}{\partial y} \nabla^2 \psi' - \frac{\partial \psi'}{\partial y} \frac{\partial}{\partial x} \nabla^2 \bar{\psi} + \frac{\partial \psi'}{\partial x} \frac{\partial}{\partial y} \nabla^2 \bar{\psi} + \beta \frac{\partial \psi'}{\partial x} = -\lambda \nabla^2 \psi' \quad (2.1)$$

where  $\psi'$  and  $\bar{\psi}$  are the disturbance and basic state streamfunctions, respectively, and the nondivergent velocity components are

$$\left. \begin{aligned} u &= -\frac{\partial \psi'}{\partial y}, & v &= \frac{\partial \psi'}{\partial x} \\ \bar{u} &= -\frac{\partial \bar{\psi}}{\partial y}, & \bar{v} &= \frac{\partial \bar{\psi}}{\partial x} \end{aligned} \right\} \quad (2.2)$$

The north and south boundaries are placed at  $y = \pm Y$ , where the disturbance streamfunction  $\psi'$  vanishes, i.e.,

$$\psi' = 0, \quad y = \pm Y. \quad (2.3)$$

The following relate the nondimensional and dimensional (denoted by an asterisk) forms of the variables:

$$\left. \begin{aligned} x^* &= Dx \\ y^* &= Dy \\ U^* &= U_{\max} U \\ T^* &= \frac{D}{U_{\max}} t \\ \beta^* &= \frac{U_{\max}}{D^2} \beta \\ \lambda^* &= \frac{U_{\max}}{D} \lambda \\ \psi^* &= DU_{\max} \psi \end{aligned} \right\} \quad (2.4)$$

Since we are considering basic flow whose streamwise variation is slow compared to its variation in the cross-stream direction, a small parameter  $\epsilon$  is defined as the ratio between the characteristic length scale of the basic flow in the cross-stream ( $y$ ) direction,  $D$ , and the characteristic length scale in the streamwise ( $x$ ) direction,  $L$ :

$$\epsilon = \frac{D}{L} \ll 1. \quad (2.5)$$

This allows us to introduce a slow scale in the  $x$ -direction

$$x_1 = \epsilon x. \quad (2.6)$$

For a truly parallel flow,  $L \rightarrow \infty$  and  $\epsilon = 0$ . For the nonparallel flow, the basic flow is a function of  $x_1$  and  $y$ . The flow profile has the form of a Bickley jet, with  $\bar{U}$  and  $\bar{V}$  fields prescribed as

$$\bar{U}(x_1, y) = -\frac{\partial \bar{\psi}}{\partial y} = U(x_1) \operatorname{sech}^2\left(\frac{y}{d(x_1)}\right) + u_0, \quad (2.7)$$

$$\bar{V}(x_1, y) = \frac{\partial \bar{\psi}}{\partial x} = \epsilon \frac{\partial \bar{\psi}}{\partial x_1} \quad (2.8)$$

where  $d(x_1)$  is the half-width of the jet and  $U(x_1)$  is the maximum wind speed across the jet at a particular  $x_1$ . The basic flow has the same profile as in TWC, so the results can be compared. The streamwise variation of the basic flow arises from the following variations in  $U(x_1)$  and  $d(x_1)$ :

$$d(x_1) = 0.85 + 0.35 \cos(x_1 + \pi), \quad (2.9)$$

$$U(x_1) = \frac{0.5}{d(x_1)} \coth\left(\frac{2}{d(x_1)}\right). \quad (2.10)$$

The characteristic values chosen for  $U_{\max}$ ,  $D$ ,  $L$ ,  $\beta$  and  $\lambda$  are

$$\left. \begin{aligned} U_{\max} &= -30 \text{ m s}^{-1} \\ D &= 1000 \text{ km} \\ L &= 10\,000 \text{ km} \\ \epsilon &= 0.1 \\ \beta &= 2\Omega(\cos 10^\circ)/a \\ \lambda &= 0.15 \times 10^{-5} \text{ s}^{-1} \end{aligned} \right\} \quad (2.11)$$

where  $a$  is the radius of the earth and  $\Omega$  is the angular velocity of the earth's rotation. The nondimensional width of the channel is equal to  $2Y = 4$ , and the streamwise variation is considered within  $-2.0 < x_1 < 2.0$ . Equations (2.9) and (2.10) show that the variation of the basic flow is symmetric with respect to  $x_1 = 0$ . The north-south profiles of  $\bar{U}$  at several streamwise locations are given in Fig. 1.

3. Solution procedure

With the introduction of (2.5)–(2.8), the coefficients in (2.1) are independent of  $x$  and  $t$ ; the normal-mode solution, which has a significant growth rate, is of the form

$$\psi' = \phi(x_1, y)e^{\theta} \tag{3.1}$$

where  $\theta$  is the phase of the normal mode. The phase is related to the wavenumber  $k$  and frequency  $\omega$  by

$$\frac{\partial \theta}{\partial x} = k(x_1), \tag{3.2}$$

$$\frac{\partial \theta}{\partial t} = -\omega. \tag{3.3}$$

The dimensional wavenumber and frequency are

$$\left. \begin{aligned} k^* &= \frac{k}{D} \\ \omega^* &= \frac{U_{max}}{D} \omega \end{aligned} \right\} \tag{3.4}$$

Since we are studying the spatial growth rate under the

influence of slow streamwise variation of the basic flow, the frequency  $\omega$  is assumed to be a constant so that the temporal growth rate is excluded. This may be viewed as forcing a wave with a fixed period (frequency) at a certain  $x_1$  and allowing it to propagate downstream. The wavenumber  $k$  can be written, following the suggestion of Benney and Rosenblat (1964), as

$$k = \sum_{n=0}^{\infty} \epsilon^n k_n = k_0 + \epsilon k_1 + \epsilon^2 k_2 + \dots \tag{3.5}$$

and  $\phi$  can be expanded asymptotically as

$$\phi = \sum_{n=0}^{\infty} \epsilon^n \phi_n = \phi_0 + \epsilon \phi_1 + \epsilon^2 \phi_2 + \dots \tag{3.6}$$

In order to eliminate some difficulties in the mathematical formulation, the phase  $\theta$  is treated as an independent variable in place of  $x$ , as proposed by Nayfeh et al. (1974). The following relations, which hold to  $O(\epsilon)$  accuracy, can be derived with the chain rule:

$$\left. \begin{aligned} \frac{\partial}{\partial x} &\rightarrow k_0 \frac{\partial}{\partial \theta} + \epsilon \left( \frac{\partial}{\partial x_1} + k_1 \frac{\partial}{\partial \theta} \right) \\ \frac{\partial}{\partial t} &\rightarrow -\omega \frac{\partial}{\partial \theta} \\ \frac{\partial^2}{\partial x^2} &\rightarrow k_0^2 \frac{\partial^2}{\partial \theta^2} \\ &+ \epsilon \left( 2k_0 \frac{\partial^2}{\partial \theta \partial x_1} + 2k_0 k_1 \frac{\partial^2}{\partial \theta^2} + \frac{k_0}{\partial x_1} \frac{\partial^2}{\partial \theta} \right) \end{aligned} \right\} \tag{3.7}$$

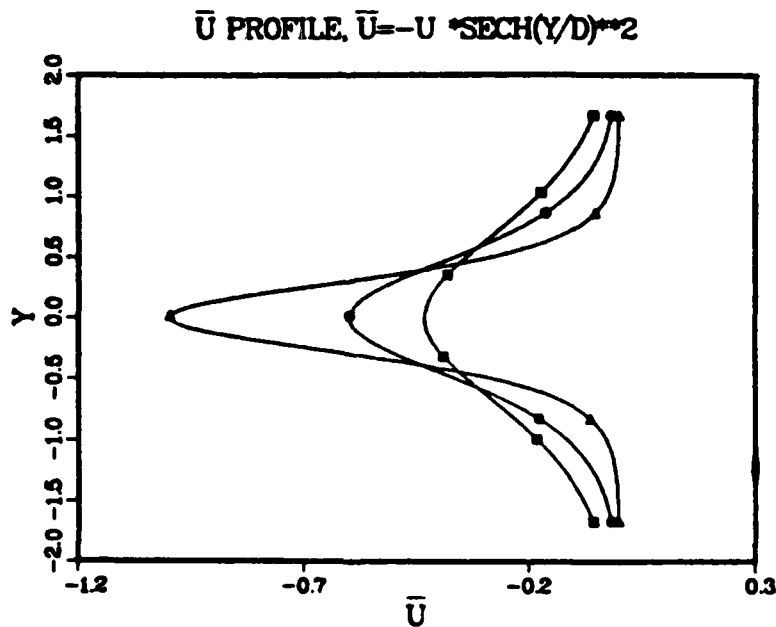


FIG. 1. The Bickley Jet  $\bar{U}$  profile [Eq. (2.7)] at three streamwise locations. The  $\square$  curve is the profile at  $x_1 = \pm 2.0$ , the  $\circ$  curve is at  $x_1 = \pm 1.0$ , and the  $\Delta$  curve is at  $x_1 = 0$ . Both the width and the maximum speed of the jet change streamwise.

Now use (3.5) and (3.6) in (3.1), and then substitute into (2.1) and (2.3). With the help of (3.7) and (2.2), we obtain a sequence of equations for different orders of  $\epsilon$ .

*O(1) problem:*

$$L(\phi_0) = \frac{\partial^2 \phi_0}{\partial y^2} - k_0^2 \phi_0 - \frac{k_0 \phi_0 (\bar{U}_{yy} - \beta)}{(k_0 \bar{U} - \omega - i\lambda)} = 0 \quad (3.8)$$

$$\phi_0 = 0 \quad \text{at } y = \pm Y. \quad (3.9)$$

The  $O(1)$  problem is identical to the problem when  $\epsilon = 0$ , i.e., parallel flow. For each  $x_1$ ,  $\bar{U}$  and  $\bar{U}_{yy}$  are prescribed by (2.7), and Eqs. (3.8)–(3.9) give an eigenvalue problem. If  $\omega$  is replaced by  $k_0 c$ , where  $c$  is the phase speed, the conventional temporal barotropic instability is obtained by setting  $k$  as a constant and solving for complex  $c$  (Kuo, 1973). In our study, where  $\omega$  is constant,  $k$  is the eigenvalue and  $\phi$  the eigenfunction. The basic flow is spatially unstable when  $k$  is complex. The imaginary part of  $k$  gives us the spatial growth rate while the real part is the local wavenumber.

Since Eqs. (3.8) and (3.9) constitute a nonlinear problem with the eigenvalue  $k$ , an iterative shooting method for the complex eigenvalue problem is employed. The fourth-order Runge–Kutta–Gill method is used to integrate Eq. (3.8) from one boundary to the other. The first guess for the eigenvalue is chosen from the range of interest. Only six or seven iterations are required for the solution to converge to the specified boundary condition with absolute error less than  $10^{-4}$ . For each  $x_1$  that has a different  $\bar{U}$  profile, the eigenvalue obtained from the previous point is used as the initial guess. With this first guess only two or three iterations are required.

*O( $\epsilon$ ) problem:*

$$L(\phi_1) = \frac{\partial^2 \phi_1}{\partial y^2} - k_0^2 \phi_1 - \frac{k_0 \phi_1 (\bar{U}_{yy} - \beta)}{(k_0 \bar{U} - \omega - i\lambda)},$$

$$= F,$$

$$= \frac{1}{(k_0 \bar{U} - \omega - i\lambda)i} \left\{ (3k_0^2 \bar{U} - 2\omega k_0 + \bar{U}_{yy} - \beta - i\lambda 2k_0) \right.$$

$$\times \frac{\partial \phi_0}{\partial x_1} + (3\bar{U}k_0 - \omega - i\lambda)\phi_0 \frac{\partial k_0}{\partial x_1} - \bar{U} \frac{\partial^3 \phi_0}{\partial y^2 \partial x_1}$$

$$+ \bar{V}k_0^2 \frac{\partial \phi_0}{\partial y} - \bar{V} \frac{\partial^3 \phi_0}{\partial y^3} + \frac{\partial \phi_0}{\partial y} \bar{V}_{yy}$$

$$\left. + ik_1 \left( 3\bar{U}k_0^2 \phi_0 - 2\omega k_0 \phi_0 - \bar{U} \frac{\partial^2 \phi_0}{\partial y^2} \right. \right.$$

$$\left. + \phi_0 \bar{U}_{yy} - \beta \phi_0 - 2i\lambda k_0 \phi_0 \right\}, \quad (3.10)$$

$$\phi_1 = 0 \quad \text{at } y = \pm Y. \quad (3.11)$$

Since the left-hand side operator of (3.10) is the same as in (3.8) for the  $O(1)$  problem, (3.10) has nontrivial homogeneous solutions that are proportional to  $\phi_0$ . In order to remove secularity so that the multiple expansion can remain valid, a solvability condition has to be imposed on (3.10). (See Nayfeh, 1981). The condition is

$$\int_{-Y}^Y F \phi_0^* dy = 0 \quad (3.12)$$

where  $\phi_0^*$  is the solution of the adjoint equation of the  $O(1)$  problem. Since the operator  $L$  in the  $O(1)$  problem is self-adjoint,  $L = L^*$ ; therefore,  $\phi_0 = \phi_0^*$ .

The unknown  $k_1$ , as well as  $k_0$ , is independent of  $y$ . Rearrangement of (3.12) gives us the following equation for  $k_1$ :

$$k_1 = \frac{H_1}{H_2}, \quad (3.13)$$

where

$$H_1 = i \int_{-Y}^Y \frac{\phi_0^*}{(k_0 \bar{U} - \omega - i\lambda)} \left\{ \frac{\partial \phi_0}{\partial x_1} (3k_0^2 \bar{U} - 2\omega k_0 + \bar{U}_{yy} \right.$$

$$- \beta - 2i\lambda k_0) + (3\bar{U}k_0 - \omega - i\lambda) \frac{\partial k_0}{\partial x_1} \phi_0 - \bar{U} \frac{\partial^3 \phi_0}{\partial x_1 \partial y^2}$$

$$\left. + \bar{V}k_0^2 \frac{\partial \phi_0}{\partial y} - \bar{V} \frac{\partial^3 \phi_0}{\partial y^3} + \frac{\partial \phi_0}{\partial y} \bar{V}_{yy} \right\} dy \quad (3.13a)$$

$$H_2 = \int_{-Y}^Y \frac{\phi_0^*}{(k_0 \bar{U} - \omega - i\lambda)} \left( 3\bar{U}k_0^2 \phi_0 - 2\omega k_0 \phi_0 \right.$$

$$\left. - \bar{U} \frac{\partial^2 \phi_0}{\partial y^2} + \phi_0 \bar{U}_{yy} - \beta \phi_0 - 2i\lambda k_0 \phi_0 \right) dy. \quad (3.13b)$$

For nonparallel flow, the spatial growth rate is, to  $O(\epsilon)$ ,

$$\text{Im}(k_0 + \epsilon k_1) \quad (3.14)$$

and the local wavenumber is

$$\text{Re}(k_0 + \epsilon k_1). \quad (3.15)$$

In order to obtain  $k_1$  as a function of  $x_1$ , terms such as  $\partial \phi_0 / \partial x_1$ ,  $\partial k_0 / \partial x_1$  and  $\partial^3 \phi_0 / \partial x_1 \partial y^2$  in (3.13) have to be known. They can be obtained by finite difference methods since  $\phi_0$ ,  $k_0$  are known at each point  $(x_1, y)$ . An alternate way suggested by Nayfeh et al. (1974) is to take  $\partial / \partial x_1$  of (3.8). This leads to an equation

$$L \left( \frac{\partial \phi_0}{\partial x_1} \right) = G \left( \frac{\partial k_0}{\partial x_1}, k_0, \phi_0, \text{etc.} \right). \quad (3.16)$$

Equation (3.16) has the same structure as Eq. (3.10), so the same solvability condition is required, i.e.,

$$\int_{-Y}^Y \phi_0^* G dy = 0. \quad (3.17)$$

An equation for  $\partial k_0 / \partial x_1$  can be obtained with similar form to (3.13), and then  $\partial \phi_0 / \partial x_1$  can be obtained from (3.16). When the finite difference method and the analytical method are compared, the results are very close.

TABLE 1. Temporal and spatial growth rates.

Parameter	Temporal growth rate	Spatial growth rate
wave structure	$e^{ikx - \omega t}$	$e^{ikx - \omega t}$
wavenumber	$k = k_r$	$k = k_r + ik_i$
frequency	$\omega = \omega_r + i\omega_i$	$\omega = \omega_r$
growth rate	$\omega_i$ (temporal)	$k_i$ (spatial)
phase speed $c$	$\omega_r/k_r$	$\omega_r/k_r$

4. Temporal growth rate versus spatial growth rate

Before discussing the results from the present study, it is necessary to examine the functional relationship between the temporal growth rate and the spatial growth rate. In TWC, the parallel-flow spatial growth rate was not obtained directly, but transformed from the temporal growth rate. This discussion will lead to an important modification of the conclusions in TWC as well as those in the nonlinear numerical study by Williams et al. (1984). The basic procedures and assumptions in obtaining temporal and spatial growth rates are different, as is indicated in Table 1.

Various efforts have been made to determine a relationship that converts one type of growth rate into another. In an experimental investigation of the boundary layer over a flat plate, a simple relation was formulated by Schubauer and Skramstad (1943) in order to compare the measured amplification rates (spatial growth rates) with the temporal growth rates given by theory. They related the temporal growth rate to the spatial growth rate with the chain rule as follows:

$$k_i = -\frac{\omega_i}{c_r} \tag{4.1}$$

where  $k_i$  is spatial growth rate,  $\omega_i$  is the temporal growth rate, and  $c_r = dx/dt$  is the phase speed. Gaster (1965) demonstrated that the transformation between the two kinds of growth rates, which uses the phase speed, introduces errors that are not negligible. However, Schu-

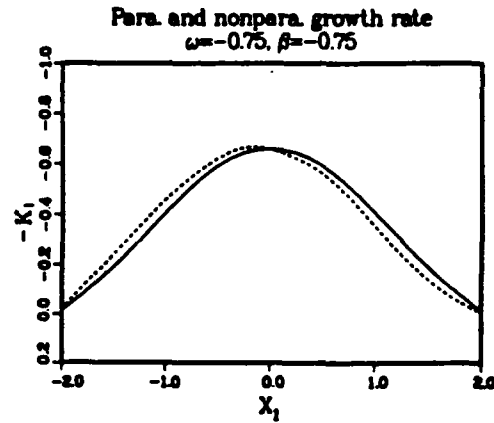


FIG. 3. The spatial growth rate corresponding to the Bickley Jet profile [Eq. (2.7)], whose streamwise variation is described by (2.9) and (2.10). The solid line is the spatial growth rate for the parallel flow, and the dashed line is the spatial growth rate for the nonparallel flow.

bauer and Skramstad did make their comparison and some correlation was found.

Gaster (1962) used a Taylor series expansion to show that when the amplification rate is small, a transformation by means of the group velocity can be formulated. In a study of the nonparallel flow stability for two- and three-dimensional flow, Nayfeh and Padhye (1979) derived a formula for the transformation between growth rates. Their formula differs from Gaster's in two respects. First, the complex group velocity is used instead of the real group velocity, which is used in Gaster's formula. Second, a correction to the wavenumber (frequency) must be added when transforming from temporal (spatial) to spatial (temporal) growth rates.

Calculations using Nayfeh and Padhye's formula [1979, Eq. (41)] show that when the amplification rate is small (i.e., the imaginary part of the eigenvalue is

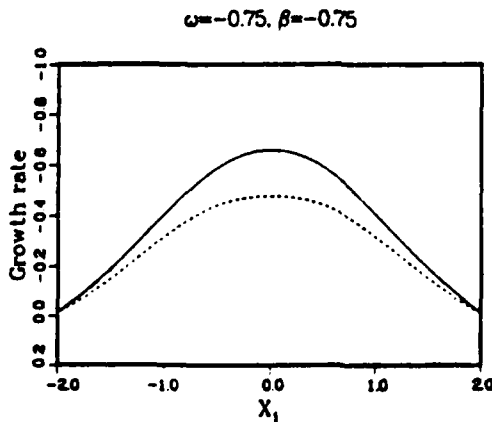


FIG. 2. Spatial growth rate for (solid line) parallel flow for  $\omega = -0.75$ ,  $\beta = -0.75$ ; and (dashed line) obtained using Eq. (4.1).

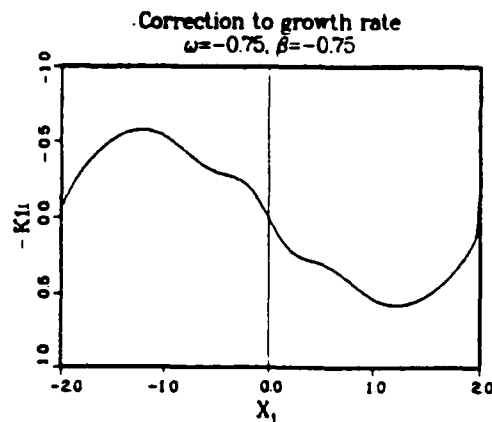


FIG. 4. The imaginary part of  $\lambda_1$ , or the  $O(\epsilon)$  correction to the spatial growth rate at each streamwise location.

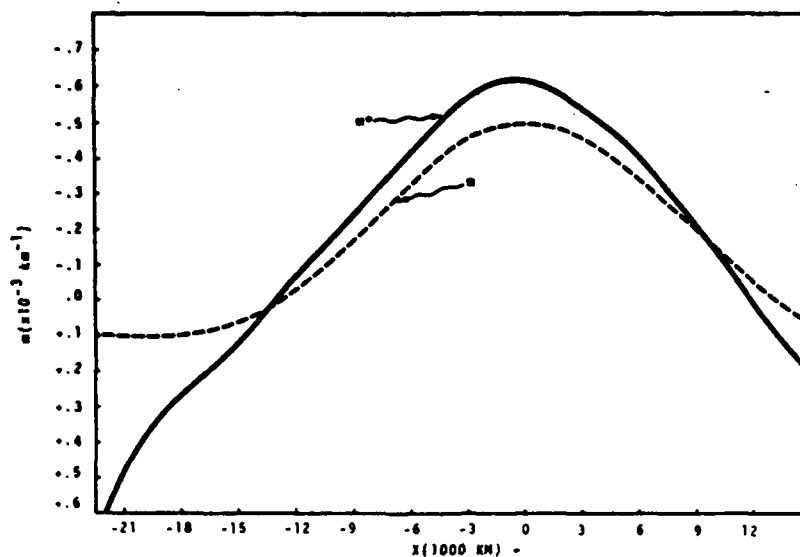


FIG. 5. Experiment 1 (from TWC): spatial growth rates  $m(x)$  from the parallel flow model and  $m^*(x)$  from the complete numerical model. When  $m < 0$  there is downstream growth. (Adopted from TWC.)

small), the transformation is very accurate. This is consistent with results given in Tables 1 and 2 by Nayfeh and Padhye (1979), where all the cases are also for small amplification. When the amplification rate increases from 0.013 to 0.65, the error increases almost linearly from 0.4% to 20%. Apparently, a small amplification rate is required to obtain accurate results using Nayfeh and Padhye's (1979) formula.

In TWC, a simple mechanistic model was formulated that leads to Eq. (4.1). As discussed above, the use of Eq. (4.1) in TWC to transform the spatial growth rates from temporal growth rate for the parallel flow introduces significant errors.

Figure 2 contains the spatial growth rate as a function of  $x_1$  for  $\bar{U}$  profiles, which are described by Eqs. (2.7), (2.9) and (2.10). The nondimensional parameter settings  $\omega = -0.75$ ,  $\beta = -0.75$  correspond to the case studied in TWC for a period of 3.25 days and with the central latitude at  $10^\circ\text{N}$ . The solid line is obtained by directly solving the parallel flow equations at each point in  $x_1$  for the complex wavenumber  $k$  as the eigenvalue. The spatial growth rate is the imaginary part of  $k$ . The dashed line is obtained as in TWC by solving the parallel flow equations for the complex frequency as the eigenvalue and then using Eq. (4.1) to calculate the spatial growth rate.

Figure 2 shows that in the maximum growth rate region, the use of Eq. (4.1) underestimates the true spatial growth rate by 27%. A similar percentage difference was also obtained by Michalke (1965). In TWC, Eq. (4.1) was evaluated with the same wavenumbers as those from their complete nonparallel numerical model where the spatial growth rates were measured directly. An alternative is to iterate the wavenumber

until the same frequency is obtained. Both methods were used in a later paper by Williams et al. (1984). In the present study it is found that keeping the same frequency in the transformation gives an improvement in growth rate of 2%–4%, compared to the transformation retaining the same wavenumber. Clearly this improvement is not significant. The percentage error that results from the use of Eq. (4.1) increases slightly from 20% to 27% when the growth rate increases from 0.013 to 0.65, respectively.

Detailed discussion concerning the transformation of the growth rate is beyond the scope of the present

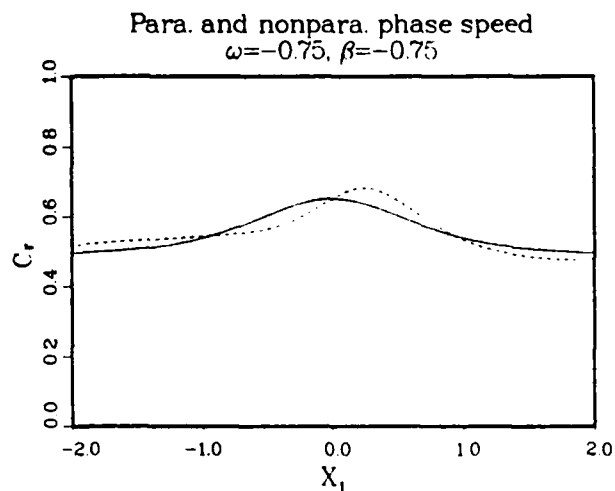


FIG. 6. The phase speed for the case whose spatial growth rate is shown in Fig. 3. Solid line: parallel phase speed; dashed line: non-parallel phase speed.

U PROFILE,  $\bar{U} = U \text{ SECH}(Y/D)^2$ ,  $D = \text{CONST}$

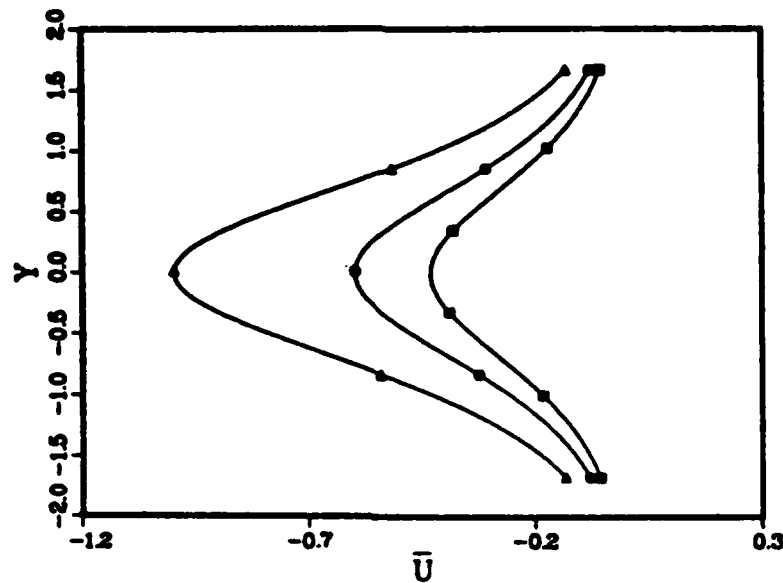


FIG. 7. As in Fig. 1 except the width of the jet is kept the same.

study and is presented in a separate paper by the authors (Peng and Williams, 1986).

5. Results

In this section we will compare the parallel and nonparallel solutions in order to determine the influence of nonparallel effects on spatial instability. Within each diagram in this section, the solid line refers to the variables for pure parallel flow, which are obtained from the  $O(1)$  problem; the dashed line refers to the variables for nonparallel flow to  $O(\epsilon)$ . The positive imaginary wavenumber gives downstream amplification of the wave amplitude when the propagation is from east to

west. The downstream growth rate is  $-k_i$ , which is plotted throughout the text. The parallel and nonparallel growth rates shown in Fig. 3 are for the parameter values used in Fig. 2. The parallel flow growth rate changes symmetrically with respect to  $x_1 = 0$ , as is expected from symmetric streamwise variation of the basic flow. The  $O(\epsilon)$  correction to the wavenumber,  $k_1$ , which is given in Fig. 4, is antisymmetric with respect to  $x_1 = 0$ . Examining (3.13), one observes that  $k_1$  is proportional to terms such as  $\partial\phi_0/\partial x_1$ ,  $\partial k_0/\partial x_1$ ,  $\bar{v}$ , etc., all of which are the first derivatives of  $\phi_0$ ,  $k_0$ ,  $\bar{\psi}$ , etc. Since  $\phi_0$ ,  $k_0$ ,  $\bar{\psi}$  are symmetric with respect to  $x_1 = 0$ , their first-order derivatives with respect to  $x_1$  are antisymmetric. Note that if we multiply the curve in Fig.

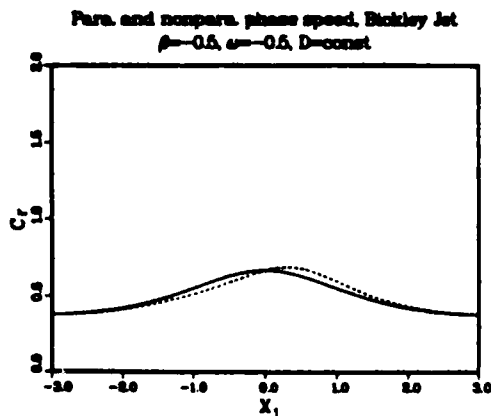


FIG. 8. The parallel (solid line) and the nonparallel (dashed line) phase speed for the jet profile shown in Fig. 7.

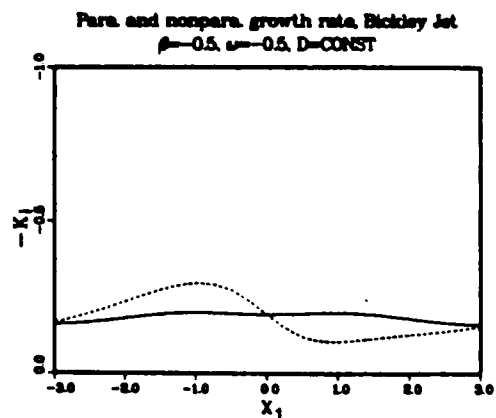
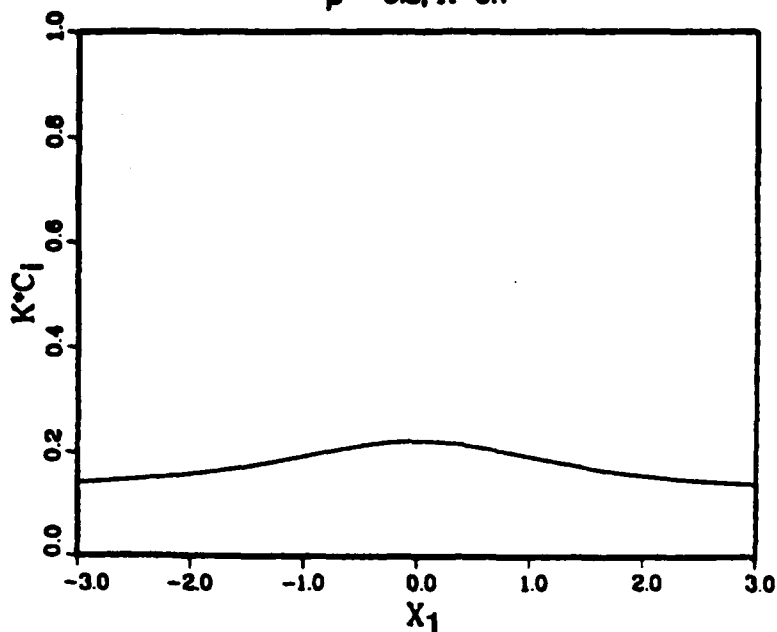


FIG. 9. As in Fig. 8 except for the spatial growth rate for the jet profile.

TEMPORAL GROWTH RATE, D=CONST  
 $\beta = -0.5, K = 0.7$



PHASE SPEED, D=CONST  
 $\beta = -0.5, K = 0.7$

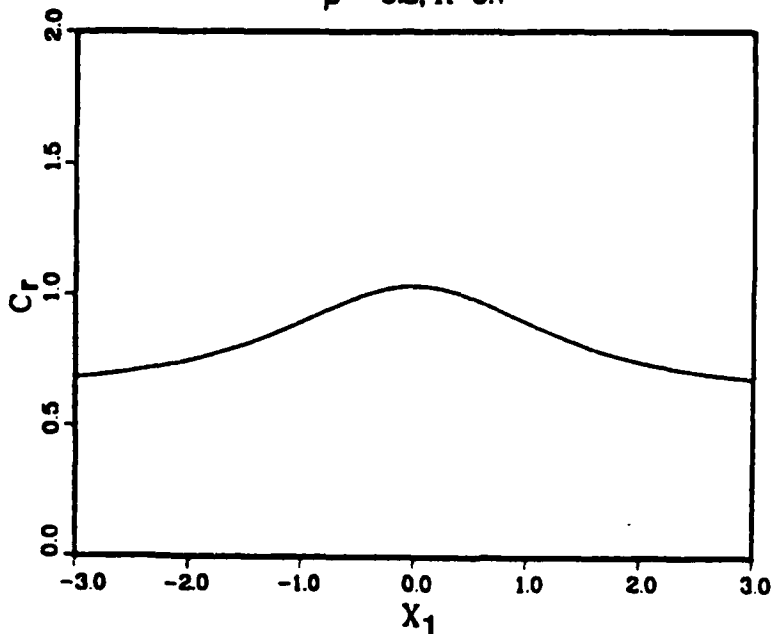


FIG. 10. (a) The temporal growth rate from parallel theory for the jet profile shown in Fig. 7. (b) The corresponding phase speed.

4 by  $\epsilon$ , we obtain the difference between the nonparallel and the parallel solutions in Fig. 3. These figures show that the maximum growth rate region is shifted downstream from the location predicted by the parallel flow

instability. At  $x_1 = 0$  where the parallel growth rate is maximum, all the first-order derivatives are zero. Therefore,  $k_1 = 0$  at  $x_1 = 0$  and the growth rates are the same for parallel and nonparallel flows.

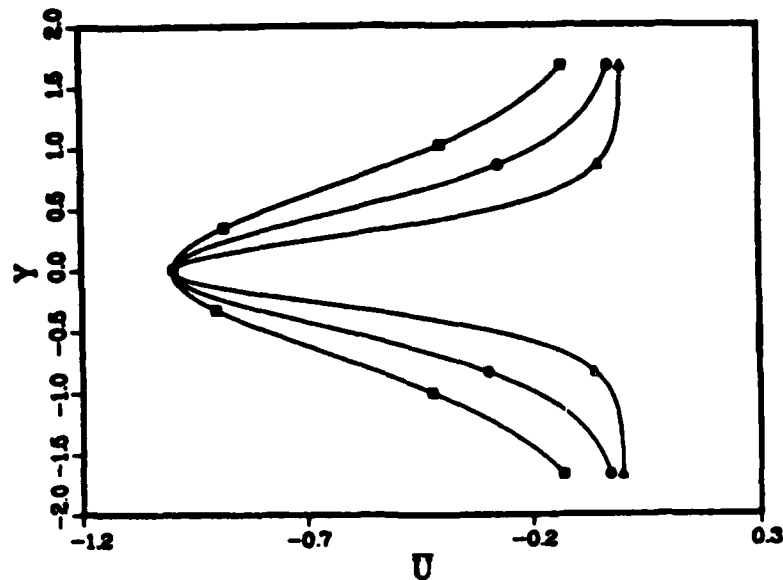
$$U \text{ PROFILE, } U = U_0 \text{ SECH}(Y/D)^2, U_0 = \text{CONST}$$


FIG. 11. As in Fig. 1 except the maximum wind speed is kept constant so that only the width of the jet varies.

The downstream shifting of the location of maximum growth rate was observed in TWC and by Williams et al. (1984). As the disturbance propagates downstream in a nonparallel flow, the disturbance structure lags with respect to the parallel flow disturbance structure. Therefore, the profile for spatial growth rate in the streamwise direction is shifted downstream from the profile calculated from the parallel flow. The dynamic damping observed in the numerical result in TWC, which was due to continuous spectrum solutions (Casé, 1960), is absent in the normal-mode solutions derived in this paper. Moreover, as shown in Fig. 5, which is adopted from TWC, the nonparallel growth rate is approximately 25% higher than the parallel growth rate calculated by them. This increase is not observed in the present study. As explained in section 4, the parallel growth rate calculated in TWC underestimates the true growth rate by approximately 27%. If this percentage is added to the parallel growth rate in Fig. 5, the results from the present analytical study and from the numerical study (TWC) are consistent. Therefore, there is no overall increase of the growth rate for nonparallel flow at the point where the parallel flow growth rate is a maximum.

The phase speed of the disturbance is

$$c = \frac{\omega}{k_r} \quad (5.1)$$

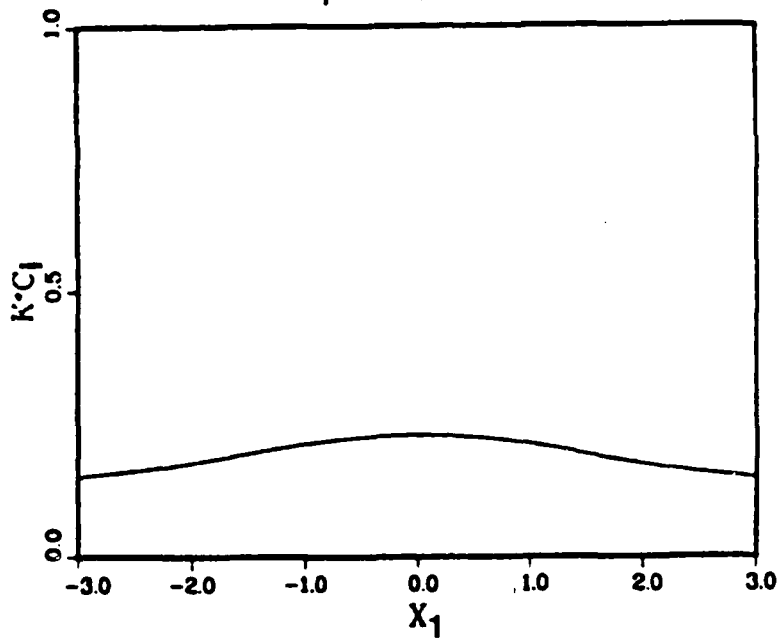
where  $k_r$  is the local wavenumber. For parallel flow,  $k_r$  equals  $\text{real}(k_0)$ , and for nonparallel flow,  $k_r = \text{real}(k_0 + \epsilon k_1)$ . The phase speed for the case shown in Fig. 3 is

plotted in Fig. 6. Upstream from the maximum growth rate point for parallel flow, i.e., where  $x_1 = 0$ , the disturbance moves faster than predicted by the parallel flow and slower downstream. It is postulated that the difference between growth rate calculated from parallel flow and nonparallel flow is closely related to the relative phase speed between them.

Equation (4.1) implies that if the phase speed for disturbance in the nonparallel flow is faster than predicted by parallel flow, the disturbance will have less time to grow according to the local instability so that the growth rate will be smaller than that predicted by parallel flow. The opposite holds for a disturbance that propagates slower than that predicted by parallel flow. Therefore, a disturbance with a faster (slower) phase speed will have smaller (larger) spatial growth rate. An experiment described in TWC in which a constant velocity  $U_0$  is added to the mean flow did show a significant reduction in local spatial growth rate. This advective effect also produced more downstream shifting of the spatial growth rate profile.

This discussion is based primarily on the approximate expression for the spatial growth (4.1). However, it is believed that this formula gives the correct dependence on the phase speed. In order to gain more insight into the influence of the phase speed rate on the spatial growth, two cases will be considered. A jet profile with a constant half width is used in the first case. The change of the basic flow shear is due to the streamwise change in the speed of the jet. Mathematically,  $d$  is set to a constant and only  $U$  varies with  $x_1$  in (2.7). Profiles of  $\bar{U}$  at several locations are shown in Fig. 7. We shall

TEMPORAL GROWTH RATE,  $U = \text{CONST}$   
 $\beta = -0.5, K = 0.7$



PHASE SPEED,  $U = \text{CONST}$   
 $\beta = -0.5, K = 0.7$

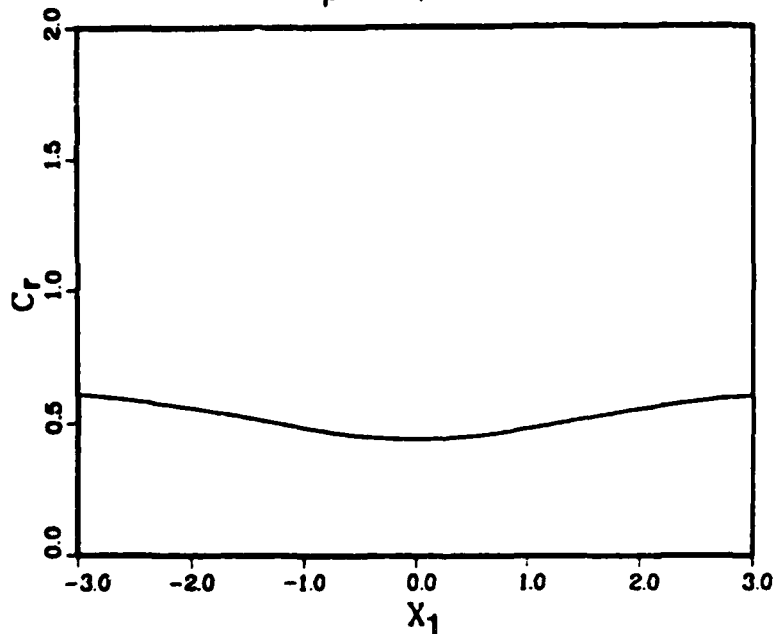


FIG. 12. As in Fig. 10 except corresponding to Fig. 11.

first examine the phase speed of the disturbance that is plotted in Fig. 8. The phase speed is larger for nonparallel flow upstream of  $x_1 = 0$  and smaller downstream, as in the previous case (Fig. 6). Therefore, the

spatial growth rate for nonparallel flow would be smaller than the parallel flow upstream and larger downstream, as indicated in Fig. 9. Notice that the growth rate for the parallel flow is nearly uniform ir-

Parallel and total spatial growth,  $U = \text{const}$   
 $\beta = -0.5, \omega = 0.5$

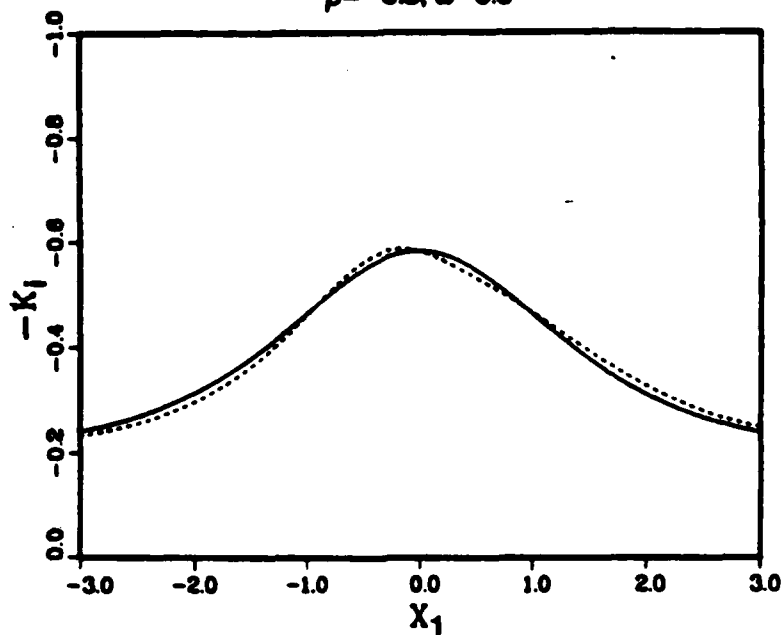


FIG. 13. As in Fig. 9 except corresponding to Fig. 11.

respective of the large variation of the jet strength. This seems to contradict the notion that barotropic instability increases as the north-south shear of the basic flow increases. However, an examination of Eq. (4.1)

reveals that for spatial instability, the growth rate is also related to the phase speed of the disturbance. Even though the temporal growth rate increases in proportion to the increase of the mean flow shear, as shown

Parallel and total phase speed,  $U = \text{const}$   
 $\beta = -0.5, \omega = 0.5$

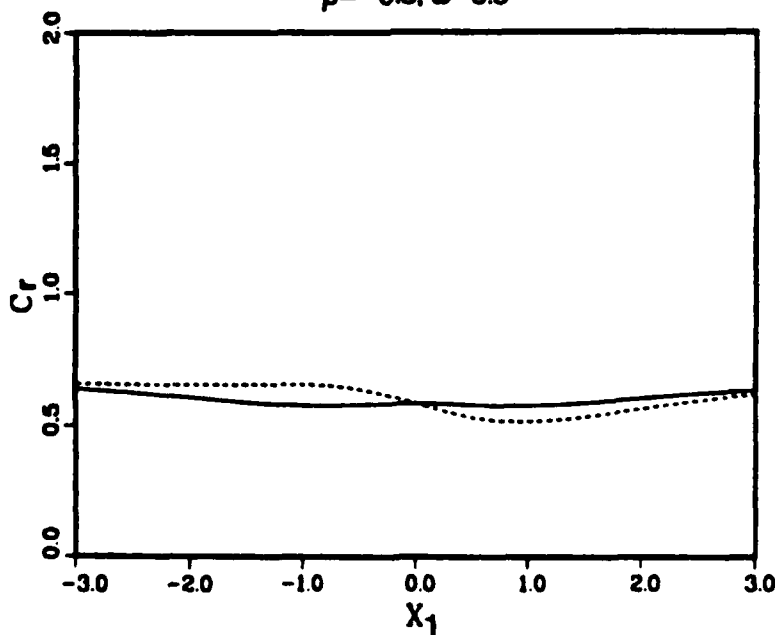


FIG. 14. As in Fig. 8 except corresponding to Fig. 11.

in Fig. 10a, the accompanying increase of the phase speed (Fig. 10b) results in a small change in the spatial growth rate. Therefore, from the point of view of spatial growth rate, which is more appropriate in a nonparallel flow, the maximum shear region is not necessarily the most unstable region.

In the second case, the jet profile is considered to have a constant maximum speed. The increase of the shear is due to the decrease of the jet half width. This is prescribed by setting  $U$  equal to a constant and by allowing only  $d$  to vary in (2.7). Mean flow profiles of  $\bar{U}$  are displayed in Fig. 11 for the same locations as in Fig. 7. For this kind of variation, the temporal growth rate increases while the phase speed decreases with the increase of the basic flow shear. (See Figs. 12a,b.) This leads to a substantial variation of the spatial growth rate for parallel flow. The nonparallel spatial growth rate is quite different from previous cases when compared to the parallel flow spatial growth (Fig. 13). In Fig. 14, the nonparallel phase speed is slower than the parallel phase speed upstream of  $x_1 = 0$  and faster downstream. If the shifting of nonparallel growth rate from that predicted by the parallel flow is due solely to the phase speed differences between the parallel and nonparallel flows, the nonparallel growth rate would be larger upstream of  $x_1 = 0$  and smaller downstream. However, this is only true in part of the region. The maximum growth rate region for nonparallel flow is still shifted downstream, which should be expected by the lag effect proposed in TWC. This indicates that the shifting is due to the combination of the two effects: one involves the lag mechanism, and the other depends on the phase speed difference between the parallel and nonparallel flows.

The example shown in Fig. 3, which is comparable to the case considered by TWC, indicates a relatively small difference between parallel and nonparallel flow. This is not a general result, as will be demonstrated with an example. Figure 15 has the same conditions as in Fig. 3 except that the frequency of the disturbance

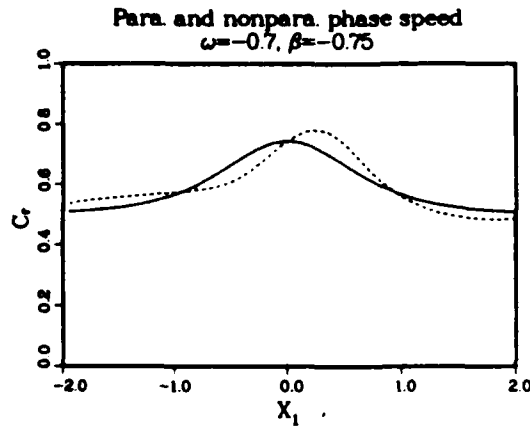


FIG. 16. As in Fig. 6 except  $\omega = -0.7$ .

is smaller, it corresponds to a period of 3.5 days whereas the frequency in Fig. 3 corresponds to period of 3.25 days. The stronger asymmetry of the growth rate curve in Fig. 15 compared to Fig. 3 is due to the larger phase speed shown in Fig. 16, which gives a larger lag effect. Differences of the phase speed between parallel and nonparallel flow are also slightly larger in this case. Further increases in the period lead to similar results.

6. Concluding remarks

In this study a two-scale expansion is used to analyze the linear instability of a barotropic jet that varies downstream. A small parameter  $\epsilon$  is introduced to measure the nonparallelism of the mean flow. The  $O(1)$  problem gives the parallel flow equation at each point in the streamwise direction. The  $O(\epsilon)$  problem gives the correction to the spatial growth rate due to the nonparallelism, which is proportional to the first streamwise derivative of the properties from the  $O(1)$  problem. This  $O(\epsilon)$  correction causes the downstream shifting of the spatial growth rate profile for nonparallel flow relative to that of the parallel flow obtained from the  $O(1)$  problem.

Results obtained here are consistent with the numerical studies by TWC after a necessary modification of their parallel flow growth rates. In the present analysis, only the normal mode solutions are considered, whereas in TWC's numerical study the continuous spectrum effects are also included. The closeness of these two results indicates that the normal modes accurately describe the solution in the region of growth. The rapid decay of the growth rate near the outflow region, which was seen in the numerical solution, is not present in the analytical solution. The decay in the numerical solution appears to have been caused by continuous spectrum effects.

Physically, the difference between the nonparallel flow solutions and the parallel flow solutions are caused by two effects. The first one, which has been discussed by TWC, is the lag effect. When the disturbance propagates through a mean flow that varies in streamwise

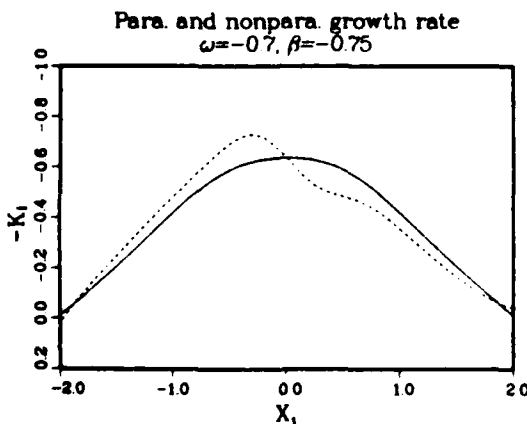


FIG. 15. As in Fig. 3 except  $\omega = -0.7$ .

direction, the disturbance lags in adjusting its structure to the local instability properties. This lagging causes a downstream shifting of the spatial growth rate profile. The second effect is due to the influence of the phase speed on the spatial growth rate. If the phase speed in the nonparallel flow is faster than that predicted by the parallel flow, the disturbance will move further in a given time interval, and therefore, the spatial growth rate will be reduced.

In a streamwise varying mean flow, it is more appropriate to study the spatial growth rate than the temporal growth rate. As is commonly known, the temporal growth rate is proportional to the cross-stream shear of the unstable zonal flow. Since the spatial growth rate depends on the propagating phase speed, the maximum shear region is not necessarily the region of the maximum spatial growth rate. This is an important consideration in the application of instability theories to synoptic examples.

*Acknowledgments.* The authors wish to thank Professor C.-P. Chang for reading the manuscript and for useful discussions on the research. The first author was supported by a National Research Council Associateship. The NRC Associate Program is sponsored by the Naval Postgraduate School Foundation Research Program, which is funded by the Chief of Navy Material. This research was also supported by the Division of Atmospheric Sciences, National Science Foundation under Grant ATM 83-15175. The manuscript was carefully typed by Miss K. Lee and the numerical computations were carried out at the W. R. Church Computer Center at the Naval Postgraduate School.

#### REFERENCES

- Benney, D. J., and S. Rosenblat, 1964: Stability of spatially varying and time-dependent flows. *Phys. Fluids*, 7, 1385-1386.
- Case, K. M., 1960: Stability of plane Couette flow. *Phys. Fluids*, 3, 143-148.
- Drazin, P. G., 1974: On a model of instability of a slowly-varying flow. *Quart. J. Mech. Appl. Math.*, 27, 69-86.
- Gaster, M., 1962: A note on the relation between temporally-increasing and spatially-increasing disturbances in hydrodynamics instability. *J. Fluid Mech.*, 14, 222-224.
- , 1965: The role of spatially growing waves in the theory of hydrodynamic stability. *Prog. Aerospace Sci.*, 6, 251-270.
- Haltiner, G. J., and R. T. Williams, 1980: *Numerical Prediction and Dynamic Meteorology*. Wiley & Sons, 477 pp.
- Krishnamurti, T. N., 1961: The subtropical jet stream of winter. *J. Meteor.*, 18, 172-191.
- Kuo, H. L., 1973: Dynamics of quasi-geostrophic flows and instability theory. *Advances in Applied Mechanics*, Vol. 13, Pergamon, 247-330.
- Merkine, L.-O., 1977: Convective and absolute instability of baroclinic eddies. *Geophys. Astrophys. Fluid Dyn.*, 9, 129-157.
- , and R. Balgovind, 1983: Barotropic instability of weakly nonparallel zonal flows. *Geophys. Astrophys. Fluid Dyn.*, 25, 157-190.
- Michalke, A., 1965: On spatially growing disturbances in an inviscid shear layer. *J. Fluid Mech.*, 23, 521-544.
- Nayfeh, A. H., 1981: *Introduction to Perturbation Techniques*. Wiley & Sons, 519 pp.
- , and A. Padhye, 1979: Relation between temporal and spatial stability in three-dimensional flows. *AIAA J.*, 17, 1084-1090.
- , W. S. Saric and D. T. Mook, 1974: Stability of nonparallel flows. *Arch. Mech.*, 26, 401-406.
- Pedlosky, J., 1976: *Geophysical Fluid Dynamics*. Springer-Verlag, 624 pp.
- Peng, M. S., and R. T. Williams, 1986: A note on the relation between temporal and spatial growth rate. Submitted to *J. Atmos. Sci.*
- Saric, W. S., and A. H. Nayfeh, 1975: Nonparallel stability of boundary-layer flows. *Phys. Fluids*, 18, 945-950.
- Schubauer, G. B., and H. K. Skramstad, 1943: Laminar boundary layer oscillations and transition on a flat plate. NACA Advanced Confidential Rep., April 1943, or 1947, *J. Res. Nat. Bur. Stand.*, 38, 251-292.
- Tupaz, J. B., R. T. Williams and C.-P. Chang, 1978: A numerical study of barotropic instability in a zonally varying easterly jet. *J. Atmos. Sci.*, 35, 1265-1280.
- Williams, R. T., H. Lim and C.-P. Chang, 1984: Nonlinear and linear effects in an easterly jet with downstream variation. *J. Atmos. Sci.*, 41, 621-636.

## Spatial Instability of a Baroclinic Current with Slow Streamwise Variation

MELINDA S. PENG AND R. T. WILLIAMS

*Department of Meteorology, Naval Postgraduate School, Monterey, CA 93943*

(Manuscript received 27 April 1986, in final form 13 December 1986)

### ABSTRACT

Spatial baroclinic instability in a mean flow with slow streamwise variation is studied with the quasi-geostrophic two-layer model. The two-scale expansion technique which was employed by Peng and Williams is used in this study. The zero-order terms give the local spatial instability solution. The next order terms determine the correction to the local solution due to the streamwise variation of the mean flow. It is found that this correction is not negligible when the  $\beta$  effect is large and the vertical shear is small. The results are explained with the lag effect, which was discussed by Peng and Williams. The lag effect occurs when the local solution changes its structure substantially in the streamwise direction. When the vertical shear is large or when the  $\beta$  effect is small, the ratio between the disturbances of the two layers is nearly uniform in the streamwise direction, even though the shear changes substantially. Thus, only a small lag effect is experienced by a disturbance as it propagates, and the streamwise effect is unimportant. The dependence of the vertical structure on the basic flow variation and other parameters is analyzed.

### 1. Introduction

The traditional studies of baroclinic instability in the atmosphere and in the ocean (Charney, 1947; Eady, 1949; Phillips, 1951) assume that the basic flow is uniform in the streamwise direction. Observations indicate that this is often not the case. Land-sea contrasts and topographic effects can lead to significant streamwise changes in baroclinicity. Therefore, it is important to examine the influence of streamwise variations in the basic flow on baroclinic stability theory. A basic current with streamwise variation can be obtained by adding a stationary long wave to a uniform zonal flow. Due to the mathematical nonseparability of nonparallel flow problems, either numerical integration or the multiple scale technique have been used. For example, Tupaz et al. (1978), Niehaus (1980), Frederiksen (1979), and Merkin and Balgovid (1983), have used numerical integration (including spectral space methods), and multiple scale techniques have been used by Drazin (1974), Ling and Reynolds (1973), Niehaus (1981) and Peng and Williams (1986). A review paper by Grotjahn (1984a) summarizes research on basic currents with streamwise variation. The finite amplitude behavior of disturbances, in a flow with abrupt streamwise variation from a weakly unstable region to a stable region (and vice versa) was studied by Pedlosky (1976).

Peng and Williams (1986) applied the multiple scale technique to the barotropic instability problem which had been solved numerically by Tupaz et al. (1978). Comparisons between these two results verified the accuracy of the multiple scale technique, and Peng and Williams were able to determine the influence of

streamwise variation of the basic flow on growth rate, wavenumber, etc. The baroclinic instability for basic flows that change in the streamwise direction is studied here using the same technique. As in Peng and Williams, the major purpose is to obtain the difference between the local stability solution for parallel flow and the nonparallel solution.

In the analysis of parallel flows, the instability is usually examined with temporal growth for real wavenumbers so that the wave is spatially periodic and the solution is bounded in space. For nonparallel flows, it is not necessary to have spatial periodicity for boundedness. Due to advection by the basic flow and propagation of the disturbance itself, the disturbance experiences environments with different stability properties as it travels. It is appropriate in this case to consider the spatial instability. The spatial growth rate comes from the imaginary part of the wavenumber, which allows the amplitude to grow in space as the disturbance moves downstream. Physically, the temporal growth rate can be linked to the spatial growth rate by a function of the phase velocity.

The most general approach is to consider both the temporal and the spatial growth simultaneously. That is, both the wavenumber and the frequency are complex (e.g., see Merkin and Shafranek, 1980). Under some circumstances, the basic flow can support absolute instability, in which case the spatial amplification will be obscured. The concept of absolute instability was first discussed in plasma physics by Briggs (1964), and introduced to geophysical fluid dynamics by Thacker (1976) and Merkin (1977). Mathematically, the existence of absolute instability requires the van-

ishing of the complex group velocity  $d\omega/dk = 0$  when the imaginary part of the frequency is positive. Physically, when the speed of the mean flow is not large relative to the shear of the flow, the envelope packet of a disturbance which is excited at some point will not be advected downstream fast enough and any point reached by the disturbance can grow exponentially in time. Therefore, for basic flows that support absolute instability, the spatially amplifying waves cannot be identified.

Thacker (1976) and Merkin (1977) obtained the criteria for absolute instability for the two-layer baroclinic model. Merkin proposed local absolute instability as a possible explanation of lee cyclogenesis, while Thacker suggested that spatial amplification of the meanders in the Gulf Stream can exist when absolute instability is not present.

Pierrehumbert (1984) used both numerical integration and an analytic approach to study a zonally varying basic flow which supports absolute instability in some region of the domain. It was found that the frequency determined by the absolute instability at the location of the maximum shear dominates the evolution of the disturbances in the domain. The growth rate determined using parallel flow theory compares favorably with those obtained from the numerical integration of the complete equations.

In the absolute instability studies mentioned above, the domains in the north-south direction were unbounded. Merkin (1977) showed that the stabilizing effect of the north-south boundaries requires a larger shear relative to the averaged mean flow to support absolute instability unless the scale of the disturbance is very large. The criteria listed as (A13) in Merkin (1977) can be obtained from the observation that for amplifying waves, the maximum spatial growth rate corresponds approximately to a frequency for which the speed of the wave is equal to the average speed of the basic flow. This criteria is verified for the parameters of this problem by direct calculation. For all the cases treated in the present paper, the basic flows do not support absolute instability. Thus, the spatial growth approach can be used effectively to study disturbances in our flow fields that contain streamwise variation. Therefore, we treat only spatial instability in the study.

This stability study uses the quasi-geostrophic two-layer baroclinic model which was originally formulated by Phillips (1951) and treated extensively by Pedlosky (1979). The two-layer model, which is very simple, has been used to capture many dynamic aspects of large-scale atmospheric flows. The model with a nonuniform basic flow is described in section 2, and the two-scale expansion procedures are given in section 3. Results for different basic flow variations are presented and discussed in section 4. In section 5, we analyze the difference in structure between the disturbances in the two layers when the vertical shear and the  $\beta$  parameter are changed. This analysis is used to further support

the interpretation of the results in section 4. The discussion and conclusion are given in section 6.

## 2. The model

The two-layer quasi-geostrophic model was derived by Phillips (1951), and the notation in the present paper follows Pedlosky (1979). The model contains two immiscible, incompressible fluid layers, each with different densities  $\rho_1$  and  $\rho_2$ , and different zonal velocities  $U_1$  and  $U_2$ . The densities  $\rho_1$  and  $\rho_2$  are kept constant while the velocities  $U_1$  and  $U_2$  change slowly in the streamwise direction. It is observed that the characteristic length scale of the basic flow in the streamwise direction is much longer than its cross-stream characteristic length scale (an example is presented in section 4). The fluid is bounded above and below by two rigid horizontal planes. Ekman friction is incorporated into the system through vertical boundary conditions. The nondimensional potential vorticity equations are as follows:

$$\left(\frac{\partial}{\partial t} + \frac{\partial \psi_n}{\partial x} \frac{\partial}{\partial y} - \frac{\partial \psi_n}{\partial y} \frac{\partial}{\partial x}\right) (\nabla^2 \psi_n \pm F(\psi_2 - \psi_1) + \beta y) = -r \nabla^2 \psi_n, \quad (2.1)$$

where  $n = 1$  and  $2$  denote the upper and lower layers, respectively. When there are two signs appearing before a term, as in (2.1), the upper sign belongs to the equation for  $n = 1$  and the lower sign belongs to the equation for  $n = 2$ . The Froude number  $F$  is the same for both layers since the two layers considered here are of equal ambient depth. The nondimensional parameters are defined as follows:

$$F = \frac{f_0^2 L^2}{g[(\rho_2 - \rho_1)/\rho_0]D} \quad (2.2)$$

$$\beta = \frac{\beta_0 L^2}{U} \quad (2.3)$$

$$r = \frac{E_0^{1/2}}{R_0}, \quad (2.4)$$

where  $\beta_0$  is the dimensional beta,  $E_0$  is the Ekman number,  $R_0$  is the Rossby number and  $D$  is the layer depth.

For channel geometry, the kinematic boundary conditions at the walls give

$$\frac{\partial \psi_n}{\partial x} = 0 \quad \text{at } y = 0, 1. \quad (2.5)$$

The total streamfunction  $\psi_n$  is

$$\psi_n = \bar{\psi}_n + \psi'_n, \quad (2.6)$$

where  $\bar{\psi}_n$  is the basic state streamfunction and  $\psi'_n$  represents the streamfunction for the disturbance field.

3. Mathematical formulation

The basic state is a nondivergent flow which varies "slowly" with  $x$ . A long spatial scale coordinate  $X$  is defined by introducing a small parameter  $\epsilon$ , so that

$$X = \epsilon x, \tag{3.1}$$

which measures the streamwise variation of the basic flow. The basic flows  $U_1$  and  $U_2$  are constants with respect to the  $y$  coordinate, and they vary with the long space scale  $X$ . For nondivergent basic flow,

$$U_n(X) = -\frac{\partial \bar{\psi}_n}{\partial y}, \tag{3.2}$$

it follows that

$$\bar{\psi}_n = -U_n(X)y, \tag{3.3}$$

$$\frac{\partial \bar{\psi}_n}{\partial x} = \epsilon \frac{\partial \bar{\psi}_n}{\partial X} = \epsilon V_n = -\epsilon \frac{\partial U_n}{\partial X} y. \tag{3.4}$$

Now we linearize (2.1) with respect to  $\bar{\psi}_n$  and then use the relations above to obtain

$$\begin{aligned} & \left( \frac{\partial}{\partial t} + \epsilon V_n \frac{\partial}{\partial y} + U_n \frac{\partial}{\partial x} \right) (\nabla^2 \psi'_n \pm F(\psi'_2 - \psi'_1) + \beta y) + \frac{\partial \psi'_n}{\partial x} \beta \\ & - \epsilon^2 \frac{\partial \psi'_n}{\partial x} \frac{\partial^2 U_n}{\partial Z^2} - \frac{\partial \psi'_n}{\partial y} \epsilon^2 \frac{\partial^2 V_1}{\partial X} \pm \frac{\partial \psi'_n}{\partial x} F(U_1 - U_2) \\ & \mp \frac{\partial \psi'_n}{\partial y} \epsilon (V_2 - V_1) F = -r \nabla^2 \psi'_n. \end{aligned} \tag{3.5}$$

The normal mode solution for the disturbance  $\psi'_n$  in Eq. (3.5) is

$$\psi'_n = \phi_n(X, y) e^{\theta} \tag{3.6}$$

where  $\theta$  is the phase angle, which is treated as an independent variable (Nayfeh et al., 1974). The wave-number  $k$  and frequency  $\omega$  are obtained from the relations

$$\frac{\partial \theta}{\partial X} = \frac{1}{\epsilon} k(X), \tag{3.7}$$

$$\frac{\partial \theta}{\partial t} = -\omega. \tag{3.8}$$

The asymptotic expansions of  $k$  and  $\phi$  in terms of  $\epsilon$  (Benney and Rosenblat, 1964) are as follows:

$$k = k_0(X) + \epsilon k_1(X) + \epsilon^2 k_2(X) + \dots \tag{3.9}$$

$$\phi_n = \phi_n^{(0)}(X, y) + \epsilon \phi_n^{(1)}(X, y) + \epsilon^2 \phi_n^{(2)}(X, y) + \dots \tag{3.10}$$

If we substitute the relations (3.6)–(3.10) into (3.5) and (2.5), we obtain a sequence of equations for different orders of  $\epsilon$ .

$O(1)$  problem

$$\begin{aligned} & -(U_n k_0 - \omega) \left( \frac{\partial^2 \phi_n^{(0)}}{\partial y^2} - k_0^2 \phi_n^{(0)} \pm F(\phi_2^{(0)} - \phi_1^{(0)}) \right) \\ & + k_0 \phi_n^{(0)} \beta \pm k_0 \phi_n^{(0)} F(U_1 - U_2) \\ & - ir \left( \frac{\partial^2 \phi_n^{(0)}}{\partial y^2} - k_0^2 \phi_n^{(0)} \right) = 0 \end{aligned} \tag{3.11}$$

$$\phi_n^{(0)} = 0 \text{ at } y = 0, 1. \tag{3.12}$$

Since the coefficients in Eq. (3.11) are not functions of  $y$ ,  $\phi_n^{(0)}$  can be sought in the form

$$\phi_n^{(0)} = \Phi_n^{(0)}(X) \sin m\pi y \tag{3.13}$$

which satisfies the boundary condition (3.12) automatically. When (3.13) is substituted into Eq. (3.11), two algebraic equations for unknowns  $\Phi_1^{(0)}$  and  $\Phi_2^{(0)}$  are obtained:

$$\begin{aligned} & i(-\omega + U_n k_0) [-(k_0^2 + m^2 \pi^2) \Phi_n^{(0)} \pm F(\Phi_2^{(0)} - \Phi_1^{(0)})] \\ & + ik_0 \Phi_n^{(0)} \pm ik_0 \Phi_n^{(0)} F(U_1 - U_2) - r(k_0^2 + m^2 \pi^2) \Phi_n^{(0)} = 0. \end{aligned} \tag{3.14}$$

The determinant of the coefficients of  $\Phi_1^{(0)}$  and  $\Phi_2^{(0)}$  in (3.14) must vanish in order for  $\Phi_1^{(0)}$  and  $\Phi_2^{(0)}$  to have nontrivial solutions. That is,

$$\begin{aligned} & -(U_1 k_0 - \omega)(U_2 k_0 - \omega)(2FK^2 + K^4) \\ & + k_0(F + K^2)[\beta k_0(U_2 + U_1) - Fk_0(U_1 - U_2)^2 - 2\omega\beta] \\ & + irK^2(F + K^2)[k_0(U_2 + U_1) - 2\omega] \\ & - k_0^2[\beta^2 - F^2(U_1 - U_2)^2] - 2irk_0K^2\beta + r^2K^4 = 0 \end{aligned} \tag{3.15}$$

where

$$K^2 = k_0^2 + m^2 \pi^2. \tag{3.16}$$

Equation (3.15) is the stability equation for parallel baroclinic flow in the two-layer model.

The vertical structure of the disturbance solution at this order is determined by the ratio between  $\Phi_1^{(0)}$  and  $\Phi_2^{(0)}$ , defined as  $R$  which is obtained from (3.14).

$$\begin{aligned} R &= \frac{\Phi_2^{(0)}}{\Phi_1^{(0)}} \\ &= \frac{(U_1 k_0 - \omega)(F + K^2) - k_0[\beta + F(U_1 - U_2)] - irK^2}{(U_1 k_0 - \omega)F} \\ &= Ae^{i\theta}, \end{aligned} \tag{3.17}$$

where  $A$  is the amplitude ratio and  $\theta$ , gives the phase angle difference between the two layers.

For conventional temporal instability, the wave-number  $k$  is a real constant in (3.15), and we seek a complex frequency  $\omega$ . For spatial instability, the frequency  $\omega$  is a real constant and a complex wavenumber  $k$  is sought where the imaginary part of  $k$  will be the spatial growth rate. Here, (3.15) will be solved for com-

plex  $k$  as a function of  $X$ . This gives the local solution for each  $X$ .

Without loss of generality,  $\Phi_1^{(0)}$  is chosen as a constant for all  $X$ . Therefore,

$$\frac{\partial \phi_1^{(0)}(X, y)}{\partial X} = \frac{\partial \Phi_1^{(0)}}{\partial X} \sin m\pi y = 0 \quad (3.18)$$

$$\frac{\partial \phi_2^{(0)}(X, y)}{\partial X} = \Phi_1^{(0)} \frac{\partial R}{\partial X} \sin m\pi y. \quad (3.19)$$

#### $O(\epsilon)$ problem

$$\begin{aligned} i(-\omega + U_n k_0) & \left[ -k_0^2 \phi_n^{(1)} + \frac{\partial^2 \phi_n^{(1)}}{\partial y^2} \pm F(\phi_2^{(1)} - \phi_1^{(1)}) \right] \\ & + ik_0 \phi_n^{(1)} \beta \pm ik_0 \phi_n^{(1)} F(U_1 - U_2) \\ & + r \left( -k_0^2 + \phi_n^{(1)} + \frac{\partial^2 \phi_n^{(1)}}{\partial y^2} \right) \\ & = -i(U_n k_0 - \omega) \left[ -2k_0 k_1 \phi_n^{(0)} + 2k_0 i \frac{\partial \phi_n^{(0)}}{\partial X} + \frac{\partial k_0}{\partial X} i \phi_n^{(0)} \right] \\ & - \left( V_n \frac{\partial}{\partial y} + iU_n k_1 + U_n \frac{\partial}{\partial X} \right) \left[ -k_0^2 \phi_n^{(0)} + \frac{\partial^2 \phi_n^{(0)}}{\partial y^2} \right. \\ & \left. \pm F(\phi_2^{(0)} - \phi_1^{(0)}) \right] - ik_1 \phi_n^{(0)} \beta + \frac{\partial \phi_n^{(0)}}{\partial X} \beta \\ & \mp F(U_2 - U_1) \left( ik_1 \phi_n^{(0)} + \frac{\partial \phi_n^{(0)}}{\partial X} \right) \pm F(V_2 - V_1) \frac{\partial \phi_n^{(0)}}{\partial y} \\ & + r \left( 2k_0 k_1 \phi_n^{(0)} + 2ik_0 \frac{\partial \phi_n^{(0)}}{\partial X} + i \phi_n^{(0)} \frac{\partial k_0}{\partial X} \right) \quad (3.20) \end{aligned}$$

$$\phi_n^{(1)} = 0 \quad \text{at } y = \pm 1. \quad (3.21)$$

The left-hand sides of (3.20) have the same structure as in the  $O(1)$  problem, (3.11). Therefore,  $\Phi_n^1$  has a homogeneous solution with the same structure as  $\Phi_n^{(0)}$ , since the boundary conditions are the same. Let

$$\phi_n^{(1)} = \Phi_n^{(1)}(X) \sin m\pi y. \quad (3.22)$$

After we substitute (3.22) and (3.13) into (3.20), we require that the terms on the right-hand side that are proportional to  $\sin m\pi y$  (i.e., the homogeneous solution) vanish in order to satisfy the solvability condition (Nayfeh, 1979). In abbreviated form, they can be written as

$$\begin{aligned} -R\Phi_1^{(1)} + \Phi_2^{(1)} & = H_1 \\ \Phi_1^{(1)} - \frac{1}{R}\Phi_2^{(1)} & = H_2 \end{aligned} \quad (3.23)$$

where  $H_1$  and  $H_2$  are given in the Appendix and  $R$  is defined in (3.17). The solvability condition is

$$\begin{vmatrix} -R & H_1 \\ 1 & H_2 \end{vmatrix} = 0. \quad (3.24)$$

Since  $k_1$  is the only unknown in (3.24), it can be solved as

$$k_1 = \frac{S_1}{S_2}, \quad (3.25)$$

where  $S_1$  and  $S_2$  are the expressions containing properties of the  $O(1)$  problem. These are also given in the Appendix.

To  $O(\epsilon)$  accuracy, the spatial growth rate of the streamwise solution is

$$\text{Im}k = \text{Im}(k_0 + \epsilon k_1), \quad (3.26)$$

and the local wavenumber is

$$\text{Re}k = \text{Re}(k_0 + \epsilon k_1). \quad (3.27)$$

#### 4. Experiments and results

Although the streamwise variation of the basic flow is small in comparison with the cross-channel variation, the total downstream variation can be large enough to be comparable to the observed variations. As an illustration, the climatological zonal mean winds at levels 200 and 700 mb of the Northern Hemisphere for the months of December, January and February, which were analyzed by Oort (1983), are presented in Fig. 1. Although the climatological mean does not represent the true basic state, this diagram does illustrate the general profile for streamwise variation. We focus our attention on the jet centered over eastern Asia; the variation of the jet in the north-south direction is not included. The appropriate scales and the resulting nondimensional parameters are as follows:

$$\begin{aligned} L & 1500 \text{ km}, \\ D & 5 \text{ km}, \\ U & 30 \text{ m s}^{-1}, \\ \epsilon & 0.2, \\ \beta & 1.5, \\ F & 10.0, \\ r & 0.0. \end{aligned} \quad (4.1)$$

The parameters  $\beta$  and  $r$  are varied in later cases.

The nondimensional basic flows  $U_1$  and  $U_2$  in streamwise direction are prescribed in general as

$$U_1 = a + b \text{sech}(X + h_1) \quad (4.2)$$

$$U_2 = c + d \text{sech}(X), \quad (4.3)$$

where  $X$  is the long spatial coordinate which is defined in (3.1). The constants  $a$ ,  $b$ ,  $c$  and  $d$  determine the magnitudes of the basic flows and the relative shear between the two layers ( $U_1 - U_2$ ). Variations of these constants allow different profiles of the streamwise variation for the jet. The location of the maximum wind region in one layer can be shifted relative to the

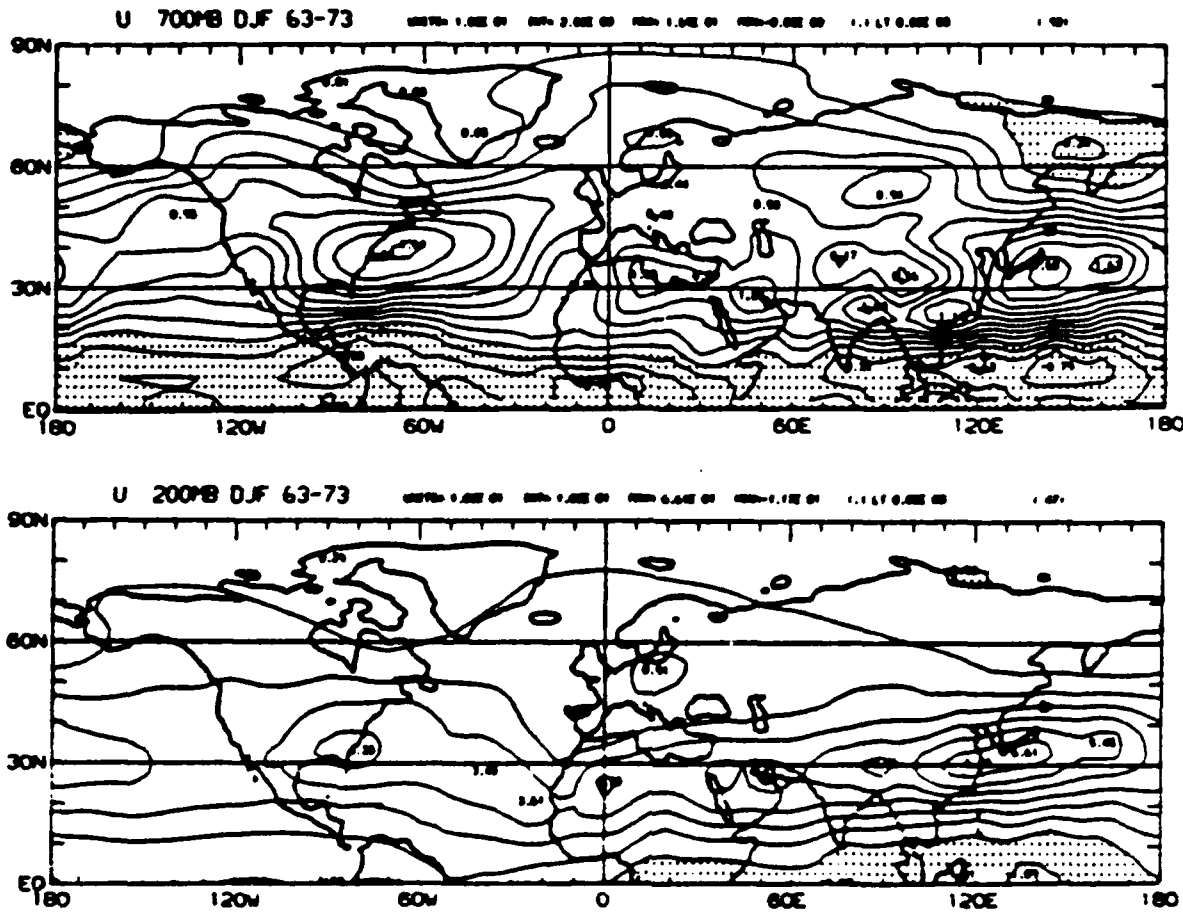


FIG. 1. Mean wintertime zonal wind speed  $U$  at (a) 700 mb; (b) 200 mb; contour interval  $5 \text{ m sec}^{-1}$  adopted from Oort (1983).

maximum in the other layer. Usually, the upper-layer structure lags the structure of the lower layer. Examination of Fig. 1 indicates that the jet maximum at the 200-mb level is located along  $125^\circ\text{E}$ , while the jet maximum at 700 mb is located along  $150^\circ\text{E}$ . In expression (4.2), constant  $h_1$  determines the longitudinal shift of the streamwise variation of the basic flows between the two layers. To understand the problem in a systematic way, some of the constants in (4.2) and (4.3) are set to zero first so that simple cases can be isolated. In the diagrams where the mean flows are plotted as functions of  $X$ , the solid line is the upper-layer mean flow and the dashed line is the lower-layer mean flow. In diagrams where the streamwise and local solutions are presented, the solid line refers to the local parallel flow solution obtained from the  $O(1)$  problem and the dashed line refers to the streamwise (nonparallel) solution. The streamwise solution is the sum of the local solution and the  $O(\epsilon)$  correction, i.e., Eqs. (3.26) and (3.27).

It is informative to review the previous study by Peng and Williams (1986) which examined the mechanism of barotropic instability in a jet with streamwise variation. In their discussion, the difference between the

spatial growth rate with streamwise variation and the local spatial growth rate is related to two effects. First, a lag effect occurs when the structure of the disturbance calculated by local parallel flow theory varies downstream due to the variation in the basic flow. As the disturbance propagates through regions of different basic flow, there is a lag in the adjustment of the disturbance structure to the local structure obtained from parallel flow theory. In regions where the parallel flow growth rate increases downstream, the nonparallel growth rate will be smaller than the local parallel growth rate and vice versa. The second effect depends on the relative phase speed between the streamwise solution and the local solution. If the phase speed for the streamwise solution is larger (smaller) than the phase speed for the local solution, the disturbance will have less (more) time to grow in space and the streamwise growth rate will be smaller (larger) than the local growth rate.

#### a. Case 1

In this case,  $h_1$  is set to zero so that there is no longitudinal shift of the basic flow structure between the

layers. We further keep the upper-layer flow constant and only allow the basic flow in the lower layer to vary downstream, i.e.,

$$\begin{aligned} U_1 &= 2.0, \\ U_2 &= 1.1 - \text{sech}(X), \\ U_1 - U_2 &= 0.9 + \text{sech}(X). \end{aligned} \quad (4.4)$$

The speeds  $U_1$  and  $U_2$  are plotted as functions of  $X$  in Fig. 2, where  $X$  is between  $-3.0$  and  $3.0$ . The vertical shear,  $(U_1 - U_2)$ , reaches a maximum at  $X = 0$ . The streamwise and local spatial growth rates for these basic flows are presented in Fig. 3. The solid line for the parallel flow solution and the dashed line which is the streamwise solution are almost identical in this case. Thus, the streamwise variation of the basic flow causes only a very small correction to the local growth rate.

Let us examine the two effects discussed in Peng and Williams (1986) to explain the present results. The streamwise and local phase speeds are plotted in Fig. 4. These two quantities are also indistinguishable, indicating that the effect due to different phase speeds (the second effect in Peng and Williams, 1986) is unimportant. The local vertical structure of the disturbance, determined by the ratio between solutions for the upper and the lower layers, is expressed as  $R$  in (3.17). This ratio, determined locally at each point as a function of  $X$ , is a complex variable and can be represented by its amplitude  $A$  and phase angle  $\theta_p$ . The two quantities for this case are given in Fig. 5a and 5b respectively. Although the vertical shear varies in the downstream direction (Fig. 2), it is interesting to note that the phase angle is almost the same everywhere and the amplitude changes only slightly. Due to this very small variation in the vertical structure, the disturbance does not need time (or space) to adjust itself to the local structure and no lag effect is experienced. This explains why the growth rates for the streamwise and local solutions are almost identical.

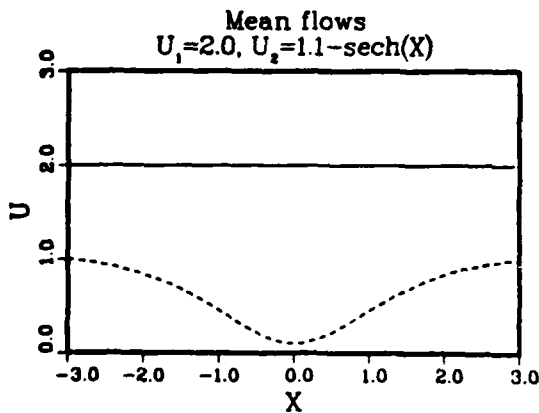


FIG. 2. Variations of the upper and lower layer mean flow  $U_1$  (solid line) and  $U_2$  (dashed line) as functions of  $X$  for case 1.

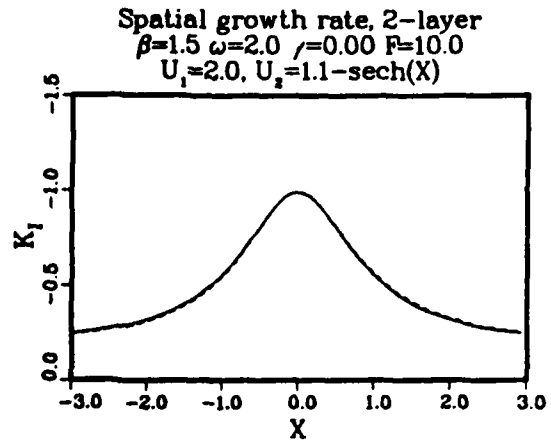


FIG. 3. Local (solid line) and streamwise (dashed line) spatial growth rates for the basic flows shown in Fig. 2 in case 1.

b. Case 2

In the second case, the basic flow for the upper layer varies while that for the lower layer remains constant. The profiles (Fig. 6) are given by

$$\begin{aligned} U_1 &= 1 + \text{sech}(X), \\ U_2 &= 0.9, \\ U_1 - U_2 &= 0.1 + \text{sech}(X). \end{aligned} \quad (4.5)$$

The streamwise variation of the vertical shear in this case is the same as in case 1, but the magnitude of the shear is smaller everywhere. The phase speeds for the streamwise and local solutions are essentially the same as those in case 1 (not shown), so that the streamwise effect due to different phase speeds mentioned above contributes little to the total solution. The local structures of the disturbances are given in Fig. 7 as a function of  $X$ . Both the phase angle (7a) and the amplitude (7b)

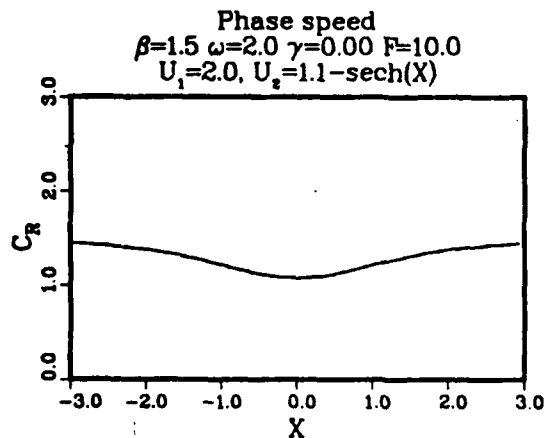


FIG. 4. Local (solid line) and streamwise (dashed line) phase speeds for case 1 as in Fig. 2.

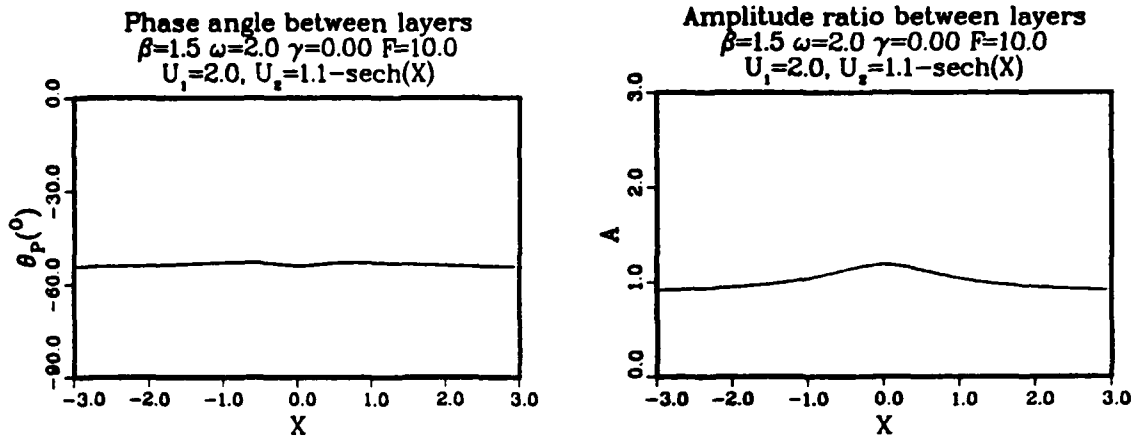


FIG. 5. Local vertical structure of the disturbance as function of  $X$ . (a) Phase angle between the upper and lower layers; (b) amplitude ratio for case 1.

show streamwise variation, especially in the entrance and outflow regions. This indicates that a lag effect is expected. The spatial growth rates in Fig. 8 clearly show the difference between the nonparallel and local solutions which is caused by the lag effect. The downstream effect, from the  $O(\epsilon)$  correction, is proportional to the first derivative of the  $O(1)$  properties with respect to  $X$ , as was discussed in Peng and Williams (1986a). With the symmetric properties of the  $O(1)$  solution, the  $O(\epsilon)$  correction is antisymmetric as observed.

c. Case 3

In this case, the flows in the upper and the lower layer change simultaneously in the streamwise direction. The profiles, displayed in Fig. 9, are:

$$\begin{aligned} U_1 &= 1 + \text{sech}(X), \\ U_2 &= 0.6 + 0.4 \text{sech}(X), \\ U_1 - U_2 &= 0.4 + 0.6 \text{sech}(X). \end{aligned} \quad (4.6)$$

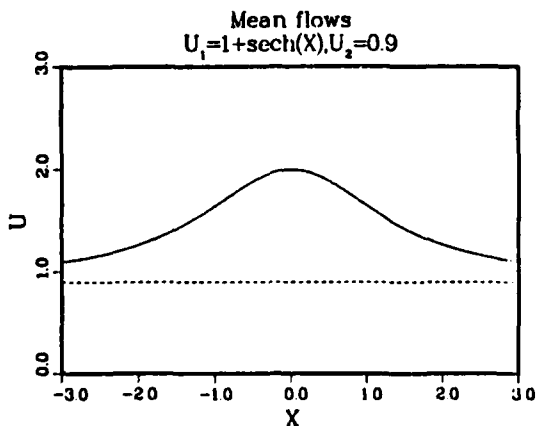


FIG. 6.  $U_1$  and  $U_2$  variations for case 2.

If temporal growth were sought, the maximum growth rate region would be located at the place where the vertical shear is maximum, i.e.,  $X = 0$  in this case. This is not always true for the spatial growth rate. Physically, the temporal growth can be linked to the spatial growth by

$$k_I = -\frac{\omega_I}{C_R}, \quad (4.7)$$

where  $C_R$  is the phase speed,  $\omega_I$  the temporal growth rate and  $k_I$  is the spatial growth rate.

In general, as discussed in Peng and Williams (1987), this equation can be treated only as a link between these two types of instability and precise values of one growth rate cannot be obtained from the other using this equation. However, for the present model, Eq. (4.7) does provide very accurate results. In this case, the dispersion relation for these two types of instability is identical with the relation  $\omega = k \cdot C$ .

Since the phase velocity  $C_R$  is proportional to the averaged flow speed, from (4.7), the spatial growth rate will be smaller for the same shear when the averaged mean flow is larger. In this case, the parallel growth rate which is the solid line in Fig. 10 has a local minimum at the center point where the shear is a maximum. The streamwise solution represented by the dashed line in Fig. 10 is very close to the parallel solution. The difference between the parallel and nonparallel phase speeds are small (not shown), with the nonparallel phase speed slightly slower than the parallel phase speed upstream of  $X = 0$  and slightly faster downstream. The amplitude of the vertical difference is almost uniform as in Fig. 11b, but the phase difference changes substantially (Fig. 11a). In order to have a significant lag effect, both the amplitude and the phase of the vertical difference have to vary substantially in the streamwise direction. Therefore, in this case, the vertical disturbance structure leads to a small lag effect (Fig. 10).

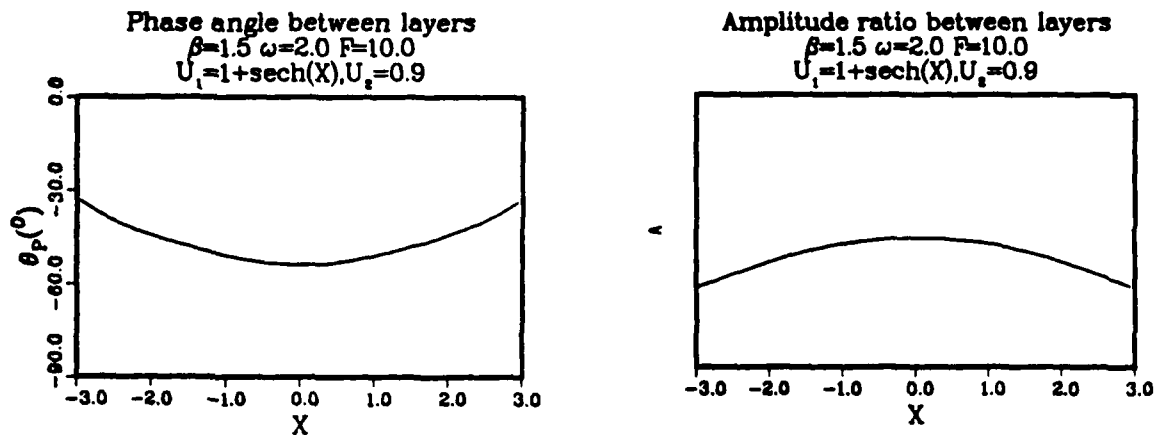


FIG. 7. (a) Phase angle between the upper and lower layer; (b) amplitude ratio for case 2.

d. Case 4

The variation of the mean flow in this case is similar to case 3, but the maximum speed region is shifted for different layers. Referring to Fig. 1, the upper flow lags the lower layer by approximately 1/6 of the length of the domain considered. The profiles, which are plotted in Fig. 12, are

$$\begin{aligned}
 U_1 &= 1 + \operatorname{sech}(X+1), \\
 U_2 &= 0.3 + 0.4 \operatorname{sech}(X), \\
 U_1 - U_2 &= 0.7 + \operatorname{sech}(X+1) - 0.4 \operatorname{sech}(X). \quad (4.8)
 \end{aligned}$$

In Fig. 13, the spatial growth rate has a minimum near  $X = 0.3$  and the nonparallel effect shows the result expected by examining the structure variation in Fig. 14.

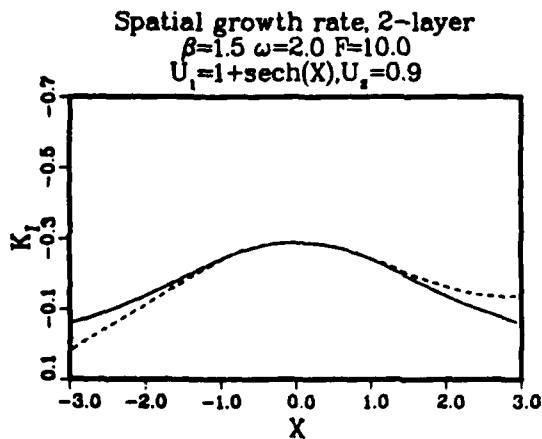


FIG. 8. Spatial growth rate for local (solid line) and streamwise (dashed line) solutions for case 2 as in Fig. 6.

e. Case 5

In this case, the upper flow has the same value as in case 4, but the speed of the lower layer is increased so that the magnitude of the vertical shear is decreased (Fig. 15), i.e.,

$$\begin{aligned}
 U_1 &= 1 + \operatorname{sech}(X+1), \\
 U_2 &= 0.6 + 0.7 \operatorname{sech}(X), \\
 U_1 - U_2 &= 0.4 + \operatorname{sech}(X+1) - 0.7 \operatorname{sech}(X). \quad (4.9)
 \end{aligned}$$

In Fig. 16, the parallel growth rate (solid line) is similar to that of case 4, yet, very significant nonparallel effects (dashed line) are observed near the minimum growth rate region, i.e.,  $X = 0.5$ . The phase speed in Fig. 17 indicates a slightly slower phase speed for the nonparallel flow upstream from  $X = 0.5$  and slightly faster phase speed downstream. From the second effect

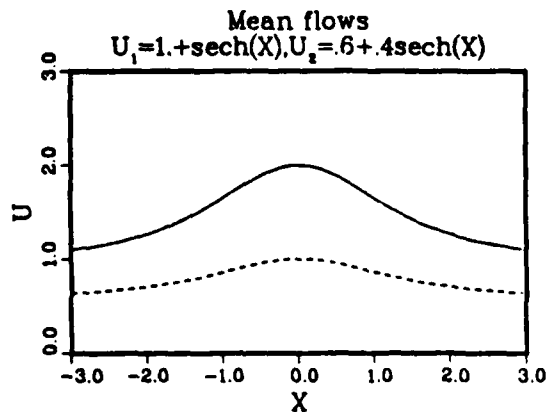


FIG. 9.  $U_1$  and  $U_2$  profiles for case 3.

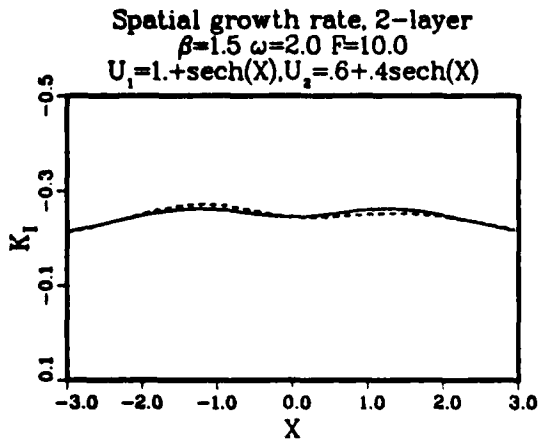


FIG. 10. Local (solid line) and streamwise (dashed line) spatial growth rate for case 3 as in Fig. 9.

proposed by Peng and Williams (1986), the nonparallel growth rate would be slightly larger than the parallel growth rate upstream of  $X = 0.5$  and vice versa downstream. Furthermore, in Fig. 18, both the phase angle and the amplitude of the vertical difference in disturbance structure show substantial variation near the minimum shear region at  $X = 0.5$ . Thus, lag effect makes the dominant contribution to the nonparallel effect in this region.

When the frictional coefficient  $r$  increases from 0.0 to 0.1, the overall growth rate decreases and the lag effect also decreases.

The five cases presented above indicate that the two effects discussed in Peng and Williams (1986) can successfully explain the streamwise effects obtained in the present study. A major result is that, although the streamwise variation of the basic flow considered here is twice the variation in previous barotropic study (i.e.,  $\epsilon = 0.2$  vs  $\epsilon = 0.1$ ), the nonparallel solutions are very close to the local parallel solutions for most of the cases considered. The smallness of downstream effects comes from the fact that the vertical structure of the disturbances is essentially insensitive to variations in the vertical shear. In the next section, we will analyze the dependency of the vertical structure on the shear and other parameters.

5. Dependency of the vertical structure of the disturbance on the shear

Equation (3.14) contains two separate equations for the disturbances of the upper ( $n = 1$ ) and lower ( $n = 2$ ) layers. The ratio  $R$  between the disturbances in the upper and lower layers, which is given by (3.17), can be obtained by setting either  $n = 1$  or  $n = 2$  in (3.14). An alternative is to add the  $n = 1$  and  $n = 2$  equations from (3.14), which gives

$$\frac{\Phi_1^{(0)}}{\Phi_2^{(0)}} = -\frac{-K^2(U_2 k_0 - \omega) + k_0 \beta + irK^2}{-K^2(U_1 k_0 - \omega) + k_0 \beta + irK^2} \quad (5.1)$$

For simplification, the frictional coefficient  $r$  is set equal to zero in (5.1). With  $\omega = kC$ , the analysis falls back to the temporal instability and (5.1) becomes

$$\frac{\Phi_1^{(1)}}{\Phi_2^{(1)}} = -\frac{[(U_2 + U_1)/2 - C_R + \beta/K^2]^2 - \frac{1}{4}(U_1 - U_2)^2 + C_I^2 + iC_I(U_2 - U_1)}{[(C - U_1 + \beta/K^2)]^2} = Ae^{i\theta} \quad (5.2)$$

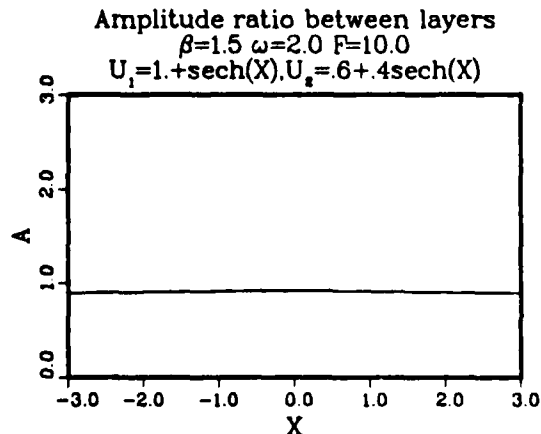
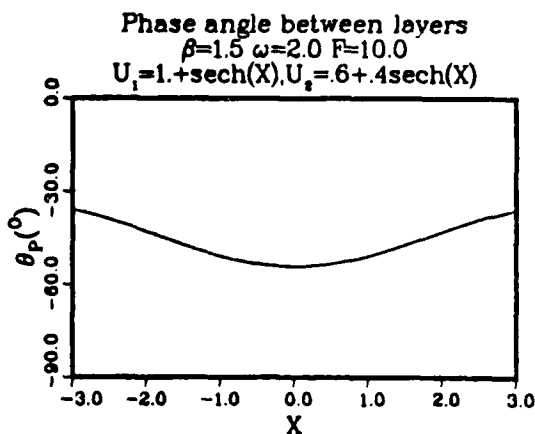


FIG. 11. (a) Phase angle; (b) amplitude ratio between the two layers for case 3 where the  $U_1$  and  $U_2$  profiles are in Fig. 9.

where  $C$  is the complex phase speed and  $C = C_R + iC_I$ . The phase angle  $\theta_p$  in (5.2) is

$$\theta_p = \tan^{-1} \left[ \frac{-C_I(U_1 - U_2)}{-\frac{1}{2}(U_1 - U_2)^2 + \left[\frac{1}{2}(U_1 + U_2) - C_R + \beta/K^2\right]^2 + C_I^2} \right] \quad (5.3)$$

and the amplitude  $A$  is

$$A = \frac{\{[(\frac{1}{2}(U_2 + U_1) - C_R + \beta/K^2)^2 - \frac{1}{2}(U_1 - U_2)^2 + C_I^2]^2 + C_I^2(U_1 - U_2)^2\}^{1/2}}{|C - U_1 + \beta/K^2|^2} \quad (5.4)$$

First, consider the situation when  $\beta = 0$ . From Eq. (7.11.9) in Pedlosky (1979),

$$C_R = \frac{1}{2}(U_1 + U_2), \quad (5.5)$$

$$C_I = \pm \frac{1}{2}(U_1 - U_2) \left[ \frac{2F - K^2}{2F + K^2} \right]^{1/2} \quad (5.6)$$

Introducing (5.5) and (5.6) into (5.3), the expression becomes

$$\theta_p = \tan^{-1} \left[ \frac{2 \cdot \left( \frac{2F - K^2}{2F + K^2} \right)^{1/2}}{\left[ -1 + \left( \frac{2F - K^2}{2F + K^2} \right) \right]} \right] \quad (5.7)$$

Therefore, when  $\beta = 0$ , the phase difference does not depend explicitly on the shear, but only on the scale of the wave which is determined by  $k_0$ . With expression (3.16) evaluated for  $m = 1$ , we have

$$\begin{aligned} 2F - K^2 &= 2F - \pi^2 - k_0^2, \\ 2F + K^2 &= 2F + \pi^2 + k_0^2. \end{aligned} \quad (5.8)$$

For very long wave,  $k_0 \sim 1$ , and  $k_0^2 \sim O(1)$  which is an order smaller than  $(2F - \pi^2)$  or  $(2F + \pi^2)$ . Thus, the variation of  $k_0$  in the streamwise direction is even smaller and it can be neglected in (5.6). For example, when  $k_0 = 1$

$$\theta_p \approx 55^\circ \quad (5.9)$$

which is about the average phase angle in our results.

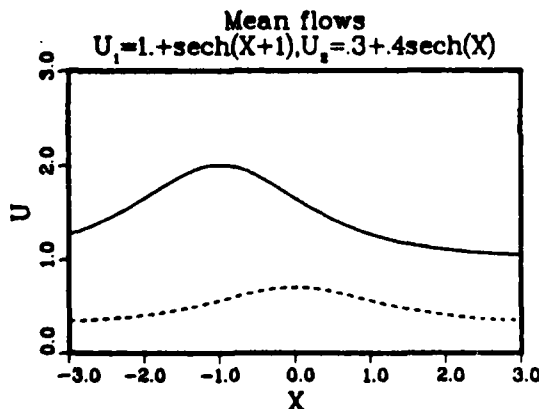


FIG. 12.  $U_1$  and  $U_2$  profiles for case 4.

For higher frequency, the wavenumber increases and contribution from  $k$  in  $2F - K^2$  is no longer small. If  $k$  is  $\sim 3.5$ , then  $2F - K^2 \sim 0$  and the phase angle between the layers approaches zero, which gives no instability. Since the wavenumber increases with the frequency, there is an upper bound of the frequency for spatial instability, as demonstrated by Merkin (1977) in his Fig. 4. The variation of  $\theta_p$  will be larger for shorter waves with larger  $k_0$ .

As for the amplitude  $A$ , when  $\beta = 0$  the expression (5.4) becomes identically equal to 1 when (5.5) and (5.6) are used. In other words, the amplitude  $A$  is totally independent of the shear and the scale of the waves when  $\beta$  equals zero.

When  $\beta \neq 0$ , Eq. (7.11.13) in Pedlosky (1979) gives

$$C_R = \frac{U_1 + U_2}{2} - \frac{(K^2 + F)}{K^2(K^2 + 2F)} \quad (5.10)$$

$$C_I = \pm \frac{1}{2K^2(K^2 + 2F)} \{4^2 F^2 - K^4 U_2^2 (4F^2 - K^4)\}^{1/2} \quad (5.11)$$

$$\theta_p = \tan^{-1} \left[ - \frac{C_I(U_1 - U_2)}{\frac{1}{2}(U_1 - U_2)^2 + \left[ \frac{F}{K^2(K^2 + F)} \right]^2 + C_I^2} \right] \quad (5.12)$$

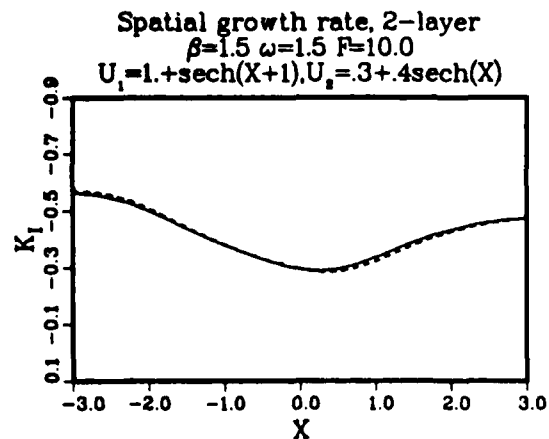


FIG. 13. Local (solid line) and streamwise (dashed line) spatial growth rate for case 4 as in Fig. 12.

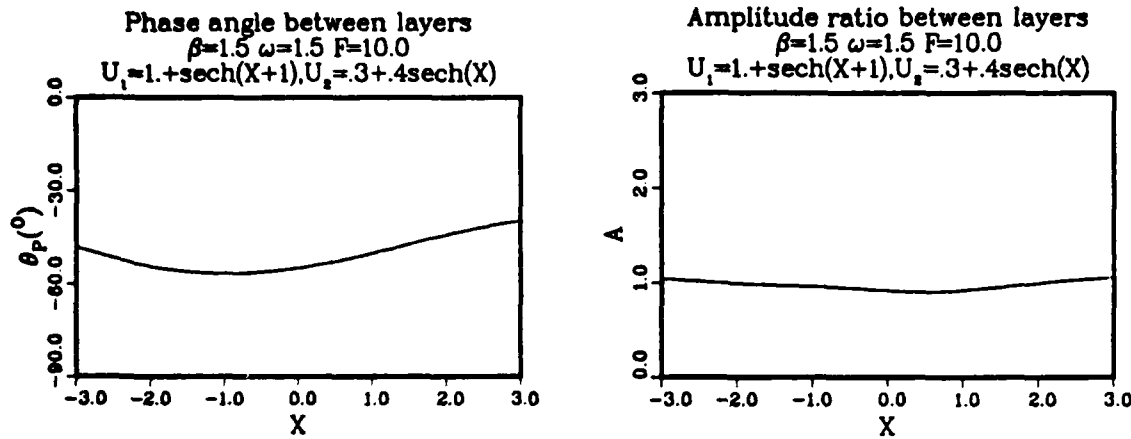


FIG. 14. (a) Phase angle; (b) amplitude ratio between the two layers for case 4 as in Fig. 12.

$$A = \frac{\left\{ \left[ \frac{\beta^2(2K^2 + 3F)^2}{K^4(K^2 + 2F)^2} - \frac{1}{4}(U_1 - U_2)^2 + C_l^2 \right]^2 + C_l^2(U_1 - U_2)^2 \right\}^{1/2}}{\left( \frac{\beta F}{K^2(K^2 + 2F)} - \frac{U_1 - U_2}{2} \right)^2 + C_l^2} \quad (5.13)$$

Now the variation of  $k_0$  and the shear would have a larger effect on the variations of  $\theta_p$  and  $A$ . When the shear is large, the  $\beta$  effect is comparatively small, and the variations of  $\theta_p$  and  $A$  are small. If the shear is small, however, the  $\beta$  effect becomes important and variations of  $\theta_p$  and  $A$  are large. For all the cases discussed in section 4, we have  $\beta \neq 0$ . In case 5, the minimum shear region is near  $X = 0.5$ , where both the phase angle and the amplitude variations are substantial and the streamwise effect is large in that region due to the lag effect. In case 2, the shear decreases toward the inflow and outflow regions, variations of the phase angle and the amplitude become large and the lag effect increases. For case 1, the streamwise variation of the shear is the same as in case 2, but the absolute shear value is much larger everywhere than in case 2. Therefore, the disturbance structure is more uniform and

the lag effect is negligible. For the same reason, the minimum shear in case 4 ( $X = 0.3$  in Fig. 12) is larger than the minimum shear in case 5 ( $X = 0.5$  in Fig. 15). Consequently, the local vertical structure in case 4 does not show a large variation near the minimum shear region (compare Fig. 14 with Fig. 18).

To verify the above analysis, case 2 is recalculated with  $\beta = 0$ , keeping all other parameters unchanged. The variation in the vertical structure is greatly reduced, as can be seen by comparing Fig. 19 with Fig. 7. The reduced variation of the disturbance structure greatly reduces the lag effect as is evident in Fig. 20. The slight nonparallel effect in this case comes from the phase speed difference mechanism. As a further illustration,  $\beta$  is kept the same as in case 2, but the shear is increased

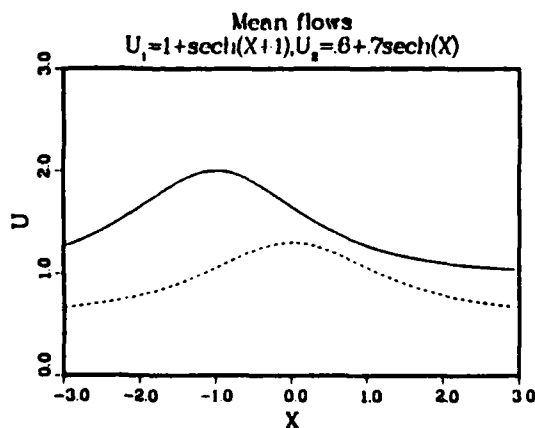


FIG. 15.  $U_1$  and  $U_2$  profiles for case 5.

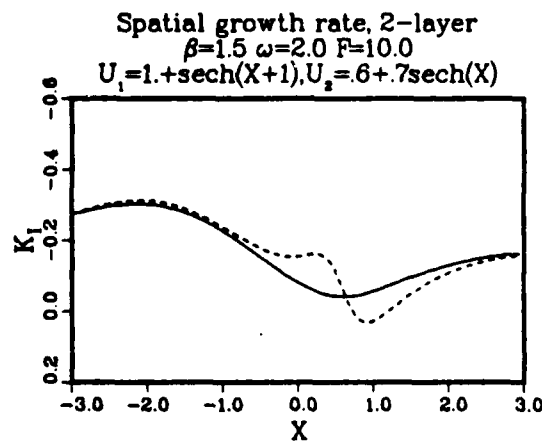


FIG. 16. Local (solid line) and streamwise (dashed line) spatial growth rate for case 5 as in Fig. 15.

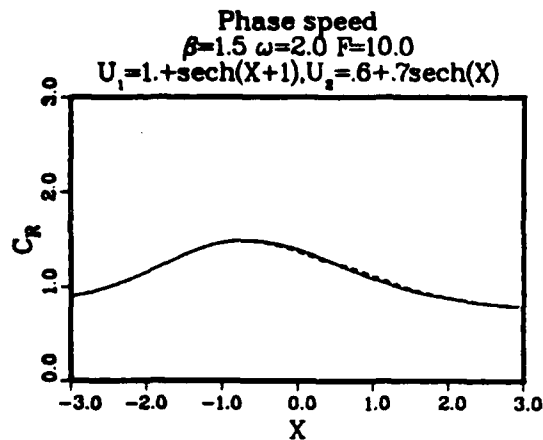


FIG. 17. Local (solid line) and streamwise (dashed line) phase speeds for case 5 as in Fig. 15.

by increasing the uniform part of the upper layer flow; i.e.,

$$\begin{aligned} U_1 &= 1.5 + \text{sech}(X), \\ U_2 &= 0.9. \end{aligned} \quad (5.12)$$

As in Fig. 19, the variation of the local vertical structure (Fig. 21) is also greatly reduced as can be seen by comparison with Fig. 7, and the nonparallel effect in Fig. 22 is the same as in Fig. 20. Therefore, increasing the shear causes the same result as decreasing the  $\beta$  effect. Both of them will reduce the variation of the vertical structure with respect to the variation of the shear, rendering the lag effect less unimportant.

## 6. Discussion

In this paper, the two-scale technique is applied to study the nonparallel effects with basic flows which vary slowly in the streamwise direction in the two-layer baroclinic model. Different streamwise variations of the basic flows are analyzed, including vertical shifting of the maximum wind speed region in the two layers.

The difference between the nonparallel flow solution and the parallel flow solution which is determined locally, is explained successfully with the mechanisms discussed previously by Peng and Williams (1986a) for the barotropic model. The nonparallel contribution is mainly dominated by the lag effect, which is determined by the streamwise variation of the vertical disturbance structure. This vertical structure is the ratio between the disturbance solutions for the upper and lower layers and is represented by its amplitude and the phase angle. The lag effect is significant when both the amplitude and the phase angle change substantially in the streamwise direction.

Variations of the vertical structure are analyzed by using the temporal instability, because  $\omega = kC$  precisely links the temporal and spatial growth for the present model. When the  $\beta$ -effect is excluded, or the magnitude of the shear is large, the disturbance structure is almost uniform in the streamwise direction irrespective of a substantial variation of the shear. In this case, the lag effect is small, and the locally determined solution is very close to the total solution. The lag effect is important when the shear is small. Therefore, the nonparallel correction is more important during the summer than the winter for the atmospheric jets.

Grotjahn (1984b) used numerical integration of a high-resolution multilevel spectral model to study baroclinic instability in an environment with long waves. In his uniform basic state, the vertical shear had a nondimensional value of 1 corresponding to our scaling. In his experiment which corresponded most closely to ours, the vertical shear increased along the jet. For this experiment he found that the disturbance vertical structure did not change appreciably downstream (Fig. 5, Grotjahn, 1984b). Although he did not compare the local and streamwise varying solutions, his finding that the disturbance structure did not vary downstream agrees with our result for large vertical shear. The consistency between his results and ours may not be fortuitous and it may indicate that our analysis concerning the vertical structure variation can

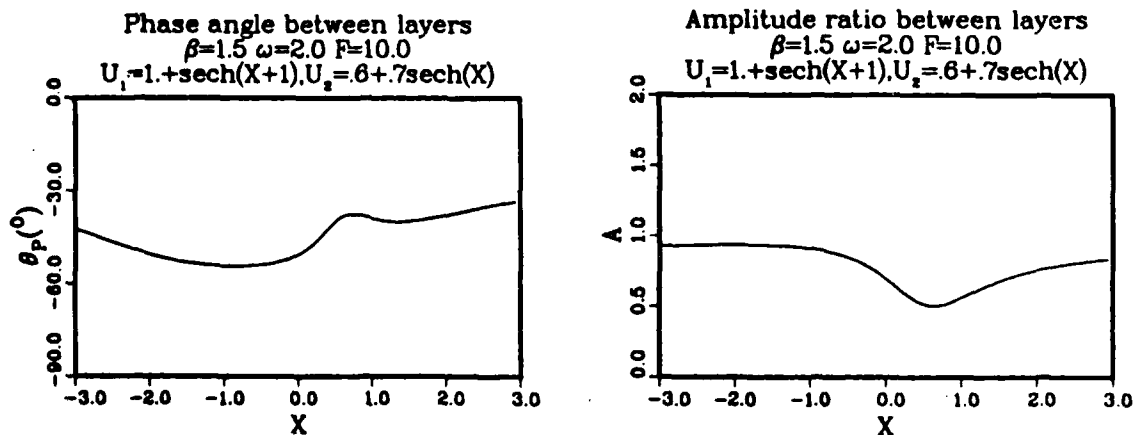


FIG. 18. (a) Phase angle; (b) amplitude ratio between the two layers for case 5 as in Fig. 15.

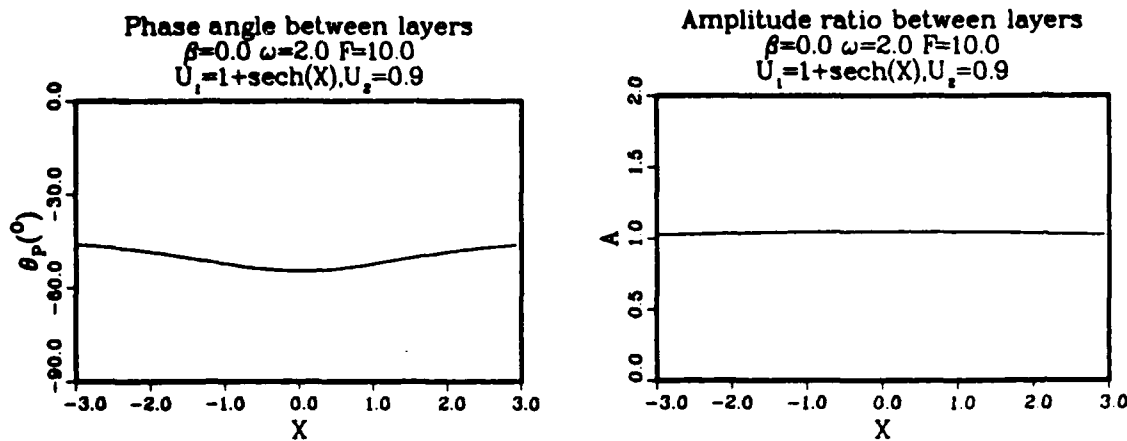


FIG. 19. (a) Phase angle; (b) amplitude ratio between the two layers with the mean flows  $U_1$  and  $U_2$  the same as in case 2 except  $\beta = 0$ .

be applied to the continuously stratified flows. More studies are needed to verify this.

As mentioned in the introduction, Pierrehumbert (1984) studied the time evolution of a baroclinic disturbance in the two-layer model in a basic flow with streamwise variation. The results from the numerical integration were compared with an analytical solution, which was obtained locally using parallel flow theory. No correction for the streamwise variation in the mean flow was included. However, the numerical results contain the streamwise effect, and the closeness of these solutions agrees with our results.

In an early study, Ling and Reynolds (1973) examined the nonparallel effect for several different types of shear flow with streamwise variation. The higher order correction was found to be important for some situations and not for others. No physical reason was given to explain their results.

From the climatological data analyzed by Blackman et al. (1978) and Lau (1979), the location of the maxi-

imum amplitude for the eddies is shifted downstream from the region of maximum shear. Frederiksen (1978, 1979, 1980) and Niehaus (1980, 1981) superimposed a long wave upon a zonally uniform flow. The temporal approach was used by them with cyclic boundary conditions. This procedure yields a single growth rate and an eigenfunction whose envelope varies in the streamwise direction. The exact reason for the downstream shifting of the envelope was not explained explicitly. Pierrehumbert (1984) elucidated this point. In his study, where the basic flow supported absolute instability in some region, the frequency obtained at the maximum absolute instability dominated the whole domain. The complex wavenumber obtained locally with that fixed frequency from the dispersion relation determined the spatial structure and spatial growth (or decay). The wave envelope had a maximum amplitude at the point where the spatial growth (the imaginary part of the wavenumber) vanished; i.e.,

$$\frac{1}{\psi} \frac{\partial \psi}{\partial x} = -k_I. \quad (6.1)$$

In barotropic studies with streamwise varying mean flows, Tupaz et al. (1978) and Williams et al. (1984) found spatially growing disturbances with a maximum amplitude downstream from regions of maximum temporal instability. Tupaz et al. integrated the equation numerically with periodic forcing on the upstream boundary. After an adjustment phase, the entire field began to oscillate with the forced frequency, since in this case there was no absolute instability. For a basic flow that does not support absolute instability, a train of waves can move into the region that is baroclinically unstable. The disturbances then grow spatially as they propagate downstream and the amplitude of the wave packet increases with distance. At the point where the spatial growth rate vanishes, the amplitude reaches a maximum. The frequency that will dominate is the one that has the largest overall spatial growth, while if there is absolute instability somewhere in the domain, the frequency would be the one excited by the maxi-

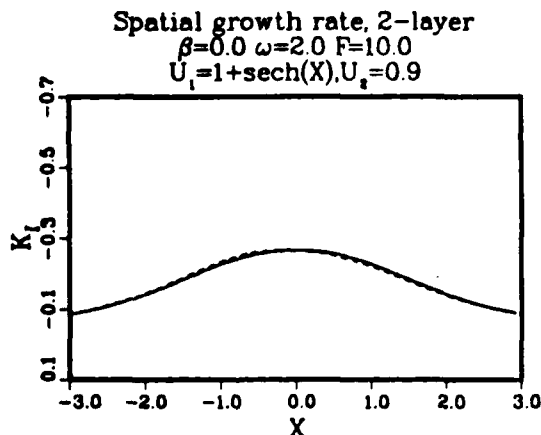


FIG. 20. Local (solid line) and streamwise (dashed line) spatial growth rate with the mean flow  $U_1$  and  $U_2$  the same as in case 2 except  $\beta = 0$ .

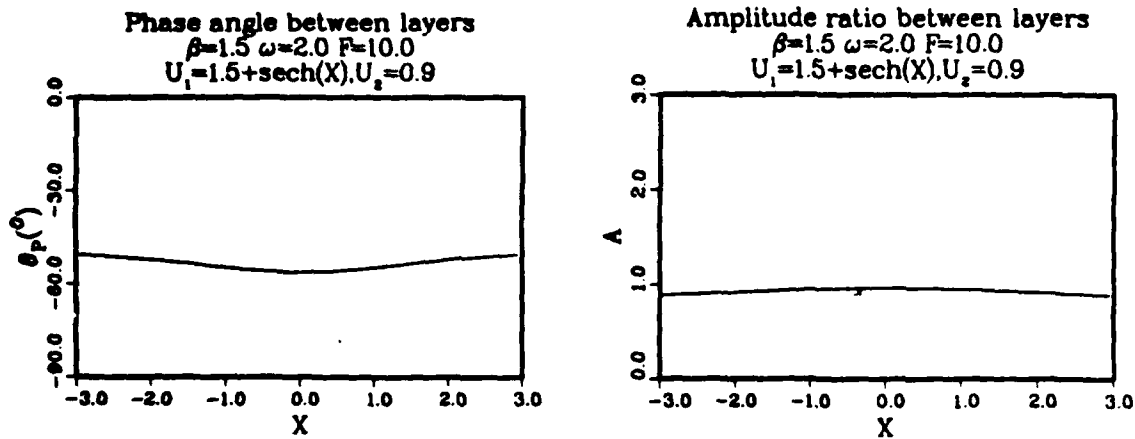


FIG. 21. (a) Phase angle; (b) amplitude ratio between the two layers for  $U_1$  and  $U_2$  profiles given in (5.12) and  $\omega = 1.5$ .

mean absolute instability as discussed in Pierrehumbert (1984). Nevertheless, with or without absolute instability, the downstream shifting of the maximum amplitude of the wave envelope is demonstrated clearly by the spatial growth. From the pure temporal instability approach, it is not clear how this can be demonstrated.

Pedlosky (1976) carried out a finite amplitude study with the two-layer quasi-geostrophic model of a flow with an abrupt change in the baroclinic stability properties. On the upwind side of the change there was a uniform weak instability and on the downwind side the flow was stable. He also considered the reversed situation. Our study differs in that we allow a smooth transition and a finite change in the stability parameter over a large distance. In his steady amplitude solutions he used the spatial growth approach. When his equations are linearized, the maximum amplitude occurs a short distance into the stable region. There is a lag effect which comes from the matching condition when

the flow passes from the unstable region to the stable region, but he did not discuss it in the linear context.

In the present study the  $O(\epsilon)$  correction to the local spatial growth rate from the streamwise variation in the mean flow is small. This suggests that under more general conditions the local spatial growth solution will give a good first estimate of the behavior as long as the streamwise scale is large compared with the disturbance scale. On the other hand, since the corrections are very small when the shear is not too small, the theory should be applicable to somewhat smaller scale streamwise variations, i.e., where  $\epsilon$  is not small. Consider, for example, the cyclogenesis problem in the lee of a long mountain range like the Rocky Mountains. Suppose that the baroclinicity is enhanced near the mountains. Since the phase speed may also increase, the local spatial growth rate may not increase, as can be seen from (4.7). Even if the growth rate is increased, the effect on the disturbance amplitude will be small if the width of the more unstable area is small. If a more realistic model were used (mean flow with horizontal shear, more vertical layers, explicit topography, etc.), the lag effect is small, and the locally-determined solution is (1986) would be more important. This lag effect would then further reduce the enhanced instability near the topography, since the disturbance would not have enough time in the region which has a larger local growth rate to take advantage of the enhanced instability.

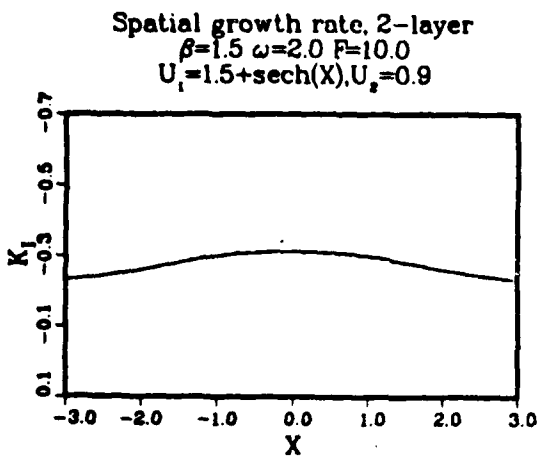


FIG. 22. Local (solid line) and streamwise (dashed line) spatial growth rate corresponding to Fig. 21.

*Acknowledgments.* The authors wish to thank Dr. William Blumen for reading the manuscript and for useful discussions on the research. The first author was supported during part of this research by a National Research Council Associateship. The NRC Associate Program is supported by the Naval Postgraduate School Foundation Research Program, which is funded by the Chief of Navy Material. This research was also supported by the Division of Atmospheric Sciences, National Science Foundation under Grants ATM 83-15175 and ATM 84-44699. The Manuscript was care-

fully typed by Miss K. Lee and the numerical computations were carried out at the W. R. Church Computer Center at the Naval Postgraduate School.

## APPENDIX

Expression for  $H_1$  and  $H_2$  in Eq. (3.24) obtained from the solvability condition imposed on  $O(\epsilon)$  problem.

$$H_1 = \frac{1}{i(U_1 k_0 - \omega)F} \left\{ k_1 [-2i\omega k_0 \Phi_1 + 3ik_0^2 \Phi_1 + iU_1 m^2 \pi^2 \Phi_1 - i\Phi_1 \beta + iF(U_2 \Phi_1 - U_1 \Phi_2) + 2rk_0 \Phi_1] - (\omega + ir) \left( 2k_0 \frac{\partial \Phi_1}{\partial X} + \Phi_1 \frac{\partial k_0}{\partial X} \right) + 3k_0 U_1 \left( k_0 \frac{\partial \Phi_1}{\partial X} + \Phi_1 \frac{\partial k_0}{\partial X} \right) + U_1 m^2 \pi^2 \frac{\partial \Phi_1}{\partial X} - \beta \frac{\partial \Phi_1}{\partial X} + F \left( U_2 \frac{\partial \Phi_1}{\partial X} - U_1 \frac{\partial \Phi_2}{\partial X} \right) \right\}$$

$$H_2 = \frac{1}{i(U_2 k_0 - \omega)F} \left\{ k_1 [-2i\omega k_0 \Phi_2 + 3ik_0^2 \Phi_2 + iU_2 m^2 \pi^2 \Phi_2 - i\Phi_2 \beta + iF(U_1 \Phi_2 - U_2 \Phi_1) + 2rk_0 \Phi_2] - (\omega + ir) \left( 2k_0 \frac{\partial \Phi_2}{\partial X} + \Phi_2 \frac{\partial k_0}{\partial X} \right) + 3k_0 U_2 \left( k_0 \frac{\partial \Phi_2}{\partial X} + \Phi_2 \frac{\partial k_0}{\partial X} \right) + U_2 m^2 \pi^2 \frac{\partial \Phi_2}{\partial X} - \beta \frac{\partial \Phi_2}{\partial X} + F \left( U_1 \frac{\partial \Phi_2}{\partial X} - U_2 \frac{\partial \Phi_1}{\partial X} \right) \right\}$$

Expression for  $S_1$  and  $S_2$  in (3.26) for the  $O(\epsilon)$  wave-number  $k$ .

$$S_1 = -i \left\{ \frac{1}{(U_1 k_0 - \omega)} \left[ -(\omega + ir) \frac{\partial k_0}{\partial X} + 3k_0 U_1 \frac{\partial k_0}{\partial X} - F U_1 \frac{\partial R}{\partial X} \right] + \frac{1}{(U_2 k_0 - \omega)} \left[ -(\omega + ir) \left( 2k_0 \frac{1}{R} \frac{\partial R}{\partial X} + \frac{\partial k_0}{\partial X} \right) + 3k_0 U_2 \left( \frac{k_0}{R} \frac{\partial R}{\partial X} + \frac{\partial k_0}{\partial X} \right) + \frac{U_2 m^2 \pi^2}{R} \frac{\partial R}{\partial X} - \frac{\beta}{R} \frac{\partial R}{\partial X} + \frac{F U_1}{R} \frac{\partial R}{\partial X} \right] \right\}$$

$$S_2 = \left\{ (2\omega k_0 - 3k_0^2 - U_1 m^2 \pi^2 + \beta + 2irk_0) \left( \frac{1}{(U_1 k_0 - \omega)} - \frac{1}{(U_2 k_0 - \omega)} \right) - \frac{F(U_2 - U_1)R}{(U_1 k_0 - \omega)} - \frac{F(U_1 - U_2)R}{(U_2 k_0 - \omega)} \right\}$$

## REFERENCES

- Blackman, M. L., J. M. Wallace, N. Lau and S. L. Mullen, 1977: An observational study of the Northern Hemisphere wintertime circulation. *J. Atmos. Sci.*, **34**, 1040-1053.
- Benney, D. J., and S. Rosenblat, 1964: Stability of spatially varying and time-dependent flows. *Phys. Fluids*, **7**, 1385-1386.
- Briggs, R. J., 1964: *Electron-Stream Interaction with Plasma*. Chapter 2, the MIT Press.
- Charney, J. G., 1947: The dynamics of long waves in a baroclinic westerly current. *J. Meteor.*, **4**, 135-163.
- Drazin, P. G., 1974: On a model of instability of a slowly varying flow. *Quart. J. Mech. Appl. Math.*, **27**, 69-83.
- Eady, E. T., 1949: Long waves and cyclone waves. *Tellus*, **1**, 33-52.
- Frederiksen, J. S., 1978: Instability of planetary waves and zonal flows in two-layer models on a sphere. *Quart. J. Roy. Meteor. Soc.*, **104**, 841-872.
- , 1979: The effect of long planetary waves on the regions of cyclogenesis. *J. Atmos. Sci.*, **36**, 195-204.
- , 1980: Zonal and meridional variations of eddy fluxes induced by long planetary waves. *Quart. J. Meteor. Soc.*, **106**, 63-84.
- Grotjahn, R., 1984a: Baroclinic instability in a long-wave environment. Part I: review. *Quart. J. Meteor. Soc.*, **110**, 663-668.
- , 1984b: Baroclinic instability in a long-wave environment. Part II: Ageostrophic energy conversions. *Quart. J. Meteor. Soc.*, **110**, 669-693.
- Lau, N., 1979: The structure and energetics of transient disturbances in the Northern Hemisphere wintertime circulation. *J. Atmos. Sci.*, **36**, 982-995.
- Ling, C.-H., and W. C. Reynolds, 1973: Nonparallel flow corrections for the stability of shear flows. *J. Fluid Mech.*, **59**, 571-591.
- Merkine, L., 1977: Convective and absolute instability of baroclinic eddies. *Geophys. Astrophys. Fluid Dyn.*, **9**, 129-157.
- , and M. Shafranek, 1980: The spatial and temporal evolution of localized unstable baroclinic disturbances. *Geophys. Astrophys. Fluid Dyn.*, **16**, 174-206.
- , and R. Balgovind, 1983: Barotropic instability of weakly nonparallel zonal flows. *Geophys. Astrophys. Fluid Dyn.*, **25**, 157-190.
- Nayfeh, A. H., 1979: *Introduction to Perturbation Techniques*. Wiley & Sons, 519 pp.
- , W. S. Saric and D. T. Mook, 1974: Stability of nonparallel flows. *Arch. Mech.*, **26**, 401-406.
- Niehaus, M. C. W., 1980: Instability of nonzonal baroclinic flows. *J. Atmos. Sci.*, **37**, 1447-1463.
- , 1981: Instability of nonzonal baroclinic flows: Multiple-scale analysis. *J. Atmos. Sci.*, **38**, 974-987.
- Oort, A. H., 1983: Global atmospheric circulation statistics, 1958-1973. NOAA Prof. Paper 14, 180 pp.
- Pedlosky, J., 1976: Finite-amplitude baroclinic disturbances in downstream varying currents. *J. Phys. Oceanogr.*, **6**, 335-344.
- , 1979: *Geophysical Fluid Dynamics*. Springer-Verlag, 624 pp.
- Peng, M. S., and R. T. Williams, 1986: Spatial instability of the barotropic jet with slow streamwise variation. *J. Atmos. Sci.*, **43**, 2430-2442.
- , and —, 1987: On the transformations between the temporal and spatial growth rate. Submitted to *J. Atmos. Sci.*
- Phillips, N. A., 1951: A simple three-dimensional model for the study of large-scale extratropical flow patterns. *J. Meteor.*, **8**, 381-394.
- Pierrehumbert, R. T., 1984: Local and global baroclinic instability of zonally varying flow. *J. Atmos. Sci.*, **41**, 2141-2162.
- Thacker, W. C., 1976: Spatial growth of gulf stream meanders. *Geophys. Fluid Dyn.*, **7**, 271-295.
- Tupaz, J. B., R. T. Williams and C.-P. Chang, 1978: A numerical study of barotropic instability in a zonally varying easterly jet. *J. Atmos. Sci.*, **35**, 1265-1280.

## On the Transformations between Temporal and Spatial Growth Rates

MELINDA S. PENG AND R. T. WILLIAMS

*Department of Meteorology, Naval Postgraduate School, Monterey, CA 93943*

23 June 1986 and 30 March 1987

### ABSTRACT

This paper compares the error distributions for three transformation formulae between temporal growth rate and spatial growth rate with the linearized barotropic vorticity equation. The  $\text{sech}^2$  and the  $\tanh$  basic-state profiles are used for illustration. The transformation which uses the phase velocity gives a moderate error which does not have a strong dependence on the growth rate. The formulae derived by Gaster, and later by Nayfeh and Padhye, which employ the group velocity, have errors that are a function of the ratio of the spatial growth rate to the wavenumber. The errors from their formulae are small when the ratio is small, but the errors increase with the ratio so that all three transformation formulae give similar errors when the ratio is of order one. Nayfeh and Padhye's formula is rederived for the barotropic vorticity equation with a procedure which shows that ratio of growth rate to wavenumber must be small for accuracy.

### 1. Introduction

Basic currents in both the atmosphere and the ocean often have appreciable downstream variation. As a result, the traditional parallel flow stability theories, which employ temporal growth, cannot be directly applied to these flows. It has been shown by Tupaz et al. (1978), Williams et al. (1984) and Peng and Williams (1986) in studies of downstream, barotropic instability that spatial instability is more appropriate with downstream varying basic flows. The spatial growth exists when the basic flow does not support absolute instability. More relevant discussion concerning this is given in Peng and Williams (1987). They used spatial instability in the two-layer baroclinic model to help explain regions of enhanced cyclonic activity. Since spatial growth rates are likely to be useful in a variety of geophysical problems, it would be very desirable to have transformation formulae to obtain spatial growth rates from temporal growth rates or vice versa. In some studies it is easier to measure one type of growth rate than the other. Meanwhile, there are some cases when one type of instability has analytical solutions but not the other, so that a transformation formula would be very useful. In this paper we evaluate the accuracy of some transformation formulae for geophysically relevant barotropic currents.

The temporally growing normal-mode solutions have complex frequencies or phase speeds and real wavenumbers, while the spatially growing solutions have complex wavenumbers and real frequencies. There is no general transformation formula which gives the exact relationship between the two types of growth rate. It was shown by Gaster (1965) that the simple

transformation formula which depends on the phase speed (Schubauer and Skramstad, 1943) will introduce errors that are not negligible. Gaster (1962) demonstrated that for the same wavenumber, if the amplification rate is small, the frequencies for temporal and spatial growth are also equal with an error of the order of (maximum growth rate)<sup>2</sup>. Under this condition, Gaster (1962) obtained a transformation from one type of growth rate to another in terms of the real group velocity. Only when the systems are nondispersive will the transformations using phase velocity and group velocity be the same. Recently, Nayfeh and Padhye (1979) reformulated this problem, and their results differ from Gaster's mainly in two aspects. First, the complex group velocity is used instead of the real group velocity as in Gaster's formula. Second, in order to obtain a proper comparison, a correction to the wavenumber (frequency) must be added when transforming the temporal (spatial) growth rate into the spatial (temporal) growth rate. The results they presented are very accurate, with almost all errors 2% or less.

In this paper these approximations are compared for barotropic instability with special emphasis on the transformation by Nayfeh and Padhye (1979) whose limitations have not been previously discussed. Two different basic flows are studied. The first one is an easterly jet with a  $\text{sech}^2$  profile, which approximates the jet that is observed south of the Tibetan Plateau at 200 mb during Northern Hemisphere summer. The second one is a  $\tanh$  profile, which resembles the basic flow in the intertropical convergence zone.

In section 2, the three approximations will be compared for the two wind profiles. Some results from Nayfeh and Padhye will also be presented for com-

parison. In section 3, their formula will be rederived for the barotropic vorticity equation in order to better understand its range of validity.

## 2. Numerical comparisons

This study uses the linearized equation for conservation of vorticity in two-dimensional flow. The governing equation in nondimensional form is (§7.3, Pedlosky, 1979),

$$\left(\frac{\partial}{\partial t} + \bar{U} \frac{\partial}{\partial x} + \lambda\right) \nabla^2 \psi' + \left(\beta - \frac{\partial^2 \bar{U}}{\partial y^2}\right) \frac{\partial \psi'}{\partial x} = 0, \quad (1)$$

where  $\psi'$  is the disturbance streamfunction,  $\lambda$  the frictional coefficient and  $\beta$  is the derivative of the Coriolis parameter (here  $\lambda$  and  $\beta$  are constants). The basic flow for the Bickley jet is described by

$$\bar{U}(y) = -a \operatorname{sech}^2\left(\frac{y}{b}\right) \quad (2)$$

where  $a$  is the maximum speed and  $b$  is the half-width of the jet. The boundary conditions for the channel domain are

$$\psi' = 0 \quad \text{at} \quad y = \pm D. \quad (3)$$

For the ITCZ flow approximation, the basic flow is

$$\bar{U}(y) = 0.5 \tanh\left(\frac{y}{d}\right) + U_0 \quad (4)$$

where  $U_0$  is the constant basic state and the boundary conditions are that the streamfunction vanishes at infinity, i.e.,

$$\psi' = 0 \quad \text{at} \quad y = \pm \infty. \quad (5)$$

When the normal mode solution

$$\psi' = A(y) e^{i(\alpha x - \omega t)} \quad (6)$$

is introduced, Eqs. (1) and (3) or (5) constitute an eigenvalue problem. If the frequency  $\omega$  is a real number, the complex wavenumber gives a spatially growing wave. When the wavenumber  $\alpha$  is a real number, complex frequency leads to a temporally growing wave. The parameters  $a$ ,  $b$  in (2) and  $d$  in (4) will be altered to change the sharpness of the jet profile in order to obtain a large range of the instability level, which is measured by the amplification rate (growth rate). We will use this problem to study the errors that arise from transforming temporal to spatial growth rates using the different relations discussed in the Introduction.

In the following equations, subscripts  $r$  and  $i$  indicate the real and imaginary parts and  $\omega_i$  is the temporal growth rate and  $\alpha_r$  is the spatial growth rate. The first transformation formula uses the phase velocity, following Schubauer and Skramstad (1943),

$$\alpha_r = -\frac{\omega_i}{c_r} \quad (7)$$

where  $c_r$  is the real phase velocity.

The second formula, which was proposed by Gaster (1962), uses the real group velocity,

$$\alpha_r(S) = -\frac{\omega_i(T)}{\partial \omega_r / \partial \alpha_r} \quad (8)$$

where  $\partial \omega_r / \partial \alpha_r$  is the real group velocity.

The third formula, which was derived by Nayfeh and Padhye (1979), is

$$\delta \alpha = -\frac{\omega_i}{\omega'} \quad (9)$$

where  $\omega' = \partial \omega / \partial \alpha$  is the complex group velocity. The real part of Eq. (9) is the transformation formula from temporal to spatial growth rate with the imaginary part of Eq. (9) being the required correction to shift the wavenumber for proper comparison. A more detailed derivation of Eq. (9) is given in section 3.

The computations of the transformed spatial growth rates for the  $\operatorname{sech}^2$  profile are summarized in Table 1, and compared with spatial growth rates from direct calculation. For the cases shown in Table 1,  $\beta = -0.75$ ,  $\omega = -0.75$  and  $\lambda = -0.05$  nondimensionally in Eq. (1).

Column 1 in Table 1 is the real wavenumber and column 2 is the corresponding spatial growth rate. The positive sign for the imaginary part of the wavenumber in column 2 is due to the easterly jet specified in Eq. (2), which indicates spatial growth in the negative  $x$  direction. Columns 4, 6, 8 are the spatial growth rates transformed from temporal growth rate using Eqs. (7), (8) and (9), respectively. Columns 5, 7 and 9 give the relative errors for columns 4, 6 and 8 with respect to column 2. These errors are calculated, for instance, for  $G$  as

$$\text{error of } G = \frac{\|\alpha_i\| - \|G\|}{\|\alpha_i\|} \quad (10)$$

The quantity  $|\alpha_i/\alpha_r|$  which is listed in column 3 is the ratio between the amplification rate ( $\alpha_i$ ) and the local wavenumber ( $\alpha_r$ ). Although in the present case,  $\alpha_i$  and  $|\alpha_i/\alpha_r|$  are of the same order, variations of all the errors due to the different transformations are discussed as functions of  $|\alpha_i/\alpha_r|$  instead of  $\alpha_i$ . The reasons for this will be explained in section 3.

The errors introduced by using phase velocity for conversion (listed in column 5), are rather uniform irrespective of the size of  $|\alpha_i/\alpha_r|$ . As expected, the errors introduced by using Gaster's formula (column 7) increase rapidly as  $|\alpha_i/\alpha_r|$  increases. However, the errors introduced by using Nayfeh and Padhye's formula (column 9) also increase rapidly as  $|\alpha_i/\alpha_r|$  increases. The values in column 6 and column 8 are very close. For clearness, these relations are graphically shown in Fig. 1, in which the error distributions for these three transformation are plotted against the ratio  $|\alpha_i/\alpha_r|$ . The solid line is the error for the phase velocity formula, the dashed line is the error for Gaster's formula and

TABLE 1. Comparison of the growth rates and errors from three different approximations.\*

1	2	3	4	5	6	7	8	9
Wavenumber	Spatial growth rate	Ratio	From Eq. (5)	Error of SS	From Eq. (6)	Error of $G$	From Eq. (7)	Error of NP
$\alpha_r$	$\alpha_i$	$ \alpha_i/\alpha_r $	(SS)		$G$		(NP)	
-1.51100	0.01353	0.0089	-0.01075	0.2055	-0.01316	0.0273	-0.01350	0.0022
-1.50556	0.04607	0.0306	-0.03636	0.2108	-0.04476	0.0284	-0.04547	0.0130
-1.49997	0.07982	0.0532	-0.06298	0.2109	-0.07720	0.0328	-0.07817	0.0207
-1.49361	0.11530	0.0772	-0.09093	0.2113	-0.11074	0.0395	-0.11188	0.0296
-1.47679	0.19164	0.1298	-0.15109	0.2116	-0.18094	0.0558	-0.18224	0.0490
-1.45168	0.27468	0.1892	-0.21610	0.2132	-0.25352	0.0770	-0.25509	0.0713
-1.39246	0.40581	0.2914	-0.31587	0.2216	-0.35848	0.1166	-0.36115	0.1091
-1.30670	0.52804	0.4041	-0.40186	0.2393	-0.44460	0.1580	-0.44982	0.1481
-1.24311	0.59223	0.4764	-0.44196	0.2537	-0.48502	0.1810	-0.49085	0.1712
-1.15617	0.65644	0.5677	-0.47594	0.2750	-0.52070	0.2068	-0.52558	0.1993

\* SS: Schubauer and Skramstad (1943); NP: Nayfeh and Padhye (1979).

the dotted line is the error for Nayfeh and Padhye's formula. When the parameters  $\omega$ ,  $\beta$  and  $\lambda$  are varied over a reasonable range, the error distributions are similar to those in Fig. 1.

For the basic flow with tanh profile [Eq. (4)], the numerical calculations are made by taking the lateral boundaries at a large distance ( $y = \pm 10$ ) instead of at infinity. The results obtained are very close to the calculations by Michalke (1965) for the same basic-state profile, indicating that it is sufficient for the present study. An example is given in Fig. 2, where  $\omega = 0.3$ ,  $\beta = 0.1$ , and  $\lambda = 0.01$ . The magnitude of the growth rate is varied by changing  $d$  in Eq. (4). In this case, the error using the phase velocity (solid line) decreases with the ratio  $|\alpha_i/\alpha_r|$  and then it increases again. Gaster's formula (dotted line) and Nayfeh and Padhye's formula (dashed line) have the same error distribution, with Nayfeh and Padhye's formula being slightly better.

Overall, when the ratio  $|\alpha_i/\alpha_r|$  is small, the transfor-

mation which uses the phase velocity has large errors around 20%–30%, and both Gaster's formula and Nayfeh and Padhye's formula give small errors. Errors from the latter formulae increase rapidly as  $|\alpha_i/\alpha_r|$  increases and they are about equal. When the ratio is large, which is the more relevant situation for atmospheric instability, all three formula give about the same error range.

As further illustration, we compute the transformed growth rate for the two-layer baroclinic model in a channel. The description of the model can be found in Pedlosky (1979). In this model, the transformed growth rate using either phase velocity or real part of the group velocity (Gaster's formula) give very satisfactory results with errors around 0.2%–2%. This is because the system is only slightly dispersive so that the phase velocity is very close to the group velocity. When the system is nondispersive or weakly dispersive, both formulae using phase speed and real part of the group velocity are very accurate and it is not necessary to consider Nayfeh and Padhye's formula.

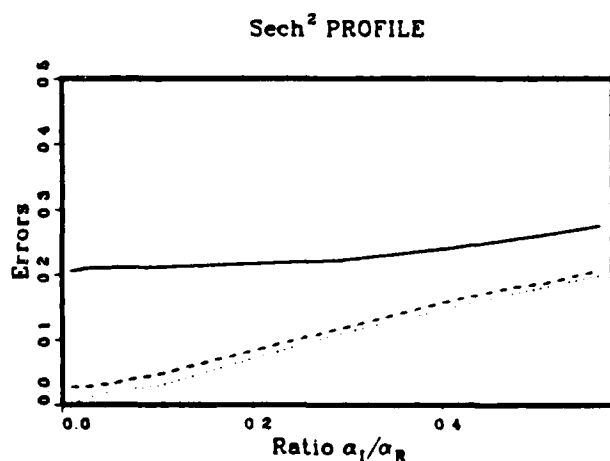


FIG. 1. Error distributions for a case with sech profile using different transformation formulae: Schubauer and Skramstad (solid line), Gaster (dashed line), and Nayfeh and Padhye (dotted line).

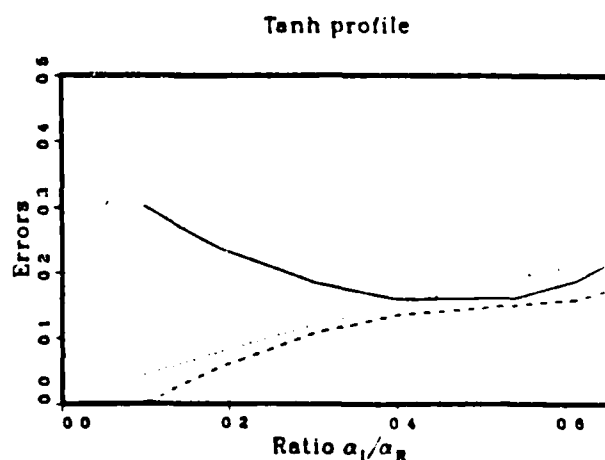


FIG. 2. As in Fig. 2, except for a case with tanh profile.

For comparison with our results, we extract data from Tables 1 and 2 of Nayfeh and Padhye to construct our Table 2, which contains their errors as a function of  $|\alpha_i/\alpha_r|$  for each case. All the errors in Table 2 are small, ranging from 0.0052 to 0.0438, while the  $|\alpha_i/\alpha_r|$  are also small, ranging from 0.00136 to 0.02325. This table shows that Nayfeh and Padhye's good results were obtained when  $|\alpha_i/\alpha_r|$  was small.

As mentioned earlier, during the transformation from one type of growth rate to another the frequency and the wavenumber cannot be kept the same. When transforming from temporal to spual growth rate, results obtained in keeping the frequency the same are slightly better than keeping the wavenumber the same, i.e., a 2-4% improvement. The correction to the wavenumber indicated by Nayfeh and Padhye (1979) is very close to the adjustment of the wavenumber in order to obtain constant frequency.

3. Analysis of source of error

In this section we will discuss Nayfeh and Padhye's analysis in order to show that the error in their relation should depend on  $|\alpha_i/\alpha_r|$ . First we will rederive their formula for barotropic vorticity equation. The following analysis was used by Pedlosky (1979) to demonstrate the physical meaning of group velocity.

Consider the motion governed by Eqs. (1) and (3). The total wave field viewed as a wave packet has two separate scales of oscillation. In the normal time scale, the local oscillation determines the period over which the wave amplitude appears to be constant. In the "slow" time scale, the amplitude of the wave field changes gradually. Due to the bounded channel domain in the  $y$ -direction, the amplitude has slow variation in the  $x$ -direction only. Two different slow scales can thus be introduced:

$$\begin{aligned} X &= \epsilon x \\ T &= \epsilon t \end{aligned} \tag{11}$$

where  $\epsilon$  is a small parameter which is a measure of the slowness of the temporal and spatial variations of the field. The derivatives in (1) are replaced by

TABLE 2. Errors extracted from Tables 1 and 2 of Nayfeh and Padhye (1979).

$ \alpha_i/\alpha_r $	Errors
0.00155	0.0260
0.01500	0.0072
0.01990	0.0059
0.02286	0.0052
0.02325	0.0072
0.01717	0.0157
0.00791	0.0281
0.00136	0.0438

$$\begin{aligned} \frac{\partial}{\partial t} &\rightarrow \frac{\partial}{\partial T} + \epsilon \frac{\partial}{\partial T} \\ \frac{\partial}{\partial x} &\rightarrow \frac{\partial}{\partial X} + \epsilon \frac{\partial}{\partial X}, \end{aligned} \tag{12}$$

and (1) becomes

$$\begin{aligned} &\left(\frac{\partial}{\partial t} + \epsilon \frac{\partial}{\partial T} + \bar{U} \frac{\partial}{\partial x} + \epsilon \bar{U} \frac{\partial}{\partial X} + \lambda\right) \\ &\times \left(\frac{\partial^2}{\partial x^2} + 2\epsilon \frac{\partial^2}{\partial X \partial x} + \epsilon^2 \frac{\partial^2}{\partial X^2} + \frac{\partial^2}{\partial y^2}\right) \psi' \\ &+ \left(\beta - \frac{\partial^2 \bar{U}}{\partial y^2}\right) \left(\frac{\partial}{\partial x} + \epsilon \frac{\partial}{\partial X}\right) \psi' = 0. \end{aligned} \tag{13}$$

Since  $\epsilon$  is a small parameter,  $\psi'$  can be expressed in terms of  $\epsilon$ :

$$\psi' = \psi_0(x, X, y, t, T) + \epsilon \psi_1(x, X, y, t, T) + \dots \tag{14}$$

Now substitute (14) into (13) and collect terms of the same order of  $\epsilon$ . The first-order terms yield

$$\left(\frac{\partial}{\partial t} + \bar{U} \frac{\partial}{\partial x} + \lambda\right) \left(\frac{\partial^2}{\partial x^2} + \frac{\partial^2}{\partial y^2}\right) \psi_0 + \left(\beta - \frac{\partial^2 \bar{U}}{\partial y^2}\right) \frac{\partial \psi_0}{\partial x} = 0, \tag{15}$$

which is an equation in the normal variables only. This equation can admit the following solution:

$$\psi_0 = R_e A(X, T) \zeta(y) e^{i(\alpha x - \omega t)}. \tag{16}$$

Substitution of (16) into (15) yields the familiar relation

$$(-i\omega + i\bar{U}\alpha + \lambda) \left(-\alpha^2 \zeta + \frac{\partial^2 \zeta}{\partial y^2}\right) + \left(\beta - \frac{\partial^2 \bar{U}}{\partial y^2}\right) (i\alpha) \zeta = 0. \tag{17}$$

The balanced equation at order ( $\epsilon$ ) is

$$\begin{aligned} &\left(\frac{\partial}{\partial t} + \bar{U} \frac{\partial}{\partial x} + \lambda\right) \left(\frac{\partial^2}{\partial x^2} + \frac{\partial^2}{\partial y^2}\right) \psi_1 + \left(\beta - \frac{\partial^2 \bar{U}}{\partial y^2}\right) \frac{\partial \psi_1}{\partial x} \\ &= -2 \left(\frac{\partial}{\partial t} + \bar{U} \frac{\partial}{\partial X} + \lambda\right) \frac{\partial^2 \psi_0}{\partial X \partial x} - \left(\frac{\partial}{\partial T} + \bar{U} \frac{\partial}{\partial y^2}\right) \frac{\partial \psi_0}{\partial y^2} \\ &\times \left(\frac{\partial^2 \psi_0}{\partial x^2} + \frac{\partial^2 \psi_0}{\partial y^2}\right) - \left(\beta - \frac{\partial^2 \bar{U}}{\partial y^2}\right) \frac{\partial \psi_0}{\partial X}. \end{aligned} \tag{18}$$

The right-hand side of which can be evaluated with the introduction of the order-one solution (16) which becomes

$$\begin{aligned} \text{rhs} &= \left[-2(-i\omega + \bar{U}i\alpha + \lambda) \frac{\partial A}{\partial X} (i\alpha) \zeta \right. \\ &- \left(\frac{\partial}{\partial T} + \bar{U} \frac{\partial}{\partial X}\right) \left(-\alpha^2 \zeta + \frac{\partial^2 \zeta}{\partial y^2}\right) A \\ &\left. - \left(\beta - \frac{\partial^2 \bar{U}}{\partial y^2}\right) \frac{\partial A}{\partial X} \zeta\right] e^{i(\alpha x - \omega t)}. \end{aligned} \tag{19}$$

Since the left-hand side of (19) has the same structure

as the first-order equation (15), the same homogeneous solution as (16) also applies to the order ( $\epsilon$ ) solution. The right-hand side of (19), which is the forcing part, oscillates with the same frequency as the homogeneous part. Therefore, the solution would contain a secular growth with time. For time ( $1/\epsilon$ ), the solution  $\epsilon\psi$  will become as large as the first-order solution and violate the expansion (14). Therefore, terms on the right-hand side of (19) which are proportional to  $\exp[i(\alpha x - \omega t)]$  have to be suppressed. With the help of (17), this leads to

$$\frac{\partial A}{\partial T} + \left[ \frac{2i\alpha\zeta(-i\omega + i\alpha\bar{U} + \lambda)}{(-\alpha^2\zeta + \frac{\partial^2\zeta}{\partial y^2})} - \frac{(-i\omega + \lambda)}{i\alpha} \right] \frac{\partial A}{\partial X} = 0. \quad (20)$$

Differentiation of the dispersion relation (17) with respect to  $\alpha$  will show that the bracket in (20) is the complex group velocity in the  $x$  direction, i.e.,

$$\frac{\partial A}{\partial T} + \omega_\alpha \frac{\partial A}{\partial X} = 0 \quad (21)$$

where

$$\omega_\alpha = \frac{\partial \omega}{\partial \alpha} = \frac{2i\alpha\zeta(-i\omega + i\alpha\bar{U} + \lambda)}{[-\alpha^2\zeta + (\frac{\partial^2\zeta}{\partial y^2})]} - \frac{(-i\omega + \lambda)}{i\alpha}. \quad (22)$$

Nayfeh and Padhye treated nonparallel flow with slow variation which allowed the separation of the problem into different orders of the small parameter  $\epsilon$ , which measures the nonparallelism of the basic flow. With the procedure similar to the above analysis, the solvability conditions at next order lead to, in two-dimensional form,

$$g_1 \frac{\partial A}{\partial t_1} + g_2 \frac{\partial A}{\partial x_1} = h_1 A, \quad (23)$$

where  $x_1, t_1$  are slow variables scaled by  $\epsilon$  and expressions for  $g_n$  and  $h_n$  are given in appendix A in Nayfeh and Padhye. For quasi-parallel flow, the nonlinear term on the right-hand side of (23) is dropped and the slow scales  $x_1, t_1$  become  $x$  and  $t$  so that (23) becomes

$$\frac{\partial A}{\partial t} + \omega_\alpha \frac{\partial A}{\partial x} = 0, \quad (24)$$

where  $\omega_\alpha = g_2/g_1$  is the complex group velocity in  $x$  direction.

In the case of temporal stability, Nayfeh and Padhye further used the following expression

$$A = a \exp(-\omega t) \quad (25)$$

so that Eq. (24) becomes

$$\frac{\partial a}{\partial t} + \omega_\alpha \frac{\partial a}{\partial x} = \omega_\alpha a \quad (26)$$

and the solution in their paper becomes

$$U = a(x, t)\zeta(y) \exp[i(\alpha x - \omega t)]. \quad (27)$$

To convert from the temporal to spatial stability, Nayfeh and Padhye constrain  $a$  to be independent of  $t$  in (26) and solve for  $a$ :

$$a = a_0 \exp(\omega_i x / \omega_\alpha). \quad (28)$$

Expressing  $\omega_\alpha$  in polar form as  $C_r \exp(i\theta)$ , and substituting into (27), it becomes

$$U = a_0 \zeta(y) \exp\{i[(\alpha + \delta\alpha)x - \omega t] + \sigma_r x\} \quad (29)$$

where

$$\sigma_r = \frac{\omega_i}{C_r} \sin\theta, \quad (30)$$

$$\delta\alpha = -\frac{\omega_i}{C_r} \sin\theta. \quad (31)$$

Equation (30) is the transformation formula with the corresponding shifting  $\delta\alpha$  in the wavenumber given by (31). Equation (9) stated in section 2 is the complex form of (30) and (31).

Equation (24) is of the same form as (21) derived above. Both formulations are based upon the following assumption

$$\frac{1}{A} \frac{\partial A}{\partial x} \ll \alpha, \quad \frac{1}{A} \frac{\partial A}{\partial t} \ll \omega \quad (32)$$

which means there is a requirement that the amplitude have slow variation (measured by the spatial growth rate) compared to the local modulation (represented by the local wavenumber). The later neglect of the nonparallel effects by Nayfeh and Padhye does not relax the slow variation requirement. Our analysis gives the condition  $|\alpha_i/\alpha_r| \ll 1$  directly because we did not include the slow variation of the basic flow initially. Since the slow variation of amplitude requirement is equivalent to the assumption that  $|\alpha_i/\alpha_r|$  be small, it is clear that this analysis agrees with the comparisons in section 2.

In summary, Nayfeh and Padhye's (1979) formula is valid when the spatial amplification rate is small compared with the local wavenumber. The applicability of Gaster's formula and Nayfeh and Padhye's formula are the same. When the amplification rate is relatively large, the relations which use group velocity or phase velocity give results with approximately the same errors. More research is required to determine more general relations between the spatial and temporal growth rates.

*Acknowledgments.* The authors wish to thank Dr. Yen Liu for reading the manuscript and providing helpful comments. This research was supported by the Division of Atmospheric Sciences, National Science Foundation under Grants ATM 83-15175 and ATM

84-44699. This manuscript was carefully typed by Miss K. Lee and the numerical computations were carried out at the W. R. Church Computer Center at the Naval Postgraduate School.

## REFERENCES

- Gaster, M., 1962: A note on the relation between temporally increasing and spatially increasing disturbances in hydrodynamic stability. *J. Fluid Mech.*, 14, 222-224.
- , 1965: The role of spatially growing waves in the theory of hydrodynamic stability. *Progress Aerospace Sci.*, 6, 251-270.
- Michalke, A., 1965: On spatially growing disturbances in an inviscid shear layer. *J. Fluid Mech.*, 23, 521-544.
- Nayfeh, A. H., and A. Padhye, 1979: Relation between temporal and spatial stability in three-dimensional flows. *AIAA Journal*, 1084-1090.
- Pedlosky, J., 1979: *Geophysical Fluid Dynamics*. Springer-Verlag, 111-120.
- Peng, M. S., and R. T. Williams, 1986: Spatial instability of the barotropic jet with slow streamwise variation. *J. Atmos. Sci.*, 43, 2430-2442.
- , and ———, 1987: Spatial instability of the baroclinic current with slow streamwise variation. *J. Atmos. Sci.*, (in press).
- Schubauer, G. B., and H. K. Skramstad, 1943: Laminar boundary layer oscillations and transition on a flat plate. NACA Advanced Confidential Report 909, 1948.
- Tupaz, J. B., R. T. Williams and C.-P. Chang, 1978: A numerical study of barotropic instability in a zonally varying easterly jet. *J. Atmos. Sci.*, 35, 1265-1280.
- Williams, R. T., H. Lim and C.-P. Chang, 1984: Nonlinear and linear effects in an easterly jet with downstream variation. *J. Atmos. Sci.*, 41, 621-636.

Shield, Kathy A., M.S. Thesis, 1985  
Possible Cross Equatorial Influence of the Northeast Monsoon on the Equatorial  
Westerlies over Indonesia

#### ABSTRACT

Objectively analysed surface, 700 and 200 mb winds of nine winters are used to study the possible cross equatorial influence of the northern winter monsoon on the zonal wind along  $10^{\circ}\text{S}$  in the Indonesia-Arafura Sea region and to prepare a nine year monthly mean climatology. Key circulation features are represented by area averaged and time composited parameters in an attempt to infer correlations between their perturbations. Specifically, the acceleration of the zonal wind along  $10^{\circ}\text{S}$  in the Indonesia-Arafura Sea region is used to define the onset of the southern summer monsoon and illustrate the timing between circulation features of interest in both hemispheres. While no conclusive results were achieved, some basic observations can be made. Mid-season active phases in the southern summer monsoon appear to be influenced by surges in the northeast appear to be primarily a result of southern Hemispheric, mid-latitude, baroclinic effects. In both cases, the meridional extent of the southern summer monsoon is limited. Even in the mid-season event, variability in area-averaged cross equatorial flow may not be indicative of the nature of forcing of the Northern Hemisphere's monsoonal winds on the southern summer monsoonal winds along  $10^{\circ}\text{S}$ .

## Nonlinear and Linear Effects in an Easterly Jet with Downstream Variation

R. T. WILLIAMS, H. LIM<sup>1</sup> AND C.-P. CHANG

Naval Postgraduate School, Monterey, CA 93943

(Manuscript received 20 July 1983, in final form 8 November 1983)

### ABSTRACT

In this study, nonlinear effects of barotropic instability in a downstream varying easterly jet are studied and compared with previous linear model results of Tupaz and others. The barotropic vorticity equation with Rayleigh friction and forcing is solved with finite differences. The initial mean flow is an easterly Bickley jet whose maximum speed and half-width vary downstream; the half-width ranges from 500 to 1200 km and the maximum speed is  $30 \text{ m s}^{-1}$ . The time-independent forcing makes the initial mean flow, which is unstable in the central jet region, a steady-state solution to the vorticity equation. A disturbance with wavenumber 10, which is predicted to be locally unstable and most dominant based on linear model results, is added to the initial mean flow. The equation is then integrated numerically for 450 days.

The solutions may be separated into two phases: 1) an initial adjustment phase which consists of several  $\sim 50$ -day cycles wherein an initial wavenumber 10 disturbance grows rapidly in the jet region, and then the disturbance energy shifts to a slightly longer wavelength and decays before the next cycle; and 2) a quasi-equilibrium phase which is achieved after 350 days. Fourier analysis of the disturbance streamfunction at each point during a typical interval in the adjustment phase shows two dominant modes with periods near 3.35 days and 3.58 days, respectively. After entering the quasi-equilibrium phase, a 4-day oscillation develops in the kinetic energy and the main periods of the streamfunction become 4 and 2 days, respectively. The former is the dominant mode and the latter is the result of the nonlinear self-interaction by the former. The frequency of the dominant mode is equal to the frequency of the most unstable mode from a parallel flow calculation based on the outflow region mean flow. However, in most of the unstable region, it is much less than the most unstable local frequency inferred from the parallel flow solution.

The dominant mode in the quasi-equilibrium phase propagates through the modified mean flow essentially as a linear wave, and its behavior can be compared with the linear model results. However, its maximum growth rate is 25% larger than the highest local growth rate for the parallel flow solution. This "enhancement effect" is also larger than was found by Tupaz and others. In addition, there is a hysteresis effect wherein the growth rate curve and the phase structure from the full model are shifted downstream relative to the parallel flow solution, similar to the linear model results. On the other hand, the wavelength is generally short in the jet region and much longer in the outer regions, opposite to the wavelength variation in Tupaz and others. With the help of a generalized Rossby wave formula, it is shown that two effects determine the downstream variation of the disturbance wavelength: 1) the variation of the latitudinal integral of the mean zonal wind and 2) the variation of the latitudinal integral of the mean absolute vorticity gradient. Due to the difference in disturbance scale, the second effect dominates in the quasi-equilibrium phase of this study while the first effect dominates the linear model used by Tupaz and others.

### 1. Introduction

Most theoretical studies of barotropic instability employ basic flows which are parallel. However, in many regions of the atmosphere, the time-averaged wind field shows appreciable downstream variation as a result of forced quasi-stationary waves. Tupaz *et al.* (1978) used a linearized model to examine the behavior of waves in such a mean flow in which a localized region is unstable. The purpose of this paper is to add nonlinear effects to this study of downstream barotropic instability.

The mean flow used by Tupaz *et al.* is modeled after the moderately strong easterly jet which develops

south of the Tibetan high near 200 mb during the Northern Hemisphere summer. Westward propagating synoptic-scale disturbances have been observed in the vicinity of this jet (Krishnamurti, 1971a,b). The jet contains regions of large vorticity gradient where the necessary condition for barotropic instability is sometimes satisfied locally. This suggests that the observed disturbances arise from barotropic instability of the basic flow. In this case, the disturbances would extract energy from the mean zonal flow and the planetary-scale waves since they combine to give large vorticity gradients south of the Tibetan high. Observational evidence of such barotropic energy conversion was provided by Kanamitsu *et al.* (1972), who showed that wavenumbers 6–8 in the wind spectrum between  $15^\circ\text{S}$  and  $15^\circ\text{N}$  receive energy from both the zonal flow and wavenumber 1.

<sup>1</sup> Present affiliation: Meteorological Service Singapore, Republic of Singapore.

Tupaz *et al.* (hereafter referred to as TWC) solved the linearized barotropic vorticity equation on a  $\beta$ -plane with finite differences. The time-mean zonal wind was specified to be a slowly varying easterly Bickley jet and the mean meridional wind was derived in such a way that the mean flow was nondivergent. The motion was confined within an open channel. A periodic forcing was applied on the inflow (eastern) boundary to generate waves which were allowed to propagate out through the western boundary. As the waves traveled through the region, they grew or decayed in response to the local instability properties of the mean flow, while at each point the fields varied periodically. The numerical results were compared with a simple mechanistic model which used local phase speeds and growth rates determined from a parallel flow model. In the unstable region, the numerical model produced waves with larger spatial growth rates than those obtained with the parallel flow model, while in the stable region, the numerical model showed strong dynamic damping. In the numerical solutions, the wavelength varied in such a way that it was a maximum near the jet maximum. When a uniform velocity was added to the mean flow, the zonal asymmetry in the spatial growth rate curve, with respect to the jet maximum, was increased as a result of a slower adjustment of the wave structure to local stability conditions.

In this paper, the numerical model developed by TWC is modified by including the full nonlinear terms and by changing the open boundary conditions to cyclic boundary conditions. A forcing term must be included to make the zonally varying mean flow a steady-state solution to the forecast equation. However, this steady-state solution is unstable to disturbances which have the proper wavelength for the unstable portion of the jet. Such disturbances will grow rapidly in the region near the jet maximum and the solution will initially resemble the solution obtained by TWC which has a maximum amplitude downstream from the jet maximum. As the wave amplitude increases, the disturbance will begin to interact with the mean flow. This interaction will stabilize the mean flow with the largest change occurring where the disturbance energy conversion is a maximum. As was shown in TWC, the maximum conversion is some distance downstream from the jet maximum. After a period of adjustment a new statistical equilibrium develops with a modified mean flow through which finite-amplitude waves propagate.

The open boundary conditions used by TWC were replaced in this study by cyclic conditions so that each forced mean flow would have its own solution regime. If the boundary conditions used by TWC were used, the nonlinearity of the solution would depend on the amplitude of the upstream boundary condition. Shapiro (1980) has carried out a study with the same formulation that is presented in this paper. However, his interest was on the short-term interactions between

finite-amplitude waves and various forced mean flows, and his results depend on the specific waves under consideration. On the other hand, the object of our study is to determine the long-term behavior of the forced system which is dependent upon the dynamics of the forced mean flow only.

In Section 2, the basic equations are formulated and the numerical technique is described. An overview of the 450-day integration is presented in Section 3. A detailed analysis of the solutions during a typical interval of the initial adjustment phase is given in Section 4. After 350 days, the fields settle into a quasi-equilibrium phase dominated by a 4-day oscillation and its solution behavior is examined in Section 5. The spatial growth rates for this phase are calculated in Section 6 and the wavelength variation is treated in Section 7. The summary and conclusions are given in Section 8.

## 2. Basic model and numerical technique

The nondivergent barotropic vorticity equation may be written

$$\frac{\partial}{\partial t} \nabla^2 \psi - \frac{\partial \psi}{\partial y} \frac{\partial \nabla^2 \psi}{\partial x} + \frac{\partial \psi}{\partial x} \frac{\partial \nabla^2 \psi}{\partial y} + \beta \frac{\partial \psi}{\partial x} = Q - \lambda \nabla^2 \psi, \quad (2.1)$$

where  $\psi$  is the streamfunction,  $\lambda$  a frictional coefficient and  $\beta$  the north-south gradient of the Coriolis parameter. The forcing function  $Q$  represents nonbarotropic and diabatic effects and it is assumed to be independent of  $\psi$ . The velocity components are

$$u = -\frac{\partial \psi}{\partial y}, \quad v = \frac{\partial \psi}{\partial x}. \quad (2.2)$$

The forcing function  $Q$ , which is given below, is designed in such a way that  $\bar{\psi}(x, y)$  is a steady-state solution to (2.1) i.e.,

$$Q = -\frac{\partial \bar{\psi}}{\partial y} \frac{\partial \nabla^2 \bar{\psi}}{\partial x} + \frac{\partial \bar{\psi}}{\partial x} \frac{\partial \nabla^2 \bar{\psi}}{\partial y} + \beta \frac{\partial \bar{\psi}}{\partial x} + \lambda \nabla^2 \bar{\psi}. \quad (2.3)$$

The forced mean zonal wind is an easterly Bickley jet which is defined by

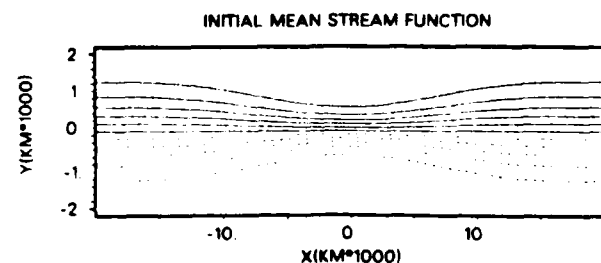


FIG. 1. The initial mean streamfunction  $\bar{\psi}$ . The contour interval is  $2.5 \times 10^6 \text{ m}^2 \text{ s}^{-1}$ . Note that the dashed contours represent negative values.

$$\bar{u} = -\partial\bar{\psi}/\partial y = -U(x) \operatorname{sech}^2[y/d(x)]. \quad (2.4)$$

Here,  $d(x)$  is the cross jet length scale and  $U(x)$  is the maximum velocity which occurs at  $y = 0$ . The basic flow streamfunction is specified to be constant at the lateral boundaries  $y = \pm D$ . Eq. (2.4) can be integrated to give

$$\bar{\psi}(x, y) = U(x)d(x)\{\tanh[y/d(x)] + \tanh[D/d(x)]\} + \bar{\psi}(x, -D), \quad (2.5)$$

where

$$U(x) = \{[\bar{\psi}(x, D) - \bar{\psi}(x, -D)]/2d(x)\} \times \coth[D/d(x)]. \quad (2.6)$$

The  $x$ -variation is given by

$$d = \begin{cases} 850 \text{ km} - 350 \text{ km} [\cos(2\pi x/\bar{L})], & |x| \leq \bar{L}/2 \\ 1200 \text{ km}, & |x| \geq \bar{L}/2. \end{cases} \quad (2.7)$$

Here,  $\bar{L}$  is the wavelength of the  $x$ -variation of the forced flow.

Figs. 1 and 2 show the forced fields of the streamfunction  $\bar{\psi}$  and the zonal velocity  $\bar{u}$  for the following parametric values:

$$\left. \begin{aligned} D &= 2125 \text{ km}, \quad \bar{L} = 36\,000 \text{ km} \\ \bar{\psi}(x, -D) &= -\bar{\psi}(x, D) = 15 \times 10^6 \text{ m}^2 \text{ s}^{-1} \end{aligned} \right\}$$

These figures show that the jet maximum is at  $x = 0$ ,  $y = 0$ , where  $\bar{u} = -30 \text{ m s}^{-1}$ . From this longitude, the central speed decreases slowly upstream and downstream to a constant value of  $-13.4 \text{ m s}^{-1}$  at  $x = \pm 18\,000 \text{ km}$ . This mean flow is the same as the one used in experiment 1 by TWC except that they used  $\bar{L} = 43\,000 \text{ km}$ ,  $D = 2000 \text{ km}$ , and their mean flow was not cyclic in the east-west direction. Fig. 3 contains the steady forcing function  $Q$ , which is given by (2.3). The field lacks symmetry about  $x = 0$  because of the presence of friction.

The vorticity equation (2.1) is integrated numerically with leapfrog time differencing except that the friction term is evaluated at the previous time. Also, the time filter developed for Robert (1966; see also Asselin, 1972) is applied to the previous time with the coefficient

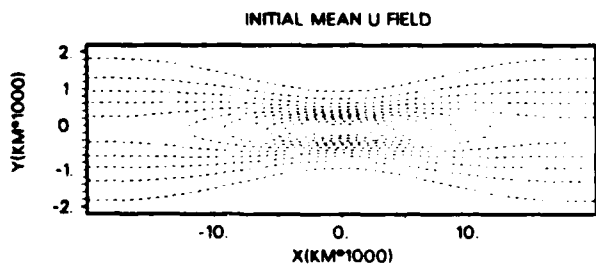


FIG. 2. The initial mean zonal velocity  $\bar{u}$ . The contour interval is  $2.5 \text{ m s}^{-1}$  and the central value is  $-27.5 \text{ m s}^{-1}$ .

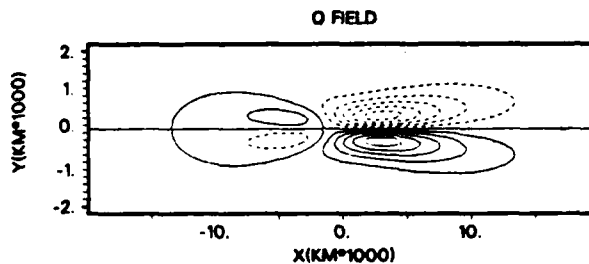


FIG. 3. The steady forcing function  $Q$ . The contour interval is  $2.5 \times 10^{-11} \text{ s}^{-2}$ .

$\gamma = 0.1$ . The nonlinear terms are approximated with the finite-difference forms that were developed by Arakawa (1966), which conserve mean enstrophy and mean kinetic energy. TWC used the same numerical procedure except that they used Euler backward time differencing. The left-hand side of (2.1) is solved for  $\partial\psi/\partial t$  with the direct method described by Sweet (1973). The following boundary conditions are employed:

$$\frac{\partial\psi}{\partial t}(x, -D, t) = \frac{\partial\psi}{\partial t}(x, D, t) = 0, \quad (2.8)$$

$$\psi(X_w, y, t) = \psi(X_E, y, t). \quad (2.9)$$

Since  $\psi$  is initially constant along  $y = \pm D$ , Eq. (2.8) indicates that  $\psi$  will not change along these boundaries. Thus the domain average of  $u = -\partial\psi/\partial y$  will be independent of time, which is appropriate for long-term integration where the mean flow must be maintained. This condition implies that the integrated source term  $Q$  must balance the frictional drag. This boundary condition is different from the appropriate condition for the inviscid unforced vorticity equation which is that the average  $u$  component along each wall be time-independent.

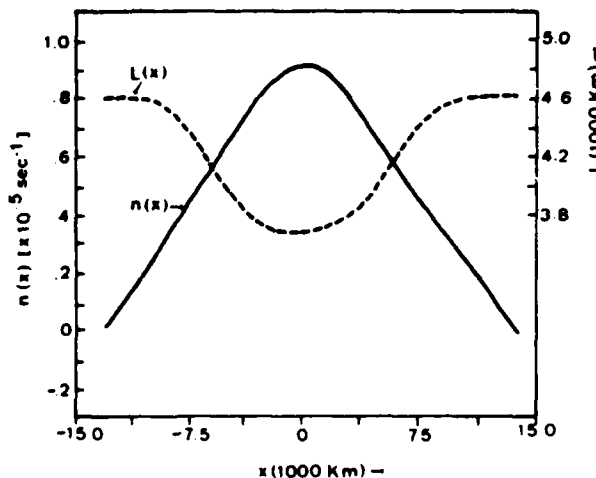


FIG. 4. The most unstable wavelength  $L$  and the corresponding local growth rate  $n$  determined from the parallel flow model applied to  $\bar{u}$ .

## 3. Overview of numerical results

The basic numerical experiment uses the following parametric values:

$$2D = 4250 \text{ km}, \quad X_E = -X_W = 20\,250 \text{ km},$$

$$\bar{L} = 36\,000 \text{ km}, \quad \lambda = 1.5 \times 10^{-6} \text{ s}^{-1},$$

$$\Delta x = 375 \text{ km}, \quad \Delta y = 125 \text{ km}, \quad \Delta t = 1 \text{ h}.$$

Here  $\Delta y$  is chosen smaller than  $\Delta x$  so that the basic flow vorticity can be more accurately calculated.

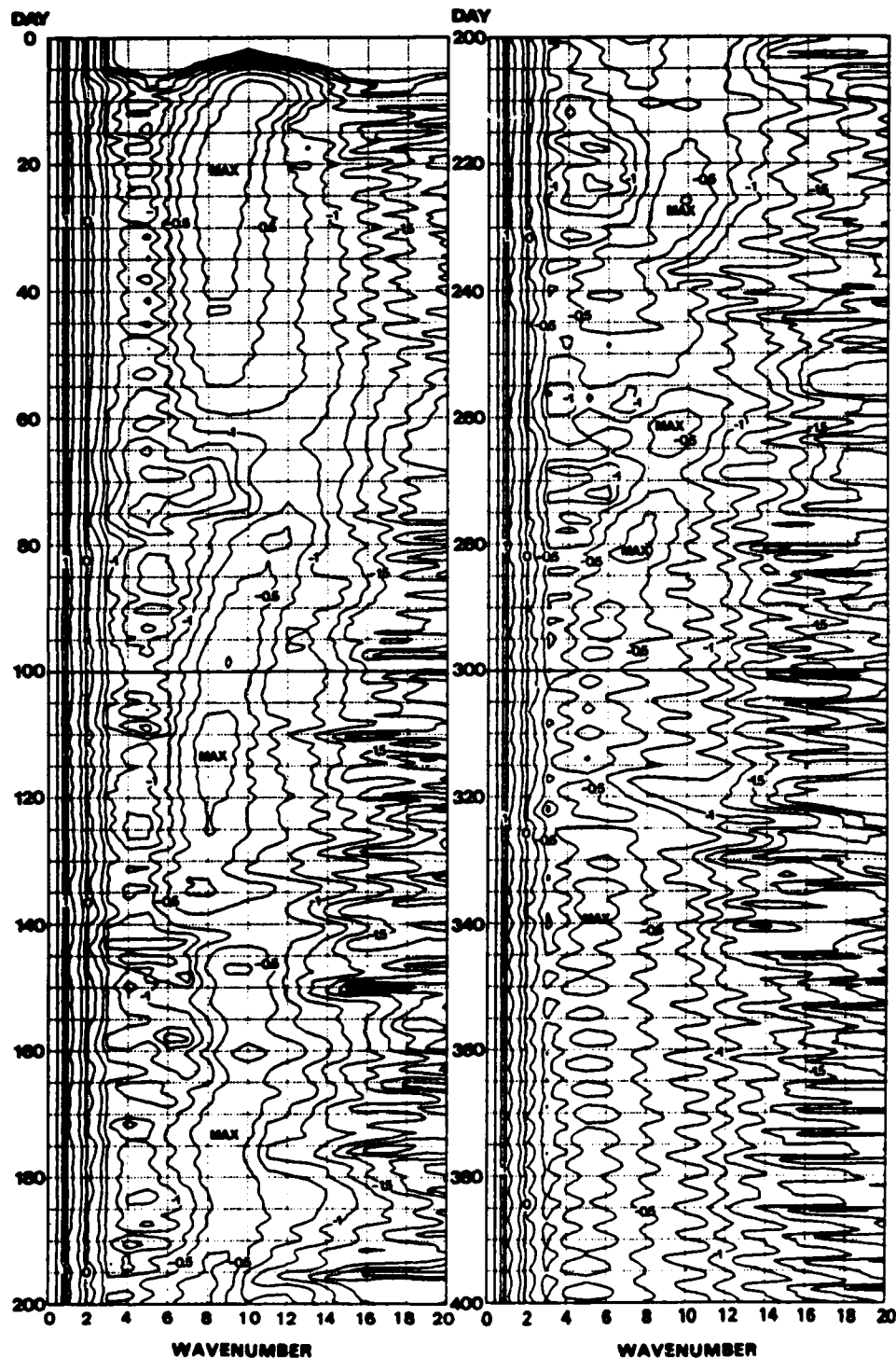


FIG. 5. Kinetic energy averaged over  $y$  as a function of time and the number of zonal waves. The contours are labeled with the logarithm of the energy.

In order to investigate the stability properties of the downstream varying jet, it is useful to apply the linearized barotropic vorticity equation for a parallel flow where  $U(y)$  is taken from  $U(x, y)$  for each longitude. As is discussed in TWC, the vorticity equation is solved with the initial value technique used by Williams *et al.* (1971). Fig. 4 shows the growth rates  $n$  corresponding to the most unstable wavelengths  $L$  as functions of  $x$  for the forced mean flow. Only the growing solutions are given. The largest growth rate occurs at  $x = 0$  where the jet is a maximum and its  $y$ -scale is a minimum. The waves are damped for  $|x| > 13\,000$  km. The most unstable wavelengths range from 3650 km at  $x = 0$  to 4600 km in the outer regions.

Based on these parallel flow stability properties of the forced basic flow, the following initial conditions are used for the basic numerical experiment:

$$\psi(x, y, 0) = \tilde{\psi}(x, y) + A \cos\left(\frac{\pi y}{2D}\right) \sin\left(\frac{2\pi x}{L_0}\right), \quad (3.1)$$

where  $A = 10^5 \text{ m}^2 \text{ s}^{-1}$  and  $L_0 = (X_E - X_w)/10 = 4050$  km. This corresponds to a maximum  $v$  component of  $0.155 \text{ m s}^{-1}$ . This initial wave is a little longer than the most unstable wave from Fig. 4 but it was found in TWC that the dominant wavelength in the downstream varying jet was longer than the most unstable wavelength.

An overview of the time evolution of the numerical solution can be obtained by examining the kinetic energy as a function of the east-west wavenumber as shown in Fig. 5. As a result of the forcing, wavenumber 1 has the maximum energy throughout the 450-day integration. In the early portion of the experiment, there is a secondary maximum at wavenumber 10 as a result of the instability of the initial disturbance. The energy in this scale reaches a relative maximum within ten days. This maximum shifts toward shorter wave-

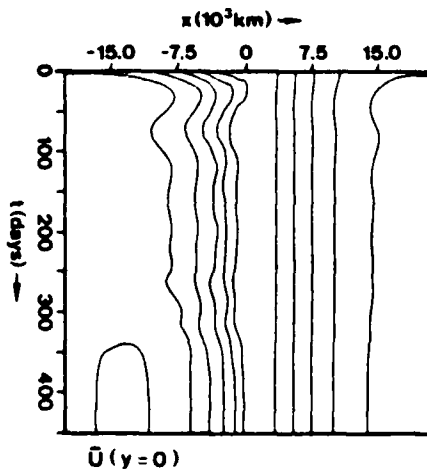


FIG. 6. The mean wind  $\bar{U}$  at  $y = 0$  as a function of  $x$  and  $t$ . The contour interval is  $3.5 \text{ m s}^{-1}$  and the two isopleths which straddle  $x = 0$  at  $t = 0$  have the value  $-27 \text{ m s}^{-1}$ .

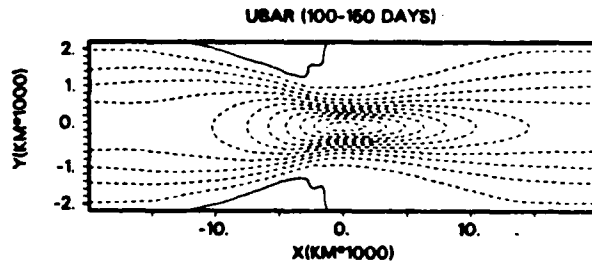


FIG. 7. The zonal wind averaged over the interval 100–150 days as a function of  $x$  and  $y$ . The contour interval is  $2.5 \text{ m s}^{-1}$  and the central value is  $-27.5 \text{ m s}^{-1}$ .

lengths (wavenumbers 8 to 9) over a 50-day interval and then it disappears. Later, new maxima appear near wavenumber 10 and they follow a similar evolution. This general behavior where growth occurs in a higher wavenumber is repeated every 50 days or so until  $\sim 300$  days. The portion of the experiment out to 350 days will be referred to as the "adjustment phase". After  $\sim 350$  days, the solution goes into a 4-day oscillation with an energy maximum at wavenumber 5. This will be called the "quasi-equilibrium phase". Early in the integration, wavenumber 5 also has a 4-day oscillation but at that time it had a minimum energy. Fig. 6 shows  $U$  at  $y = 0$  as a function of  $x$  and  $t$ .  $U$  is time filtered in such a way that periods  $< 10$  days are removed. Oscillations with periods of  $\sim 50$  days are present during the first 300 days, and these correspond to the energy variations in Fig. 5. Most of the mean flow oscillations occur downstream ( $x < 0$ ) from the jet maximum. This is consistent with the prediction in TWC that the nonlinear interaction between the disturbances and the mean flow would stabilize the mean flow downstream from the jet maximum. Fig. 6 shows that the speeds in this region are greatly reduced and it will be shown that the jet profile is also broadened. These changes reduce the magnitude of  $\partial^2 U / \partial y^2$  which stabilizes the flow.

#### 4. Analysis of the adjustment phase: Interval 100–150 days

To examine the behavior of a typical portion of the adjustment phase, the solutions in the interval 100–150 days are analyzed in this section. By this time, the mean flow has been extensively modified, but it is still evolving. Fig. 7 shows the zonal wind averaged over this interval, where the averaging interval should remove the 50-day oscillations. When this field is compared with the initial  $U$  (Fig. 2), it is seen that  $U$  is greatly modified downstream from the jet maximum ( $x < 0$ ). The speed is reduced and the jet is considerably broadened. The stabilization of the mean flow in this region is caused by interaction with the disturbances which have a large amplitude downstream from the jet maximum.

Daily fields of  $\psi$  are given in Fig. 8 from  $t = 120$  days to  $t = 124$  days. Reference to Fig. 5 shows that this 4-day sequence occurs at the end of one of the regimes of energy shift to smaller wavenumber. The waves, which have negligible amplitude upstream, reach a maximum amplitude downstream from the jet maximum ( $x = 0$ ) and they then decay further downstream.

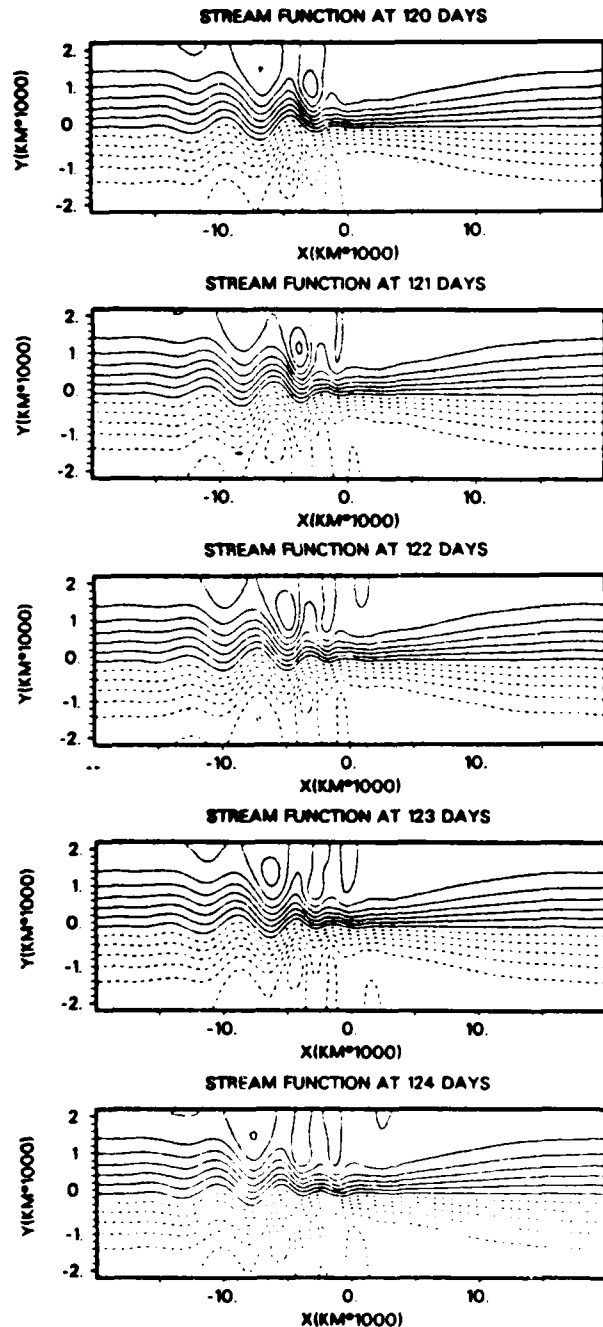


FIG. 8. Daily fields of the streamfunction  $\psi$  are given from  $t = 120$  days to  $t = 124$  days. The contour interval is  $2.5 \times 10^6 \text{ m}^2 \text{ s}^{-1}$ .

TABLE 1. Dominant frequencies of  $\psi'$  for the 100–150 day interval during the adjustment phase. Here  $\nu_{\text{range}}$  gives the spatial range of frequency,  $\nu_{\text{max}}$  is the frequency at maximum amplitude of  $\psi'$  and  $P_{\text{max}}$  is the corresponding period.

Mode	$\nu_{\text{range}}$ ( $10^{-5} \text{ s}^{-1}$ )	$\nu_{\text{max}}$ ( $10^{-5} \text{ s}^{-1}$ )	$P_{\text{max}}$ (days)
1	2.15–2.20	2.17	3.35
2	1.80–2.04	2.03	3.58

The perturbation streamfunction  $\psi'$  is calculated from

$$\psi' = \psi - \bar{\psi},$$

where  $\bar{\psi}$  is the average over the interval  $t = 100$ –150 days. When the power spectrum of  $\psi'$  is computed as a function of frequency  $\nu$  and the east–west wavenumber, a strong peak is found near  $\nu = 2 \times 10^{-5} \text{ s}^{-1}$ . However, this peak is spread out over a range of wavenumbers. This is consistent with the disturbances in Fig. 5, where the wavelength varies downstream and the disturbances have very little amplitude in the upstream region. Because the disturbances have a strong spatial variation in structure, it is better to use the Fourier analysis of  $\psi'$  at each spatial point as described by Bloomfield (1976). With this technique the amplitudes and phases of the strongest periodicities in a time series can be obtained.

The time series for  $\psi$  are analyzed for the seven frequencies which give the largest contribution to the variance of  $\psi$ . The analysis was carried out at selected spatial grid points (every other point in  $y$  and every third point in  $x$ ) and the two strongest modes are given in Table 1. Unlike the solutions given by TWC, the frequency for each mode varies spatially because of nonlinear effects and also because the solution has not reached quasi-equilibrium. Figs. 9 and 11 give the amplitudes of  $\psi'$  for modes 1 and 2 respectively, in the lower half of the channel. Mode 1 has a maximum amplitude which is approximately twice as large as the maximum amplitude for Mode 2. Both modes show rapid downstream growth beginning upstream from  $x = 0$ , and slow decay after maxima around  $x = -5000$  km. This disturbance structure is evident in the synoptic series which is given in Fig. 8.

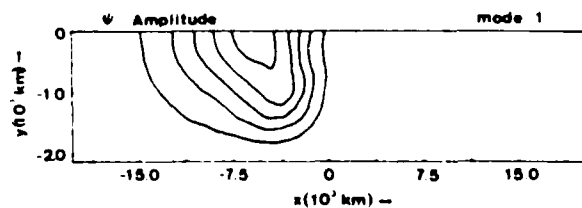


FIG. 9. The amplitude of  $\psi$  for mode 1 from the interval 100–150 days in the lower half of the channel. The contour interval is  $10^6 \text{ m}^2 \text{ s}^{-1}$ .

Figures 10 and 12 show the phase lines for modes 1 and 2, respectively. The phase lines are not given in regions where the amplitude is very small, since the phase is poorly estimated there. The conversion of zonal mean kinetic energy to disturbance energy [Haltiner and Williams (1980) p. 75] is given by

$$\{\bar{K} \cdot K'\} = -\frac{k}{2} \int_{-D}^D \Psi_k^2 \frac{\partial \theta_k}{\partial y} \frac{\partial U}{\partial y} dy, \quad (4.1)$$

where  $\Psi_k$  is the amplitude and  $\theta_k$  the phase of wave-number  $k$ . This formula was derived for a parallel mean flow, but TWC have shown that the  $v$  terms in the energy equation are unimportant. Upstream from  $x = 0$  in the central region ( $|y| \leq 500$  km), the phase lines tilt in such a way that  $\partial \theta / \partial y$  and  $\partial U / \partial y$  are of opposite signs so that disturbances draw energy from the mean flow. This behavior is more noticeable with mode 1 which has better defined phase lines because of the larger amplitude. For mode 1, the shortest wavelength occurs just upstream from  $x = 0$ , and for mode 2 the minimum wavelength occurs downstream near the location of the amplitude maximum. Mode 2 has the smallest scale which seems inconsistent with its lower frequency, but the structure of this mode is not as well-defined because of its smaller amplitude. Perhaps the presence of mode 2 is itself indicative of the adjustment phase.

An indication of the local stability properties of the  $U$  field given in Fig. 7 can be obtained by computing the growth rates from a linearized parallel flow model applied at various longitudes ( $x$ 's) as was done by TWC. The initial value technique used by Williams *et al.* (1971) gives growth rates and phase speeds as a function of wavenumber for each wind profile. Since the frequency can be computed for each phase speed and wavenumber, the growth rate can be given as a function of frequency which is convenient for comparison with the previously obtained modes. Fig. 13 contains the parallel flow growth rates at various longitudes as a function of frequency. At  $t = 0$ , the maximum growth rate was at  $x = 0$  and the growth rate was symmetric about  $x = 0$  (see Fig. 4). In Fig. 13, the maximum  $n$  is still near  $x = 0$ , but the growth rates downstream from  $x = 0$  are greatly reduced relative to the upstream or initial values. This is consistent with the greatly reduced values of  $|\partial^2 U / \partial y^2|$  in the downstream region

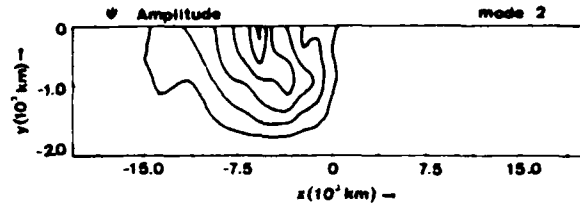


FIG. 11. The amplitude of  $\psi$  for mode 2 from the interval 100–150 days. The contour interval is  $0.4 \times 10^6 \text{ m}^2 \text{ s}^{-1}$ .

in Fig. 7. This downstream region was stabilized by the interaction of the disturbances with the mean flow.

The frequencies for modes 1 and 2, which are marked on the sides of the figure, are within the unstable interval at each longitude. These modes are near the most unstable frequency at  $x = 9375$  km and they are higher than the most unstable frequency at  $x = -3750$  km, which is at the other end of the unstable region. The maximum growth rate (which is at  $x = 0$ ) occurs for a higher frequency than either of the observed modes. This was also found by TWC who noticed that the observed wavelength was greater than the most unstable wavelength based on the parallel flow theory. The maximum amplitudes for modes 1 and 2 (Figs. 9 and 11) occur at longitudes which are somewhat downstream from the longitudes where the parallel flow growth rates are zero for each mode. The phase tilts in Fig. 10 are consistent with upstream growth for mode 1 in Fig. 13.

#### 5. Analysis of the quasi-equilibrium phase: Interval 400–450 days

The solutions after 350 days achieve a quasi-equilibrium state with a 4-day oscillation and this behavior does not change. Fig. 14 shows the zonal wind averaged over the interval 400–450 days. The  $U$  is generally similar to  $U$  for the interval 100–150 days as seen in Fig. 7. However, in the downstream region ( $x < 0$ )  $|U|$  is reduced relative to the speeds given in Fig. 7 and a minimum along  $y = 0$  is present at  $x = -14$  000 km. Also, the isolines are spread further apart in the downstream region.

Daily fields of  $\psi$  are given in Fig. 15 from  $t = 400$  days to  $t = 404$  days. The first and last maps are es-

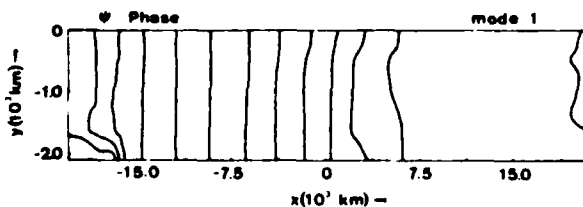


FIG. 10. The phase lines of  $\psi$  for mode 1 from the interval 100–150 days. The contour interval is  $180^\circ$  and the phase increases from right to left.

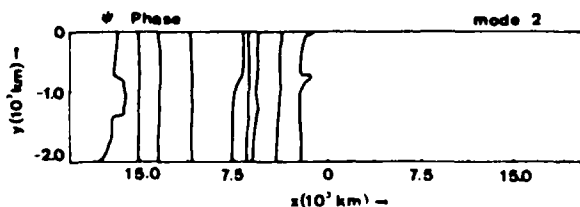


FIG. 12. The phase lines of  $\psi$  for mode 2 from the interval 100–150 days. The contour interval is  $180^\circ$  and the phase increases from right to left.

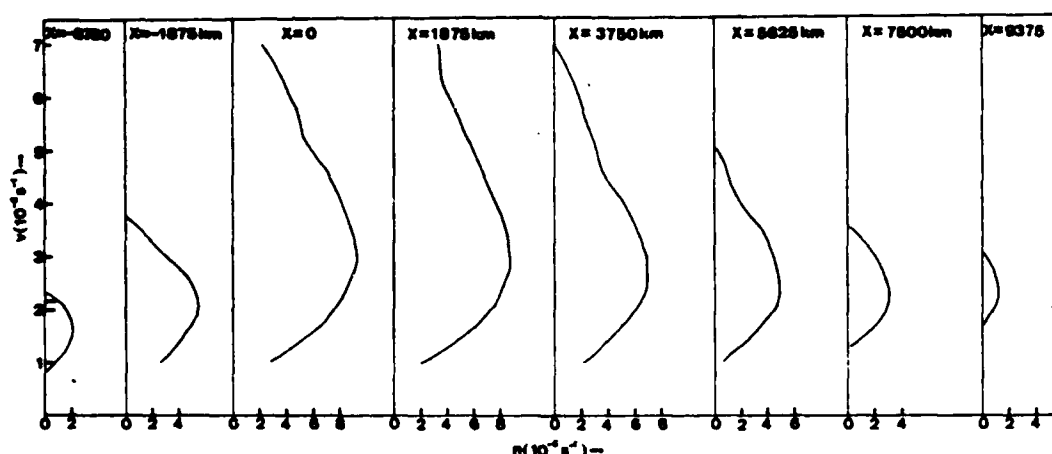


FIG. 13. Growth rates  $n$  as functions of frequency  $\nu$ , for various longitudes from the linear parallel flow model applied to  $\bar{U}$  from the interval 100–150 days.

essentially identical which is consistent with a four-day oscillation in  $\psi$ . The maps are generally similar to the maps given in Fig. 8 for the earlier series, but there are some important differences. Waves are now detectable in the upstream region and the wavelength varies by a factor of two between the outer regions and the large amplitude region near  $x = 0$ .

The time series for  $\psi'$  is Fourier analyzed at selected spatial points as was done in the previous section and the dominant modes are given in Table 2. In this case, the frequencies for mode 1 do not vary appreciably from point to point as was the case with the earlier interval. Mode 1 corresponds to the 4-day period which is apparent in Figs. 4 and 15, and mode 2 corresponds to a 2-day period. Figs. 16 and 18 give the amplitudes of  $\psi'$  for modes 1 and 2, respectively, in the lower half of the channel. The ratio of the amplitudes of the 2-day mode to 4-day mode varies from 0.01 in the upstream region to a maximum of 0.17 at  $x = -2250$  km. The structure of the 4-day mode is much more similar to the modes obtained from the 100–150 day time interval (see Figs. 9 and 10). The amplitude of

the 2-day mode has a much smaller scale in both  $x$  and  $y$  than the 4-day mode. Figs. 17 and 19 give the phase lines for modes 1 and 2, respectively. The 4-day mode has the proper tilt for energy conversion in the interval  $-3750 \text{ km} \leq x \leq 7500 \text{ km}$  [see Eq. (4.1)]. The wavelength, which can be obtained from the spacing of the phase lines, varies by almost a factor of 2 from the minimum near  $x = -4000$  km to the maximum near  $x = 15000$  km. The spatial variation of the wavelength is quite different from the variation which was obtained by TWC, and it will be examined in more detail in Section 7. The wavelengths derived from the phase line spacings in Fig. 19 are much smaller than the wavelengths for the 4-day wave.

It strongly appears that the 2-day mode is the result of the direct interaction of the 4-day mode with itself. For example, if a quadratic nonlinear term is calculated with

$$\psi' \sim e^{i(kx + \omega t)},$$

the nonlinear term will be proportional to

$$\text{N.L.} \sim e^{i(2kx + 2\omega t)},$$

and a wave with twice the frequency and twice the wavenumber will be forced. Mode 2 does have twice the frequency of mode 1 and Figs. 18 and 19 show that mode 2 has a much smaller horizontal scale than mode 1. Also, the variation of the ratio of the amplitudes of mode 2 to mode 1 is consistent with the view that mode 2 is forced by mode 1 since the ratio is largest when the amplitude of mode 1 is large.

Figure 20 contains the parallel flow growth rates at various longitudes as a function of frequency for the  $U$ -field given in Fig. 14. Comparison with Fig. 13 shows smaller growth rates in Fig. 20, with the largest differences occurring for  $x \leq 0$ . These differences in

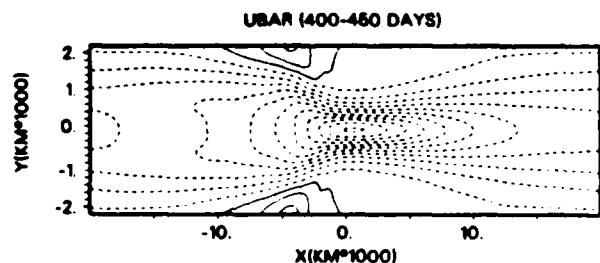


FIG. 14. The zonal wind averaged over the interval 400–450 days. The contour interval is  $2.5 \text{ m s}^{-1}$  and the central value is  $-25 \text{ m s}^{-1}$ .

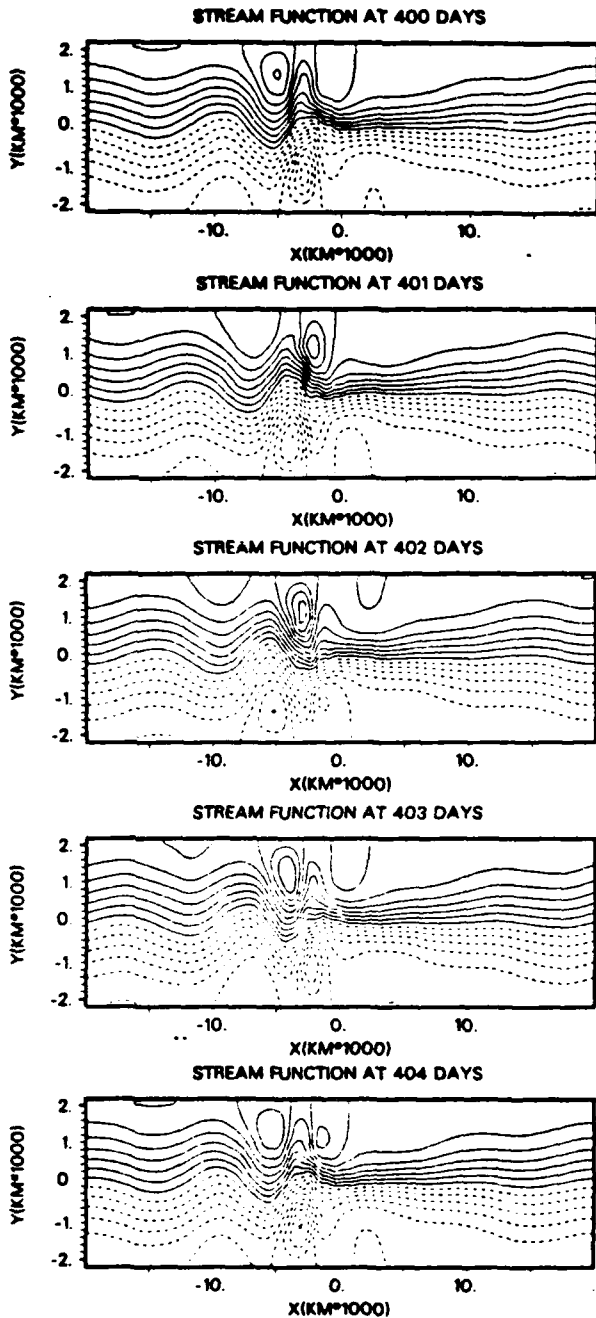


FIG. 15. Daily maps of the streamfunction  $\psi$  are given from  $t = 400$  days to  $t = 404$  days. The contour interval is  $2.5 \times 10^6 \text{ m}^2 \text{ s}^{-1}$ .

growth rate are reasonable when Figs. 7 and 14 are compared because the latter has smaller values of  $|\partial^2 U / \partial y^2|$  in the downstream region. The frequencies for modes 1 and 2 are marked on the sides of the figure. Mode 1 has the maximum growth rate in the outflow region ( $x = -1875 \text{ km}$ ) and this may help the disturbance propagate through the stable region before it re-

TABLE 2. As in Table 1 except the dominant frequencies for the quasi-equilibrium phase.

Mode	$\nu_{\text{max}}$ ( $10^{-3} \text{ s}^{-1}$ )	$\nu_{\text{min}}$ ( $10^{-3} \text{ s}^{-1}$ )	$P_{\text{max}}$ (days)
1	1.81	1.81	4.02
2	3.87-3.54	3.61	2.01

enters the unstable portion of the jet. Neither mode is unstable at the upstream entrance ( $x = 9375 \text{ km}$ ), while in the interval 100-150 days during the adjustment phase, both modes were unstable. At the longitude of maximum growth rate ( $x = 1875 \text{ km}$ ), mode 2 has a larger growth rate than mode 1. The  $x$ -integrals of the growth rate from  $x = 9375 \text{ km}$  to  $x = -1875 \text{ km}$  are approximately equal for the two modes. Thus, the growth of mode 2 relative to mode 1 by a factor of 15 can only be explained by nonlinear forcing from mode 1.

6. Spatial growth rates and wave properties for mode 1

In the last section it was shown that the time-dependent portion of the solution in the quasi-equilibrium phase is dominated by mode 1 which has a period of 4 days. Although mode 2 with a period of 2 days is present, its amplitude is small and it is apparently directly forced by mode 1. There is a strong nonlinear interaction between mode 1 and the mean flow which stabilizes the jet in the outflow region. On the other hand, mode 2 has very little effect, because the square of its amplitude is very small compared to mode 1. The propagation of mode 1 through the modified mean flow should be a linear process since the energy loss to mode 2 is small. Also, it will be shown in the next section that the wavelength variation can be explained with a linear equation. In this section, the growth rates, phase speeds and wavelengths for mode 1 will be compared with values from the parallel flow model. These results will then be interpreted in view of the main features found in TWC.

Figure 21 shows the wavelengths at  $y = 0$  and  $y = \pm 750 \text{ km}$  as a function of  $x$ , computed from the

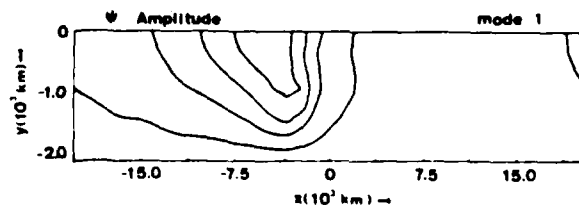


FIG. 16. The amplitude of  $\psi$  for mode 1 from the interval 400-450 days. The contour interval is  $2 \times 10^6 \text{ m}^2 \text{ s}^{-1}$ .

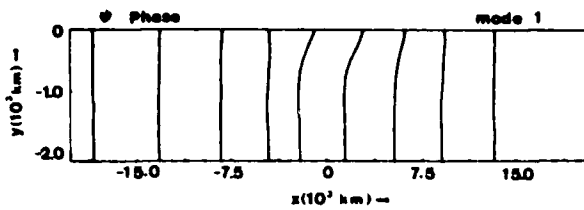


FIG. 17. The phase lines of  $\psi$  for mode 1 from the interval 400–450 days. The contour interval is  $180^\circ$  and the phase increases from right to left.

phases given in Fig. 17. These curves differ in the jet region because of the downstream variation of wave tilt which was also found by TWC. The third curve shows the wavelength obtained from the parallel flow model for the frequency corresponding to mode 1 (see Fig. 20). In this case, only the unstable solutions are shown because the initial value technique used in the parallel flow model may not be representative of the dispersion relation. The overall variation of the wavelength with  $x$  is very different from the variation found by TWC. In the jet region, the scale is generally small and it is much larger in the outer regions, whereas TWC found the maximum scale near the jet maximum. This maximum was attributed to the downstream dilatation of the phase lines due to the increase in the mean wind speed. In fact, this effect can be seen in Fig. 21 between  $x = 5000$  km and  $x = -5000$  km, where the wavelength increases and decreases in relation to changes in the mean wind speed. The wavelengths from the parallel flow model show a similar variation, but they are everywhere less than in the numerical model. The overall problem of the downstream variation of wavelength will be treated in Section 7.

Figure 22 contains the phase speed calculated from the relation

$$c = -L\nu/2\pi, \quad (6.1)$$

for  $y = 0$ , where  $\nu$  is the frequency of mode 1. The parallel flow values are also included. The patterns are the same as in Fig. 21 since  $c$  is proportional to  $L$  in (6.1).

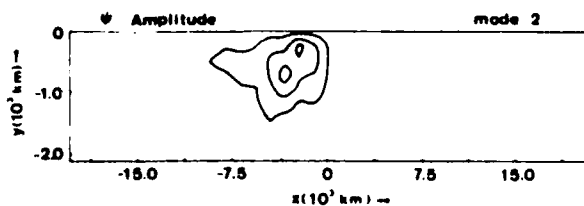


FIG. 18. The amplitude of  $\psi$  for mode 2 from the interval 400–450 days. The contour interval is  $0.4 \times 10^9 \text{ m}^2 \text{ s}^{-1}$ .

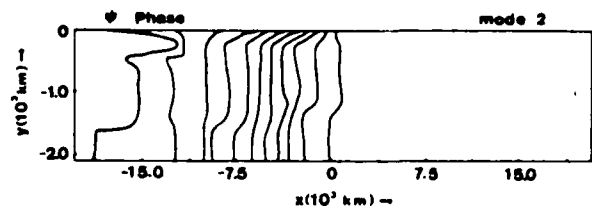


FIG. 19. The phase lines of  $\psi$  for mode 2 from the interval 400–450 days. The contour interval is  $180^\circ$ , and the phase increases from right to left.

Figure 23 shows the amplitude of mode 1 along  $y = 0$  on a log-linear plot. There is a region of downstream, exponential growth between  $x = 6000$  and  $x = -2000$  km. This can be compared with Fig. 10 in the paper by TWC which shows a much broader peak with the maximum much further downstream. This difference is due primarily to the downstream erosion of the jet in the nonlinear experiment, which eliminates the instability in that part of the jet.

The spatial growth rate  $m$  is given in Fig. 24. For the numerical model, the spatial growth rate can be computed from the relation

$$m^* = \frac{1}{x_2 - x_1} \ln \left[ \frac{A(x_2, 0)}{A(x_1, 0)} \right], \quad (6.2)$$

where  $A(x, y)$  is the amplitude for mode 1 (see Fig. 16), and  $x_2 - x_1 = 3\Delta x$ . The growth rates  $m'$  and  $m''$  are obtained from the parallel flow model with the relation

$$m = n/c, \quad (6.3)$$

The curve  $m'$  uses the  $n$  and  $c$ , for the wavenumber which satisfies (6.1) with  $\nu$  the frequency of mode 1. However,  $m''$  is calculated with the  $n$  and  $c$ , for the observed wavelength at  $y = 0$  which is given in Fig. 21. The latter procedure was used by TWC. In Fig. 24, the maximum downstream growth rate from the numerical model is over 25% larger than for both the parallel flow calculations. A similar relation was found by TWC, but in the present case the difference is larger. Also, the parallel flow curves are shifted upstream relative to  $m^*$ , which shows a hysteresis effect wherein the wave structure lags in adjusting to the local stability properties. This was also found by TWC.

Figure 25 compares the observed phase structure for mode 1 with the structure predicted by the parallel flow theory at various longitudes. Along the longitude of maximum parallel flow growth rate ( $x = 1875$  km), the phase structure is very close in the central region ( $|y| \leq 500$  km) where most of the energy conversion is, and in the outer region the phase difference increases to about  $20^\circ$  at the boundary. At the upstream end of the jet ( $x = 7500$  km), the observed phase tilt is much less than the tilt predicted by parallel flow theory.

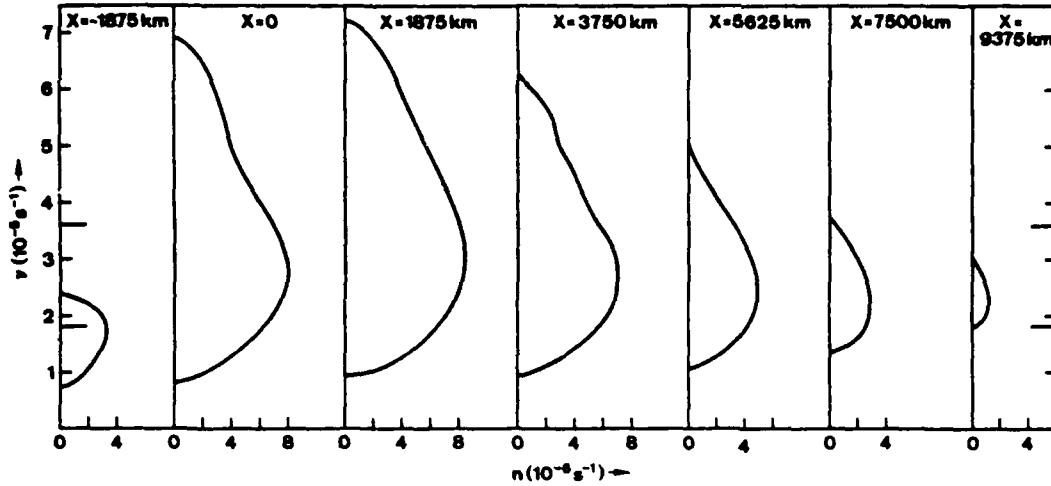


FIG. 20. Growth rates  $n$  as functions of frequency  $\nu$ , for various longitudes from the linear parallel flow model applied to  $\bar{U}$  from the interval 400–450 days.

This hysteresis behavior, wherein the structure of a wave which is moving into a more unstable region lags with respect to the parallel flow structure, was observed by TWC. At the downstream end of the unstable region ( $x = -1875$  km), the phase tilt for mode 1 is much larger than the parallel flow tilt in the central region where the mean shear is large. This is the opposite of what occurs at the upstream end, but it shows the same hysteresis effect found by TWC where the upstream structure is partially advected downstream.

7. Discussion of wavelength variation

One of the most striking features of the quasi-equilibrium phase is the downstream variation of wave-

length (Fig. 21). Tupaz *et al.* found that the wavelength varied in rough proportion to the mean wind speed, whereas in the current study it seems to vary in the opposite sense. To understand this behavior, the following generalized Rossby wave formula is derived (see Appendix):

$$c = [U] - \frac{[\beta]}{k^2 + \alpha^2}, \tag{7.1}$$

where  $[U]$  (A13) and  $[\beta]$  (A14) represent the weighted meridional averages of the mean zonal flow and mean absolute vorticity gradient, respectively. The weighting function varies from 1 in the center of the channel to 0 at the walls.

Figure 26 contains  $[U]$  and  $[\beta]$ , which are calculated by numerical integration over  $y$  from the  $U$  field in Fig. 14 at each longitude. The  $[U]$  field has a maximum

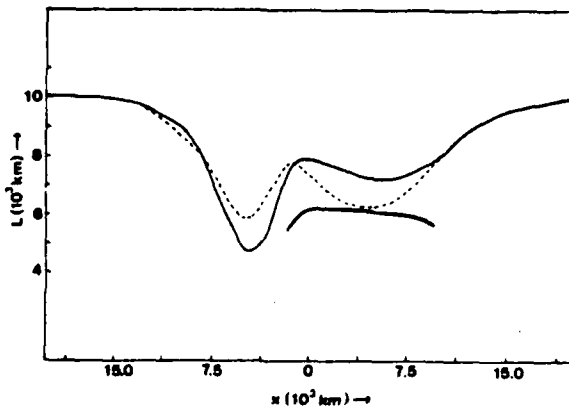


FIG. 21. The wavelengths from mode 1 in the 400–450 day interval as follows: 1) numerical model at  $y = 0$  (dashed line), 2) numerical model at  $y = -750$  km (solid line), 3) parallel flow model with mode 1 frequency (bold line).

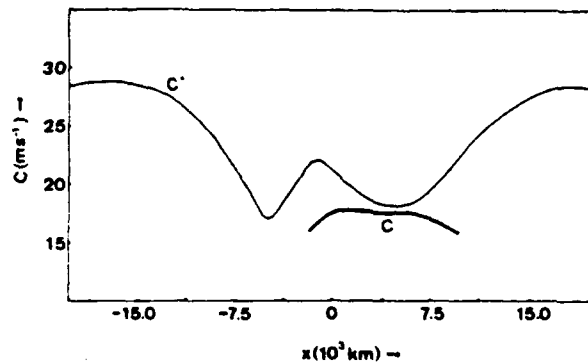


FIG. 22. The phase speeds from mode 1 in the 400–450 day interval. Here  $c^*$  is from the numerical model at  $y = 0$ , and  $c$  is from the parallel flow model at the frequency of mode 1.

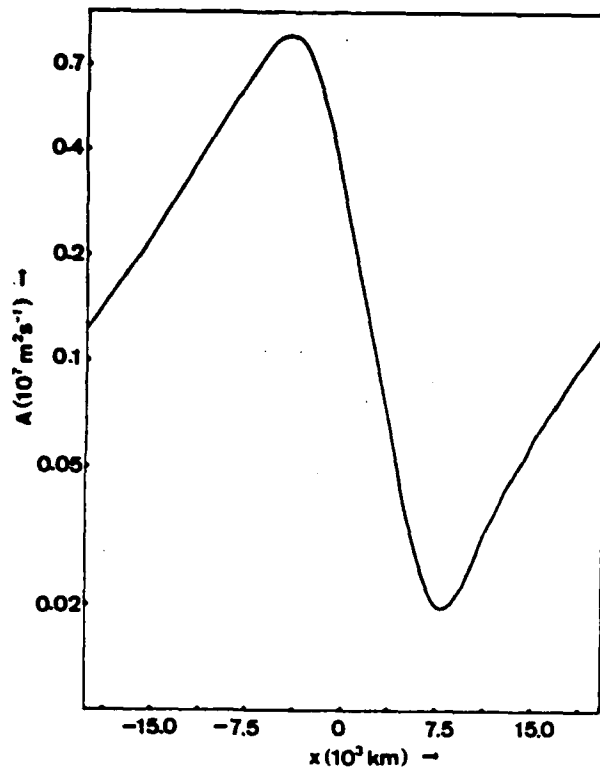


FIG. 23. The amplitude  $A$  of  $\psi$  for mode 1 along  $y = 0$  on a logarithmic scale.

magnitude at  $x = -700$  km, while the maximum speed in Fig. 14 occurs for  $x > 0$ . This difference in maximum location arises because, although the downstream portion of the jet is slowing down, it is also broadening relative to the upstream portion. This leads to a relatively larger response when multiplied by the  $\cos^2(\alpha y)$  weighting function (see Fig. 14). The weighted average of  $\partial^2 U / \partial y^2$  must be positive at each longitude because

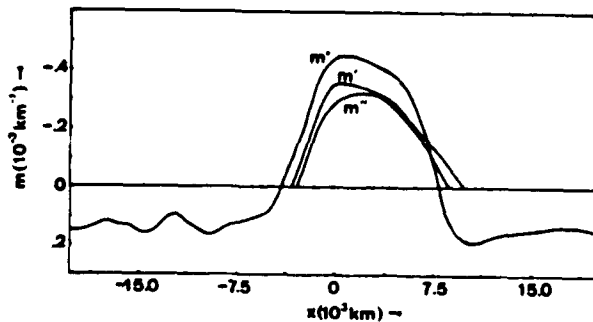


FIG. 24. The spatial growth rate  $m$  for mode 1 as follows:  $m^*$  is calculated from the numerical model with Eq. (6.2);  $m'$  and  $m''$  are obtained from the parallel flow model through Eq. (6.3), where  $m'$  has the frequency of mode 1 and  $m''$  has the wavelength from the numerical model at  $y = 0$ .

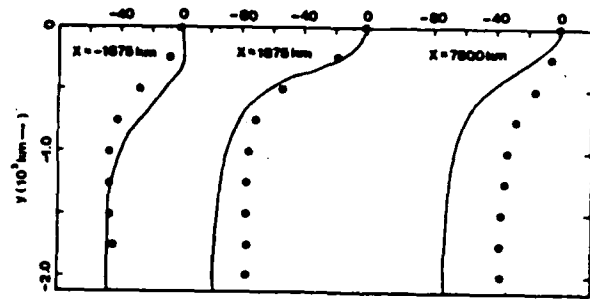


FIG. 25. The phase (deg) for mode 1 at various longitudes. The dots are from the numerical model and the curves are from the parallel flow model with the frequency of mode 1.

$[\beta]$  is everywhere less than  $\beta = 2.24 \times 10^{-11} \text{ m}^{-1} \text{ s}^{-1}$ . The values of  $[\beta]$  are small in the central region. In fact,  $\beta - \partial^2 U / \partial y^2$  must become negative at some latitudes in the unstable region as indicated by the necessary condition for barotropic instability. However, because of the  $\cos^2 \alpha y$  weighting term, the minimum  $[\beta]$  occurs downstream from the jet maximum near the point where  $[u]$  is also an extreme.

In order to assess the accuracy of (7.1) for our numerical experiment, the  $c_f$  from (7.1) is compared with  $c^*$  from the numerical experiment in Fig. 27. The curves are remarkably close, with the largest differences occurring in the central region. In the unstable portion of this region ( $-2000 \text{ km} \leq x \leq 10000 \text{ km}$ ), it would be expected that the formula derived in the Appendix would be very poor because it does not even permit instability. It can be seen in the Appendix that if the zero-order mean flow is stable, the phase speed from (7.1) will always be real. This behavior is related to the difficulty in expanding in  $\epsilon$  across the stability boundary where the solution is not analytic in  $\epsilon$ . Apparently, Eq. (7.1) provides useful estimates of the real part of the phase speed even in regions which have a significant imaginary part. We would also expect larger differences between the parallel flow phase speed and  $c^*$  in the downstream region where the mean flow is changing rapidly. Clearly,  $c_f$  approximates  $c^*$  well enough that (7.1) can be used to understand the downstream variation of wavelength or wavenumber  $k$ .

The frequency  $\nu$  can be obtained by multiplying (7.1) by  $k$ , which gives

$$\nu = k[U] - \frac{k[\beta]}{k^2 + \alpha^2}. \quad (7.2)$$

When  $\nu$  is constant in the domain, Eq. (7.2) gives the downstream variation of wavenumber. If this equation is differentiated with respect to  $x$  we obtain

$$\frac{1}{k} \frac{dk}{dx} = \frac{(k^2 + \alpha^2)^2 \left[ \frac{d}{dx} [U] - \frac{1}{k^2 + \alpha^2} \frac{d}{dx} [\beta] \right]}{[\beta](\alpha^2 - k^2) - 2k^2(k^2 + \alpha^2)[U]}. \quad (7.3)$$

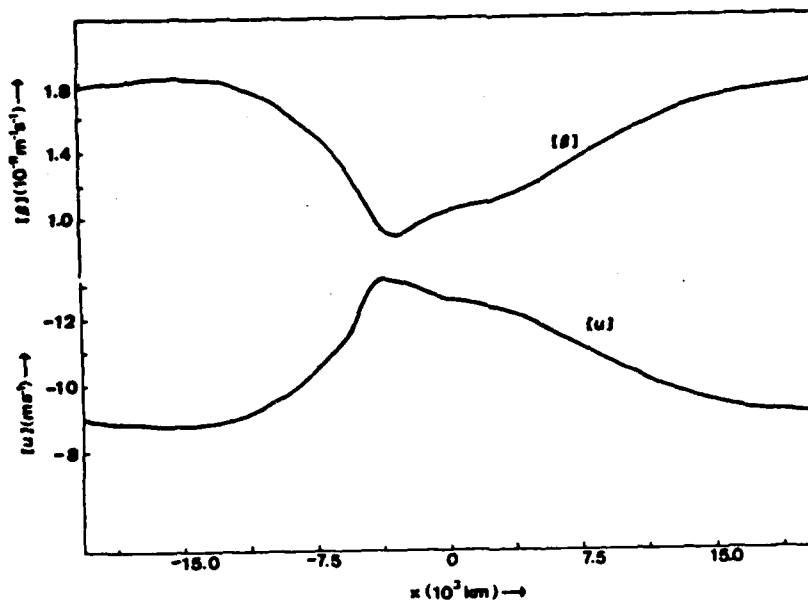


FIG. 26. The quantities  $[U]$  and  $[\beta]$  which are defined by Eqs. (A.13) and (A.14) respectively.

where  $\nu$  and  $\alpha$  are taken to be constant in  $x$ . The denominator remains positive throughout the channel. The first term in the numerator causes the wavelength to increase in proportion to downstream increases in mean wind speed. The second term causes the wavelength to increase downstream with easterly mean flow when  $[\beta]$  increases downstream. The  $[U]$  and  $[\beta]$  variations given in Fig. 26 indicate that the terms are of opposite sign and the observed wavelength variation (Fig. 21) shows that the  $[\beta]$  variation term is largest except near the jet maximum. Since the second term is proportional to the square of the disturbance scale, it should be dominant except near the jet maximum where the scale is small. This is different from the

results of TWC where the  $[U]$  variation term in (7.3) dominated because of the smaller disturbance scale.

### 8. Summary and discussion

In this paper the previous linear study of barotropic instability in a downstream varying easterly jet by TWC is extended to include nonlinear effects. The basic model is the nondivergent barotropic vorticity equation with Rayleigh friction. The flow is confined in an east-west channel with cyclic east-west boundary conditions, instead of the inflow periodic forcing and outflow radiation boundary conditions used by TWC. The initial mean flow is an easterly Bickley jet whose maxi-

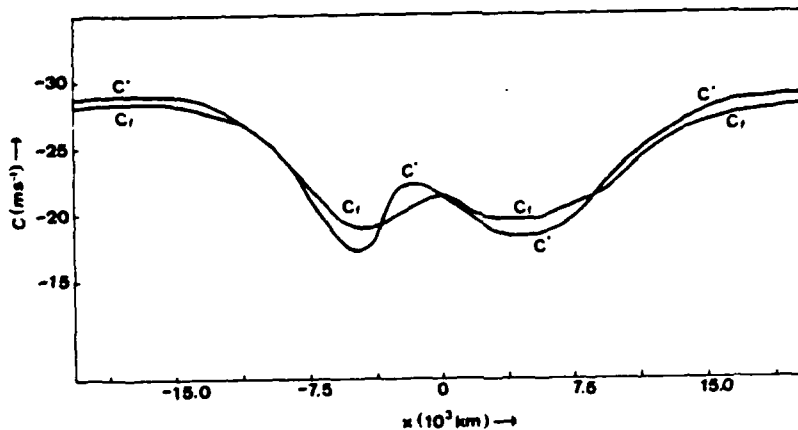


FIG. 27. Comparison of the phase speed  $c^*$  from the numerical model with the phase speed  $c_l$  from Eq. (7.1).

imum speed and half-width vary downstream. A forcing term is included which renders the initial mean flow a steady-state solution to the vorticity equation.

The model is initialized by adding a small-amplitude disturbance of wavenumber 10 to the initial mean flow. The mean flow is unstable in the central region where the jet is strongest and the waves grow rapidly in this region. The energy in wavenumber 10 reaches a relative maximum within 10 days, and the mean flow downstream from the original jet maximum is greatly modified. This modification arises from the energy loss to the growing disturbances which, as was pointed out by TWC, is largest downstream from the most unstable portion of the jet. This can be seen from Eq. (4.1) which shows that the energy transformation is dependent on the square of the wave amplitude and the wave tilt. Roughly speaking, the amplitude is a maximum well downstream where the growth rate is zero. However, the tilt is proportional to the growth rate. Thus, the maximum conversion occurs between the jet maximum and the point where the local growth rate vanishes. After the rapid initial change, the mean flow comes into approximate balance where the energy removed from the mean flow by the disturbances is balanced by the forcing term.

The disturbance kinetic energy maximum which begins at wavenumber 10 shifts from 8 to 9 over the first 50 days, and then dies out. A new maximum then forms near wavenumber 10 and follows a similar evolution as the first energy maximum. This sequence repeats until  $\sim 300$  days. The adjustment phase ends after 350 days when the solution goes into a quasi-equilibrium 4 day oscillation with an energy maximum at wavenumber 5.

The interval 100–150 days is chosen to study the adjustment phase. Growth rates are calculated from a parallel flow model where the interval average zonal wind at each longitude is used. The growth rates in the downstream ( $x < 0$ ) region are greatly reduced relative to the upstream ( $x > 0$ ) domain. This is consistent with reduced values of  $|\partial^2 U/\partial y^2|$  in the downstream region. Fourier analysis of the disturbance streamfunction at each point shows two dominate modes with periods of 3.35 and 3.58 days, respectively, which are somewhat different from the 3.25-day period found in TWC's linear model. However, the frequencies of the two modes vary from point to point as a result of nonlinear effects and lack of equilibrium. When the parallel flow growth rates are plotted as a function of frequency, it can be seen that observed frequencies are much lower than the values which have the largest growth rates except in the entry region of the jet. Both modes have the shortest waves near  $x = 0$ , in contrast to the results obtained by TWC where the longest waves were found in this region.

The numerical solution achieves statistical equilibrium after 350 days when a 4-day oscillation develops

in the disturbance kinetic energy. The interval 400–450 days is chosen to analyze the solution behavior in the quasi-equilibrium phase. The mean zonal wind for this interval shows a further reduction in  $|\partial^2 U/\partial y^2|$  in the downstream region when compared with the mean over 100–150 days. The parallel flow growth rates for the quasi-equilibrium phase are correspondingly reduced in the downstream region relative to the adjustment phase. Fourier analysis of the disturbance streamfunction at each point gives two modes with periods of 4 days and 2 days. The spatial variation of the frequency for mode 1 is very small. The frequency of mode 1 gives the maximum growth rate in the outflow region and this may help the disturbance to propagate through the stable region before it reenters the unstable portion of the jet. However, throughout most of the unstable region, the frequency of mode 1 is considerably less than the most unstable frequency.

It strongly appears that mode 2 (2-day period) is the result of nonlinear interaction of mode 1 with itself. Mode 2 has twice the frequency of mode 1 and it also has a smaller spatial scale. The ratio of the amplitudes of mode 2 to mode 1 varies from 0.01 far upstream to 0.17 near the maximum amplitude of mode 1. When the growth rates from the parallel flow model are integrated across the unstable region, the integrals are approximately the same for the two modes. Therefore, the growth of mode 2 relative to mode 1 by a factor of 15 can only be explained by nonlinear forcing from mode 1.

Mode 1 has a strong interaction with the mean flow which greatly modifies the original mean flow in the downstream region ( $x < 0$ ). However, the propagation of mode 1 through the modified mean flow field should be a linear process, since mode 2 is so small relative to mode 1. Thus, the various wave properties of mode 1 can be profitably compared with the linearized wave properties obtained by TWC. The main differences between mode 1 and the experiment I obtained by TWC are the periods of oscillation—4 days in the former and 3.25 days in the latter—and the mean flow. For  $x > 0$ , the mean flows are very similar, but in the downstream region ( $x < 0$ ), the mean jet for mode 1 is slower and broader than the jet used by TWC.

With mode 1 the wavelength is generally small in the jet region and much larger in the outer regions. This is quite different from the wavelength variation in TWC where the wavelength was a maximum near the jet maximum. In the upstream region where the jet speed is increasing, mode 1 does not have the same type of variation as the solution obtained by TWC. The phase speed is directly proportional to wavelength so that for mode 1, the speed is generally small in the jet region and large in the outer regions. TWC found opposite behavior with the maximum speed near the jet maximum. For mode 1 the maximum spatial growth rate is over 25% larger than the extreme for

the parallel flow model. This is a larger difference than was found in TWC and may be related to the more rapid downstream variation of the mean flow in the outflow region. Also, with mode 1 there is a hysteresis effect wherein the growth rate curve from the full model is shifted downstream relative to the parallel flow solution. Similarly, the phase structure in the full model lags the structure from the parallel flow model. These effects were also evident in the study by TWC. In general, the main effects from downstream variation of the mean flow which were found by TWC are more accentuated for mode 1 of the present study. The exceptions are the downstream variation of wavelength and phase speed which are quite different.

A generalized Rossby wave formula is derived which contains latitudinal integrals of the mean zonal wind and the mean absolute vorticity gradient. When this formula is applied at each longitude, the phase speed from the formula gives a close approximation to the real part of the phase speed for mode 1. This shows that the dispersion properties of mode 1 are well approximated by the generalized Rossby wave formula. The formula shows that the wavelength increases in the downstream region because the northward absolute vorticity gradient is larger in this region than near the jet maximum. This effect increases with the spatial scale as compared with the mean flow effect. The scale found by TWC was smaller (which is consistent with the shorter period), and the advection dominated so that the wavelength decreased when the mean flow decreased in speed. Thus, the differences in wavelength variation between mode 1 and the variation found by TWC are related to the difference in frequencies and associated mean wavelengths.

This numerical experiment is not to be regarded as a detailed simulation of the easterly jet which develops south of the Tibetan high near 200 mb during the Northern Hemisphere summer. In particular, the jet varies seasonally which could preclude the development of the quasi-equilibrium. However, an experiment with a wavenumber 5 initial disturbance showed a rapid development of the quasi-equilibrium phase, and it may turn out that the main features of the quasi-equilibrium phase will be present with a slowly varying forcing. In any case, the dynamic mechanisms studied in this paper should be important in the summer easterly jet and in other jet regions of the atmosphere. These mechanisms include: 1) nonlinear interaction between waves and mean flow which stabilizes the downstream portion of the jet; 2) enhanced growth in jet region; 3) hysteresis effect wherein the disturbance growth lags the local stability conditions; 4) the downstream variation of phase speed and wavelength described by a generalized Rossby wave formula.

*Acknowledgments.* We wish to thank Professor C. Y. Tsay for performing the energy analysis (Fig. 5)

and Mrs. O. Haney for carrying out the computer integrations. The latter were performed at the W. R. Church Computer Center of the Naval Postgraduate School. This research was supported by the Division of Atmospheric Sciences, National Science Foundation under Grant ATM 80-13153. The manuscript was carefully typed by Ms. M. Marks and a portion of the figures were drafted by Miss K. Lee.

#### APPENDIX

##### Approximate Formula for Phase Speed

In this Appendix, an approximate formula for the real part of the phase speed will be derived from the linearized parallel flow vorticity equation following Grotjahn (1979). When (2.1) is linearized about a parallel mean flow  $U(y)$  the equation becomes

$$\frac{\partial}{\partial t} \nabla^2 \psi' + U \frac{\partial}{\partial x} \nabla^2 \psi' + \left( \beta - \frac{d^2 U}{dy^2} \right) \frac{\partial \psi'}{\partial x} = -\lambda \nabla^2 \psi', \quad (\text{A1})$$

where  $\psi'$  is the perturbation streamfunction. If the normal mode form

$$\psi' = \Psi(y) \exp[ik(x - ct)]$$

is substituted into (A1), we obtain

$$(U - c) \left( \frac{d^2 \Psi}{dy^2} - k^2 \Psi \right) - \left( \frac{d^2 U}{dy^2} - \beta \right) \Psi = 0, \quad (\text{A2})$$

where the friction term has been dropped. The boundary conditions are

$$\Psi(\pm D) = 0. \quad (\text{A3})$$

In this procedure, the mean wind is expanded as follows:

$$U = U_0 + \epsilon U_1(y), \quad (\text{A4})$$

where  $U_0$  is a constant and  $\epsilon$  is a small parameter. The other quantities in (A2) are expanded similarly giving

$$\Psi = \Psi_0 + \epsilon \Psi_1 + \dots, \quad (\text{A5})$$

$$c = c_0 + \epsilon c_1 + \dots. \quad (\text{A6})$$

We now substitute (A4), (A5) and (A6) into (A2) and equate the coefficients of each power of  $\epsilon$  to zero, which leads to

$$\epsilon^0: \mathcal{L}(\Psi_0) = (U_0 - c_0) \left( \frac{d^2 \Psi_0}{dy^2} - k^2 \Psi_0 \right) + \beta \Psi_0 = 0, \quad (\text{A7})$$

$$\epsilon^1: \mathcal{L}(\Psi_1) = (U_1 - c_1) \left( \frac{d^2 \Psi_0}{dy^2} - k^2 \Psi_0 \right) - \frac{d^2 U_1}{dy^2} \Psi_0, \quad (\text{A8})$$

with similar expressions for successive  $\epsilon$  terms. A solution to (A7) which satisfies (A3) is

$$\Psi_0 = \cos[\pi y/(2D)], \quad (\text{A9})$$

$$c_0 = U_0 - \frac{\beta}{k^2 + (\pi/2D)^2}. \quad (\text{A10})$$

In order to avoid resonance in solving (A8) for  $\Psi_1$ , it is necessary to require that the right-hand side has no component which is proportional to  $\Psi_0$  (the solution of the homogeneous equation). Thus, we evaluate the right-hand side of (A8) with (A9), multiply by  $\Psi_0$ , integrate from  $y = -D$  to  $y = D$ , and set the integral to zero. This gives the following expression for  $c_1$ :

$$c_1 = \frac{\int_{-D}^D U_1 \cos^2(\alpha y) dy}{\int_{-D}^D \cos^2(\alpha y) dy} + \frac{\int_{-D}^D \frac{d^2 U_1}{dy^2} \cos^2(\alpha y) dy}{(k^2 + \alpha^2) \int_{-D}^D \cos^2(\alpha y) dy}, \quad (\text{A11})$$

where  $\alpha = \pi/(2D)$ . If we now retain only the first two terms in (A6) and use (A10) and (A11) we obtain

$$c = [U] - \frac{[\beta]}{k^2 + \alpha^2}, \quad (\text{A12})$$

where

$$[U] = \frac{\int_{-D}^D U \cos^2(\alpha y) dy}{\int_{-D}^D \cos^2(\alpha y) dy}, \quad (\text{A13})$$

$$[\beta] = \frac{\int_{-D}^D \left( \beta - \frac{d^2 U}{dy^2} \right) \cos^2(\alpha y) dy}{\int_{-D}^D \cos^2(\alpha y) dy}. \quad (\text{A14})$$

#### REFERENCES

- Arakawa, A., 1966: Computational design for long-term numerical integration of the equations of atmospheric motion. *J. Comput. Phys.*, **1**, 119-143.
- Asselin, R. A., 1972: Frequency filter for time integrations. *Mon. Wea. Rev.*, **100**, 487-490.
- Bloomfield, P., 1976: *Fourier Analysis of Time Series: An Introduction*. Wiley, 258 pp.
- Grotjahn, R., 1979: Cyclone development along weak thermal fronts. *J. Atmos. Sci.*, **36**, 2049-2074.
- Haltiner, G. J., and R. T. Williams, 1980: *Numerical Prediction and Dynamic Meteorology*. Wiley, 477 pp.
- Kanamitsu, J., T. N. Krishnamurti and C. Depradine, 1972: On scale interactions in the tropics during northern summer. *J. Atmos. Sci.*, **29**, 698-706.
- Krishnamurti, T. N., 1971a: Observational study of the upper troposphere motion field during the Northern Hemisphere summer. *J. Appl. Meteor.*, **10**, 1066-1096.
- , 1971b: Tropical east-west circulations during the Northern Hemisphere summer. *J. Atmos. Sci.*, **28**, 1342-1347.
- Robert, A. J., 1966: The integration of a low order spectral form of the primitive meteorological equations. *J. Meteor. Soc. Japan*, Sec. 2, **44**, 237-245.
- Shapiro, L. J., 1980: The effect of nonlinearities on the evolution of barotropic easterly waves in a nonuniform environment. *J. Atmos. Sci.*, **37**, 2631-2643.
- Sweet, R. A., 1973: A generalized cyclic reduction algorithm. *SIAM J. Num. Anal.*, **10**, 506-520.
- Tupaz, J. B., R. T. Williams and C.-P. Chang, 1978: A numerical study of barotropic instability in a zonally varying easterly jet. *J. Atmos. Sci.*, **35**, 1265-1280.
- Williams, R. T., T. K. Schminke and R. L. Newman, 1971: Effect of surface friction on the structure of barotropically unstable tropical disturbances. *Mon. Wea. Rev.*, **99**, 778-785.

## Initial Distribution List

	No. Copies
1. Defense Technical Information Center Cameron Station Alexandria, Virginia 22314	2
2. Library, Code 0142 Naval Postgraduate School Monterey, California 93943	2
3. Research Administration, Code 012 Naval Postgraduate School Monterey, California 93943	1
4. National Science Foundation Division of Grants and Contracts Post-Award Project Branch Washington, D.C. 20550	2
5. Ms. Pamela Stephens Global Atmospheric Research Program National Science Foundation Washington, D.C. 20550	1
6. AIT-CCNAA Cooperative Science Program Division of International Programs National Science Foundation Washington, D.C. 20550	1
7. Professor C.-P. Chang, Code 63Cp Department of Meteorology Naval Postgraduate School Monterey, California 93943	5
8. Professor R.T. Williams, Code 63Wu Department of Meteorology Naval Postgraduate School Monterey, California 93943	2
9. Professor R.J. Renard, Code 63Rd Department of Meteorology Naval Postgraduate School Monterey, California 93943	1
10. Professor Gordon Schacher, Code 06 Dean of Sciences and Engineering Naval Postgraduate School Monterey, California 93943	1

END

FILMED

MARCH, 19 88

DTIC